High precision photometry of exoplanet transits and occultations - insights on hot atmospheres from ground-based optical and near IR observations

Lendl, Monika

UNIVERSITÉ DE GENÉVE
Département d'astronomie

FACULTÉ DES SCIENCES
Professeur Didier Queloz

High Precision Photometry of Exoplanet Transits and Occultations

-

Insights on Hot Atmospheres from Ground-based Optical and Near IR Observations

THÈSE

présentée à la Faculté des sciences de l'Université de Genève
pour obtenir le grade de Docteur ès sciences,
mention Astronomie et Astrophysique

par

Monika LENDL

de

SALZBURG (AUTRICHE)

Thèse N° 4649

GENÈVE
Observatoire de Genève
2014

UNIVERSITÉ
DE GENÈVE
FACULTÉ DES SCIENCES

Doctorat ès sciences
Mention astronomie et astrophysique

Thèse de *Madame Monika LENDL*

intitulée :

"High Precision Photometry of Exoplanet Transits and Occultations
-
Insights on Hot Atmospheres from Ground-based Optical and Near IR Observations"

La Faculté des sciences, sur le préavis de Monsieur D. QUELOZ, professeur ordinaire et directeur de thèse (Département d'astronomie), Monsieur S. UDRY, professeur ordinaire (Département d'astronomie), Madame C. CHARBONNEL, professeure associée (Département d'astronomie), Monsieur M. GILLON, docteur (Université de Liège, Département d'Astrophysique, Liège, Belgique) et Monsieur K. HENG, Professeur (Université de Berne, Center for Space and Habitability, Berne), autorise l'impression de la présente thèse, sans exprimer d'opinion sur les propositions qui y sont énoncées.

Genève, le 28 février 2014

Thèse - 4649 -

Le Doyen, Jean-Marc TRISCONE

N.B. - La thèse doit porter la déclaration précédente et remplir les conditions énumérées dans les "Informations relatives aux thèses de doctorat à l'Université de Genève".

Ce travail de thèse a donné lieu à des publications dont la liste se trouve à la page 141.

RESUMÉ

Le nombre de planètes confirmées au-delà du système solaire ne cesse de croître. Sur les plus de 1000 planètes acuellement connues, celles qui passent devant le disque stellaire ou *transitent*, jouent un rôle important dans l'étude des exoplanètes, car leurs masses et rayons peuvent être mesurés. Beaucoup de ces planètes qui transitent font partie de la famille des *Jupiters chauds*, des planètes qui ont une masse et un rayon similaires à Jupiter, mais qui orbitent autour de leur étoile hôte en moins de 10 jours. Occupant un espace de paramètres différent de celui du système solaire, ces planètes, de par leur existence, composition et évolution, représentent une des énigmes les plus intrigantes de l'astronomie contemporaine.

Parmi les plus de 300 planètes en transit confirmées à ce jour, environ 130 ont été découvertes par des projets de recherche de transits depuis le sol tels que WASP (Wide Angle Search for Planets). Bien que ces systèmes ne soient pas assez sensibles pour détecter des planètes de faible masse, ils excellent dans la découverte de Jupiters chauds autour d'étoiles brillantes. Ces planètes occupent une région favorable de l'espace de paramètres, car leurs transits sont fréquents et profonds. Du fait de la proximité de leur étoile hôte, ces géantes gazeuses possèdent des atmosphères chaudes et étendues, en faisant des cibles idéales pour l'étude de leurs atmosphères par spectrophotométrie de transmission et d'occultation.

Lors de l'occultation, le flux provenant de la face éclairée de la planète disparaît. Par comparaison des flux pendant et en dehors de l'occultation, le flux relative de la planète par rapport à l'étoile peut être mesurée. Des observations dans différentes bandes spectrales permettent de mesurer la distribution spectrale d'énergie de la planète. Il est ainsi possible de déterminer la structure atmosphérique de température, l'efficacité de redistribution de la chaleur, l'albédo, et de contraindre la composition atmosphérique. A partir de l'observation de transits à différentes longueurs d'onde, il est possible de mesurer la dépendance en longueur d'onde du rayon planétaire effectif. Celle ci témoigne essentiellement de la composition chimique et la stucture nuageuse de l'atmosphère planétaire.

Au cours de mon doctorat, j'ai contribué à la fois à la détection et à la caractérisation des Jupiters chauds. Dans le cadre de la confirmation de candidats planétaires fournis par WASP, j'ai été impliquée dans l'installation et l'exploitation d'une nouvelle caméra CCD sur le télescope Suisse Euler au Chili : EulerCam. Ce nouvel instrument a permis d'obtenir des observations photométriques à haute précision, qui ont ensuite conduit à la caractérisation de planètes ainsi que de candidats planétaires. Ces efforts ont contribué à de nombreuses découvertes de planètes, en particulier celle des deux Jupiters chauds WASP-42 b et WASP-49 b.

Grâce à la photométrie de haute précision avec EulerCam et à l'instrument en proche infrarouge de l'ESO *HAWK-I*, des occultations de l'une des planètes les plus chaudes connues, WASP-19 b, ont été mesurées. Ces observations ont mené, pour la première fois depuis le sol, à la détection d'une émission planétaire avec un télescope de la classe de 1 mètre. Elles ont également permis d'étendre la couverture en longueur d'onde du spectre d'émission de cette planète vers les courtes longueurs d'onde.

La dernière étape de cette thèse m'a menée vers la spectroscopie de transmission de la planète à faible densité WASP-49 b. L'instrument *FORS2* de l'ESO a été utilisé afin d'observer des transits avec la lumière dispersée spectralement. L'obtention de mesures simultanées de la profondeur du transit, du rouge optique au proche infra-rouge, a permis de contraindre la composition de l'atmosphère planétaire. Les modèles atmosphériques correspondant le mieux aux donnés sont ceux d'atmosphères présentant des brumes ou enrichies en carbone.

FOREWORD

The field of extrasolar planets is not only one of the youngest fields in astronomy but also one of its most dynamic and active. After all, foreign planets and the looming possibility of extraterrestrial life have attracted not only some of the brightest minds but also sparked popular interest in astronomy to a high. Yet, after about two decades of discovery-driven science the field has been undergoing a paradigm shift. In the late 1990s and early 2000s, each planet discovery was a major scientific achievement, and celebrated in its own right. The success of instruments such as HARPS and Kepler, have told us that planets really are *everywhere*, and these days a single new planet is really no big deal any more. Nowadays, we try to have a closer look at these planets, find out what they are made of, where they come from and why many of them are so different from our own Solar System.

In this new scientific direction, *transiting* planets have a prominent position. These planets, solely though chance, have their orbits aligned in a way that they pass directly between the observer (us) and their host star. During this passage, the *transit*, they obscure part of the host star creating a flux drop in the overall system brightness. Precise measurements of these lightcurves reveal many details about the planets, from its size and density on information on its orbital configuration and finally atmospheric properties such as composition, temperature and the prevalence of clouds.

The overall drive of the study of transiting exoplanets is directed towards the study of Earth-like planets. Yet, no Earth twin has been discovered yet, and albeit it might not take too long until the first exo-Earth is found, it will take a a great deal of technological advances until instruments will be precise enough to study it. Today, we hone our skills by working on targets more amenable to study, larger planets with more extended atmospheres: gas giants. In this respect nature has provided a fertile playground for us in the shape of *hot Jupiters*.

These gas giants are located very close to their host stars, orbiting so close-in that they complete a year in the course of as little as one (Earth-) day. The very existence of this class of planets has been a great surprise to the astronomical community and beyond, as they are nothing like the cold gas giants we know from the Solar System. And exactly this fact makes them not only amenable to study but also scientifically rewarding targets. Were these planets initially the same as our cold giants or do they have an entirely different origin? What happens to a giant planet at temperatures of more than 1000 K? How does its atmosphere adapt to the high level of irradiation? We have just started trying to answer some of these questions and many more. Yet, it seems that each answer is opening up many more questions.

These are exciting times for the field of exoplanets, and during the last four years I have done my best to add to this great effort. In this work, I summarize my contribution.

THANKS

Many people have had a place in the story of my PhD. Be it trough scientific exchange, lending me a hand in various non-scientific matters, and personal encouragement in times of doubt, the following people deserve their place here.

It has been a privilege and inspiration to have Didier Queloz as my supervisor. Didier, thank you for opening up many great opportunities for me, allowing me to develop my skills while guiding me through the labyrinth the scientific world can mean to a beginner. And most importantly, you have always had my back.

I am greatly indebted to Michaël Gillon who made me feel part of two instead of one research groups. Michael, thank you for providing me with ample data, sharing many of your tools with me and for putting me in charge of papers and proposals. You have been a true critic at times, and true critics are rare and priceless.

Being part of the Geneva exoplanet group has been a fantastic experience. I was lucky to exchange and discuss with this select group of people who I value not only for their scientific knowledge but also for remaining easily approachable even in moments of high stress, and a human environment of integrity and respect. I was very lucky to share office with Roi Alonso for the two first years. He has never tired of answering the most stupid of my questions, and shared many tricks and pieces of code with me. I benefited greatly from discussions with David Ehrenreich and Amaury Triaud, the latter of who initially motivated me to pursue a PhD in Geneva.

The WASP collaboration has played a big role throughout my PhD. It has been a privilege to contribute to this amazingly successful project along with many great astronomers and having the opportunity to learn from and work with them.

A group of fellow PhD students have made life at the observatory not only scientifically interesting but also fun. I have found friends rather than colleagues in many of you. During the lows of the last four years, there were always open doors, and laughs to be found. Thank you Richard Anderson, Janis Hagelberg, Marion Neveu, Ati Motalebi, David Martin, Pedro Figueira, Xavier Dumusque and many others.

Geneva observatory is a very pleasant place to work, and this atmosphere is maintained by a number of people who keep the place running as smooth as can be. Thanks go to everyone involved in the upkeep of the facilities, the IT group and the accountants. I would like to express my gratitude to the team involved in the installation of EulerCam. Without your work this thesis would not be existing in this form.

I would not have been able to go through this rollercoaster ride of a PhD without the continuing support from my family. Mein Dank gilt meinem Vater der mir nur zu kurz die Wunder der Natur zeigen konnte, und meiner Mutter die mir schon vor 20 Jahren meine ersten Astronomie Kinderbücher geschenkt hat. Du hast mich immer ermutigt hat, ob in Salzburg, Wien, Heidelberg oder Genf, meinen Weg zu gehen. Danke. Meinen Geschwistern Bernhard, Otmar und Barbara und ihren Familien (groß und klein) danke ich besonders dafür, dass sie die gefühlte Distanz von Wien und Genf um mindestens zwei Größenordnungen reduziert haben.

Words have only limited power to express my gratitude to Klaas Vantournhout. Klaas, you have shown me that the most beautiful parts of life are not found between the stars. Thank you.

Contents

Science makes people reach selflessly for truth and objectivity; it teaches people to accept reality, with wonder and admiration, not to mention the deep awe and joy that the natural order of things brings to the true scientist.

Liese Meitner

1 INTRODUCTION

Transiting exoplanets are those planets that have their orbits oriented in such a way that they pass in front of their host star as seen from an Earth-based observer. During transit, as they obstruct part of the stellar disc, a characteristic dip is created in the lightcurve of the star. From this lightcurve the planetary radius can be inferred, and together with a mass estimate, this gives an immediate measure of the planet's density. More detailed measurements can reveal many more details about the planet, it's orbit, atmosphere, but also provide some insights on the host star. More than 300 planets are known to be in this configuration at the time of writing, constituting a good body of objects from which the overall properties of planets can be studied. In this chapter, I will introduce the various means by which information can be obtained from a transiting planet.

1.1 Radial Velocities

A smile or two might escape the modern astronomer reading Christian Doppler's „Über das farbige Licht der Doppelsterne“ (Doppler 1842). The author not only attributes the colors of binaries to their orbital motion, but, well in context with the state of physics during the mid 1800s, also freely speculates about stars with masses several million times that of the sun and stars moving about at speeds exceeding the speed of light. Yet Doppler's fundamental principle that light emitted from receding sources is shifted towards longer wavelengths while light from approaching sources is blueshifted has had a profound impact on nearly all areas of astronomy and astrophysics. In the field of extrasolar planets the slight motion of the star about the system's center of mass has been an excellent tool for the discovery of planets. For an object receding at velocity V_r, the wavelength shift $\Delta\lambda$ with respect to the rest wavelength λ_0 can be expressed as

$$\frac{\Delta\lambda}{\lambda_0} = \frac{V_r}{c}, \tag{1.1}$$

provided $V_r \ll c$ (with c denoting the speed of light).

The use of the radial velocity (RV) technique for the discovery and confirmation of extrasolar planets is the direct extension of its application to spectroscopic binary stars of type SB1, i.e. binary stars that show only the components of the brighter star in their spectra while the fainter component remains hidden. A summary on this subject can be found e.g. in Hilditch (2001). One relies on the precise measurement of the position of spectral lines over time, which in turn measures the radial component of the stellar velocity relative to the observer. Using the true anomaly ν, the orbital eccentricity e and the longitude of periastron ω, the stellar RV variation V_r caused by the planet's orbital motion is described by

$$V_r = V_\gamma + K_1 \left[\cos(\nu + \omega) + e\cos\omega\right] \tag{1.2}$$

where the system velocity, usually a constant offset, is denoted by V_γ and K_1 is the RV amplitude. In order to compare the model (Equation 1.2) to RV values $V_{r,i}$ at given times t_i, one needs to convert the true anomaly ν to the eccentric anomaly E and compute the mean anomaly M via the Kepler Equation

(Kepler 1609)

$$M = \frac{2\pi}{P}\left(t - t_{\max}\right) = E - e\sin(E). \tag{1.3}$$

Here the orbital period P and the time of periastron passage and hence maximum RV $t_{\max}$ enter the system. From the RV amplitude K_1, the eccentricity e, and the period P, one can now calculate the minimum mass of the planet via

$$M_p \sin(i) = \left(\frac{P}{2\pi G}\right)^{\frac{1}{3}} K_1 M_*^{\frac{2}{3}} \sqrt{1-e^2}, \tag{1.4}$$

where the assumption $M_P \ll M_*$ has been made.

Thus, given an estimate of the stellar mass, RV orbits allow us to measure the product $M_p \sin i$, giving a minimum estimate for the planet mass. In the case of transiting configurations, the orbital inclination i is near 90°, and consequently the true planetary mass is very close to the minimum mass.

The precision on RV measurements has been improving by several orders of magnitude over the last two decades, going from precisions of $\sim$0.3 $\mathrm{km\,s^{-1}}$ in Duquennoy & Mayor (1991) down to the recent demonstrations of a precision down to 0.5 $\mathrm{m\,s^{-1}}$ by Dumusque et al. (2012). This remarkable improvements is due to refined methods, both on the hardware side, through the use of CCDs instead of photomultipliers, thermally isolating the instruments, but also in perfecting the data reduction procedures, including an optimization of the observing schedules to minimize the influence of stellar activity.

The Cross Correlation Technique

High precision RVs are measured by means of a mask that encodes the line positions in the stellar spectrum. Masks exist for many spectral types, and must be selected based on the nature of the target. The mask is then matched against the stellar spectrum for a wide range of RV values, and the total transmission is recorded at each step constructing the Cross Correlation Function (CCF). The minimum of the CCF, together with a calibration spectrum of e.g. a Th-Ar lamp, then gives the target's RV. Griffin (1967) pioneered this method by using actual stellar spectra. More recently, one has turned to binary masks that contain zero values at the positions of spectral lines (Baranne et al. 1996), and attributing weights to each line depending on its strength (Pepe et al. 2002). The CCF itself becomes a very precise measure of the mean spectral line shape, and can be used e.g. to detect signatures of stellar activity (Queloz et al. 2001).

1.2 Transiting Planets

Among the great number of exoplanetary systems, transiting planets have a privileged position. These systems are oriented in a way so that the planet passes right between its host star and the observer. As the host star is not resolved, the planetary transit manifests itself as a dip in the apparent brightness of the star, producing a characteristic shape in the stellar lightcurve. A large number of insights may be gained about planet and star, making these systems corner stones for our understanding of exoplanets. The total lightcurve shape is shown in Figure 1.1 , and I will walk the reader through the information it encodes in the following pages.

1.2.1 Transit Probability

The probability of any given planet to transit P_{tra} is strongly dependent on the planetary semi-major axis a_p:

$$P_{\mathrm{tra}} = \frac{(R_* + R_p)}{a_p} \cdot \frac{1 + e\cos(\pi/2 - \omega)}{1 - e^2} \approx \frac{(R_* + R_p)}{a_p}. \tag{1.5}$$

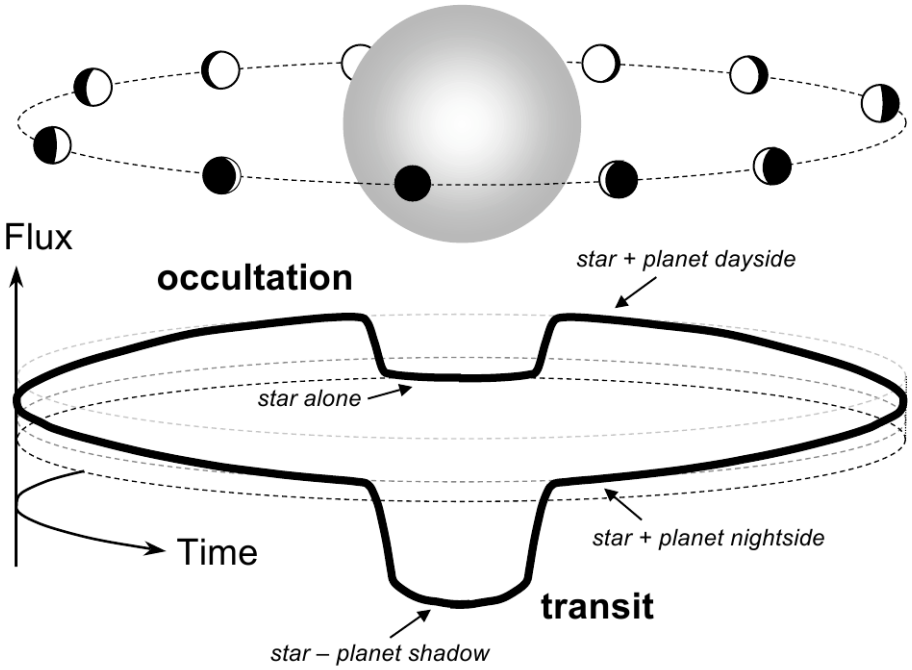

Figure 1.1 : The orbital phase together with a full orbit lightcurve of a transiting extrasolar planet. Transit, occultation and phase curve are labeled in the graphic. Note that the total brightness is slightly modulated as the flux component from the planet varies. Figure credit: Winn (2011)

Close-in orbits may have an inclinations substantially different form 90° while still showing a transit (for example WASP-19 b (Hebb et al. 2010) has an inclination of 79.5°). Earth-analogs however need their inclination to be larger than 89.734° for a transit to be visible to an Earth-based observer. This fact is important to keep in mind when discussing transit surveys (see Section 1.3), as they have a large inherent (yet well-understood) bias towards planets on close-in obits. The stellar and planet sizes play only a limited role in terms of transit probabilities. For non-zero eccentricity, the orbital orientation has considerable impact as the transit probability is large if the periastron is pointed towards the observer but decreases if the planet is near its maximum separation from the star during inferior conjunction.

1.2.2 The Transit Lightcurve

The transit lightcurve (shown in Figure 1.1) encodes many pieces of information on planet and host star, the most prominent being the **planetary radius**. Disregarding secondary effects discussed further below, the transit depth is determined by the amount of stellar flux blocked by the planet, i.e. the square of the ratio of the two radii:

$$DF_{\mathrm{tra}} = \left(\frac{R_p}{R_*}\right)^2. \tag{1.6}$$

Transit lightcurves provide a measurement of the **orbital inclination** i, and with this knowledge, equation 1.4 can be solved for the planet mass. With a mass estimate available for the planet, either from RV observations or through dynamical means, the planetary radius gives direct access to the precious quantity of the **planetary mean density**. This way it allows for a first glimpse towards the planets composition.

Next to its depth, the transit lightcurve is characterized by the four points of contact that mark the beginning (T_1) and end (T_2) of the ingress as well as the beginning (T_3) and end (T_4) of the egress (see Figure 1.2 for a sketch of the transit geometry). The second and third points of contact are inexistent

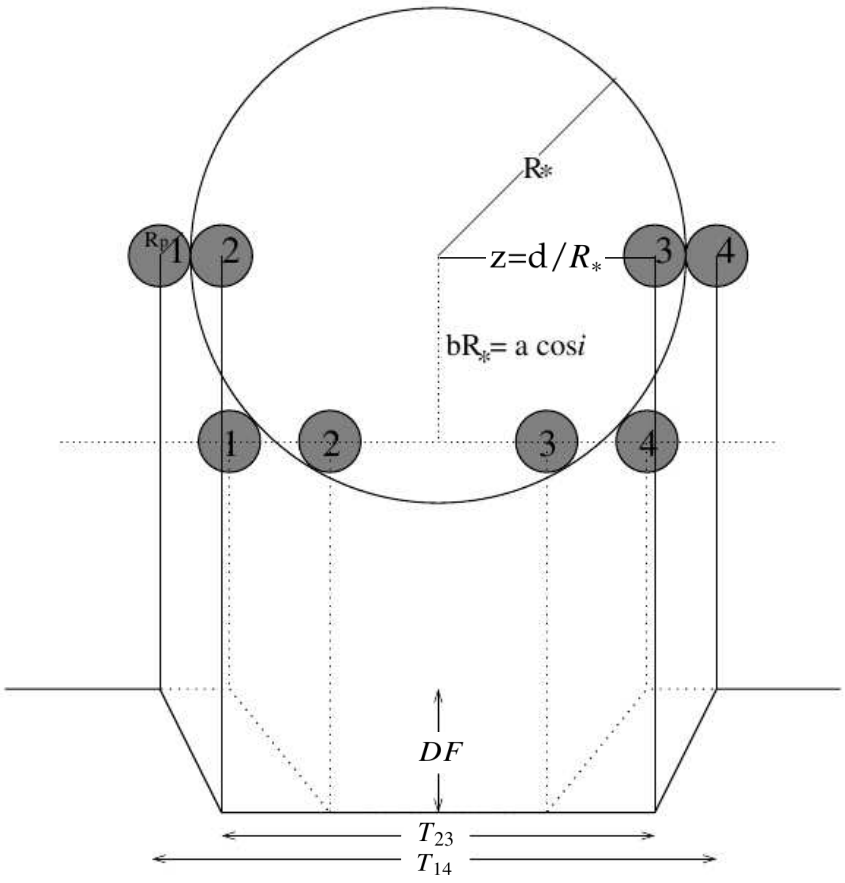

Figure 1.2 : The transit geometry showing the four points of contact as well as the definition of the impact parameter. The theoretical light curve is presented disregarding limb-darkening. The different lightcurve shapes of a central transit ($i = 90\,\mathrm{deg}$, solid line) and an transit at higher stellar latitudes (dotted line) are shown. The figure has been adapted from Seager & Mallén-Ornelas (2003).

for the rare case of a grazing transit where the planet is never located entirely in front of the stellar disc. Provided an estimate for the planetary period P is known (e.g through RV measurements or the observation of several subsequent transits), relatively straight-forward geometrical considerations lead to the following expressions for the total transit duration T_{14} and the time between second and third contact T_{23}:

$$T_{14} = \frac{P}{\pi} \arcsin \left[\frac{R_*}{a} \left(\frac{\left[1 + (R_p/R_*)\right]^2 - \left[(a/R_*)\cos i\right]^2}{1 - \cos^2 i} \right)^{\frac{1}{2}} \right] \tag{1.7}$$

$$T_{23} = \frac{P}{\pi} \arcsin \left[\frac{R_*}{a} \left(\frac{\left[1 - (R_p/R_*)\right]^2 - \left[(a/R_*)\cos i\right]^2}{1 - \cos^2 i} \right)^{\frac{1}{2}} \right] \tag{1.8}$$

These equations or their simplified versions (Sackett 1999, Seager & Mallén-Ornelas 2003) are giving the planetary **semi-major axis** a/R_*, **radius** R_p/R_* and **orbital inclination** i. To simplify certain expressions, one often one uses the **transit impact parameter** $b = a/R_* \cos i$ that gives the position of the transit chord on the stellar disc. One major drawback is that transit lightcurves do not provide us with physical values for the planetary radius and semi-major axis, but the relative quantities with respect to

the stellar radius. As a consequence we need to resort to other means such as stellar evolution models to obtain true physical values. Usually these models are the main error source for the determination of the planetary parameters, and obtaining stellar radii (and masses) with the necessary precision remains one of the challenges.

Some insights however may be gained from the transit lightcurves themselves. As shown by Seager & Mallén-Ornelas (2003), by using Kepler's third law, one can calculate the **stellar mean density** ρ_* via

$$\frac{\rho_*}{\rho_\odot} = \frac{M_*/M_\odot}{\left(R_*/R_\odot\right)^3} = \frac{4\pi^2}{GP^2}\left(\frac{a}{R_*}\right)^3 . \tag{1.9}$$

This independent knowledge of the stellar mean density has a multitude of practical applications. It may be used together with stellar evolutionary paths to determine the stars evolutionary state and constrain the system age. In combination with the stellar effective temperature and metallicity, it can be used to infer the stellar mass and radius (Enoch et al. 2010), using a calibration based on a large sample of eclipsing binaries with well known parameters (Torres et al. 2010). The stellar mean density is also frequently used to assess the quality of planet candidates, as unphysical values point towards false positives, or low values indicate large evolved stars requiring the transiting object to be outside the planetary size range. Multiplanet systems may also be verified as compatible stellar densities need to be inferred from each transiting component.

If the RV semi-amplitude is known, the **planetary surface gravity** g_P may be inferred from the lightcurve parameters directly (Southworth et al. 2007):

$$g_p = \frac{2\pi}{P}\frac{\sqrt{1-e^2}K_1}{\sin i}\left(\frac{a}{R_*}\right)^2 . \tag{1.10}$$

Stellar Limb Darkening

When dealing with real data, one immediately notices that transit lightcurves are not completely flat during transit but show a round "U" shape, which is particularly pronounced for observations at short optical wavelengths (see Figure 1.3 for an example of a multi-band lightcurve). This is due to **stellar limb darkening**, i.e. the decrease in brightness observed towards the edge of the stellar disk. At the midpoint of the stellar disk, the line of sight is normal to the stellar surface, but closer to the limb, the stellar surface is viewed under an angle $\pi/2 - \theta$, where θ is the angle between the surface normal of the star and the line of sight. This translates to different stellar density and temperature structures in the line of sight, and a given optical depth corresponds to layers of different temperature, depending on the viewing angle. Towards the limb of the star, the emission stems from cooler and thus less emissive regions, creating the apparent dimming of the stellar limb (Schwarzschild 1906, Milne 1921).

There are several parametrizations for stellar limb darkening, the most frequently used is *quadratic limb darkening*,

$$\frac{I(\mu)}{I(1)} = 1 - a\left(1-\mu\right) - b\left(1-\mu\right)^2, \tag{1.11}$$

where the position on the stellar surface is given by $\mu = \cos\theta$. $I(1)$ is the specific intensity at the center of the disc, and a and b are the two quadratic limb-darkening coefficients, usually obtained from stellar models (e.g. Claret 2000, Claret & Bloemen 2011).

Model Lightcurves

Model transit lightcurves, including the effect of stellar limb darkening, need to be calculated in order to make comparisons of models and data. Mandel & Agol (2002) have provided the most widely used

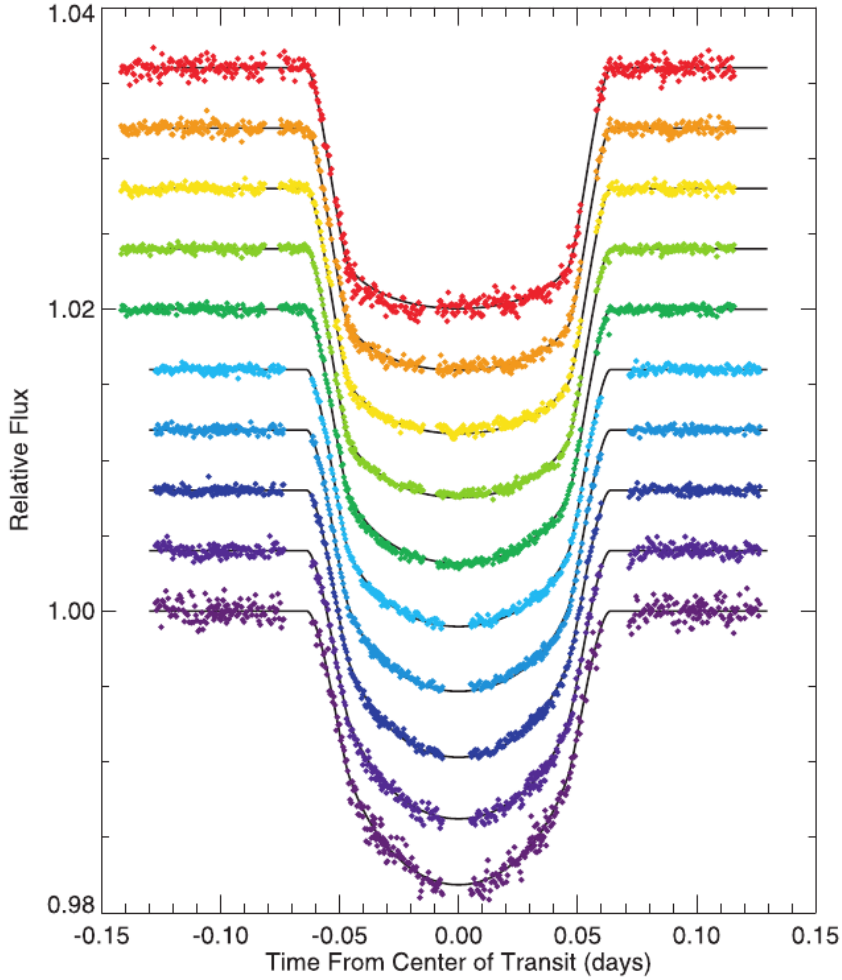

Figure 1.3 : Transit lightcurves of HD 209458 observed with STIS on the Hubble Space Telescope (Knutson et al. 2007c). The data cover a wavelength range between 290 (bottom) and 1030nm (top), showing clearly the varying impact of stellar limb darkening.

routines to calculate model lightcurves based on inputs of the the planet-star radius ratio R_p/R_* and the stellar limb-darkening coefficients. The positioning of the planet in front of the stellar disk is defined via the parameter $z(t) = d(t)/R_*$, where d is the projected separation between the star and planet centers (see Figure 1.2). For a circular orbit of a given period P, inclination i, and semi-major axis a, z(t) is calculated via

$$z(t) = \frac{a}{R_*}\left[\left(\sin\left(\frac{2\pi}{P}t\right)\right)^2 + \cos(i)\left(\cos\left(\frac{2\pi}{P}t\right)\right)^2\right]^{\frac{1}{2}}. \tag{1.12}$$

The determination of the most probable planet parameters based on a set of data points is usually carried out via an Markov chain Monte Carlo approach (see e.g. Tegmark et al. 2004). This approach relies on creating chains of tens of thousands of model evaluations, while the input parameters are vaired from each accepted link to the next. At each link, this merit function, e.g. a χ^2, evaluates the fit of the model to the data. If the new result is a better match to the data than the previous one, the input parameters are accepted and are used as the basis for the next link in the chain. If the fit to the data is worse than at the previous step, the input parameters only occasionally get passed along to the next step. Finally, the posterior probability density distribution of the transit and physical parameters is represented by the parameters of all accepted links in several long MCMC chains.

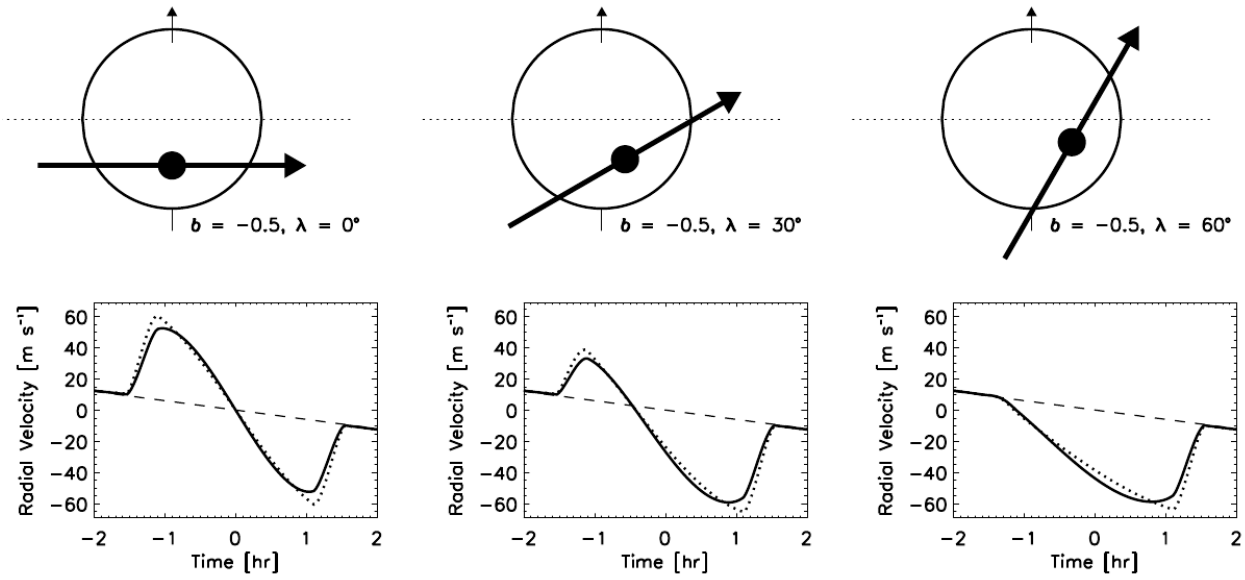

Figure 1.4 : The effect of different projected spin-orbit angles on the transit RV curve. Upper panel: three different alignments producing identical transit lightcurves (from left to right): aligned, slightly misaligned, and heavily misaligned. Lower panel: The resulting the RV anomalies during transit. Figure credit: Winn (2011).

Stellar Activity

Another factor impacting the transit lightcurve shape can be stellar activity. Similar to limb-darkening, active stellar regions impact the uniformity of the stellar surface brightness. Dark spots or bright faeculae are usually fairly localized areas on the star, and cause short irregularities during transit. If several consecutive transit of the same planet are observed, the movement of spot signatures in the lightcurve can be used to infer the relative orientation of the stellar spin and planetary orbit axes (Sanchis-Ojeda et al. 2011, Nutzman et al. 2011).

Transit Timing Variations

High-quality photometry of transits gives a precise measurement of the mid-transit time T_c. If other massive bodies, such as additional planets or moons are present in the system, their gravitational impact causes the time between successive transits to vary. **Transit Timing Variations** were proposed initially (Agol et al. 2005, Holman & Murray 2005) as a means to detect additional low-mass planets near mean-motion resonances, but have proven just as useful for the determination of planet masses in the absence of RV measurements (Holman et al. 2010).

1.2.3 Transits Observed in Radial-Velocity

In recent years a great interest has developed in RV observations of transits. As the planet transits across the stellar disc, it obscures light that has a Doppler shift corresponding to the radial component of stellar rotation at the position of its emission. As there is flux of a certain RV missing, an asymmetry in the stellar CCF is produced and the final RV is slightly shifted. Depending on the path the planet takes across the stellar disc, the signatures in the RV curve take different shapes, that allow to constrain the angle between the projected stellar rotation and planetary orbit axes. See Figure 1.4 for examples of three configurations and their respective RV signatures. This effect has been first observed for the bright binaries Algol and β Lyrae by Rossiter (1924) and McLaughlin (1924), and is hence known as

the "Rossiter McLaughlin effect". Its amplitude depends largely on the projected stellar rotation speed $V_* \sin(I_*)$ making the effect more pronounced for planets orbiting relatively fast rotating stars. The first observation of this effect for exoplanets has been carried out by Queloz et al. (2001), and since then has been detected for a large number of systems (e.g. Winn et al. 2006, Narita et al. 2007, Triaud et al. 2010).

1.2.4 Occultations

Typically half an orbit after transit the planet finds itself at superior conjunction. Just as we did for the transit, we may describe the probability of the planet passing behind the stellar disc as

$$P_{\rm occ} = \frac{(R_* + R_p)}{a_p} \frac{1 + e\cos(3\pi/2 - \omega)}{1 - e^2}. \tag{1.13}$$

This expression is exactly the same as that for a transit, but we replace the true anomaly at transit ($\nu_{\rm tra} = \pi/2 - \omega$) with the true anomaly at occultation ($\nu_{\rm occ} = 3\pi/2 - \omega$). It is clear that transiting planets having a low orbital eccentricity are also undergoing occultation.

As the planet passes behind the star, one can measure a flux drop $DF_{\rm occ}$ caused by the elimination of the flux component stemming from the planet. This signal scales as

$$DF_{\rm occ} = \frac{\pi R_p^2}{\pi R_*^2} \frac{I_p}{I_*} = DF_{\rm tra} \frac{I_p}{I_*}, \tag{1.14}$$

where I_p and I_* are the planetary and stellar disc-averaged intensities at the time of occultation. These two quantities are wavelength dependent, and thus the occultation amplitude strongly varies with wavelength. While the stellar intensity is solely determined by the stellar spectrum, the planetary intensity is made up from two components: the planets thermal radiation and the scattered starlight. The thermal component may be estimated by defining the **planetary equilibrium temperature**

$$T_{\rm eq} = T_{\rm eff,*} \left[f(1 - A_B) \right]^{\frac{1}{4}} \left(\frac{R_*}{a} \right)^{\frac{1}{2}} \tag{1.15}$$

where A_B is the planetary Bond albedo, and f ($\frac{1}{4} \leq f \leq \frac{2}{3}$) gives the distribution efficiency of energy from the planetary day to the night side (Seager et al. 2005, Burrows et al. 2008). Assuming both star and planet emit as black bodies, the occultation depth is given by the ratio of the two black bodies, integrated over the observed wavelength range. Since the planet is cooler than the star, its emission peak lies further in the red. There the contrast between star and planet is decreased and thus the occultation is more pronounced at longer wavelengths, as illustrated in Figure 1.5 .

Of course star and planet are not perfect black bodies, and it is the deviation of the planetary SED from a perfect black body that is used to infer its thermal structure and chemical abundances. This will be discussed in detail in Section 2.4. Yet, one often refers to the **brightness temperature**, defined as the temperature derived from a specific occultation depth measurement, assuming the planet is a black body.

At short wavelengths the dominant component is the **reflected stellar light** rather than the planetary emission. Here, the occultation depth is given by the planetary geometric albedo A_g together with the planetary radius R_p and orbital separation a:

$$DF_{\rm occ,re} = A_g \left(\frac{R_p}{a} \right)^2. \tag{1.16}$$

In principle this quantity may be in the order of several 100 ppm given a large close-in planet, but hot massive planets have proven to be rather dark, with albedoes mostly below 0.2 (Heng & Demory 2013). On the contrary, the albedos of Jupiter and Saturn are 0.5 and 0.48, respectively (Karkoschka 1994).

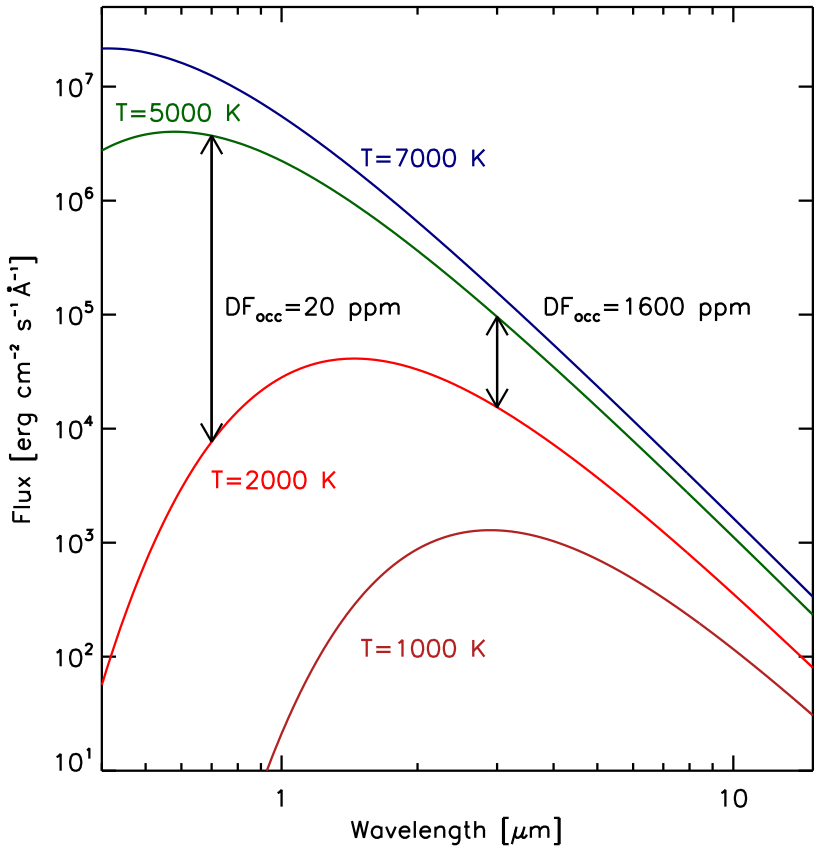

Figure 1.5 : Black body emission for objects of (from top to bottom) 7000 K, 5000 K, 2000 K, and 1000 K, the lower two curves are representative for hot irradiated planets, the upper two curves represent planet host stars. The vertical arrows indicate variations in the flux ratio, and thus the wavelength dependency of the occultation depths. Occultation depths of 20 ppm at 0.7 μm, and 1600 ppm at 3 μm have been calculated assuming a transit depth of 1%, a planetary temperature of 2000 K and a stellar temperature of 5000 K.

Eccentricity Constraints from Transit and Occultation Timing

From the relative timing of occultation and transit measurements one may obtain a measurement of the orbital eccentricity. Intuitively this is quite evident as, for $e \neq 0$ and $\omega \neq \pm\pi/2$ the positions of transits and occultations are not aligned symmetrically along the orbit when compared to the line of sight. For $e \neq 0$, $\omega \neq 0$ and $\omega \neq \pi$, the planet has different speeds during occultation and transit, and thus occultation and transit have different durations. The following expressions describe these using the measurable parameters:

$$\frac{\pi}{2P}\left(T_{c,\mathrm{trans}} - T_{c,\mathrm{occ}} - \frac{P}{2}\right) = e\cos\omega, \tag{1.17}$$

$$\frac{(T_{14,\mathrm{occ}} - T_{14,\mathrm{tra}})}{(T_{14,\mathrm{occ}} + T_{14,\mathrm{tra}})} = e\sin\omega, \tag{1.18}$$

where $T_{c,\mathrm{trans}}$ and $T_{c,\mathrm{occ}}$ refer to the mid-transit and mid-occultation times, and $T_{14,\mathrm{tra}}$ and $T_{14,\mathrm{occ}}$ refer to the duration of transit and occultation. The second parameter can usually not be calculated with the same precision as the first one as it relies more strongly on the precise measurement of the eclipse shape instead of the overall timing.

If RV data are available next to eclipse photometry, the combination of photometric and RV data provide an additional constraint on the eccentricity. As the transit occurs at a true anomaly $\nu = \pi/2 - \omega$,

the Keplerian RV at mid-transit becomes (using Equation 1.2)

$$V_r(T_{c,\mathrm{trans}}) = V_\gamma + K_1 e \cos\omega. \tag{1.19}$$

A precise timing of the transit with respect to the RV curve thus provides a supplementary measurement of $e\cos\omega$[1].

1.2.5 Exoplanet Phase Curves

If the photometric observations cover not only the eclipses but extend throughout a significant part of the orbital period of the system, the **planetary phase curve** is recorded. For these observations, photometry of very good precision and temporal stability needs to be acquired, as is only possible with space-based facilities such as CoRoT (Baglin et al. 2006), Kepler (Borucki et al. 2010) or Spitzer (Werner et al. 2004). In this regime the flux emerging from the planetary night side can no longer be neglected, and the difference of day and night side fluxes (F_{day} and F_{night}) give the phase curve amplitude DF_{phase},

$$DF_{\mathrm{phase}} = \frac{F_{\mathrm{day}} - F_{\mathrm{night}}}{F_*} = A_g \left(\frac{R_p}{a}\right)^2 + \frac{I_{P,\mathrm{day}} - I_{P,\mathrm{night}}}{I_*}\left(\frac{R_p}{R_*}\right)^2. \tag{1.20}$$

If the scattered component is neglected, I_p and I_* are the planetary and stellar disc-averaged intensities and A_g is the geometrical albedo. Depending on the wavelength of observation either the reflective (first) term or the thermal (second) term dominates. Again, we may approximate the emission from star and planet as black body radiation. Yet this time, we allow the planet to have unequal flux on day and night sides, transforming Equation 1.21 to

$$\frac{F_{\mathrm{day}} - F_{\mathrm{night}}}{F_*} = \frac{B\left(T_{\mathrm{day}}\right) - B\left(T_{\mathrm{night}}\right)}{B\left(T_*\right)}\left(\frac{R_p}{R_*}\right)^2, \tag{1.21}$$

where $B(T)$ refers to the Planck function temperature T. This lets us define the day and night side brightness temperatures T_{day} and T_{night}. Note that phase curves are not limited to transiting planets, and phase curves have been detected for non-transiting planets (e.g. Harrington et al. 2006).

Further Effects

Next to the planetary phases, two other effects are present in the light curves:

Doppler beaming describes the modulation of the stellar flux induced by the reflex velocity of the host star. The emitted radiation is beamed in the direction of stellar motion, thus creating an effect with a period equal the planetary orbital period but offset from the phase curve by $\sim \pi/2$ as the maximum light corresponds to the time of maximum stellar motion directed towards the observer.

Ellipsoidal variations occur if the planet's gravitational influence is large enough to distort the stellar shape. This means that the emissive stellar surface facing towards the observer has a variable size and thus variations in the lightcurve are created. These variations occur with a period half the planetary orbital period.

Both Doppler beaming and ellipsoidal variations depend on the planetary mass, and in turn if these effects are detected, the planetary mass can be inferred (e.g. Barclay et al. 2012). Finally, if occultation lightcurves of very good quality are available, the shape of ingress and egress together with the phase curve map the 2D brightness distribution on the planet surface (de Wit et al. 2012, Majeau et al. 2012).

1.2.6 Multi-color Observations

Most observational advances on the atmospheres of transiting exoplanets have been the result of measuring the parameters described above at several wavelengths and then using models for the structure and composition of planets to try to explain the observations.

[1] Amongst others, the detection of the eccentric orbit of WASP-38 b (Barros et al. 2011) relied on this constraint.

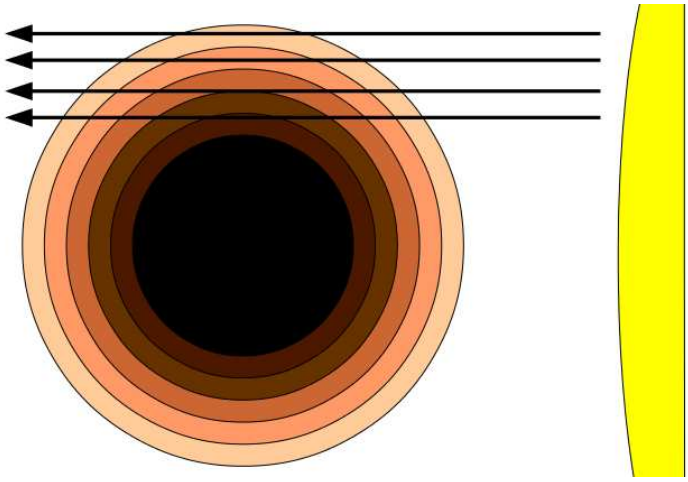

Figure 1.6 : The geometry of stellar radiation and planetary atmosphere as probed during transit. The stellar radiation is predominantly passing through the outer layers of the planetary atmosphere and hence only the top layers of the planetary atmosphere can be studied with this technique.

Multi-color Transits

So far we have made the assumption that the planetary radius, and thus the ratio R_p/R_* is wavelength-independent. However, this is not accurate for planets possessing an atmosphere. During transit, the stellar radiation passes through the planetary atmosphere, and, depending on the atmosphere's extension, temperature and composition, the transmission varies as a function of wavelength. This promotes the definition of the wavelength- dependent effective planetary radius $R_{p,\lambda}$ via

$$DF_\lambda = \left(R_{p,\lambda}/R_*\right)^2 . \tag{1.22}$$

Measurements of this quantity across many wavelengths are referred to as the **planet's transmission spectrum**. As the starlight passes through the planetary atmosphere at the day-night terminator region, it samples the atmosphere at a lower temperature than occultation measurements. Also, as the stellar radiation passes through the planetary atmosphere in a tangential direction to the planetary surface, it mostly samples the outer layers of the atmosphere (see Figure 1.6).

The size of the transmission signal can be estimated via the planetary atmospheric scale height H. H is the distance over which the atmospheric density decreases by a factor of e, and can be calculated via

$$H = \frac{k_b T_p}{\mu_m g_p} , \tag{1.23}$$

where k_b is the Boltzmann constant, T_p is the planetary temperature, μ_m is the (atmospheric) mean molecular weight and g_p is the planetary surface gravity. For the Earth and Saturn this value is ~8.5 km and ~59.5 km, respectively. A feature of an amplitude of one atmospheric scale height then leads to a variation in the transit depth of

$$DDF = 2\left(\frac{R_p}{R_*}\right)^2 \frac{H}{R_p} . \tag{1.24}$$

This means that the largest variations are obtained for planets showing deep transits and having a large atmospheric scale height, i.e. hot planets with a low atmospheric mean molecular weight and a small mass. For hot planets with a mass near that of Saturn, the amplitude reaches several 100 ppm, while for an Earth twin the predicted amplitude is near 1 ppm.

The observable signatures in the planetary atmosphere are of various origin, and manifest themselves at different wavelengths. In Figure 1.7 , example transmission spectra are shown. The predicted features for a clear hot Jupiter atmosphere are the following:

- At wavelengths bluewards of 500 nm, the effective planetary radius increases due to Rayleigh scattering by e.g. H_2.
- The optical is dominated by the prominent absorption features of Na (589 nm) and K (770 nm), or (for hot atmospheres) TiO and VO.
- At wavelengths redwards of 900 nm, molecular features of water, methane, and carbon monoxide are seen.

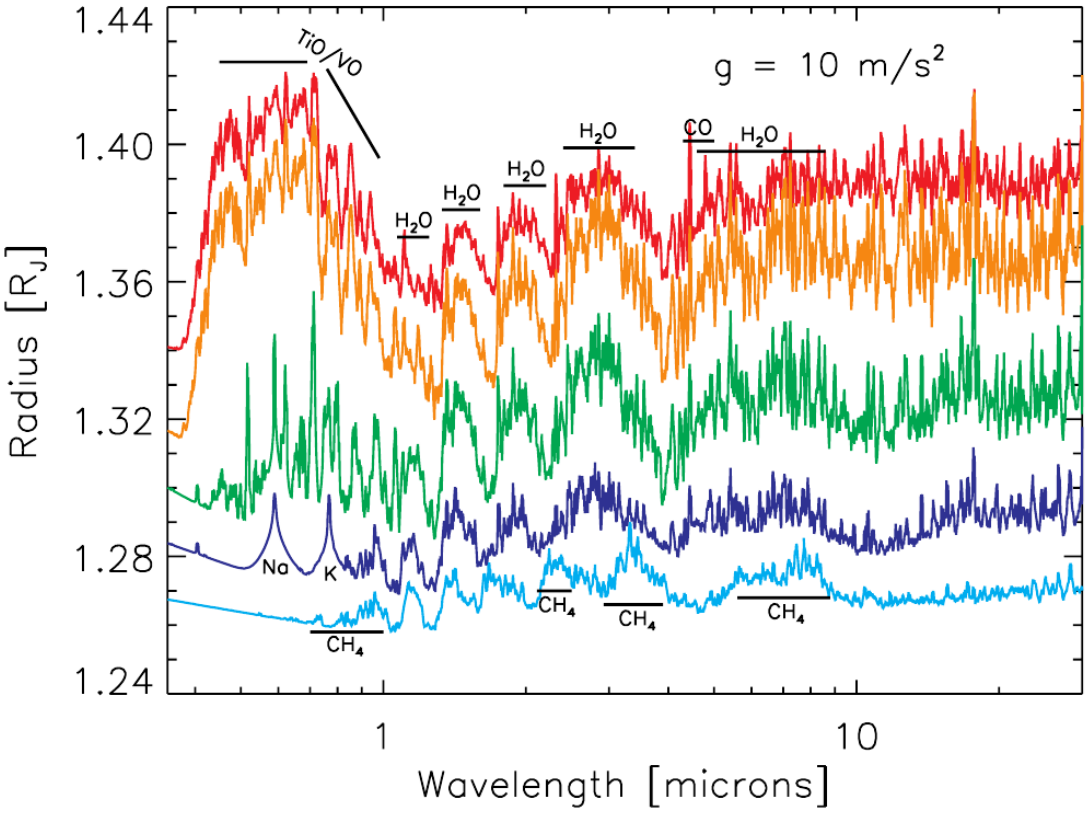

Figure 1.7 : Examples of predicted transmission spectra for a Jovian planets with equilibrium temperatures of 2500, 2000, 1500, 1000, and 500 K (from top to bottom). The planets are assumed to have a clear atmosphere, a radius of 1.25 Rjup at a pressure level of 10 bar, and a gravity acceleration of 10 $\mathrm{m\,s^{-2}}$. The prominent absorption features are labeled. Rayleigh scattering is visible as a steady rise at short wavelengths for the lower curves, that also show the Na and K features. At 2500 and 2000 the optical opacities are dominated by TiO and VO. The main contributors in the near IR are H_2O, CO and, at lower temperatures, CO_2. Figure credit: Fortney et al. (2010).

The strongest of these features, in particular the alkali absorptions, can produced features with amplitudes of several atmospheric scaleheights in the observed spectra. Next to the actual atmospheric composition, several factors such as clouds and haze can drastically influence the planetary transmission spectra. I will provide a more detailed picture in Section 2.3.

In order to measure the transmission spectrum of an exoplanet, one needs to obtain transit lightcurves at as many wavelengths as possible. However a limitation in this approach can be set by the host star itself. Since each transit is essentially a measurement of the amount of light blocked by the planet, a variation in the stellar brightness outside the transit chord can cause slight changes in the transit depth. Star spots can be the origin of these kind of variations. E.g. a variation of the overall stellar brightness by 1% can induce an effect in the measured transit depth of 100 ppm, right at the level of atmospheric signatures. To be as independent as possible from the effects of stellar activity it is preferable to obtain

simultaneous radius measurements at several wavelengths. One approach to obtain such measurements is *spectrophotometry*, and I will present my own spectrophotometric work in Chapter 6.

Multi-color Occultations

I have already noted in Section 1.2.4 that the occultation depth is highly dependent on the wavelength of observation, with generally larger signals in the IR than at optical wavelengths. This is a simple consequence of the stellar and planetary SEDs.

Compared to transmission spectra, occultations give a quite complemetary view on the planetary atmosphere. Here, we are not observing the stellar radiation passing through the planetary atmosphere but measure the planetary emission. Occultations give the ratio of planet and stellar fluxes, so in order to derive the **planetary emission spectrum**, stellar models need to be assumed, as can be done using the models of Castelli & Kurucz (2004). The emission spectrum is stemming from the hot planetary dayside, which can (depending on the energy redistribution efficiency) be significantly different from the atmosphere at the day-night terminator with regard to temperature and chemistry. The occultation amplitude depends largely on the planetary temperature and thus the most favorable systems for the observation of occultations are those with very hot, large planets on close-in orbits (i.e. P $<$ 2d).

The shape of the planetary emission spectrum is defined by the atmospheric thermal structure and chemical composition. Particularly the presence of a thermal inversion (i.e. an increase of temperature in the outer part of the planetary atmosphere) determines if the molecular signatures are shown as peaks or depressions in the emission spectrum. The gradient of the vertical temperature structure manifests itself in the amplitude of the molecular features. As an example, the near-IR transmission spectrum of WASP-19 b is shown in Figure 1.8 together with models of different composition and thermal structure. The total planetary emission spectrum then is a combination of these molecular components. I provide a more detailed description of the astrophysical inferences from exoplanet emission spectroscopy in Section 2.3.

Occultations are less dependent on fluctuations of the stellar brightness. For example, to achieve a variation of 100 ppm on a 1000 ppm occultation, the stellar brightness needs to increase by of 10%, ten times more than the analogous case for the transmission signal. This means that simultaneous observations are not as imperative for planetary emission specta as for transmission spectra. However if one hopes to go to measuring time-dependent variations in the planetary SED, simultaneous observations will be a great advantage.

1.3 Finding Transiting Planets

1.3.1 Targeted Searches

The importance of transiting planets has been recognized early on (Lardner 1858, Belorizky 1938, Struve 1952). The first planets have been found from RV searches (Mayor & Queloz 1995, Marcy & Butler 1996), among them several hot Jupiters with reasonable transit probabilities. The most straight forward approach then was to monitor these systems photometrically for transits. The awaited success arrived with the discovery of the transiting 0.7 M_J planet HD 209458 b (Charbonneau et al. 2000, Henry et al. 2000, Mazeh et al. 2000). At this point it was finally possible to measure the true mass and the radius of an extrasolar planet confirming its nature as a short-period gaseous planet.

Since this discovery several surveys have routinely checked RV planets for transits and several other remarkable transiting planets have been found. The most prominent transiting planets discovered in conjunction with RV surveys are:

- HD 209458 b (Charbonneau et al. 2000, Henry et al. 2000, Mazeh et al. 2000) is a hot Jupiter orbiting a $V = 7.65$ mag G0 host star. Owing to its brightness this is one of the most intensely studied planets. Together with HD 189733 b it makes up the *great duo* of bright hot Jupiters with well-characterized atmospheres.

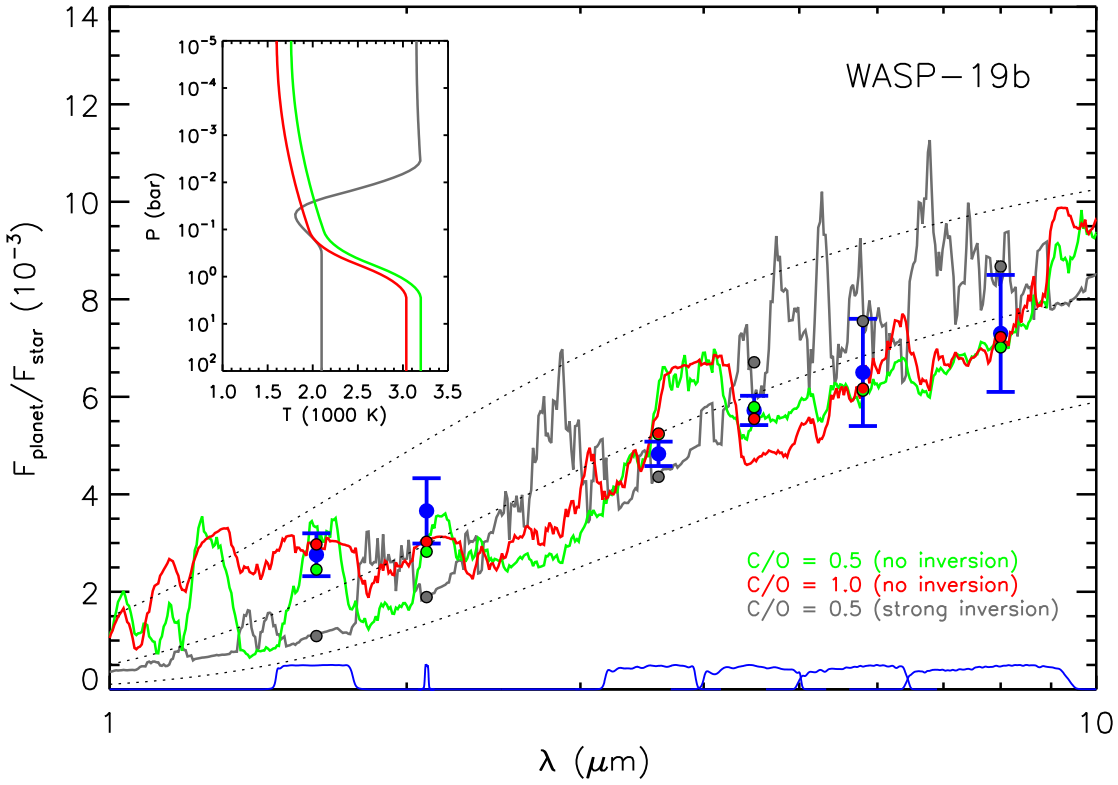

Figure 1.8 : The *Spitzer* broad band emission spectrum of WASP-19 b as presented by Anderson et al. (2013b). A model containing a temperature inversion (i.e. the temperature increasing outwards in the atmosphere) is shown in grey, while models with no inversion but different elemental abundances are shown in color (red: carbon-rich, green: oxygen-rich). Note how the grey model is showing emission peaks. The blue curves indicate the *Spitzer IRAC* channel sensitivities.

- HD 189733 b (Bouchy et al. 2005), a hot Jupiter orbiting a K dwarf. Due to its favorable radius ratio and bright host star, this planet has become a benchmark target for atmospheric studies.
- HD 80606 b (Naef et al. 2001, Moutou et al. 2009), a highly eccentric (e=0.93) 3 M_J planet on a 111 d orbit.
- GJ 436 b (Butler et al. 2004, Gillon et al. 2007), a Neptune-mass $M_P = 23M_\oplus$ transiting planet, and to date the closest (d=10.2 pc) transiting system.
- 55 Cnc e (McArthur et al. 2004, Demory et al. 2011, Winn et al. 2011), a $7.8M_\oplus$, $2.1R_\oplus$ super-Earth in a multi-planet system transiting a K0 star. The $V = 5.95$ mag host star is the brightest star known to host a transiting planet.

1.3.2 Ground-based Transit Searches

In principle transiting planets can be found in any set of observations that monitor a large number of stars over a time span of several weeks at a cadence and precision that allows the detection of repetitive flux decreases by 1%. The Optical Gravitational Lensing Experiment OGLE (Udalski et al. 1992) is such a survey, initially aimed at the detection of gravitational lensing in the galactic bulge. A handful of planets have been found in OGLE data (Konacki et al. 2003, Bouchy et al. 2004, Konacki et al. 2004, Pont et al. 2004, amongst others).

As the efficiency of transits as a detection method for planets was evident, several surveys optimized for the detection of transiting planets were starting up: the relatively short-lived TrES (Alonso et al.

2004), XO (McCullough et al. 2005) projects and finally the two most prominent large-scale surveys HAT (Bakos et al. 2004) and WASP (Pollacco et al. 2006). While the above surveys started in the North, both HAT and WASP have expanded their facilities to southern hemisphere (Wilson et al. 2008, Bakos et al. 2013), uncovering the planets located in in the Southern sky. The key objective in all of these transit surveys is to monitor large fields using small ($\sim$10 cm) aperture telescopes and then identify the candidates showing periodic dips in their lightcurves. These candidates are then followed up to reject instrumental or astrophysical false positives. The most common astrophysical false positives are eclipsing binaries blended with a third star, eclipsing binaries having a large radius ratio, and grazing eclipsing binaries. Instrumental false positives can be caused by bad pixels, flat field problems or anomalous data clumping. I will give a more detailed description of the WASP survey, which I have been involved in in Chapter 4.

1.3.3 Space-based Transit Searches

Naturally the two major disadvantages of ground-based transit surveys are atmospheric limitations on the photometric precision and the diurnal/seasonal gaps in the data. Both these limitations can be avoided by going to space. In the field of exoplanets, there have been two satellite missions contributing immensely to the discovery and understanding of planets.

Convection, Rotation and planetary Transits (CoRoT)

The CoRoT satellite has been launched in December 2006 with the aim to study stellar properties and find planetary transits. Until contact to the satellite was lost in December 2012, *CoRoT* was highly productive and searched more than 20 fields for planetary transits. All fields are located within the two visibility cones often called *CoRoTs* "eyes" (Figure 1.9), one directed towards the Galactic center and one directed towards the anti-center.

CoRoT has pioneered space-based high precision photometry, and has discovered several highly valuable transiting systems. The target stars have a brightness in the range of $V = 12 - 16$ mag, making ground-based RV follow-up using spectrographs such as HARPS (Mayor et al. 2003) challenging. However, it has been successful for a considerable number of objects. Undoubtedly the most spectacular discovery of *CoRoT* has been that of the first transiting super-Earth, CoRoT-7b (Léger et al. 2009, Queloz et al. 2009), but also CoRoT-9 b (Deeg et al. 2010), a $P = 95$ d transiting planet with a relatively low (e=0.11) eccentricity, and CoRoT-3 b (Deleuil et al. 2008), a $M_P = 21 M_J$ object in the brown dwarf desert.

The instrumental point spread function (PSF) of *CoRoT* is quite particular. The light is very slightly dispersed by a prism producing elliptical stellar images of approximately $35'' \times 23''$ (Almenara et al. 2009). The advantage of this choice of PSF is that for each target lightcurves can be recorded in three colors, yet the disadvantage is that as this PSF is large. The *CoRoT* fields are rather crowded, and so the targets are very often blended with other stars, making astrophysical false positives frequent. At the time of writing 23 planets found by *CoRoT* have been confirmed, and an approximate 190 candidates are still awaiting classification.

Kepler

The impact of the *Kepler* satellite (Borucki et al. 2010) on exoplanet science has been seminal. The 1.4 m telescope was launched in March 2009, and is located in an Earth-trailing orbit. It observed a single field (shown in Figure 1.10) throughout its entire mission with the main objective of discovering transiting planets. Secondary objectives include asteroseismology, and studies of stellar activity. The 115 deg^2 field is covered by 42 single CCDs, and the data are downloaded for a selected target list of approx. 156,000 stars. Due to the failure of two out of four spacecraft reaction wheels, the mission was discontinued in May 2013. At the time of writing, a new operation strategy for *Kepler* has been

suggested, regarding the observation of several fields in the ecliptic plane. The target sample of *Kepler* is fainter (the bulk of candidates are between V=13 mag and V=16 mag) than that of ground-based surveys. This means that most candidates can not be followed up using RV measurements. However the Kepler team has resorted to other means for verifying the planetary nature of candidates, either by evaluating the false alarm probability of different blend scenarios based on all available data (Torres et al. 2011), or by using TTVs to measure the planetary system's dynamical interactions (Holman et al. 2010). As candidate verification can be time consuming, an updated list of planet candidates is released to the public in regular time intervals, the latest bringing their number up to above 2300 (Batalha et al. 2013).

The photometric precision of Kepler data is outstanding, allowing to detect signals down to amplitudes of $\lesssim 10$ ppm (e.g. Barclay et al. 2012, 2013b, Mazeh et al. 2012). The most prominent scientific highlights include:

- The discovery of several densely-packed transiting planetary systems (i.e. systems with more than one planet transiting). The record holder is KIC 11442793 with 7 planets (Cabrera et al. 2013, Schmitt et al. 2013).
- Transiting planets around eclipsing binaries (P-type), showing that planets can form in exterior orbits to close binary systems (Doyle et al. 2011, Orosz et al. 2012a,b, Welsh et al. 2012, Schwamb et al. 2013).
- The discovery of transiting planets smaller than the Earth (Barclay et al. 2012, Borucki et al. 2013, Muirhead et al. 2012)
- The discovery of 1.4 - 1.7 $R_\oplus$ planets in the habitable zone (Borucki et al. 2013, Barclay et al. 2013a).
- The frequency of small planets increases for later spectral types (Howard et al. 2012).
- There is no correlation between the host star metallicity and the presence of small planets (Buchhave et al. 2012).
- Probably the most profound results from Kepler concern the overall planet population. Howard et al. (2012) show that the frequency of planets increases towards small radii, with 0.13 planets per star with a radius between 2 and 4 $R_\oplus$, but only 0.023 and 0.013 planets of $4-8R_\oplus$ and $8-32R_\oplus$, respectively. Also, there are fewer planets at small orbital separations. Petigura et al. (2013) extended these statistics to Earth-size planets, finding that 26 ± 3% of stars host a planet with a radius between $1-2R_\oplus$ and a period between 5 and 100 d. They further infer that 11 ± 4% of Solar-type stars are orbited by planets receiving fluxes between 1 and 4 times the flux that the Earth receives from the Sun.

1.3.4 Future Facilities

Many projects aiming at the discovery and characterization of transiting planets are currently in the planning phase. I will highlight only four of these, all of which have been selected for implementation.

CHaracterising ExOPlanets Satellite (CHEOPS)

CHEOPS is an ESA S-class mission that will be launched in 2017. It is equipped with a 0.32 m mirror and will obtain high-precision photometry of selected targets. The main scientific goals of CHEOPS are the detection of transits of low-mass planets known from RV surveys, the measurement of planetary occultations at optical wavelengths and measuring precise radii for known transiting planets.

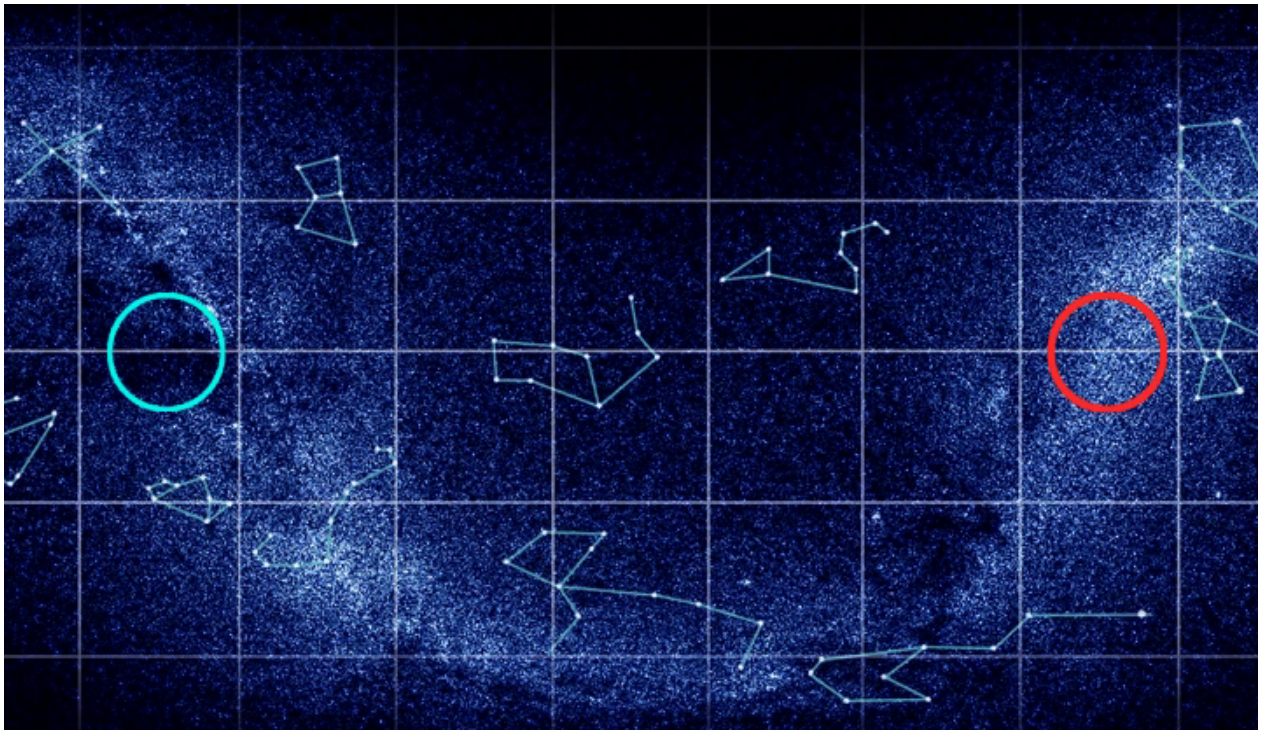

Figure 1.9 : The "eyes" of CoRoT: all pointings of the satellite are located inside one of the two circled fields. The blue field is located near the galactic center while the red field points towards the galactic anti-center. Image credit: `http://exoplanetarchive.ipac.caltech.edu`

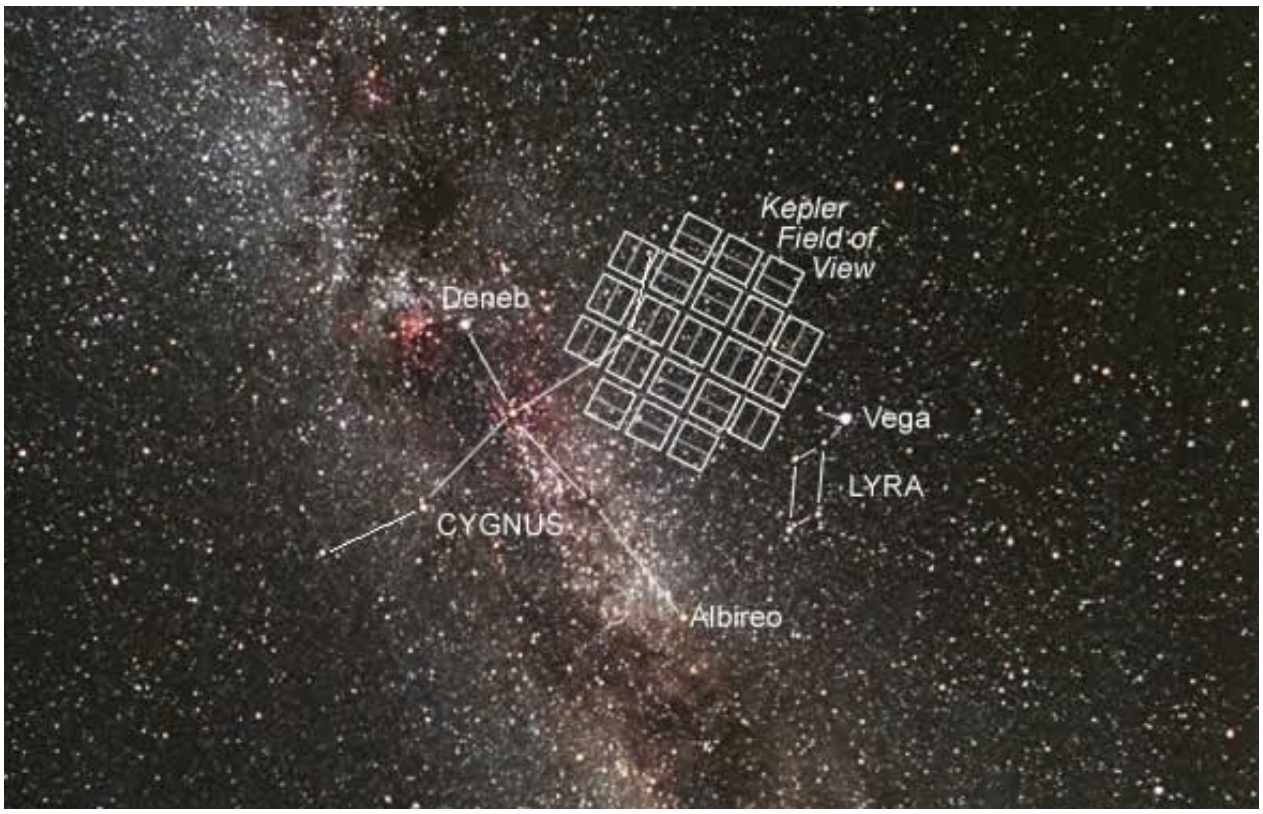

Figure 1.10 : The 115 deg^2 field of view of the Kepler satellite, shown overlaid on an optical sky image. Image credit: `http://kepler.nasa.gov/multimedia/Images/photogallery`

Transiting Exoplanets Survey Satellite (TESS)

TESS is a NASA satellite scheduled for launch in 2017. It will scan almost the entire sky in segments of 23×23 deg, remaining 27 days on each field. The high-precision photometry is optimized for bright stars, aiming to discover the transiting planets closest to our own solar system. The polar fields of TESS overlap and will benefit from nearly continuous monitoring.

Next Generation Transit Survey (NGTS)

NGTS (Wheatley et al. 2013), is a transit survey building on the experience from WASP. Using 12 independent 20 cm telescopes, the survey is targeting relatively bright (V<13) K stars. The use of high-end CCDs together with a high stability of the system will allow the discovery of Neptune-sized transiting planets orbiting bright stars, a population known to exist from RV surveys (Mayor et al. 2011). These planets will be prime targets to be characterized using ground and space based facilities.

Search for habitable Planets EClipsing ULtra-cOOl Stars (SPECULOOS)

SPECULOOS is a project using 1 m class telescopes paired with latest-generation CCDs, aimed to discover the planets orbiting very late-type (M5 and cooler) stars. As these stars have small radii the transit signature of Earth-sized planets is greatly enhanced, allowing their detection from the ground. On top of that, as these are cool stars, their habitable zone is located very close to the star, boosting the transit probability of any putative habitable planet.

1.4 Planet Discovery in the Year 2010

When I started my PhD in January 2010 the exoplanet zoo was still considerably less exotic than it is today.

Ground-based RV searches were running at full speed, discovering increasing numbers of Neptune-mass and lower planets (e.g Bouchy et al. 2009, Mayor et al. 2009b), down to near an Earth-mass (GJ 581 e, Mayor et al. 2009a). It had already been noticed (Marcy et al. 2008) that the planet frequency rises for small masses, a tendency that was to be confirmed in subsequent years from both *Kepler* (Howard et al. 2012) and HARPS (Mayor et al. 2011). Most importantly, it was becoming clear that these small planets are very often located in *planetary systems* such as HD 40307 (3 planets, Mayor et al. 2009c), GJ 851 (then, 4 planets Mayor et al. 2009a), or 55 Cnc (5 planets, Fischer et al. 2008).

Transit searches from the ground, most prominently HAT (Bakos et al. 2004) and WASP (Pollacco et al. 2006) had also been around for a while. They were efficiently uncovering the hot Jupiter population around bright stars, but missing nearly all lower-mass planets due to their limited photometric precision. Only one low-mass planet, the super-Earth GJ1214 (Charbonneau et al. 2009), had been found by a ground-based transit survey. Together with GJ436 (Butler et al. 2004, Gillon et al. 2007), these two planets were the only low-mass planets accessible for detailed characterization.

The benefit of space-based transit searches was being demonstrated by the *CoRoT* satellite that had been operational for three years and had just discovered the first transiting super Earth, CoRoT-7 b (Léger et al. 2009, Queloz et al. 2009), and allowed the first measurement of reflected light from an exoplanet (Alonso et al. 2009, Snellen et al. 2009). *Kepler* had been in orbit for little more than half a year, but was already producing lightcurves of unprecedented quality, such as the optical phase curve of HAT-P-7 (Borucki et al. 2009).

1.5 The Scope of this Dissertation

My PhD truly has been a journey, taking me from working on instrumental aspects to the detection and finally the characterization of transiting planets. In this work, I aim to give a concise summary on the

subject of hot Jupiter planets and then summarize the various projects I have been involved in during the last four years.

After having covered the general aspects of transiting planets in this first Chapter 1, in Chapter 2, I zoom in on the main subject of this thesis: hot giant planets. I aim to give an overview on what has been understood about these planets, how this knowledge has been assembled, and point towards the many open questions that yet need to be understood.

When I arrived in Geneva in early 2010, a new instrument for the 1.2 m Euler-Swiss telescope was in development: EulerCam. With this new CCD imager we aimed at bringing the capability of high precision photometry to the Euler telescope. My first year was mostly spent with the installation and characterization of this instrument as well as the setup of an optimal photometric reduction procedure. These efforts are summarized in Chapter 3.

The performances of the new instrument turned out to be very good, and EulerCam started to become one of the workhorses for the confirmation and characterization of planets and planet candidates found by the WASP survey. In this context, I have become an active member of the WASP collaboration, contributed to many discoveries, and finally took charge of the publication of two hot sub-Jupiter planets. The WASP survey and my work in relation to this project are described in Chapter 4.

With photometric precisions well below the milli-magnitude, I extended the use of EulerCam to study one of the most intriguing hot Jupiters in more detail. I pursued and intense campaign of occultation photometry of WASP-19, finally detecting the planet's occultation in z'-band. At the same time, I was allowed access to infra-red occultation data of WASP-19 from the HAWK-I instrument at the VLT, the analysis of which presented some new challenges. In Chapter 5, I introduce the reader to the concepts of high-precision photometry, present my work on WASP-19 b and place it into context with more recently published results.

The last leg in this journey took me to using a new observational technique: spectrophotometry. I spent most of my fourth and last year of PhD analyzing spectrophotometric data of three transits of the hot Saturn WASP-49 b observed with the FORS2 instrument at the VLT. The analysis of these data has resulted in a transmission spectrum for this planet that is currently under more detailed analysis. I present the results of this project in Chapter 6.

Finally a short summary of my work and my outlook on the field of exoplanet research is presented in Chapter 7.

Ausnahmen sind nicht immer Bestätigung der alten Regel; sie können auch die Vorboten einer neuen Regel sein.

Marie von Ebner-Eschenbach

2 Hot Close-in Planets

2.1 What is a *Hot Jupiter*?

Among the many exoplanets discovered to date, there is a subset of planets inhabiting a parameter space where, initially, nobody expected them to exist. These planets have masses and radii similar to those of the gas giants in our own Solar system, but they are located very close to their host stars having orbital periods of only a few days. As their densities are known, it is clear that these planets can not be composed of solids, but must possess envelopes of volatile materials containing large fractions of Hydrogen and Helium. Fittingly, these planets have been given the name "*hot Jupiters*". The definition of *hot Jupiters* in terms of mass and radius is quite blurred, extending to planets with masses below that of Saturn (95 $M_\oplus$). Similarly planets of $M_p \lesssim 30\ M_\oplus$ are referred to as *hot Neptunes*, while planets of $M_p \lesssim 10\ M_\oplus$ are known as *hot super-Earths*.

At the time of writing, ~300 planets are known to transit their host stars. Compared to planets found by other means, the transiting planets are most prominently found at small orbital separations, clearly a consequence of the transit geometry and the detection efficiency of ground-based transit sur-

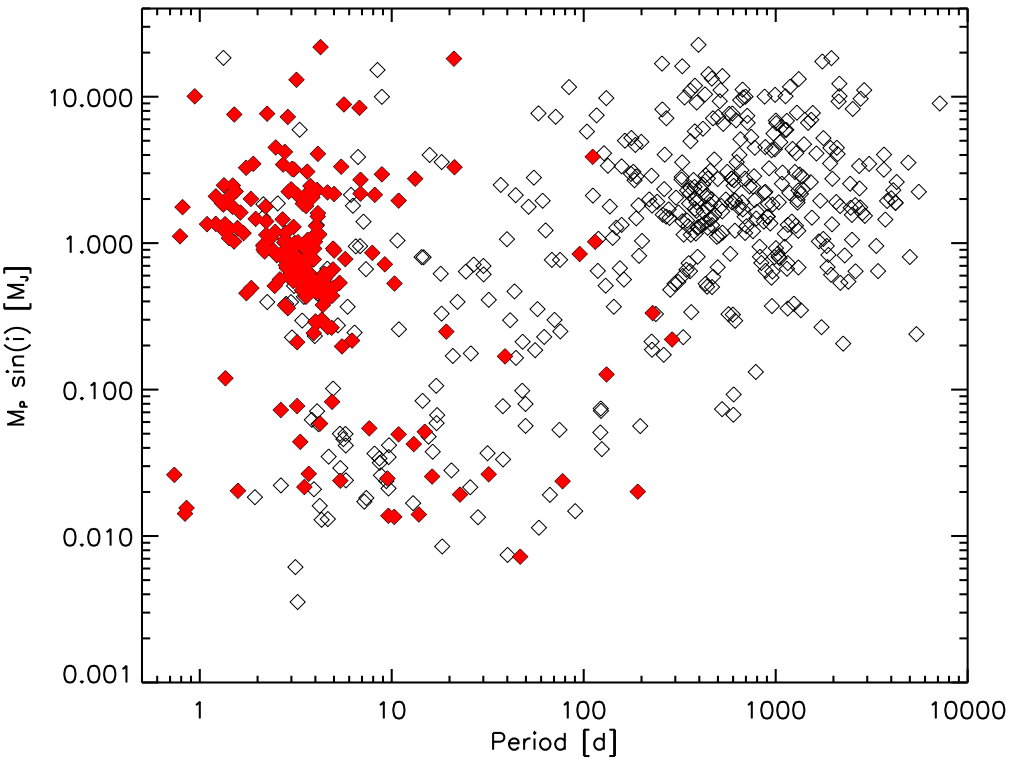

Figure 2.1 : The period-mass diagram of all exoplanets known at the time of writing. Only objects with measured masses have been included. Open diamonds refer to objects detected by RV surveys while the filled red diamonds indicate transiting objects. The data has been obtained from `http://www.exoplanets.org` on 29 October 2013.

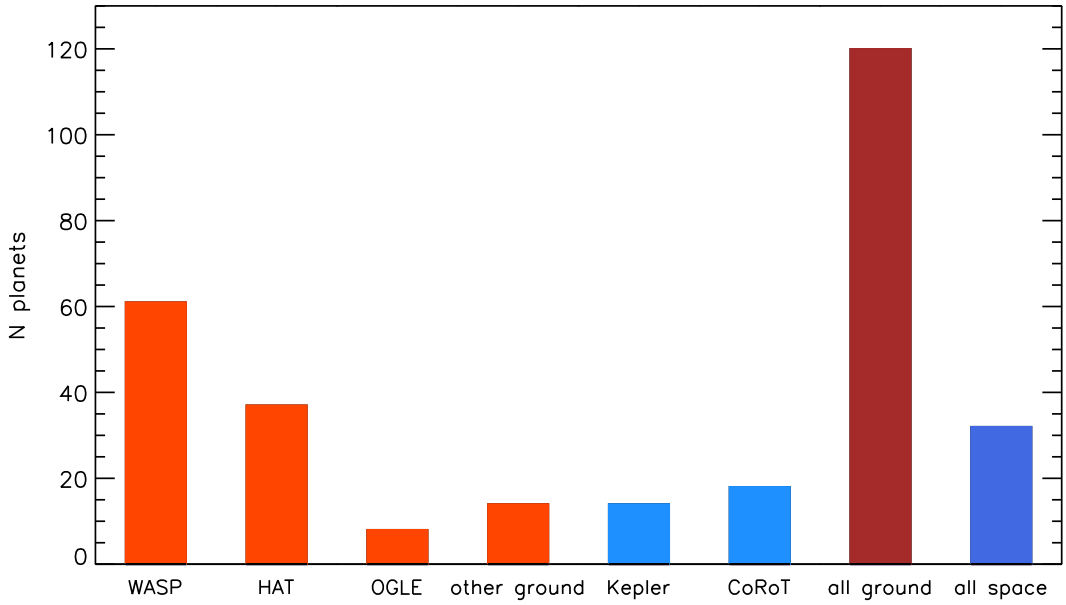

Figure 2.2 : The contributions to the detection of transiting hot Jupiters from ground-based (blue) and space-born (red) surveys.

veys. The position of the transiting planets in the period-mass plane of known exoplanets is shown in Figure 2.1 , the majority have orbital periods below 10 days and masses above 0.2 M_J. It is precisely these transiting hot Jupiters that I focused on detecting and characterizing during my PhD years. As they have no analogues in the Solar system, very little is known about hot gaseous planets, and the techniques to characterize their orbits, internal structures and atmospheres are just emerging. In this chapter I will summarize what we already know about hot Jupiters, sketch the theories of their formation, and describe where we stand in understanding their structure and composition.

2.1.1 The Hot Jupiter Population

Albeit the first known hot Jupiter, 51 Peg (Mayor & Queloz 1995) was discovered with the RV method, most of the hot Jupiters known to date have been found by transit surveys. This is nicely illustrated by the data shown in Figure 2.1 , from which we can define a subset of bona-fide hot Jupiters as the planets with masses above 0.2 M_J and periods below 10 days. In this subset, the total number of planets is 189, a whooping 155 of which are transiting. Only three out of these 155 transiting hot Jupiters were initially found from RV measurements, all others have been identified from photometric surveys. The contribution of the most prominent surveys to these discoveries is shown in Figure 2.2 . Together the wide-angle ground-based surveys make up for more than 75% of the discovered hot Jupiters. This means that ground-based surveys have an inherent advantage at discovering close-in planets compared to RV and space-based surveys.

Since the photometric precision of these ground-based surveys is indisputably inferior to CoRoT and Kepler, this discrepancy can not be based on S/N limitations. The essential difference between these surveys is the observing strategy. RV searches survey a sample of a few hundred to about 2000 of stars, and the space-based surveys stay long on single fields in order to be sensitive to long-period planets. Surveys such as WASP and HAT scan nearly the entire sky, obtaining good photometry for all stars in their appropriate magnitude range. The strength of ground-based surveys lies in the great number of stars searched. The WASP survey surveyed several millions of stars, but only scored $\sim$ 100 planet detections. This low detection rate points to a key property in the hot Jupiter population: hot Jupiters

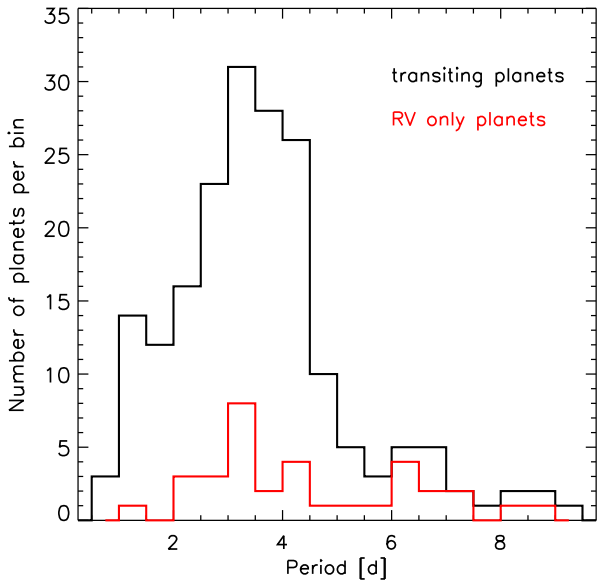

Figure 2.3 : A histogram plot of all confirmed hot Jupiters. The RV detections are shown in red, while the transiting planets are shown in black.

are *rare*. This means that whatever process is bringing in gas giants to form hot Jupiters, it either must be uncommon or lead to the destruction of nearly all planets undergoing it.

Estimates of the occurrence rate of hot Jupiters based on RV surveys have been provided by Marcy et al. (2005), Cumming et al. (2008), Howard et al. (2010), Udry & Santos (2007), Mayor et al. (2011) and Wright et al. (2012) giving values between 0.8% and 1.5%. Similar studies of the transit surveys OGLEIII (Gould et al. 2006) and Kepler (Howard et al. 2012) have produced even smaller values, 0.4% and 0.5%. The reason for this discrepancy is most likely to be found in the difference in stellar samples. While RV surveys probe the solar neighborhood, OGLEIII and Kepler monitored fainter stars located towards the Galactic bulge and offset from the galactic disc. These regions are home to a different, more metal-poor stellar population. As it has been shown by Santos et al. (2004), Fischer & Valenti (2005) and Mayor et al. (2011), there is a strong positive correlation between host star metallicity and the frequency of giant planets.

In terms of orbital period, an over density of hot Jupiters has been observed near 3 days, known as the *3-day pileup* (Cumming et al. 1999, Udry et al. 2003). Any theory aiming to explain the origin and evolution of hot Jupiters needs to come forward with an explanation why this period range is densely populated with respect to shorter and longer periods. In Figure 2.3 , the period distribution for hot Jupiters is shown. The 3-day pileup is evident for transiting planets, while it is less pronounced for planets found by RV surveys. In Figure 2.3 , I do not account for the planets missed by the surveys, a non-negligible factor for the ground-based transit surveys, but less critical for the RV detections where detection probabilities decrease less sharply for longer orbital periods. Howard et al. (2012) have included incompleteness in their evaluation of the Kepler data, still the 3-day peak remains at a factor of three above the underlying planet population.

When looking at low-mass stars, the statistics on the presence of hot Jupiters become highly unreliable. At the time of writing only one hot Jupiter is known to orbit a M-star (KOI-254, Johnson et al. 2012). In fact, even KOI-254 is an early ($M_* \sim 0.6 M_\odot$) M-star, not far from the two late K-type planet hosts WASP-80 (Triaud et al. 2013) and WASP-43 (Hellier et al. 2011a). From the WTS survey, which performed a targeted search for hot Jupiters around late star, Kovács et al. (2013) derive an upper limit of 2% for the hot Jupiter frequency around M0 - M4 hosts. The occurrence rate for giant planets with larger periods has been shown to decrease for low-mass stars (Johnson et al. 2007, Cumming et al. 2008), somewhat lowering expectations to detect a transiting hot Jupiter around a mid to late M-star.

2.2 How to Make a Hot Jupiter

The discovery of the first hot Jupiters came as a great surprise to what must have been the vast majority of the scientific community. Theories were tuned to the Solar system, where giant planets are found at orbital separations of > 5 au while the inner region is populated by small rocky planets. The exoplanet population uncovered in the late 1990s and shortly after the turn of the millennium didn't fit at all into the ruling paradigm. Suddenly massive planets were all over the place, many of them on highly eccentric orbits. Some careful rethinking was necessary of the understanding of planet formation.

2.2.1 A Short Note on Planet Formation

At the time of writing, there are two competing theories for the formation of planets, the *core-accretion* and the *disk-instability* models that I will briefly sketch below.

Core-accretion: This model is based on the bottom-up buildup for planets form smaller bodies. First, dust grains in the protoplanetary disc coagulate to form larger particles of ∼cm size. These particles settle to the disc midplane where they continue to grow forming *planetesimals*, small ∼km sized bodies. The planetesimals then collide with each other and keep growing through inelastic collisions, the more massive ones growing exceedingly fast until they start to gravitationally dominate their surroundings, a process called *oligarchic growth*. Out of the swarm of planetesimals the most massive grow into a small number of *planetary embryos*, having masses of that of the Mars or more. The planetary embryos continue to grow by accreting the smaller bodies in their feeding zones, which extend out to several Hill radii, rapidly (on timescales of several 10^5 years) reaching a mass of about ten times that of the Earth. At some point they are massive enough so the escape velocity at their surface exceeds the thermal speed of the gaseous component of the protoplanetary disc, and the protoplanet starts accreting gas. At first the gas accretion is slow, as it is limited by how fast the protoplanet can release its gravitational energy, contract and thus absorb more gas. In this phase, taking ∼2 Myrs, the planet reaches its maximum radius. The mass of the protoplanet grows slowly until it reaches a critical value (about 32 $M_\oplus$, with a core of 16 $M_\oplus$), beyond which the envelope can not remain in thermostatic equilibrium. The envelope collapses, the planet contracts strongly and enters the *runaway accretion* phase where it rapidly accretes all gas delivered to it from the disk. At this point we have formed a gas giant, with a core of several Earth masses and a large gaseous envelop. The accretion is slowed once the planet is massive enough so that it tidally influences the disk, creating a gap around its orbital position. Finally, the planet is left to continue contracting slowly as the leftover protoplanetary disk is dispersed. Literature on this subject is vast, but the interested reader is referred to Pollack et al. (1996), Ida & Lin (2004), Alibert et al. (2004) and the review by D'Angelo et al. (2011) for details.

Disk-instability: This top-down model for giant planet formation relies on the fragmentation of the young protoplanetary disk into several self-gravitating clumps (Boss 1997). These clumps then contract, cool and become giant planets with a composition equal to that of the initial gas clump. Planetary cores form from sedimentation of heavy elements. To reproduce the abundances seen in the Solar System planets, further accretion of metal-rich planetesimals or gas is invoked (e.g. Helled et al. 2006). The process of planet formation via gravitational instability is very rapid, occurring on a timescale of a few tens of orbital periods. To allow for planet creation via this process, the protoplanetary disk needs to fulfill two conditions: First, it must fragment. Fragmentation should occur if the disks Toomre parameter (Toomre 1964) is lower than $Q \sim 1.7$, as is the case for cold and/or massive disks. Second, the fragments must cool quickly to form planets before being reheated. This will work only in the outer reaches ($a \approx 100$ au) of the protoplanetary nebula. For further reading on this subject, see e.g. the reviews by Durisen et al. (2007) and D'Angelo et al. (2011).

Comparing these two formation pathways to the observed planet population, a lot speaks for the *core-accretion* model to be the dominant one. The efficiency of *core-accretion* depends on the disk metallicity, as more metals mean more available material to build the planetesimals. This matches very well the host star – metallicity correlation described in Section 2.1.1 (Kornet et al. 2005, Mordasini

et al. 2009b). The heavy-element content of the Solar System planets is easily accounted for, and ice giants can be explained by protoplanets not growing fast enough to undergo runaway accretion. Yet, direct imaging has revealed massive planets at very large orbital separations (e.g. HR8799, Marois et al. 2008) where the *core-accretion* is too slow to be the creating process. These planets may well have formed via *disc-instability* (Boss 2011).

2.2.2 Migration Pathways

From either process of planet formation it is clear that the hot Jupiters have not formed at their current locations in the close proximity of their host stars. In fact the preferred formation location of giant planets is further out in the disc, where the temperatures are low enough to provide for ample reservoirs of molecules (Water, Carbon Dioxide etc.) in their solid form (see e.g. Mordasini et al. (2009a), D'Angelo et al. (2011) and references therein). This means that there must be a process acting to move a small percentage of the formed giants to small orbital separations, creating the observed population of hot Jupiters. Ample research has been devoted to understanding the migration processes, and they can be divided into two major mechanisms: *Disc-planet interactions* and *Multi-body interactions*, that I will briefly introduce below.

Disc Migration

Since the protoplanets are embedded in a gaseous disc, it is expected for interactions to take place between the planet and the protoplanetary disc (Goldreich & Tremaine 1980, Lin & Papaloizou 1986). Depending on the planet mass and the location of the interacting gas, the planet-disc interactions are usually divided into two regimes (Ward 1997).

Type I migration occurs while the planet is still well-embedded in the protoplanetary disc, but massive enough ($M_P \gtrsim M_\oplus$) for it to impact the disc density structure (Goldreich & Tremaine 1980). It does so by creating spiral waves propagating away from the planet at the inner and outer Lindblad resonances. The locations of the Lindblad resonances (e.g. Binney & Tremaine 1987) is given by positions in the disc is determined by relating epicyclic frequency κ to an integer multiple m of the orbital frequency difference of planet and gas ($\Omega_p - \Omega_r$).

$$m(\Omega_r - \Omega_p) = \pm\kappa \tag{2.1}$$

where the sign on the right-hand side indicates outer ($-\kappa$) and inner ($+\kappa$) resonances. The higher-order Lindblad resonances are located between the position of the planet and that of the 1st order Lindblad resonance. These inhomogeneities in the disc structure exert torques on the planet, with the outer resonances causing an inward migration and the inner resonances causing an outward migration of the planet. The sign of the direction of migration is determined by which side dominates, and thus by the properties of the protoplanetary disc (Ward 1997). Substantial torques can also come from the gas located near the planet, at $\Omega_r \sim \Omega_p$. Here the gas does follow the Keplerian disc flow but exerts Horseshoe-orbits around the planet. The net migration is determined by a precise evaluation of all contributing torques. It has been shown (e.g. Ward 1997) that the migration is usually directed towards the star, and occurs on timescales shorter than the planet formation timescale. If migration is included in the calculation of the corotation torques, asymmetries may arise (Masset & Papaloizou 2003), speeding up the migration. This process, also referred to as *Type III migration*, can potentially erode the planets orbit over the course of a few orbital periods only. The main question raised by these predictions is why so many giant planets remain at large orbital separations.

Type II migration occurs when the planet is massive enough ($\sim 0.25\ M_J$, Bate et al. 2003) to open a gap in the protoplanetary disc. Once this happens, the migration slows down (Lin & Papaloizou 1986, Ward 1997), as the planet becomes coupled to the viscous evolution of the disc. For large planetary masses, the coupling between disc and planet weakens, and once the planetary mass is large compared to the disk mass, the migration comes to a stop (e.g. Trilling et al. 1998).

Disc migration has the potential to effectively bring in further out planets to become hot Jupiters, while it at the same time provides fresh material in the planet's feeding zone, decreasing the time needed to form a massive planet (Alibert et al. 2005). However disc migration is perhaps *too efficient*, as the timescales for type I migration are considerably shorter ($\sim 10^5$ years, Nelson et al. 2000, Bate et al. 2003) than the lifetimes of the protoplanetary disc. One would expect protoplanets formed before the main depletion of the disc to end up in the vicinity of, or get accreted on the star. Once the disc is sufficiently depleted to no longer allow substantial type I migration, not enough material is left to form gas giants (Ida & Lin 2008). Several processes have been suggested to slow down or reverse type I migration. Modifications of the disk pressure/temperature structure alter the strength of the interior/outer torques and thus the migration rate. This could be the case in certain regions inside the disk (e.g. Menou & Goodman 2004) or caused by material piling up inside the planetary orbit (Ward 1997). Also non-isothermal material in the the corotation region may alter the corotation torque towards outwards directed migration (e.g. Paardekooper & Mellema 2006). Further, a magnetic field in the disk can add additional resonance regions and thus torques (Terquem 2003).

Multi-body Migration

Next to the gas disc, other bodies in the system may be the cause of major changes in the planets' parameters. These can either be other planets, or stellar companions.

Planet-planet interactions: dynamical interactions in a system hosting several giant planets can cause to significant angular momentum exchange between the planets, increasing the eccentricities of some planets to the point where their periastron distance falls below 0.1 au. Then, via tidal circularization, these orbits are circularized forming a hot Jupiter (Rasio & Ford 1996, Weidenschilling & Marzari 1996). At the same time, other planets may be scattered outwards, even ejected from the system. On top of potentially creating close-in giant planets, scattering of several giant planets create a large population of eccentric further-out planets, a fact well matched by the observed planet population (Chatterjee et al. 2008).

Interactions in an inclined binary: A particular form of multi-body interactions are Kozai cycles (Kozai 1962), that can occur if the planetary system has an outer stellar companion which is on an orbit inclined to that of the planet. In this case, the orbital plane of the planet oscillates with respect to that of the binary. Through conservation of angular momentum this triggers a reflex oscillation in planetary eccentricity. Again, the hot Jupiter is created from the circularization of an eccentric orbit (Eggleton & Kiseleva-Eggleton 2001, Wu & Murray 2003).

2.2.3 The Dynamical Environment of Hot Jupiters

As described in Section 1.2.3, measurements of the projected spin-orbit angle of the planetary systems are possible via the RV anomaly during transit, called the "Rossiter McLaughlin effect" (Rossiter 1924, McLaughlin 1924, see Section 1.2.3). While the first bunch of planets studied in this way showed well aligned orbits (Queloz et al. 2000, Winn et al. 2006, Narita et al. 2007, etc.), Hébrard et al. (2008) first found a substantial misalignment of the stellar spin and planetary orbital axes of XO-3. Several other similar discoveries followed suite (e.g. Johnson et al. 2009, Winn et al. 2009, Triaud et al. 2010) and it became clear that misalignment, and even retrograde orbits, is a characteristic trait of the hot Jupiter population. This immediately poses constraints on the migration mechanism responsible for the formation of hot Jupiters. Given the formation of giant planets occurs in a well-aligned protoplanetary disc (as in Goldreich & Tremaine 1980), some mechanism producing hot Jupiters must be altering the planets' orbital plane away from the stellar rotation plane.

The best candidates are dynamical processes: planet-planet scattering (Rasio & Ford 1996), Kozai interactions (Eggleton & Kiseleva-Eggleton 2001, Wu & Murray 2003), or secular interactions involving a gas giant or brown dwarf located at a few tens to a hundred au (Naoz et al. 2011). Predictions for the obliquity distribution of hot Jupiters have been produced for planet-planet scattering and Kozai migra-

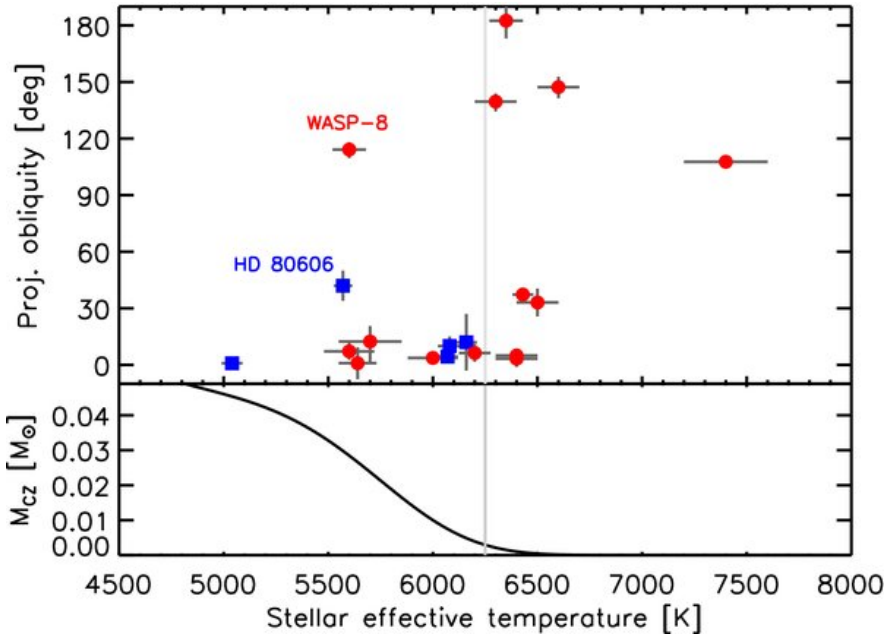

Figure 2.4 : The planetary misaligned is shown against the stellar temperature. With a few exceptions of planet that probably have long obliquity dampening timescales, the planets orbiting stars above 6250 K show high degrees of misalignment. The lower panel shows the size of the stellar convective envelop. Figure credit (Winn et al. 2010).

tion by Fabrycky & Winn (2009) and Morton & Johnson (2011). These authors argue that there appear to be two populations of hot Jupiters in terms of obliquity: an aligned fraction in good agreement with the predictions from disc migration and a population showing a wide distribution of spin-orbit angles compatible best with planet-planet scattering. Based on a larger sample Triaud (2011) including more misaligned systems, Triaud (2011) find a better match with the prediction of Kozai migration. A further plus to a dynamical history of the hot Jupiters is the presence of the 3 day pileup (see Section 2.1.1), which corresponds to distances near or above twice the Roche limit. While this small but substantial separation is predicted for dynamical processes, migration in a disc should have continued further towards the star (Ford & Rasio 2006, Wu et al. 2007).

A particularity of the distribution of misaligned planets has been pointed out by Winn et al. (2010) (see Figure 2.4), who showed that nearly all misaligned systems are orbiting stars with temperatures above 6250 K, a trend which has been confirmed by more recent observations (see Albrecht et al. 2013 and references therein). This divide in the obliquity distribution coincides with the disappearance of the stellar convective envelope. The argument now pursued by Winn et al. (2010) is that the stellar envelopes have decoupled from the radiative cores and now align with the planetary orbit to produce a seemingly aligned system. This process occurs within a smaller time frame than the alignment of the planetary orbit with a uniformly rotating star. Fast realignment is also supported by Triaud (2011) who found indications that high obliquities coincide with younger host stars and Albrecht et al. (2012, 2013), who estimate the circularization timescales and find that the number of misaligned systems increases for slow tidal dissipation.

As the time span of follow-up for hot Jupiters increases, it has become possible to search for companions on further-out orbits. It turns out that for quite a few of them further-out companions do exist (e.g. WASP-8 (Queloz et al. 2009), HAT-P-13 (Bakos et al. 2009), HAT-P-44, HAT-P-45, and HAT-P-66 (Hartman et al. 2013)), whether already with well-measured orbits or just as drifts seen in the RVs. Characterizing this population of hot Jupiter companions will provide an essential piece in the understanding of which migration process has been at work.

A further property of close-in giant planets is that their orbits can be unstable against tidal interac-

tions (Rasio et al. 1996, Levrard et al. 2009, Matsumura et al. 2010). Depending on the efficiency of tidal dissipation (a parameter largely unconstrained for planet and star), the planets survival time may be smaller than the stellar main-sequence lifetime, and planets on very short orbits such as WASP-19b (Hebb et al. 2009) may be on their way to being accreted by the star (Brown et al. 2011, Hellier et al. 2011a). This model nicely explains the paucity of very short-period (P $<$ 1 d) hot Jupiters.

2.3 How to Study a Hot Jupiter

While we have so far established that there is a population of hot Jupiters, and have come forward with various theories to explain their existence, we have yet to zoom in on the planets, and try to find out as much as we can about their properties. The main questions which we can try to answer at many levels of detail are: what are these planets made of, and what do their atmospheres look like? This endeavor is at the forefront of observational astronomy, constantly challenging instrumentation, observing and modeling techniques. Here, I will summarize the observational approaches, and lay out how the data are interpreted to draw conclusions on the properties of transiting planets.

2.3.1 Observations: Transmission and Emission Spectroscopy

The concept of transmission and emission spectra has already been introduced in Section 1.2.6. In short, one is looking for wavelength-dependent variations in the effective planetary radius, or the planetary dayside emission. A variety of instruments have been used for this purpose, and I attempt to give an overview of them here.

Before discussing the various instruments, let me define the three main observing strategies.

- **Photometry** refers to observations that produce transit or occultation lightcurves in a single wavelength band, and that are usually created using an imaging device, for example a CCD camera such as EulerCam. The lightcurves are created via relative photometry and can only be obtained simultaneously in several filters if multi-channel instruments are used or if the filters are alternated during one transit sequence.

- **Spectrophotometry** designates transit or occulation lightcurves obtained from low- to mid-resolution spectra. The target field (containing usually at least one good reference star) is observed using a multi-object spectrograph or similar instrument. All spectra are binned into wavelength bins and relative lightcurves are created for each wavelength bin.

- **Spectroscopy** refers to work done with spectra of a high resolution. Here either the strength in single lines is measured during and outside transit, or the molecular signatures stemming from the planet are identified. Lightcurves are rarely produced from high resolution spectroscopic observations, and if so, they usually focus on a narrow spectral region, such as in- and next to a prominent absorption feature.

Naturally the space telescopes are ideal instrumentation to study the atmospheres of exoplanets. They avoid effects from the the Earth's atmosphere and are able to observe in wavelength bands not accessible from the ground due to strong atmospheric extinction. They have thus played an important role in the study of exoplanet atmospheres.

The Hubble Space Telescope (HST)

As the HST is located in low-earth orbit, the duration of continuous observations is limited by the occultation of the target by the Earth and passages through the South Atlantic anomaly. This means that the observations are usually interrupted after approx. 55 minutes, and are continued some 40 minutes later. For transit observations this means that the transits are sampled in several pieces, and several

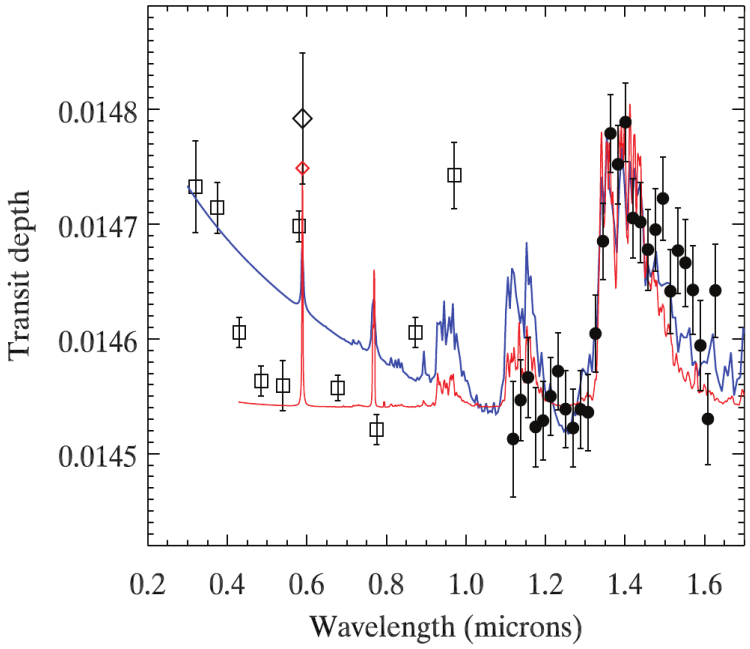

Figure 2.5 : *HST* measurements of HD209458b's transmission spectrum are shown. The open squares are *STIS* data of Knutson et al. (2007c) analyzed by Deming et al. (2013), the open diamond is the Na feature measured by Charbonneau et al. (2002), and the solid points are *WFC3* results of Deming et al. (2013). Figure credit: Deming et al. (2013)

visits of the target each lasting three to four spacecraft orbits are needed to accumulate a complete transit lightcurve.

Shortly after the discovery of transits of the hot Jupiter HD 209458 (Charbonneau et al. 2000) this very same object was observed in transit using the ***S**pace **T**elescope **I**maging **S**pectrograph (**STIS**)* on board the HST (Brown et al. 2001). *STIS* is a versatile instrument, able to carry out spectroscopic observations between 150 nm and 1 µm, with several gratings and detectors available to provide various spectral windows. For this first transit lightcurve, the flux over the wavelength range from 582 to 638 nm was summed up to produce one lightcurve of impressive quality. The very same data were used shortly afterwards to obtain the first detection of an element in an exoplanetary atmosphere (Charbonneau et al. 2002), who found excess Na absorption. In numerous subsequent observations, the spectral flux was summed in several wavelength intervals to obtain spectrophotometric measurements. These observations have produced a wealth of insights on the transmission spectra of the observationally favorable planets, most importantly HD209548 b (Knutson et al. 2007c, Barman 2007, Désert et al. 2008, Sing et al. 2008b) and HD189733 b (Sing et al. 2011b, Huitson et al. 2012). Sodium features have been identified for both planets, however they appear to be considerably weaker than expected (Charbonneau et al. 2002), in particular for HD189733 b (Huitson et al. 2012).

Further spectro-photometric measurements have been obtained with HST's ***A**dvanced **C**amera for **S**urveys* (ACS), which is an optical to near-IR imaging detector that can be operated with grisms in order to provide spectrally dispersed images. Together with the the information gained from *STIS*, these indicate that HD189733 b (and to a lesser extent also HD209458 b) are covered by a layer of clouds or haze, decreasing the amplitude of elemental signatures (Pont et al. 2007, 2008).

Infrared capabilities on HST used to be provided out to 2.5 µm by the ***N**ear **I**nfrared **C**amera and **M**ulti-**O**bject **S**pectrometer (**NICMOS**)*. Several groups have used *NICMOS* to obtain transmission and/or emission spectro-photometry of HD209548 b (Swain et al. 2009a), HD189733 b (Swain et al. 2008), HD149026 b (Carter et al. 2009), XO-1 b (Tinetti et al. 2010), XO-2 (Crouzet et al. 2012), and GJ436 b (Pont et al. 2009). Detections of molecules were claimed for CH_4, H_2O, CO_2, and CO (Swain et al. 2008, 2009a,b, Tinetti et al. 2010). However, other teams obtained diverging results analyzing some of the above data sets (Sing et al. 2009, Gibson et al. 2011, Crouzet et al. 2012). Finally the molecule detections were put in question as systematic effects most probably are at the root of the transit/occultation depth variations.

Further support for this criticism has been provided by the becoming available of ***W**ide **F**ield **C**amera **3***

(WFC3), installed at the telescope in 2009. *WFC3* is a multi-purpose imager that can observe either between 200 and 900 nm or between 600 and 1700 nm. The instrument is equipped with grisms to obtain spectral information. An increasing number of targets (including HD209458, XO-1 (Deming et al. 2013) and WASP-19 (Huitson et al. 2013)) have been observed with *WFC3*, and the results show only shallow H_2O features. For an example of *WFC3* and *STIS* data see Figure 2.5 .

Other pieces of information have been gathered from *STIS* data. From the shape of the Na features Sing et al. (2008a) and Huitson et al. (2012) have inferred the presence of *thermospheres*, i.e. high temperatures at high altitudes at the top of the atmospheres of HD209458 b and HD189733 b. By using *STIS* in the UV, Vidal-Madjar et al. (2003) have found larger-than-expected transit depths of HD209548 b in the Lyman-α line, indicating the planet is surrounded by an envelop of gas escaping its atmosphere. Similar observations have been made for other elements and planets (Vidal-Madjar et al. 2004, Ehrenreich et al. 2008, Lecavelier Des Etangs et al. 2010), and have been confirmed with the *Cosmic Origins Spectrograph* on board HST (Fossati et al. 2010, Linsky et al. 2010).

The Spitzer Space Telescope

The *Spitzer Space Telescope* has a mirror diameter of 85 cm and is located in an Earth-trailing heliocentric orbit. It has the capacity to carry out astronomical observations at wavelengths between 3 and 160 μm (Werner et al. 2004). The telescope was launched in 2003 and relied on liquid Helium for the cooling of its detectors. The telescope has remained in operation since the exhaustion of this coolant in spring 2009 (*"Warm Mission"*), however only the two shortest-wavelength detectors are left for scientific use. The instruments on board *Spitzer* are

- ***I**nfra**R**ed **A**rray **C**amera **(IRAC)***: with four bands, centered on 3.6, 4.5, 5.8, and 8 μm, *IRAC* provides imaging capabilities in the near-IR (Fazio et al. 2004). The 3.6 and 4.5 μm channels remain in operation during *Spitzer's warm mission*. Although correlated photometric noise is large due to intra-pixel sensitivity variations and telescope pointing drifts, this noise is well-characterized and the instrument is the most-used *Spitzer* instrument for exoplanet science. *IRAC* has been used on more than 40 planetary systems, measuring predominantly near-IR occultation depths, starting with the hot Jupiter TrES-1 b (Charbonneau et al. 2005), but including also lower-mass planets such as GJ436 b (Deming et al. 2007a, Demory et al. 2007) and 55 Cnc e (Demory et al. 2012). It also has supplemented transmission spectra of several planets, most prominently HD209458 b (Beaulieu et al. 2010), and HD189733 b (e.g. Désert et al. 2009, Ehrenreich et al. 2007, Knutson et al. 2007a). On top of that, for a few systems phase curves have been obtained with *IRAC*, either through continuous observations (HD189733 b (Knutson et al. 2007a, 2012), HD149026 b (Knutson et al. 2009a), and HAT-P-2 b (Lewis et al. 2013)), or by sampling the planetary orbit at several discrete phases (HD209458 b, HD179949 b and 51 Peg b (Cowan et al. 2007)). Given its ability to provide high-precision photometry throughout several hours, *IRAC* has also been used to search for (and in some cases, find) transits of small planets (Demory et al. 2011, Gillon et al. 2013).

- ***I**nfra**R**ed **S**pectrograph **(IRS)***: *IRS* could be used to obtain spectra, or to obtain imaging photometry in a 5 μm wide band centered on 16 μm (Houck et al. 2004). For exoplanet science, either the 7.4-14.51 μm spectroscopic mode, or the 16 μm photometric mode have been used. The detector showed a characteristic time-dependent slope for time-series observations caused by charge pile-up (Deming et al. 2006). A small number of eclipses have been measured with *IRS* in photometric mode (Deming et al. 2006, Stevenson et al. 2010), supplementing transmission and emission photometry. For the planets HD209458 b and HD189733 b, spectroscopic observations were obtained during occultation (Richardson et al. 2007, Grillmair et al. 2007, 2008).

- ***M**ultiband **I**maging **P**hotometer for **S**pitzer **(MIPS)***: *MIPS* (Rieke et al. 2004) was *Spitzer's* far-IR imager, operating at 24, 70 or 160 μm. For exoplanet science only its shortest wavelength

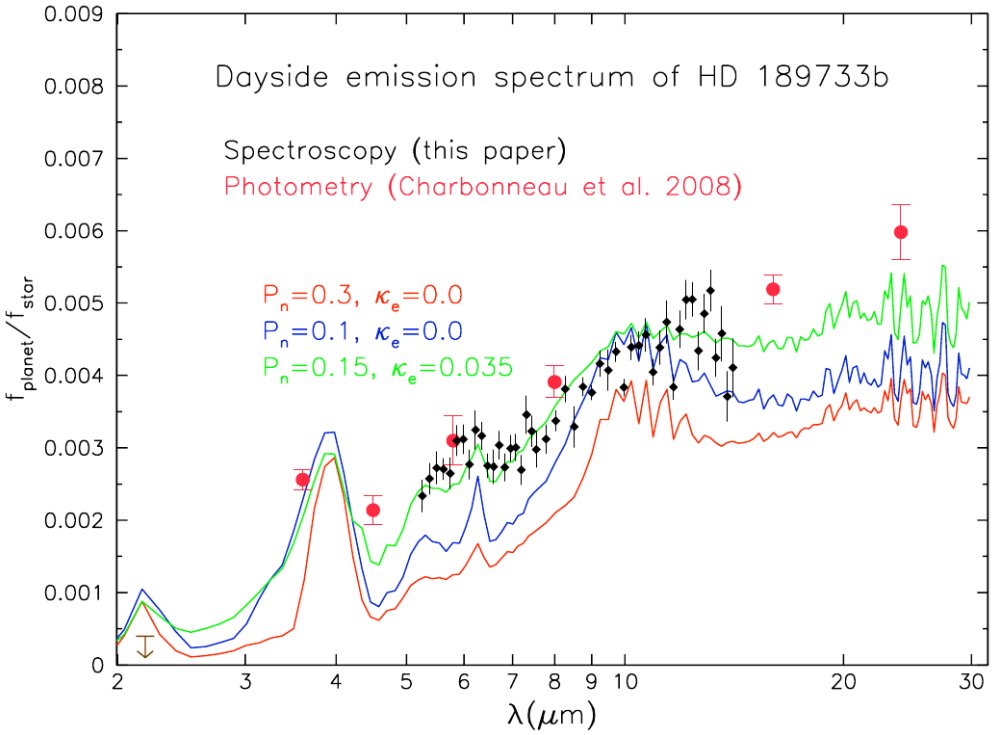

Figure 2.6 : The emission spectrum of HD189733 b as obtained by Grillmair et al. (2008) with *IRS* together with models created using different day-night energy redistribution efficiencies P_n, and different high-altitude opacities κ_e.

mode has been used. Observations were obtained for some of the brightest targets, (HD209548 b (Deming et al. 2005), HD189733 b (Charbonneau et al. 2008, Knutson et al. 2009a), and GJ436 b (Stevenson et al. 2010)) including non-transiting hot Jupiters (Crossfield et al. 2010, Harrington et al. 2006). Also *MIPS* was affected by characteristic trends in the photometry: a steep ramp followed by a slight flux decrease (see e.g. Crossfield et al. (2010) for a description).

The planet best-studied by *Spitzer* is HD189733 b, with a well-determined emission spectrum between 5 and 15 μm obtained by Grillmair et al. (2008). From these data, shown in Figure 2.6 the authors inferred the presence of water in the planetary atmosphere. The same target has phase curve measurements at wavelengths of 3.6, 4.5, 8, and 24 μm by Knutson et al. (2007a, 2009a, 2012). The offset of its maximum from the time of occultation shows that there is a hot spot on the planetary surface which is moved away from the substellar point, probably due to strong equatorial winds on the planet (Knutson et al. 2007a).

Spitzer has contributed immensely to the science of exoplanet atmospheres, in particular via a large number of occultation measurements. Some systems, such as GJ436 (Deming et al. 2007a, Demory et al. 2007, Stevenson et al. 2010), have been observed in all *Spitzer* bands, leading to constraints on their composition (high CO and low CH_4 mixing ratios in the case of GJ436 b (Stevenson et al. 2010, Line & Yung 2013, Moses et al. 2013)). However, for many hot Jupiters only two or four IRAC channels have been obtained. These data allow some insights on the atmospheric temperature-pressure profile and energy recirculation efficiency (e.g. Machalek et al. 2009, Gillon et al. 2010, Anderson et al. 2013b). These observations need to be supplemented with data from other instruments to allow constraints on the atmospheric composition.

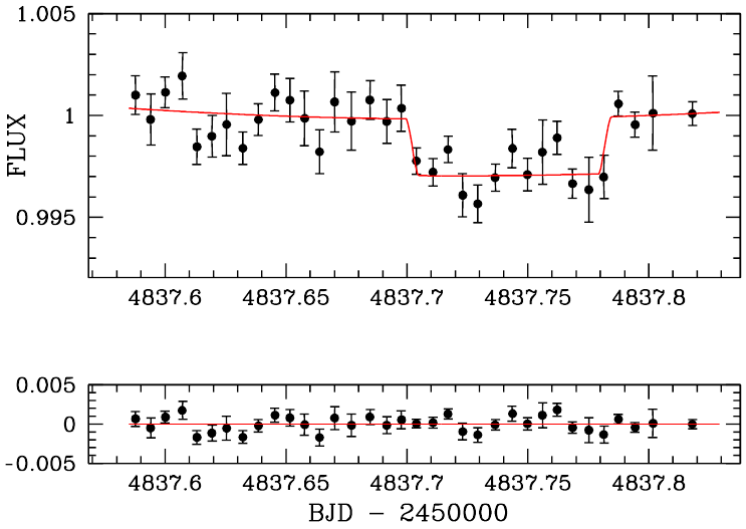

Figure 2.7 : One of the first ground-based detections of IR radiation from an exoplanet: CoRoT-1, observed at 2 μm with *HAWK-I* by Gillon et al. (2009).

Ground-based Facilities

Although space-based telescopes have made a major contribution to the study of exoplanet atmospheres, observations from the ground are picking up speed. In recent years they have provided an increasing number of atmosphere measurements, both in transmission and emission. Let me break up the extensive ground-based efforts into three groups, depending on the wavelength resolution employed for the observations: *photometry*, i.e. observations through photometric filters, whether simultaneous or not; *Spectrophotometry*, i.e. the observation of low-resolution spectra providing simultaneous lightcurves in several bands; and *High-resolution Spectroscopy* aiming to measure individual spectral features.

- **Photometry:** The number of follow-up observations of exoplanet **transits** employing classical relative CCD photometry has become vast. This is due to the easy observational access to hot Jupiter transits: transits can be readily detected even with basic instrumentation available to amateurs[1]. The transit observations of hot Jupiters have undergone a transformation in recent years. Early campaigns were aimed at providing precise lightcurves of the small number of known planets, with the goal to provide precise planetary parameters (radius, inclination, period), and to search for transit timing variations that might reveal additional components in the system (e.g. Holman et al. 2006, Southworth et al. 2009). While these aims are still part of current-day campaigns, the observers have taken to obtaining lightcurves in several filters, hoping to identify signatures in the transmission spectra. As outlined in Section 1.2.6, simultaneous observations have the advantage of limited impacts from stellar variability. A few instruments are providing simultaneous multi-band photometry: *GROND* (Greiner et al. 2008) at the ESO/MPG 2.2 m telescope can observe in 4 optical and 3 IR channels simultaneously and has been used to measure wavelength-dependent planetary radii on several targets, starting with OGLE2-TR-L9 b (Lendl et al. 2010), and most recently WASP-19 b (Mancini et al. 2013). In the North, *BUSCA* (Reif et al. 2000) at the 2.2 m telescope on Calar Alto is providing simultaneous lightcurves in four optical bands (e.g. Mislis et al. 2010), and most recently simultaneous observations in tree optical bands from the *MITSuME* telescope and *J, H,* K_s from *SIRIUS* at IRSF have been made public (Fukui et al. 2013, Narita et al. 2013). *ULTRACAM* (Dhillon et al. 2007), a visitor instrument at various telescopes, has contributed measurements in three simultaneous optical bands (Bento et al. 2013, Copperwheat et al. 2013). A similar approach is to alternate exposures in different filters, as has been done by Croll et al. (2011) in the J and K_s bands at CFHT, and Colón et al. (2010) with a tunable filter in two narrow bands centered on 790 and 794.4 nm with *OSIRIS* at the Gran Telescopio Ca-

[1]An overview of the impressive effort by amateur astronomers can be obtained from the *Exoplanet Transit Database:* `http://var2.astro.cz/ETD/`

narias (GTC). In a similar way, Sing et al. (2011a) detected potassium absorption for XO-2 using tunable filters at GTC/*OSIRIS*.

The astrophysical interpretation of these transit data have been limited by the filter's widths, that are too large to identify molecular signatures, combined with insufficient measurement precision, as well as offsets introduced by non-simultaneous observations, or non-uniformity in the data reduction.

The detection of **occultations** from the ground has been a difficult endeavor. While at optical wavelength the amplitudes are very small, in the near-IR instrumental effects and the effects of variable water absorption in the Earth's atmosphere need to be overcome. After a few unsuccessful attempts (Snellen 2005, Deming et al. 2007b, Knutson et al. 2007b, Snellen & Covino 2007), the year 2009 saw the ground-based detection of IR radiation from the hot Jupiters TrES-3 (de Mooij & Snellen 2009) and CoRoT-1 (Gillon et al. 2009, Rogers et al. 2009). The instruments used were *Liris* at the WHT in K_s-band (de Mooij & Snellen 2009, Rogers et al. 2009), and *HAWK-I* at the VLT (Gillon et al. 2009) paired with a narrow-band filter centered at 2 μm (shown for illustration purposes Figure 2.7). The subsequent years have shown several more near-IR occultation detections from *HAWK-I* (Anderson et al. (2010), Gibson et al. (2010), Lendl et al. (2013) for WASP-19 b, and Gillon et al. (2012) for WASP-43 b), CFHT/*WIRCam* (Croll et al. (2010a,b, 2011) for TrES-1 b, -2 b, and WASP-12 b) and WHT/*Liris* (de Mooij et al. (2011) and de Mooij et al. (2013) for HAT-P-1 b and WASP-33 b). These measurements have allowed some constraints on the planets' energy recirculation efficiencies and temperature structures.

The ground-based observation of occultations at wavelengths shorter than 1 μm has only produced very few results. Sing & López-Morales (2009) showed a z'-band occultation of OGLE-TR-56 b from observations with FORS2 at the VLT and MagIC-E2V at the Magellan telescopes. This work was followed by López-Morales et al. (2010) and Smith et al. (2011) who presented z'-band occultations of WASP-12 b and WASP-33 b from the Apache Point Observatory and ACAM at the WHT, respectively. While the López-Morales et al. (2010) detection has not been followed-up, WASP-12 b has been reobserved in occultation by Föhring et al. (2013), who find a result only marginally compatible (within 3 σ) with the previous value. Several z'-band occultations have been observed of WASP-19 by Burton et al. (2012), Abe et al. (2013), Mancini et al. (2013), Zhou et al. (2013) and myself (Lendl et al. 2013). Discussion about WASP-19 b is ongoing, and the reader is referred to Section 5.3 for details.

- **Spectrophotometry:** An improvement to observations in separate bands comes from spectrophotometry, as this approach allows to split the spectra in any wavelength bin which is deemed interesting, instead of being limited by the available filters. Spectrophotometry provides simultaneous lightcurves with a wavelength range set by the dispersion and noise properties of the observation. This technique has only been applied to transiting exoplanets in recent years, and has the potential of becoming one of the major workhorses for exoplanet science.

  The first ground-based spectrophotometric results have been presented by Bean et al. (2010), who observed the super-Earth GJ1214 b during transit using the *FORS2* instrument at the VLT in multi-object spectroscopy (MXU) mode at a wavelength range between 0.78 and 1 μm. These observations were supplemented with additional spectrophotometry between 0.61 and 0.85 μm (VLT/*FORS2*) and 2.09 to 2.36 μm (Keck/*MOSFIRE*) (Bean et al. 2011). The data revealed a flat transmission spectrum of GJ1214 b, which is shown in Figure 2.8 . Several other planets have been studied with this technique. XO-2 b has been observed in the optical by Sing et al. (2012) using the *OSIRIS* instrument at the GTC, leading to the detection of Sodium absorption. No sodium but a flat transmission spectrum was found by Gibson et al. (2013) from Gemini-South/*GMOS* observations of Wasp-29. Gemini-North/*GMOS* has been used to study the atmosphere of WASP-12 b in transmission by Stevenson et al. (2013), and a flat transmission spectrum of WASP-6 b has been observed with *IMACS* at the Baade telescope (Jordán et al. 2013).

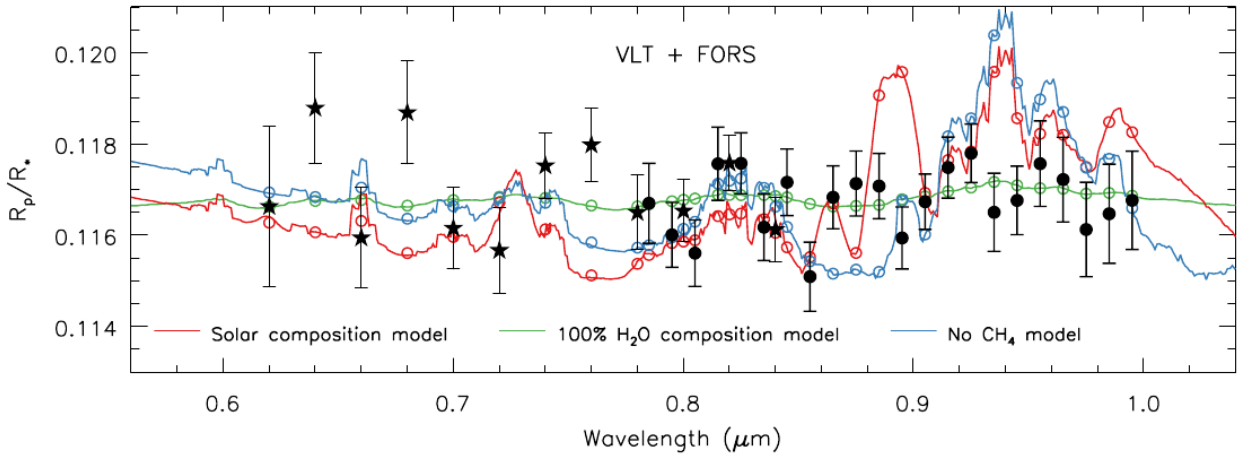

Figure 2.8 : The optical transmission spectrum obtained by Bean et al. (2010) and Bean et al. (2011) with the VLT/*FORS2* instrument in multi-object spectroscopy mode. The spectrum is remarkably flat.

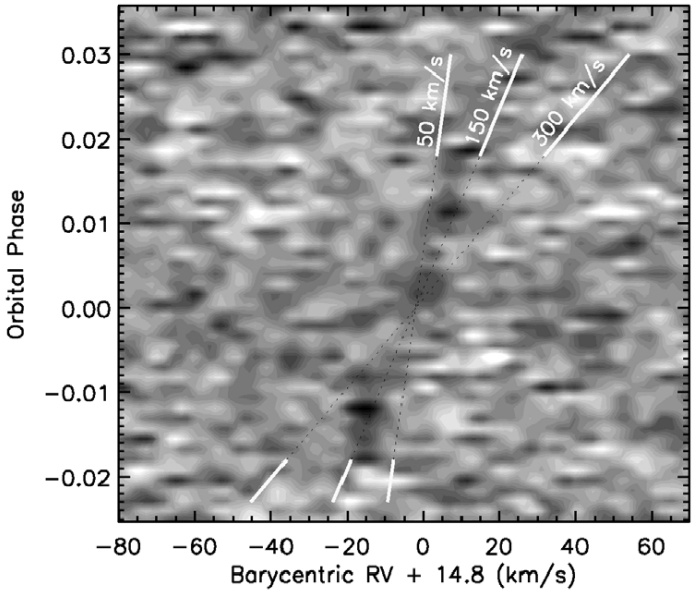

Figure 2.9 : The trace of CO absorption visible at changing RV during a transit of HD209458 b, as presented by Snellen et al. (2010). Note that time, given in units of the orbital phase, is represented on the ordinate axis, while the strength of the signal is shown in grey-scale for the RV values given on the x-axis.

In the near IR, a transmission and emission spectrum between 1.25 and 2.35 µm of WASP-19 b has been obtained by Bean et al. (2013) using *MMIRS* at the Magellan II telescope, and and transits of the hot Uranus GJ3470 b have been observed by Crossfield et al. (2013) (using Keck/*MOSFIRE*) in wavelength range from 2.09 to 2.36 µm.

- **High-resolution Spectroscopy:** The detection of elements in high-resolution spectra obtained throughout transit has been first achieved from space (Charbonneau et al. 2002). However also in this domain ground-based observations have caught up and provided a number of detections. From data obtained with the Hobby-Eberle-Telescope (HET), Redfield et al. (2008) detected Sodium in the atmosphere of HD189733 b. Further detections from the HET include absorption in $H\alpha$ (Jensen et al. 2012), Sodium (Jensen et al. 2011) and Calcium (Astudillo-Defru & Rojo 2013) in HD209458 b. Sodium absorption has been confirmed for HD209458 b with Subaru/*HDS* (Snellen et al. 2008) and Keck/*HIRES* (Langland-Shula et al. 2009). Finally, Sodium absorption has also been found in WASP-17 b by Zhou & Bayliss (2012) (using Magellan/*MIKE*) and Wood et al. (2011) (using VLT/*GIRAFFE*).

  Using the IR spectrograph VLT/*CRIRES*, Snellen et al. (2010) detected CO absorption lines and

their shift due to the planets orbital movement. The change in location of the lines due to the planet's orbital motion is visible from these data (see Figure 2.9). Further VLT/*CRIRES* observations have been obtained for τ Boo b (Brogi et al. 2012, Rodler et al. 2012), where the signal of CO was detected in emission, HD189733 b (CO absorption de Kok et al. 2013), and 51 Peg b (CO and H_2O absorption, Brogi et al. 2013). This method to study exoplanets was also applied to data from Keck/*NIRSPEC* by Rodler et al. (2013) detecting CO in HD189733 b.

Not only do these measurements constrain elemental abundances in the planetary atmospheres, they also give a direct measurement of the planetary radial velocity, which in turn allows to solve directly for both the stellar and planetary masses.

2.3.2 Atmosphere Models

To go from any kind of astronomical measurement to the physical properties of the targets, it is necessary to have model predictions the data can be compared to. In the case of planetary atmospheres, this means that we need to construct models for the stellar and planetary emission and their ratio as seen from occultation measurements, and the transmission of stellar light through the outer layers of a planetary atmosphere as seen during transit.

Models of exoplanet spectra, be it for the transmissive or emissive case, rely on calculations of radiative transfer across the planetary atmosphere. The principle here is to follow the specific intensity (I) of a beam as it passes through the layers of the atmosphere. Following the notation of Mihalas (1978), the *specific intensity* $I(\mathbf{r},\mathbf{n},\nu,t)$ is defined as the radiation at a position $\mathbf{r}$ in direction $\mathbf{n}$, having a frequency ν, at time t transporting the energy E in a frequency interval $(\nu,\nu+d\nu)$ across an area dS into a solid angle $d\omega$ during the time dt,

$$\delta E = I(\mathbf{r},\mathbf{n},\nu,t)dS\cos(\theta)d\omega d\nu dt\,. \tag{2.2}$$

Here ϕ is the angle between the beam direction and the surface normal. I has the units $[Jm^{-2}sr^{-1}Hz^{-1}]$ and is related to the observed quantity *Flux* $\mathbf{F}(\mathbf{x},\nu,t)$ having the units $[Jm^{-2}s^{-1}Hz^{-1}]$ via

$$\mathbf{F}(\mathbf{x},\nu,t) = \int_{\omega} I(\mathbf{r},\mathbf{n},\nu,t)\mathbf{n}d\omega\,. \tag{2.3}$$

The change in intensity at a position $\mathbf{r}$ across a distance ds in direction $\mathbf{n}$ at a frequency ν and time t is defined by the *transfer equation*,

$$\left[\frac{1}{c}\left(\frac{\delta}{\delta t}\right)+\left(\frac{\delta}{\delta s}\right)\right] I(\mathbf{r},\mathbf{n},\nu,t) = \eta(\mathbf{r},\mathbf{n},\nu,t) - \chi(\mathbf{r},\mathbf{n},\nu,t)I(\mathbf{r},\mathbf{n},\nu,t)\,, \tag{2.4}$$

with c being the speed of light. χ is the *extinction coefficient* (a measure of *opacity* in units of $[m^{-1}]$), controlling the fraction of beam intensity that is lost across ds. The extinction coefficient is made up by κ stemming from the absorbed radiation, and σ stemming from the radiation scattered out of the beam:

$$\chi(\mathbf{r},\mathbf{n},\nu,t) = \kappa(\mathbf{r},\mathbf{n},\nu,t) + \sigma(\mathbf{r},\mathbf{n},\nu,t)\,. \tag{2.5}$$

Analogously, η (having the units $[Jm^{-3}sr^{-1}s^{-1}Hz^{-1}]$) is called the *emissivity* and represents the contribution to the beam stemming from the material inside ds, either via radiative (η_t) or scattering (η_s) processes.

$$\eta(\mathbf{r},\mathbf{n},\nu,t) = \eta_t(\mathbf{r},\mathbf{n},\nu,t) + \eta_s(\mathbf{r},\mathbf{n},\nu,t)\,. \tag{2.6}$$

In *(local) thermodynamic equilibrium (LTE)* the radiative part of the emissivity is given directly from the radiative extinction coefficient and the gas temperature T by *Kirchhoff's law*

$$\eta_t(\mathbf{r},\mathbf{n},\nu,t) = \kappa(\mathbf{r},\mathbf{n},\nu,t)I(\mathbf{r},\mathbf{n},\nu,t) = \kappa(\nu)B_\nu\left(T(\mathbf{r},t)\right)\,, \tag{2.7}$$

where $B_\nu(T)$ denotes the Planck function at temperature T. In the most simple case of isotropic scattering, the scattering contribution is given by the scattering coefficient $\sigma(\mathrm{r},\nu)$ together with the mean intensity J, $J(\mathbf{r},\nu,t) = (4\pi)^{-1} \oint I(\mathbf{r},\mathbf{n},\nu,t)\, d\omega$, as

$$\eta_s(\mathbf{r},\nu,t) = \sigma(\mathrm{r},\nu) J(\mathrm{r},\nu)\,. \tag{2.8}$$

In this way, the microscopic processes governing the passage of radiation through a medium are contained in the coefficients $\chi(\mathbf{r},\mathbf{n},\nu,t)$ and $\eta(\mathbf{r},\mathbf{n},\nu,t)$. Their accurate calculation involves accounting for the atoms and molecules in the planetary atmosphere, their various energy states and their absorption and scattering crossections. In particular for molecules with a vast amount of lines calculating these coefficients is a tedious process.

For the approximation of a static one-dimensional planar atmosphere, the *transfer equation* (Equation 2.4) reduces to

$$\mu \left[\frac{dI(z,\mathbf{n},\nu)}{dz} \right] = \eta(z,\mathbf{n},\nu) - \chi(z,\mathbf{n},\nu) I(z,\mathbf{n},\nu)\,. \tag{2.9}$$

where $\mu = \cos\theta$, with θ being the angle between the surface normal and the beam direction. It is useful to define the *source function*, $S(\mathbf{z},\nu)$,

$$S(z,\nu) = \frac{\eta(z,\nu)}{\chi(z,\nu)} \tag{2.10}$$

and the *optical depth* $\tau(z,\nu)$,

$$\tau(z,\nu) = \int_z^{z=0} \chi(z',\nu) dz'\,, \tag{2.11}$$

that can be used as a position measurement in the atmosphere. The optical depth is related to the *mean free path*, $l = 1/\chi$ via

$$d\tau = \frac{1}{l} dz\,. \tag{2.12}$$

In LTE, the relation $S(\tau',\mu,\nu) = B(\tau',\mu,\nu)$ holds. In the absence of a scattering contribution to $\eta(z,\mathbf{n},\nu)$, an illustrative analytical solutions exists as

$$I(\tau_1,\mu,\nu) = I(\tau_2,\mu,\nu) e^{\frac{-(\tau_2-\tau_1)}{\mu}} + \frac{1}{\mu} \int_{\tau_2}^{\tau_1} S(\tau',\mu,\nu) e^{\frac{-(\tau'-\tau_1)}{\mu}} d\tau'\,. \tag{2.13}$$

Here the first term represents the attenuation of the radiation entering at the bottom of the atmosphere, and the second term represents the emission from the atmosphere itself including for its subsequent attenuation in higher layers. Assuming a hypothetical atmosphere of infinite depth, the initial intensity can be neglected and the intensity leaving the atmosphere ($\tau = 0$) is given by

$$I(0,\mu,\nu) = \frac{1}{\mu} \int_0^\infty S(\tau',\mu,\nu) e^{\frac{-\tau'}{\mu}} d\tau' = \frac{1}{\mu} \int_0^\infty B(\tau',\mu,\nu) e^{\frac{-\tau'}{\mu}} d\tau'\,. \tag{2.14}$$

Thus, for a given wavelength, the emerging intensity is given by the value of the Planck function B over the ranges of τ where the emission that occurs manages to escape the atmosphere without being reabsorbed[2]. Inside molecular bands the absorption coefficients χ_b are larger and consequently (Equation 2.12) the optical depth $\tau_b = 2/3$ is reached at higher altitudes z_b in the planetary atmosphere,

[2]The emitted radiation stems from an average optical depth of $\tau = 2/3$, as described by the *Eddington-Barbier relation* (see e.g. Mihalas (1978) for a derivation).

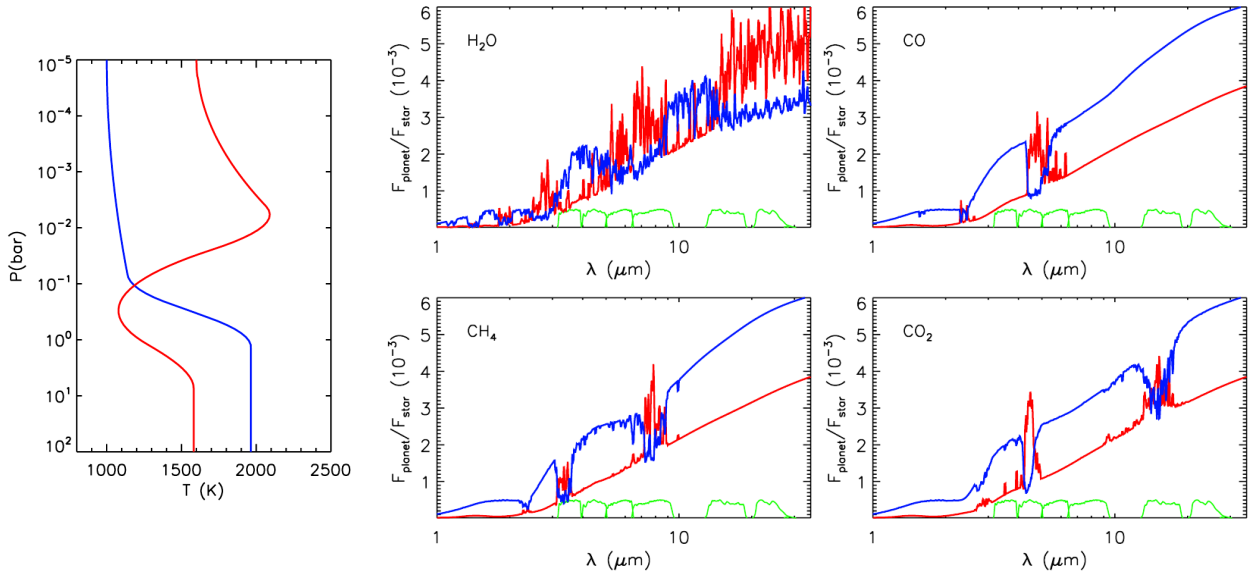

Figure 2.10 : The contributions of H_2O, CO, CH_4, and CO_2 to the total planetary emission spectrum assuming two different thermal profiles (shown on the left): a profile containing a temperature inversion (red), and a profile with a temperature declining monotonically outwards (blue). Figure credit Madhusudhan & Seager (2010)

where the temperature is T_b. For wavelengths outside molecular bands or atomic absorption lines, χ_c is smaller and the radiation stems from a different region of temperature T_c in the atmosphere. It is then the temperature differences between the emitting regions that define the shape of planetary emission spectrum. A high temperature in regions of high opacity ($T_b > T_c$) will create emission features, but a low temperature in the same region ($T_b < T_c$) will create absorption features. Thus the emission spectrum gives us not only information about which elements are present in the planetary atmosphere but also map the temperature structure of the atmosphere. Figure 2.10 shows the contributions of the most important molecules to atmosphere with distinct temperature structures.

The theory for transmission spectra is essentially the same, but different boundary conditions need to be applied to account for the stellar radiation entering on the far side of the planet. Due to the geometry, the stellar radiation passes mostly through the outer layers of the planetary atmosphere, where densities are low. For the study of extended planetary envelopes at very low densities, the LTE assumption is not necessarily justified, complicating the calculations (e.g. Menager et al. 2013).

In practice the calculation of exoplanet emission and transmission spectra is an complex process that has been carried out numerically by a number of teams, e.g. Seager & Sasselov (1998), Sudarsky et al. (2003), Fortney et al. (2005), Burrows et al. (2006). The models account for contributions of a variety of molecules present at different mixing ratios depending on the temperature and pressure at a given point in the planetary atmosphere. Motivated by the observation of emission features (Knutson et al. 2008), some model calculations include additional opacities at high altitudes triggering a temperature inversion or stratosphere (e.g. Burrows et al. 2007b, Fortney et al. 2008). Also, haze or clouds that have been detected in transmission spectra (Pont et al. 2008) have been included (e.g. Heng et al. 2012, Marley et al. 2013). To date, 3-D models (e.g. Fortney et al. 2006a, Showman et al. 2008) have replaced initial 1-D models, providing a more global picture on the emission from exoplanets.

Atmospheric retrieval approaches (e.g. Madhusudhan & Seager 2009, Lee et al. 2012, Line et al. 2012) sample the parameter space of possible solutions for a given set of measurements, aiming to find the model best fitting to the data. This can be computationally expensive and therefore simplifications e.g. parametrization of the T-P profile (Madhusudhan & Seager 2009) are used.

When it comes to the interpretation of exoplanet spectra, large uncertainties are ubiquitous. First,

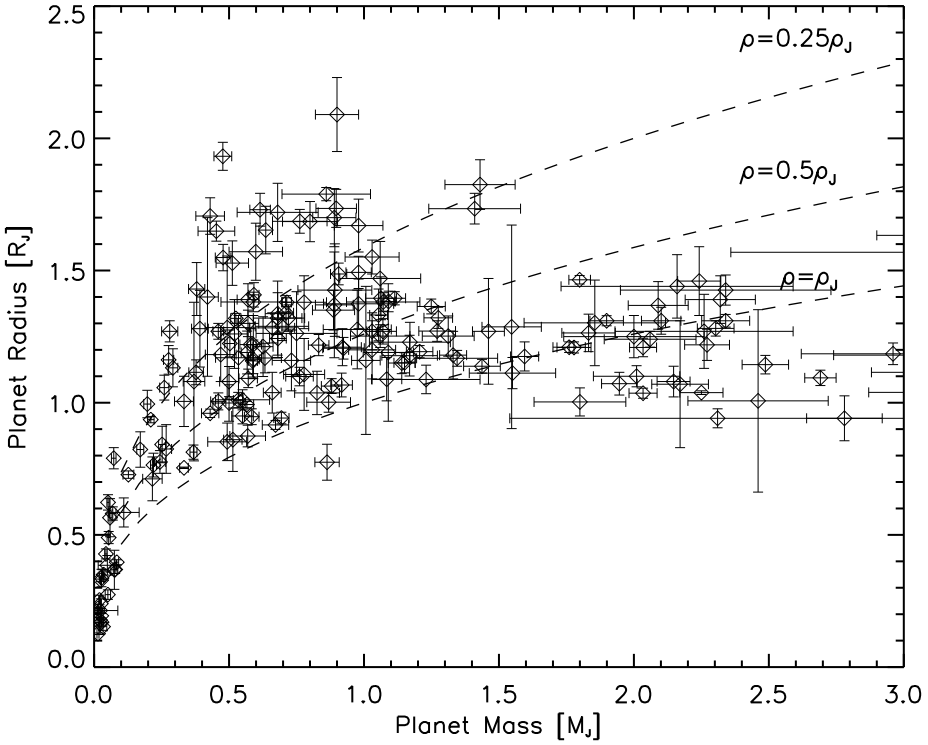

Figure 2.11 : The mass-radius diagram of transiting exoplanets, zoomed in on the area where many hot Jupiters with inflated radii are found. The dashed lines refere to curves of densitis of 1, 0.5 and 0.25 times that of Jupiter. In the range of 0.3 to 1.5 R_J, a single planet (WASP-59 b) has a density larger than that of Jupiter. On the contrary, densities as lower than 0.25 ρ_J are very common.

our data are far from precise. On the contrary to high-resolution spectra that are available for bright astronomical objects, the spectra of exoplanets are mapped with a hand full of points. Also, the elements are usually assumed to be in chemical equilibrium, with their abundances being determined by the temperature and pressure at their location in the atmosphere. Observations and modeling (Cooper & Showman 2006, Moses et al. 2011, Knutson et al. 2012) have already hinted that this is not always accurate.

2.4 Atmospheres of Highly Irradiated Planets

Once we have been able to infer the properties of hot Jupiters, they need to be put into context with predictions from physical models. There are several aspects of hot Jupiters that have been challenging to explain, and I will elaborate on them below. Two major schemes have been proposed to classify hot giant planets, following their temperature profile and composition.

2.4.1 The Radius Anomaly

The most essential piece of information obtained from transit lightcurves is the planetary radius. Given a mass estimate (e.g. from RV data) a Mass-Radius diagram can be constructed. Doing so for the sample of hot Jupiters (see Figure 2.11) reveals that a large part of these planets are much less dense than Jupiter. Less dense even as standard models for irradiated atmospheres (Fortney et al. 2007) predict. The origin of this *radius inflation* has been under a great deal of scrutiny during the last years.

One piece of information has been added to the puzzle by Demory & Seager (2011) and Laughlin

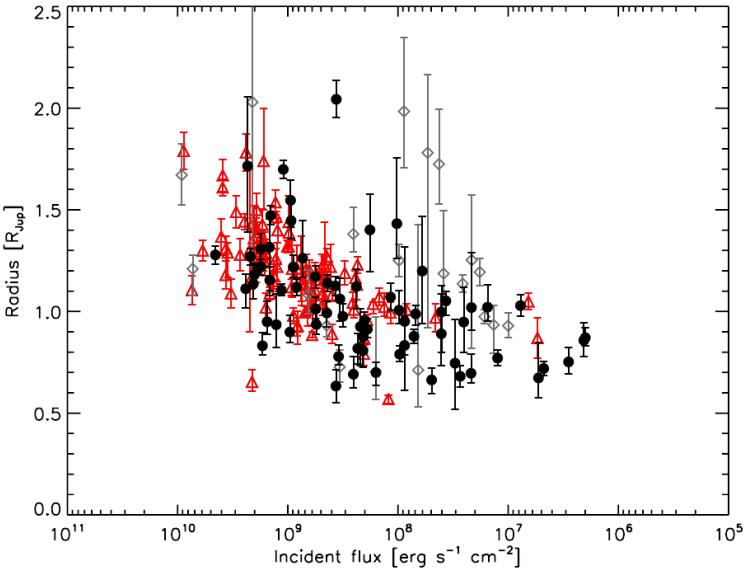

Figure 2.12 : The transiting hot Jupiter planets including *Kepler* candidates studied by Demory & Seager (2011). The red triangles denote confirmed planets (including those from ground-based surveys), the black filled circles denote good *Kepler* candidates, while the gray trapezoids denote *Kepler* candidates with a high false positive probability. A positive correlation between the incident flux and the planetary radius is seen.

et al. (2011): As shown in Figure 2.12 , radius inflation is most pronounced for hot planets, i.e. planets receiving a large incident stellar flux, while it vanishes for planets receiving 2×10^8 erg s^{-1}cm^{-2} or less. In terms of temperature, this transition occurs for planets of an equilibrium temperature (see equation 1.15) of $\sim$ 1300 K. This means that whatever mechanism is causing the inflated radii of hot Jupiters, it must depend on either the incoming stellar flux or the proximity of the planet to a massive host star.

While the subject is still under heavy debate, several mechanisms have been proposed to account for the mass-radius anomaly.

- **Atmospheric circulation:** One of the initial propositions for processes possibly responsible for the inflated radii has been made by (Showman & Guillot 2002) on the basis of numerical simulations of atmospheric circulation. In their simulations, they find that strong winds are created from the large stellar irradiation, they penetrate into the deeper atmospheric layers and deposit the equivalent of $\sim$ 1 % of the incident stellar flux well inside the planet. Little support has been provided for this model in recent years, and the downward energy flux has not been reproduced by newer simulations (Burkert et al. 2005).

- **Enhanced opacities:** Instead of external energy being deposited into the planet, Burrows et al. (2007a) suggest that super-solar metallicities may be playing an important role. Higher metallicities increase the opacities in the planet atmosphere and therefore slow the energy loss and thus the contraction of the planet. While enhanced opacities can reproduce the radii of some planets (Burrows et al. 2007a), several caveats remain. First, this mechanism is not dependent on the incident stellar radiation, and thus does not fit well with the observations. Second, Burrows et al. (2007a) did not account for gravitational settling, and the increase of molecular weight going in hand with an increase in metallicity (Guillot 2008). Finally, Liu et al. (2008) showed that enhanced opacities alone can not explain the observed planetary radii. Thus, while opacities have a part to play in determining the planetary radii, they do not appear to be the dominant factor.

- **Layered convection:** Another approach independent of stellar irradiation is provided by Chabrier & Baraffe (2007). Here, the heat transport efficiency of the planet and thus its contraction is slowed by "Double diffusive convection", i.e. the break-up of convection into several layers. As *enhanced opacities*, this process does not reproduce the observed correlation of planetary radii with incident flux.

- **Tidal dissipation:** Probably the best-studied process for the inflation of hot Jupiter radii is the heating of the planet by tidal forces (Bodenheimer et al. 2001). Provided the planet has an eccen-

tric orbit or non-synchronous rotation, the dissipation of tides within the planet create heat which then acts to slow contraction or even inflate previously contracted planets (Gu et al. 2003). Several teams (Ibgui & Burrows 2009, Miller et al. 2009, Leconte et al. 2010, Ibgui et al. 2011) have performed simulations of planetary evolution including tidal heating. Tides due to circularization and synchronization, and in some cases also realignment (Winn & Holman 2005) are efficient at inflating planets, and most of the known systems can be reproduced either by tidal heating alone or by a combination of tidal heating and enhanced opacities (e.g. Liu et al. 2008, Miller et al. 2009, Leconte et al. 2010). However, they do so only on limited timescales (e.g Miller et al. 2009, Leconte et al. 2010).

A possible solution to this problem of timescales has been proposed in the form of *thermal tides* (Socrates 2013): tides that are created on the planet by the incident stellar radiation, as the hot and cold parts of the atmosphere have different densities. As the thermal inertia of the atmosphere is nonzero, the thermal tides are offset from the substellar point and the gravitational pull of the star acts to slightly spin up the planet. This causes a permanent non-synchronous spin and an energy source for the inflation of the planet.

Tidal processes have the advantage that they are most effective for close-in planets and thus fit well with the observed sample of inflated hot Jupiters.

- **Ohmic heating:** Suggested by Batygin & Stevenson (2010) and Perna et al. (2010), *ohmic heating* is a process that efficiently allows the energy from stellar irradiation to be deposited low enough in the planetary atmosphere to cause radius inflation. At atmospheric temperatures above ~1500 K the alkali (predominantly Na and K) in the planetary atmosphere are partially ionized. The charged particles are advected with atmospheric winds and give rise to a magnetic field, which exists next to the "background" planetary field. This in turn causes an induced current that is driven in towards deeper atmospheric layers where it dissipates ohmically, heating the surrounding material. This process is promising as it provides a correlation with the incident flux, albeit with some scatter due to varying atmospheric properties such as metallicity and clouds or haze (Heng 2012). However Spiegel & Burrows (2013) argue that the necessary wind speeds can not be sustained and the energy is not deposited deep enough to keep the atmosphere from contracting.

2.4.2 Composition

One of the most intriguing and perhaps *the* most intensely sought after information on extrasolar planets is their composition. Compositions of exoplanets may be inferred from wavelength-dependent signatures in the planets' transmission and emission spectra, and both the observational and the modeling approach have been discussed in the previous sections. Here I provide an overview of the results, and point towards a number of difficulties that persist in the interpretation of planetary transmission and emission spectra.

Early Detections

The first detection of elements in exoplanet atmosphere were obtained from *STIS* high-resolution data. Increased absoprtion by Sodium (Charbonneau et al. 2002) and Hydrogen (Vidal-Madjar et al. 2003) were found during transits of HD209458 b.

From the publication of the first *Spitzer* occultation measurements (Charbonneau et al. 2005, Deming et al. 2005) on, forward models were matched to the data (Burrows et al. 2005, Fortney et al. 2005, Seager et al. 2005). While no constraints on the presence of single elements was possible at that time, Fortney et al. (2005) do note that a more metal-rich atmosphere gives a better match to the data. As the wavelength coverage increased, and in particular with the becoming available of *IRS* spectra (Grillmair et al. 2007, Richardson et al. 2007) and spectrophotometry from *STIS* (Knutson et al. 2007c), it became

possible to make some more precise constraints on planet atmospheres. Barman (2007), Burrows et al. (2007b) and Fortney et al. (2007) found that the inclusion of water in their models of HD209458 b is required for to match the data.

In the following years, further data were acquired and compared to forward models bringing about announcements of detections of several more molecules, in particular from HST/*NICMOS*. Announcements were made for detections of CH_4, H_2O, and CO_2 on HD209458 b, CH_4, H_2O, CO_2, and CO on HD189733 b (Swain et al. 2008, 2009b), and CH_4, H_2O, CO_2 on XO-1 b (Tinetti et al. 2010). These measurements were contrasted by the detection of an optically thick haze layer on HD189733 b (Pont et al. 2008, Sing et al. 2009) extending out to 1.6 μm (Gibson et al. 2012). A similar, yet less pronounced structure was found on HD209458 b (Sing et al. 2011b). Finally Gibson et al. (2011) pointed out that *NICMOS* suffered from severe correlated noise, and the accuracy of the above detections is hence in question, as the measurements have not been reproduced.

Detections with Atmospheric Retrieval

In the last ∼5 years, both the inference method but also tone of announcement have changed quite drastically when it comes to studying the composition of exoplanet atmospheres. With the becoming available of retrieval methods (Madhusudhan & Seager 2009, Lee et al. 2012, Line et al. 2012) it is now possible to test a much larger parameter space in composition and temperature structure, finding the best solution and identifying degeneracies between model parameters. Using retrieval procedures, spectra of a considerable number of planets have been analyzed. The degree to which the abundances are constrained naturally depends on the amount, wavelength range and precision of the available data. Yet, any inaccuracies existing due to systematic errors affecting the measurements remain present. An illustration of the change in the observed spectrum given variations in the H_2O and CO_2 abundances is shown in Figure 2.13 .

Some of the signatures identified have been H_2O, CO, CH_4, and CO_2 on HD209548 and HD189733 (Madhusudhan & Seager 2009, Line et al. 2013a). The inferences also depend on the degree of flexibility in the model composition (i.e. non-equilibrium chemistry, non-solar C/O ratios), as the molecular bands overlap. Thus, at least at the current resolution, certain features may be caused by different molecules.

Non-standard Mixing Ratios

Several works have studied the impact of allowing for non-Solar chemical mixing ratios. Madhusudhan & Seager (2010), Madhusudhan et al. (2011), Madhusudhan (2012) and Line et al. (2013b) included *enhanced C/O ratios* ($C/O \gtrsim 1$, $C/O_{solar} \sim 0.5$), producing diverging results. Madhusudhan et al. (2011) and Madhusudhan (2012) are able to explain several planets (CoRoT-2 b,WASP-12 b,WASP-19 b,WASP-33 b and XO-2 b) better with carbon-rich atmospheres than with solar C/O ratios. In contrast, Line et al. (2013b) find no evidence for carbon enhancement in the atmospheres of the very same planets. Moses et al. (2013) studied the subject with a forward modeling approach using general circulation models, supporting the carbon-rich nature of WASP-12 b, XO-1 b, and CoRoT-2 b.

The subject of *disequilibrium chemistry* has been touched by a number of authors (e.g. Moses et al. 2011, Knutson et al. 2012, Kopparapu et al. 2012, Line & Yung 2013). Chemical disequilibrium is expected to occur in exoplanet atmospheres due to stellar irradiation (and thus photochemical processes) as well as due to vertical transport of molecules ("quenching") (e.g. Moses et al. 2011). The predicted effects on the observed spectra are too small to be detected for the transiting hot Jupiters (Moses et al. 2011, Line & Yung 2013) with current instruments. However Line & Yung (2013) find a disequilibrium chemistry solution for the directly imaged planet HR8799 b, and Knutson et al. (2012) infer an atmosphere in chemical disequilibrium from multi-color phase curves of HD189733 b. Also for the lower-mass planet GJ 436 b, disequilibrium chemistry seems to be required to match observations (Madhusudhan & Seager 2011, Moses et al. 2013).

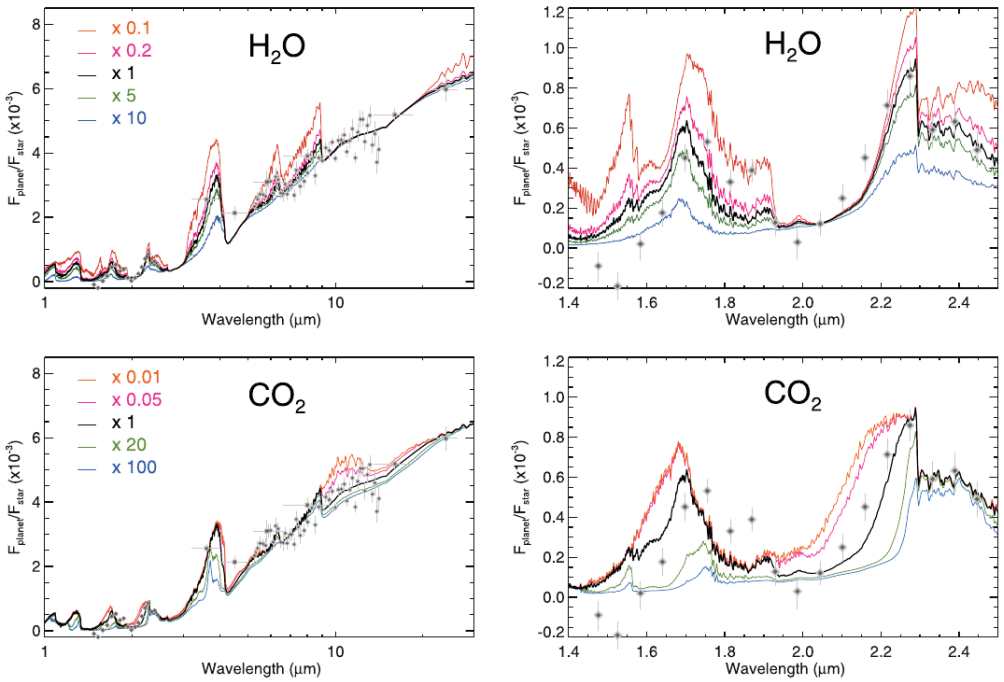

Figure 2.13 : The impact of variation in the abundance of H_2O and CO_2 on the measured emission (left) transmission (right) spectrum of HD189733 b. The best fit model of (Lee et al. 2012) is shown in black and the colored lines are the resulting spectra calculated from models changing the molecular abundance of H_2O (top) and CO_2 (bottom) by the factors given in the figures. Figure credit: Lee et al. (2012).

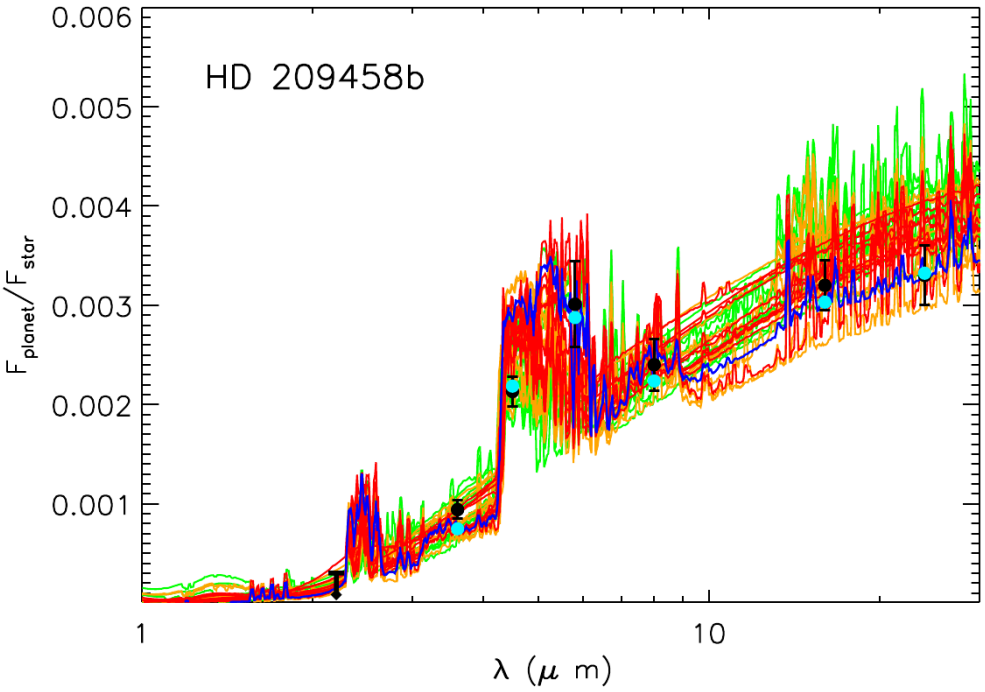

Figure 2.14 : The dayside emission spectrum of HD209458 b as observed by *Spitzer* (Deming et al. 2005, Knutson et al. 2008) together with an upper limit from Richardson et al. (2003). The measurements are best fit by an atmosphere containing a temperature inversion. The best-fit model of Madhusudhan & Seager (2009) is shown in blue while the other colors represent models with a lower goodness of fit. Figure credit Madhusudhan & Seager (2009).

High-Resolution Spectroscopy

As already mentioned previously, high resolution spectroscopy has yielded some reliable detections of elements in planetary atmospheres. This has been achieved either in the optical or UV via detections in single lines (e.g. Charbonneau et al. 2002), or via the identification of a set of molecular lines moving at the planetary Doppler velocity (e.g. Snellen et al. 2008). These methods have yielded detections of Na (e.g. Charbonneau et al. 2002, Redfield et al. 2008), K (Lewis et al. 2013), H (Jensen et al. 2012), Ca (Astudillo-Defru & Rojo 2013), CO (e.g. Snellen et al. 2008, Rodler et al. 2013), and H_2O (Brogi et al. 2013) on some of the most favorable planets. Signatures of H (e.g. Vidal-Madjar et al. 2003), C, Si (Linsky et al. 2010), and Mg (Vidal-Madjar et al. 2013) have been detected in the evaporating envelops of a few planets.

2.4.3 Temperature Inversions

Perhaps *the* most studied parameter from exoplanet emission spectrophotometry are the atmospheric pressure-temperature (P-T) profiles. From the shape of the molecular signatures determined from occultation measurements the temperature of the emitting material can be determined. As different wavelengths probe different depths (i.e. pressure levels) in the planetary atmosphere, the temperature can be inferred as a function of altitude. Simply speaking, if wavelengths probing inside molecular bands (where the opacity is high and thus the radiation stems from relatively high up in the atmosphere) show a lower flux than regions outside these bands, the temperature higher up in the atmosphere is lower than in the further-down regions. On the contrary, if the molecular signatures are seen in emission, the temperature must be greater at higher altitudes in the atmosphere than further down.

The Eath's atmospheric P-T profile shows an increase in temperature (a "stratosphere") at an altitude of $10 - 50$ km (e.g. de Pater & Lissauer 2010) caused by the absorption of Solar flux in the ozone layer. Predictions for a similar effect in highly irradiated exoplanets have been made by Hubeny et al. (2003) and Fortney et al. (2006b). They were shown to be compatible with the observed occultation depths of HD209458 b (e.g. Burrows et al. 2006, 2007b, Knutson et al. 2008, Madhusudhan & Seager 2010). In Figure 2.14 , the *Spitzer* broad band data on HD209458 b are shown together with models including a temperature inversion. The high-altitude absorbers necessary for causing the temperature inversion have been suspected to be TiO and VO (e.g. Hubeny et al. 2003, Fortney et al. 2006b), however this might be problematic as TiO could be depleted in the upper atmospheres of most of the known hot Jupiters due to gravitational settling (Spiegel et al. 2009). Zahnle et al. (2009) suggested that the absorbers could also be sulfur compounds (HS and S_2).

To identify the presence of a temperature inversion one requires fewer datapoints than for the inference of molecular abundances. Typically a set of broadband photometric points suffices. Among others, the planets XO-4 b, HAT-P-6 b, and HAT-P-8 b have been found to show an inversion, no inversion, and a small or no inversion, respectively (Todorov et al. 2012) based on only the 3.6 and 4.5 μm *Spitzer* channels. Since the 4.5 μm *IRAC* band probes a region of high CO and H_2O opacities, but the 3.6 μm *IRAC* band is much less affected by these molecules, their flux ratio (in comparison to a black-body model) is a good proxy for the existence of an inversion (Knutson et al. 2010) that remains accessible even during the *Spitzer warm mission*. It has become clear that a significant fraction of hot Jupiters possess inversions, as an increasing number of planets have been studied in occultation with *IRAC*.

There must be a physical reason why some planets show inversions while others do not. Given the inversions are in fact caused by TiO and VO absorption, the initial idea was that inversions occur in atmospheres hot enough to allow for these molecules to exist in their gaseous phase in the upper atmosphere (Fortney et al. 2008). Figure 2.15 shows the dependence of the predicted temperature structure for hypothetical planets at different semi-major axes and hence temperatures.

However it has turned out that several planets do not fit into this scheme. As an example, the relatively "cool" hot Jupiter XO-1 b was found to possess an inversion (Machalek et al. 2008), while the highly irradiated WASP-19 b is showing no sign of a stratosphere (Anderson et al. 2013b). To account

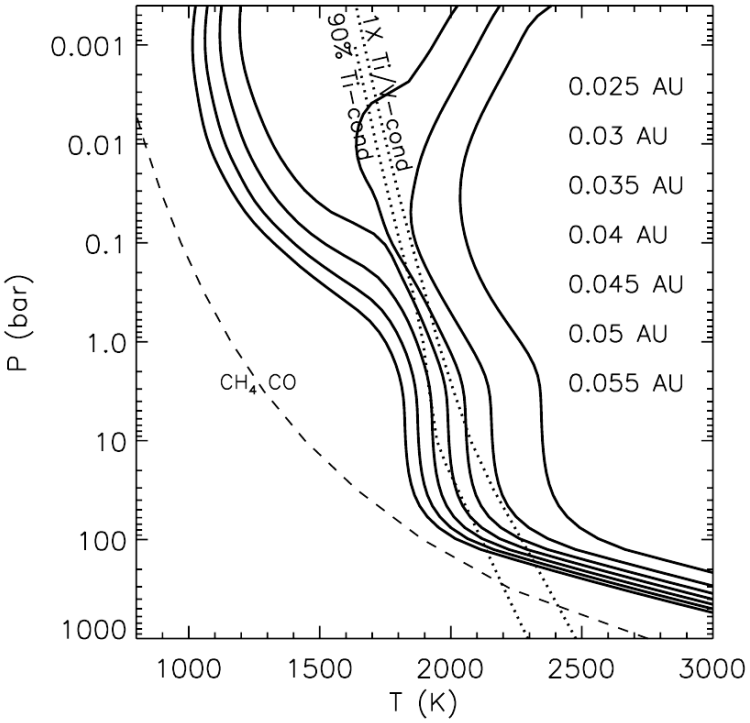

Figure 2.15 : The atmospheric P-T profile is shown for planets of decreasing orbital separation and hence increasing temperature (left to right). The dotted lines indicate the condensation curves of TiO/VO (right) and the curve below which 90% of Ti is removed from the atmosphere (left). The dashed line indicates the transition between CH_4 and CO as the main carbon carrier. Figure credit: Fortney et al. (2008)

for this, Knutson et al. (2010) proposed that the presence of an inversion may depend more strongly on the activity level of the host star than on the irradiation of the planet. Active stars possess a higher UV flux that destroys the high-opacity compounds and consequently inhibit the formation of an inversion. The corresponding distribution of temperature, activity level and P-T profile is shown in Figure 2.16 .

Madhusudhan (2012) added the planetary chemistry as an additional factor influencing the atmospheric P-T profiles. For carbon rich planets (i.e. planets with C/O $\gtrsim$ 1), the TiO and VO abundances naturally decrease, leaving less high-opacity material in the upper atmospheres. As a consequence, the creation of an inversion is inhibited. The prediction of this model is thus that only planets with an oxygen-rich atmosphere and high stellar irradiation have stratospheres. Together with the activity - inversion connection by Knutson et al. (2010), the prediction becomes even more stringent: only planets with an oxygen-rich atmosphere, high stellar irradiation *orbiting low-activity stars* have stratospheres. These predictions warrant an intense observational efforts directed at the atmospheric characterization hot Jupiters, and the work I present in Sections 5.3.3 and 6 should be seen as my present contribution to this subject.

2.4.4 Classification Schemes

Based on temperature, chemistry and P-T structure, two classification schemes have been devised that should be briefly discussed.

- **pM – pL:** Fortney et al. (2008) devised this scheme based on planet temperature. For planets belonging to the hotter pM class, the atmosphere is showing a thermal inversion at high altitudes caused by the absorption of stellar flux by TiO and VO. pM-class planets have high fluxes in the near IR due to their hot stratospheres, and have a low redistribution efficiency of energy from the day to the night side. This is due to the fact that at high temperatures time scales for radiation are shorter than those for advection and hence the flux is reemitted before the hot material has moved to the night side.

- **O1 – O2 – C1 – C2:** Madhusudhan (2012) modified the above classification scheme by adding in a second dimension: that of the C/O abundance ratio. Planets with low/high incident radiation *and*

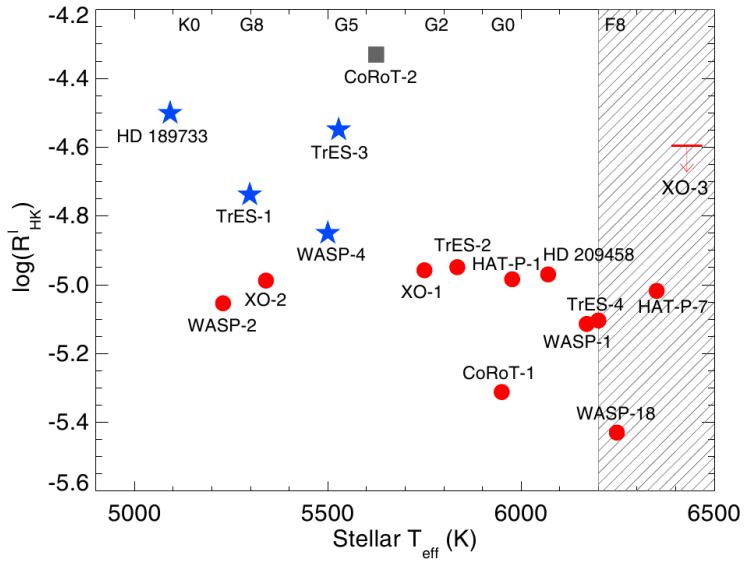

Figure 2.16 : The stellar activity - inversion connection as represented by Knutson et al. (2010). Red filled circles refer to planets with temperature inversions, while blue stars denote planets with a monotonically decreasing P-T profile. Note that there is a divide between the two samples at $log(R'_{HK}) \sim -4.9$. The shaded region refers to temperatures where the $log(R'_{HK})$ diagnostic becomes unreliable. Figure credit: Knutson et al. (2010)

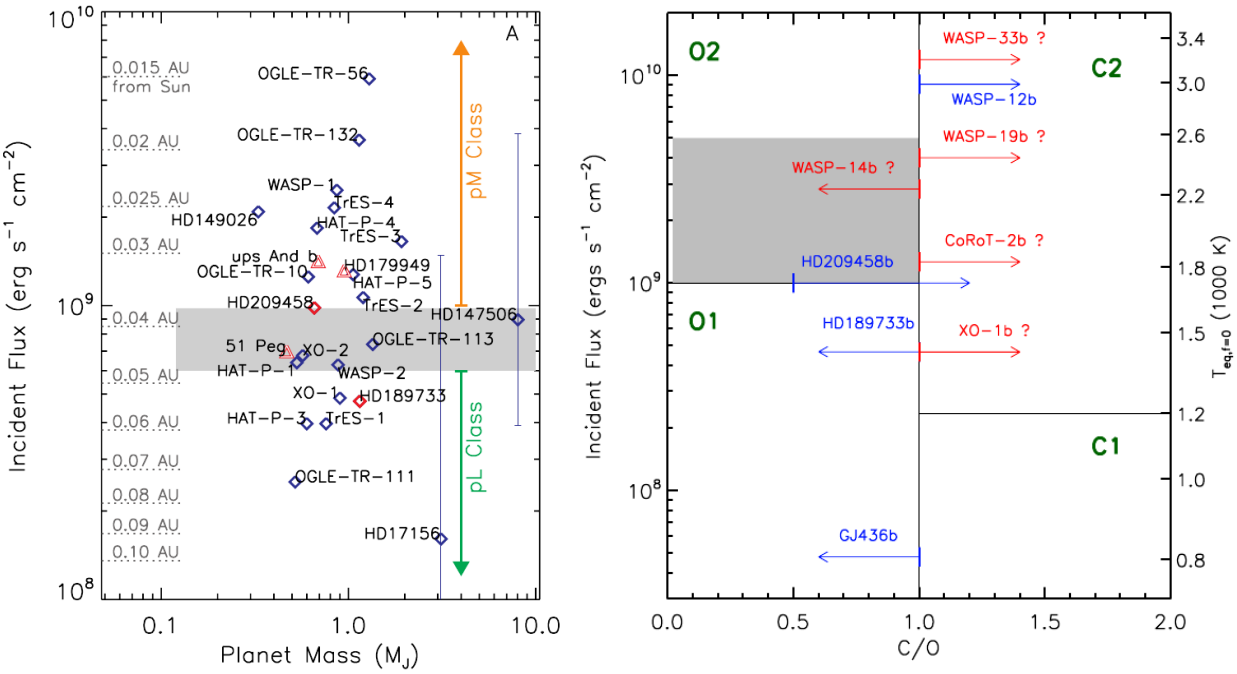

Figure 2.17 : The two classification schemes used at the time of writing. Left: the pM – pL scheme of Fortney et al. (2008), dividing the planets per incident flux. The shaded region denotes a possible overlap between the two classes. Right: the 2D O1 – O2 – C1 – C2 scheme of Madhusudhan (2012), that adds the planetary composition as a second dimension. The shaded region denotes the temperature range for which TiO/VO might be removed from the upper atmosphere due to gravitational settling (Spiegel et al. 2009).

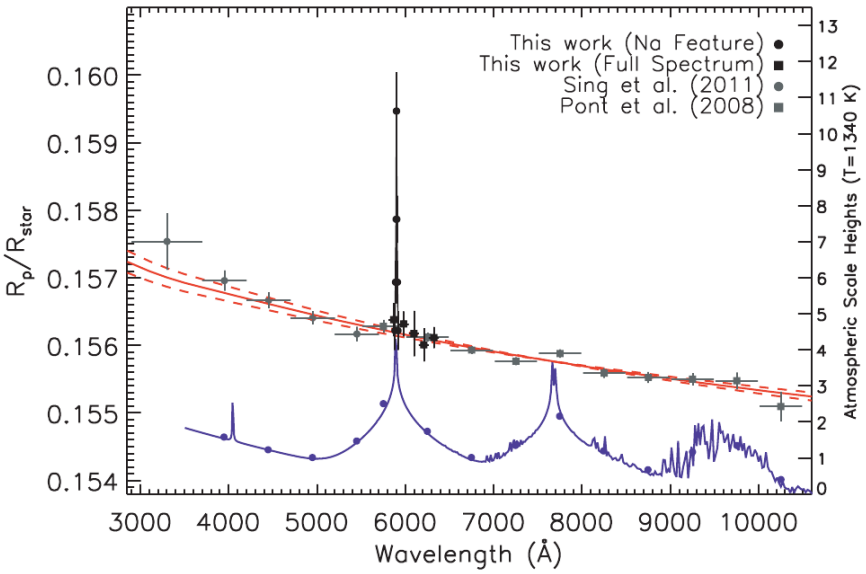

Figure 2.18 : The transmission spectrum of HD189733 b obtained by Pont et al. (2008), Sing et al. (2011b) and Huitson et al. (2013). The model of Fortney et al. (2010) is shown as a solid blue line, with the filled circles denoting the model binned to the spectral resolution of the data. The red line shows the model for Rayleigh scattering of Lecavelier Des Etangs et al. (2008). Figure credit: Huitson et al. (2012)

and oxygen-rich composition belong into the O1/O2 class, and carbon-rich planets of low/high incident radiation are divided into the C1/C2 classes. The distinction between the O1 and O2 class is made based on the presence of TiO/VO which may translate into the presence of an inversion. The distinction between C1 and C2 is made based on the main carbon-carrying molecule, CH_4 for C1 versus CO for C2.

2.4.5 Clouds and Hazes

For geometrical reasons, transmission spectra show a greater sensitivity to opacity sources in the outer atmospheric layers than emission spectra. Predictions on the shape of transmission spectra of large H-dominated atmopsheres were made early on by (Seager & Sasselov 2000, Brown 2001, Hubbard et al. 2001). They found that the optical range is dominated by the large alkali absorption features of Na at 589 nm and K at 766 nm. Shortwards of ~500 nm, Rayleigh scattering by H_2 produces a slope. Redwards of 900 nm molecular absorption features, predominantly those of water, shape the transmission spectra.

When the transmission spectrum of HD189733 b was obtained at optical wavelengths (Pont et al. 2008, shown in Figure 2.18 together with several other measurements), it was quite different than predicted. Instead of the alkali signatures, the transmission spectrum is flat, showing only a slight slope. The conclusion from these measurements is that the spectral signatures are obscured by an optically thick cloud or haze deck. Lecavelier Des Etangs et al. (2008) found that the observations are well-fit by Rayleigh scattering of $MgSiO_3$ haze. Recently, (Huitson et al. 2012, see Figure 2.18) have detected the narrow line core of the sodium feature protruding out of the haze.

The equally well-studied HD209458 b is showing the predicted spectral signatures, Rayleigh scattering from H_2, Sodium and Potassium, and possibly TiO absorption (Désert et al. 2008, Sing et al. 2008b). The signature of H_2O in the transmission spectrum was found by (Deming et al. 2013), however it is smaller than expected. Similarly also the Na signature found by (Charbonneau et al. 2002) is smaller than predicted. This indicates that to some extent haze is also present on HD209458 b, however less opaque than on HD189733 b.

As an increasing number of exoplanets have been studied with transmission spectroscopy, it appears that thick clouds or hazes are in fact common. The recently studied planets WASP-6 b (Jordán et al. 2013), WASP-19 b (Bean et al. 2013), WASP-29 b (Gibson et al. 2013), are showing flat transmission spectra. WASP-49 b, the planet I studied during my last year of PhD, is in line with this trend (see Chapter 6).

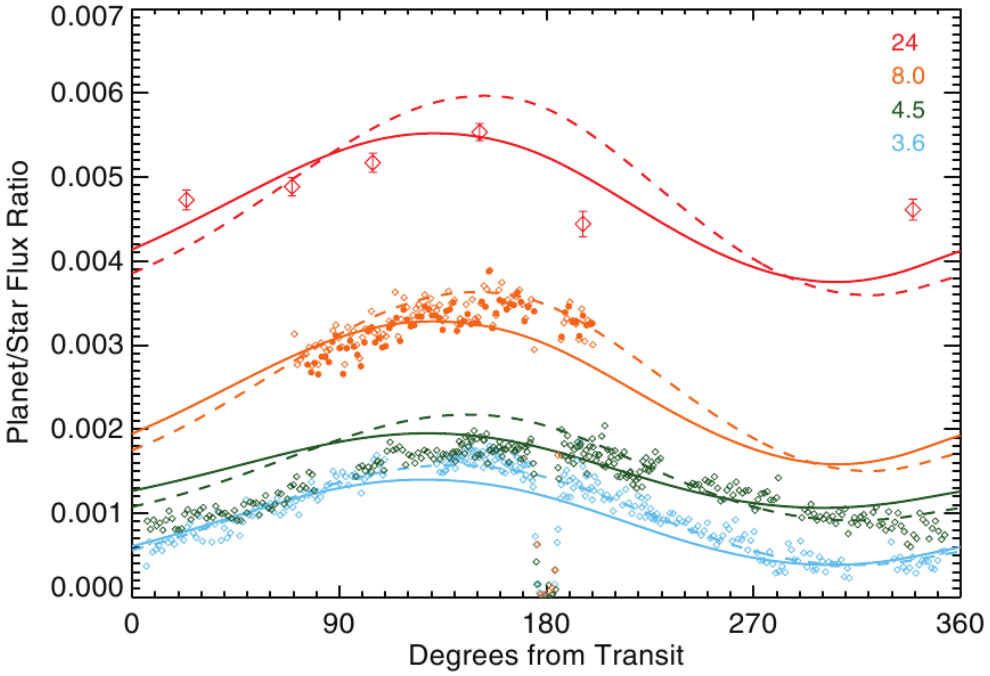

Figure 2.19 : The multi-wavelength phase curves of HD189733 b obtained by (Knutson et al. 2007a, 2009a) and (Knutson et al. 2012) together with models reflecting solar-metallicity models (solid) and models with a high (5× solar) metallicity (Showman et al. 2009). Image credit Knutson et al. (2012).

2.4.6 Beyond Eclipses

Occultations and transits allow snapshots of the exoplanet atmosphere at its dayside and terminator, but a few more insights have been obtained from phase curves and eclipse mapping.

On the observational side, phase curves have been obtained for a handful of targets showing amplitudes indicative of varying day-night redistribution efficiencies. For HD189733 b phase curves have been obtained at several wavelengths (shown in Figure 2.19) (Knutson et al. 2007a, 2009a, 2012) and have lead to some insights on the planets properties. Already from the first observation a hot spot offset from the substellar point was identified (Knutson et al. 2007a). This is consistent with the theoretical predictions (Showman & Guillot 2002, Cooper & Showman 2005) of a super-rotating jet that advects the hot material eastward. The difference of the in-occultation flux and the flux inferred from the phase curve to be occurring during transit (if the transit signal is removed), a *nightside* emission spectrum can be constructed. Further, the phase curves can be compared to models of the atmospheric circulation (so-called *General Circulation Models, GCM*, e.g. Showman et al. 2009, Mayne et al. 2013) and yield information about the rotation rate, advection efficiencies and chemical compositions in the 3D atmosphere. For HD189733 b it seems that the variability in wavelength of the signature can not be explained by models including chemical equilibrium.

A 2D map of the planetary dayside can be constructed by combining the phase curves with precise occultation data. During the occultation ingress and egress the flux stemming from the planet is sampled in slices slightly inclined to the planet meridian, and this inclination is not the same for ingress and egress, revealing a two-dimensional planet map (de Wit et al. 2012, Majeau et al. 2012).

2.5 The 2010 State of the Art

Very few fields in astronomy have undergone such profound advances in the last four years as the observation of exoplanet atmospheres. When I started my PhD work in January 2010, the observational

studies of planetary atmospheres were much less numerous than today.

Ground-based observations targeting the atmospheric properties of exoplanets had all but just begun. At that moment in time, any ground-based occultation detection was a major achievement with only de Mooij & Snellen (2009), Gillon et al. (2009), Rogers et al. (2009) (around 2 μm) and Sing & López-Morales (2009) (z'-band) having succeeded so far. On the contrary a major investment of ground-based telescope time was directed towards the search for transit timing variations (e.g. Holman et al. 2006, Díaz et al. 2008, Gibson et al. 2008), however not producing any confirmed TTV detections. As it turns out, the problem here was not the technique per-se (which has proven its value repeatedly with *Kepler* planets (e.g. Holman et al. 2010, Fabrycky et al. 2012)), but the paucity of companions to hot Jupiters capable of creating TTVs that stand out from instrumental and stellar noise. Yet, on the side of high-resolution spectroscopy progress had been made and the planetary Na signature had been confirmed for HD209458 b (Snellen et al. 2008) and HD189733 b (Redfield et al. 2008).

From the space based instruments, atmospheric inferences on hot Jupiters were possible and had been carried out with considerable effort. From *HST* data Na detections and spectrophotometry had been obtained (starting with Charbonneau et al. 2002 and Knutson et al. 2007c), revealing the haze or clouds obscuring the spectral features of HD189733 b (Pont et al. 2008). The detection of H_2O, CO_2, CO, and CH_4 had been announced based on *NICMOS* data (Swain et al. 2008, 2009a,b), but independent analyses of the same data (Sing et al. 2009) were diverging. Evaporation from HD209548 had been observed in Lyman α (Vidal-Madjar et al. 2003), showing that the planet is losing mass. *Spitzer* data were already fairly abundant by the end of 2009, however still focused on a small number of targets. In particular HD209458 b and HD189733 b had been intensely observed and provided well-characterized emission spectra in the IR (among others by Deming et al. 2005, Richardson et al. 2007, Grillmair et al. 2007 and Knutson et al. 2008). It had become evident that some planets (e.g. HD209548 b) have hot stratospheres (Knutson et al. 2008), and TiO and VO had been proposed to be the strong absorbers of stellar radiation needed to heat the outer atmosphere (Hubeny et al. 2003, Burrows et al. 2007b, Fortney et al. 2008). The irradiation level of the atmosphere had been suggested as a reason why only some hot Jupiters show thermal inversions, while others have T-P profiles that monotonically decrease outwards (Fortney et al. 2008). From phase curves of HD209458 b (Knutson et al. 2009b), the existence of a hot spot offset from the substellar point had been seen indicating an advection of the hot material in the planetary atmosphere. The comparison of observed and model spectra relied on a number of forward models (e.g. Burrows et al. 2008, Fortney et al. 2008) calculated for different abundances and temperatures, as retrieval codes were just starting to become available (Madhusudhan & Seager 2009).

A scientist in his laboratory is not a mere technician: he is also a child confronting natural phenomena that impress him as though they were fairy tales.

Marie Curie

3 EULERCAM

During the first 18 months of my PhD I spent a big part of my time on setting up, installing and testing a new instrument at the Euler-Swiss telescope on La Silla (Chile). EulerCam is an optical light CCD imager at the Cassegrain focus of the Euler-Swiss telescope. It has been optimized to attain the best performances for time-series photometry of stars with magnitudes between $V = 10$ and $V = 13$, the range for which the WASP survey is most efficient (see Chapter 4 for details). In this chapter I will give an account of the key points during the installation of the detector, and describe the procedures I set up for the data reduction.

3.1 Charge Coupled Devices (CCDs)

Almost all current optical-light instruments, be it for imaging or spectroscopic purposes, use CCDs for the detection of the incoming photons. Photon detection in CCDs relies on the photoelectric effect (Einstein 1905) that causes the incoming photons to produce free electrons, that are then collected and counted to estimate the amount of incident radiation. The big advantage of CCDs is their high quantum efficiency, linearity and dynamic range.

A classical CCD is made up of a $\sim$300 μm base layer of a semiconductor material (usually Silicon), covered by an insulating layer and a set of electrodes at its surface. The Silicon is "doped" meaning that a different element has been inserted in its crystal structure. If the added atoms have more valence electrons than Si (e.g. Phosphorus), then additional electrons are present in the Si structure ("n-type Silicon") and if the added atoms have less valence electrons than Si (e.g. Gallium), then the Si structure shows "holes" ("p-type Silicon"). Both holes and electrons are able to move inside the Si grid, potentially changing its charge distribution. If p- and n- type Si layers are placed in contact with each other, the holes and electrons disperse across this border, creating an electric field, with an overall positive charge on the p-doped side and an overall negative charge on the n-doped side. This field can be intensified by applying an external voltage, as is done in CCDs, to create a deep potential well dedicated to collecting electrons that have been freed by the incident radiation.

The first astronomical CCDs were illuminated from the top, i.e. the side equipped with electrodes needed for the detector readout (see below). However, these components are absorbing some of the incident photons decreasing the detector quantum efficiency. A better quantum efficiency can be achieved if the detector is illuminated from the back side. For that it is necessary to remove part of the substrate and make the detector thin enough for the electrons to be created at a point close enough to the potential well and to be collected there. This means that standard *thinned back-illuminated* CCDs have a typical thickness of 20 μm. This in turn is problematic if good quantum efficiency at wavelengths beyond 800 nm is desired, as the detector becomes transparent to these long-wavelength photons. This problem has been solved by the development of *deep-depletion* Si detectors. Here a p-doped Si with a lower impurity level is used, creating a higher resistance. Now the electric field can extend all the way through a detector thick enough to allow the absorption of long-wavelength photons. A sketch of the CCD components is shown in Figure 3.1 . The readout of a CCD is carried out by shifting the accumulated charges along the rows of pixels. For this purpose, each pixel is equipped with three electrodes, their voltages tuned in such a way that the charges have accumulated in the central one during the exposure. For the readout, their voltages are adapted in a cyclic way (the clocking) so that the electrons

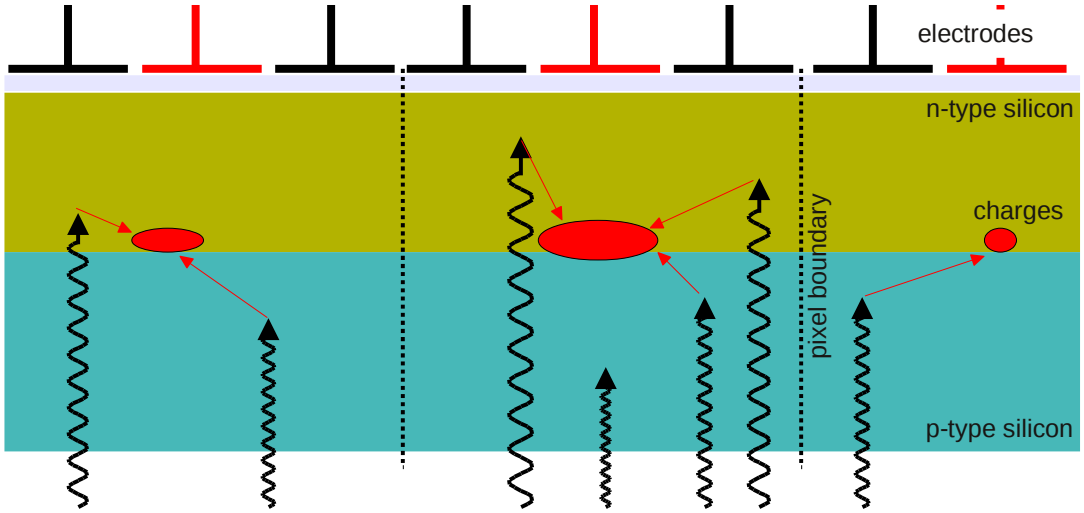

Figure 3.1 : The layout of a back-illuminated CCD. The different types of doped Si are shown, as well as the charge packets accumulating at their border. The electrodes for the readout are located on top, with the one with a positive voltage, keeping the charges in place, shown in red.

are moved towards the edge of the detector, where they, in a similar fashion, get transferred in the serial direction towards the amplifier and analog to digital converter.

3.2 Installation and Detector Characterization

3.2.1 Introducing EulerCam

EulerCam is a back-illuminated deep-depletion CCD that has been produced by *e2v* (model CCD231). It has been installed at the Cassegrain focus of the Euler-Swiss telescope in September 2010, replacing the older *C2* instrument. The instrument is operated at a temperature of $-115°$ C which is achieved via cooling by liquid Nitrogen that is stored in a vessel surrounding the instrument and refilled twice per day. The detector is optimized to be most sensitive in the red part of the optical spectrum and its sensitivity stretches out to 1 µm, with the quantum efficiency falling below 50 % near 900 nm. The filters installed at the telescope are: the *Geneva* filter system comprised of *U, B, B1, B2, G, V, V1* (Rufener & Nicolet 1988), an *I-Cousins* filter, *r'*- and z'-Gunn filters, a wide 520-880 nm filter designed for the *NGTS* transit survey, and a transparent filter. In Figure 3.2 the detector quantum efficiency (black curve) and the transmission curves of the filters (colored curves) are shown. The detector has a size of 6.14×6.14 cm, and consists of 4096 by 4112 pixels of 15 µm. On sky, the spatial filed if view is 14.708 by 14.765 arcmin, yielding resolution of 0.215 arcsec per pixel. There are two readout modes available: either reading the entire chip through one amplifier, or using four ports, each reading a quarter of the image. Obviously, the readout time for one-port readout (25s) is larger than the readout time of the four-port mode (6.5s), however it yields a homogeneous image with unique noise levels, and may thus be the preferred mode for low-cadence observations. On top of the readout times, additional overheads amounting to $\sim$10s arise from tracking (see below), image registration and system delays.

The instrument is not equipped with a guide camera, but a stable pointing is assured by using an on-image tracking. This system, dubbed *ABsolute TRacking (ABTR)* is based on calculating the precise position of an image by extracting its sources and matching them with a catalog. Offsets between successive images are compensated by refining the telescope pointing. This process yields an average pointing stability of 2 pixels (mean radial displacement from the mean position), and assures a stability better than 4 pixels (maximal radial displacement from the mean position) at airmasses smaller than

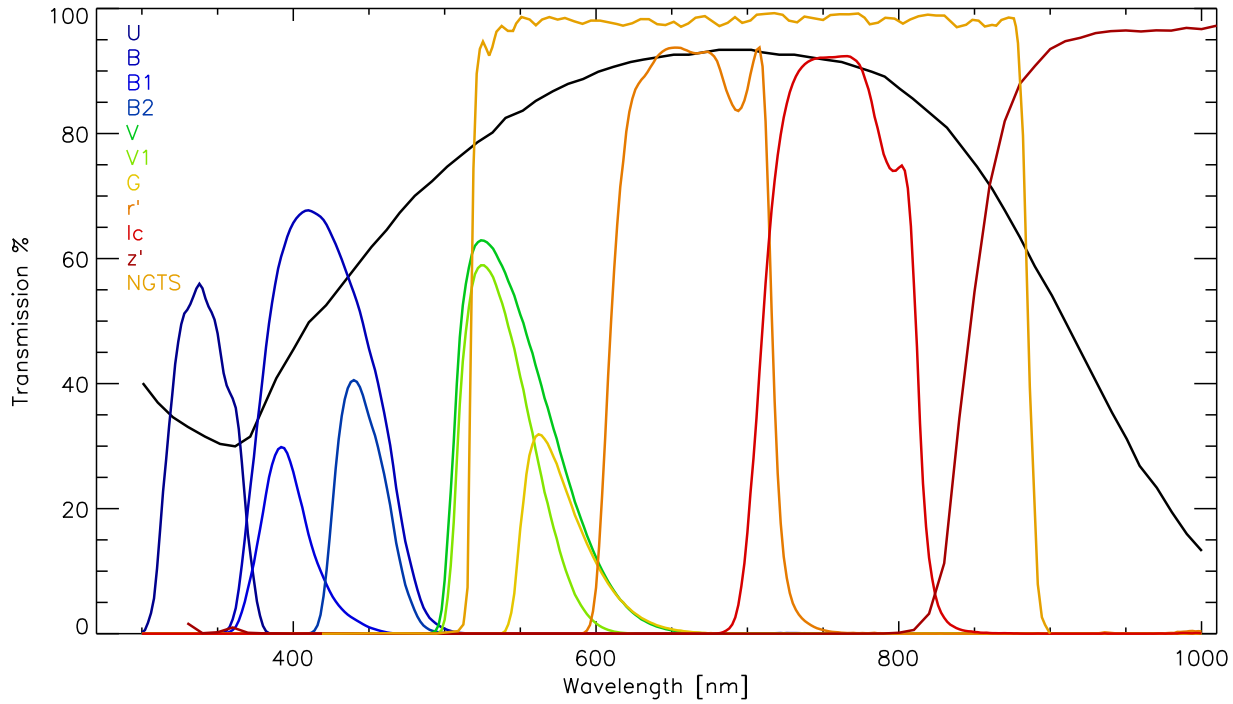

Figure 3.2 : The detector quantum efficiency (black) together with the filters installed at the Euler-Swiss telescope. The color-coding is given in the upper-left corner.

AM = 1.8.

3.2.2 Key Parameters

During the installation process a few key parameters had to be calculated very frequently. In this section I describe how this has been carried out.

Readout Noise

The term *readout noise* refers to the collection of noise effects introduced during the process of converting the detector electrons to a digital pixel value. This comprises effects of the charge transfer, signal amplification, analog/digital conversion, and any other noise introduced during the readout process, e.g from interference with other electronic components.

The calculation of the detector readout noise is quite straight forward. Let B_1 and B_2 be two bias images, cropped to avoid clearly visible defects, and B_{12} their difference image. Now an estimate of the read noise in ADU can be calculated via the standard deviation of this difference image $\sigma_{B_{12}}$

$$\sigma_{\mathrm{RON}} = \frac{\sigma_{B_{12}}}{\sqrt{2}} \tag{3.1}$$

Of course a more accurate value can be obtained by using more than just two bias frames. Then, from a sequence of N bias frames, $N(N-1)/2$ values for the readout noise may be calculated. For the determination of the EulerCam readout noise I used sequences of around 20 images. To transform the ADU values of the readout noise into e^- values, the values need to be multiplied with the instrument's gain.

Gain

One of the basic characteristics of any detector is its gain. It relates the amount of electrons detected to the number of Analog to Digital Units (ADUs) that are saved in the image files. To determine the gain, one uses the fact that photon noise follows Poisson statistics, and thus the error σ_e of a signal N_e is it's square root

$$\sigma_e = \sqrt{N_e}. \tag{3.2}$$

On an equally illuminated region on the image, one may measure the average counts N_{ADU} and the count standard deviation σ_{ADU}, which relate to their electron-unit counterparts via

$$N_e = N_{\mathrm{ADU}}\, g \tag{3.3}$$
$$\sigma_e = \sigma_{\mathrm{ADU}}\, g, \tag{3.4}$$

where g denotes the gain. The total error is given by

$$\sigma_e^2 = \sigma_{\mathrm{RON},e}^2 + (\sqrt{N_e})^2 = \sigma_{\mathrm{RON},e}^2 + N_e. \tag{3.5}$$

By converting this equation to ADU units and solving for σ_{ADU}^2, one obtains

$$\sigma_{\mathrm{ADU}}^2 = \frac{1}{g} N_{\mathrm{ADU}} + \sigma_{\mathrm{RON}}^2, \tag{3.6}$$

where σ_{ADU}^2 and N_{ADU} are observables. This means the gain can be derived by obtaining a series of images of a homogeneous source with a wide range of count levels, and then populating a $N_{\mathrm{ADU}} - \sigma_{\mathrm{ADU}}^2$ diagram. The best way to obtain such a sequence is to use a stable artificial source (in our case an LED) and variable exposure times. A linear regression of the data will reveal the gain and provide an additional measurement of the readout noise. See Figure 3.7 for an example of such a diagram.

However there is a relevant limitation to this approach: any non-uniformity of the source will add additional noise to the derived values, impacting the gain measurement. In the case of EulerCam, this is particularly relevant for the sequences obtained at the telescope, where the LED image is clearly not smooth (see Figure 3.6 for an image). To compensate for inhomogeneities one may obtain two images (I_1, I_2) at each count level, which have mean values of M_1 and M_2 in the regions chosen for the gain calculation. To compensate for any variation in the source flux between the two images, one image is scaled to the same level as the others, $I_{2b} = I_2 M_1 / M_2$. Then the difference image is calculated $D = I_1 - I_{2b}$, ideally having a mean M_D of zero. In this difference image, the inhomogeneities have been removed while the noise characteristics remain, and one may produce the variance values for the $N_{\mathrm{ADU}} - \sigma_{\mathrm{ADU}}^2$ diagram by

$$\sigma_{\mathrm{ADU}}^2 = \frac{1}{2}\sigma_D^2 \tag{3.7}$$

where σ_D is the standard deviation of the difference image in the region used for the gain calculation.

To obtain good gain measurements for EulerCam, I carried out gain measurements on 81 100 by 100 pixel regions for each quadrant, and calculated the final values by as the mean of the measurements, rejecting values clearly affected by detector defects.

Dark Current

Dark current is an additional noise source that, in the case of well-cooled CCDs, usually remains small. The effect is caused by electrons that are not produced from incoming radiation, but are thermally produced inside the detector. They are read out and stored just as “good” electrons are and produce an additional background on the image. To measure the dark current, the detector needs to be in a

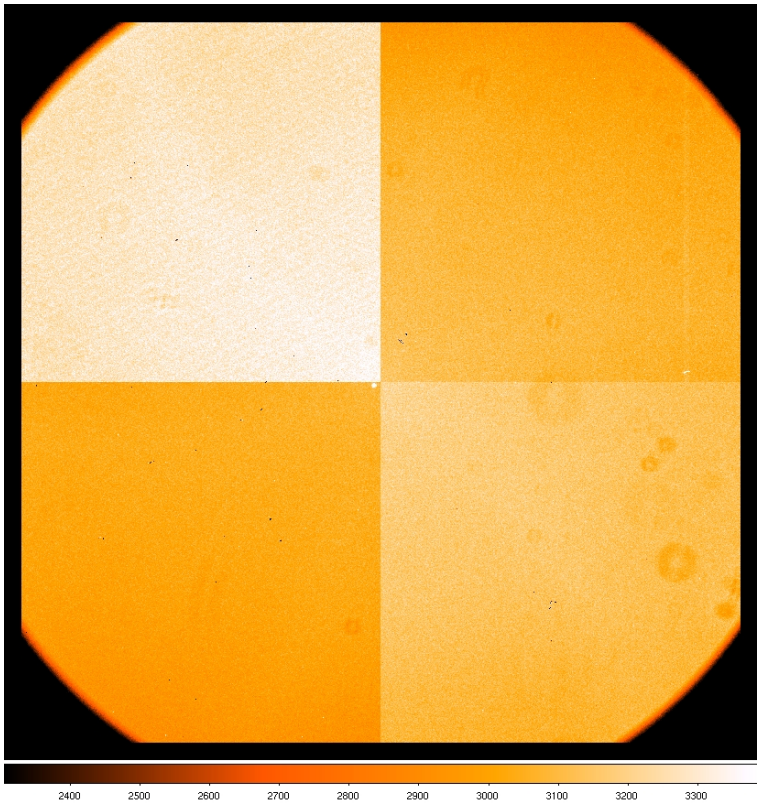

Figure 3.3 : The very first on-sky image obtained with EulerCam, a 10s V-band exposure of the 8th magnitude star HD204941 with a strangely high background.

completely dark environment, where a series of long exposures are taken. In the case of EulerCam, darks were taken with exposure times between 15 and 60 minutes, during nights of bad weather and with a closed shutter. A masterbias computed from bias frames before and after the dark exposure is then removed from the images to leave only the thermal component present. As these long exposures are badly affected by cosmic rays, the sequence is combined into an average image while outliers are rejected. The value of the dark current is usually measured in $e^- s^{-1}$ is then the level of the combined image divided by the exposure time.

3.2.3 Installation

Before shipping the detector to Chile, we performed a "sanity check" in the optical lab of the Geneva observatory. For this, the detector was cooled to a temperature of $-115°$ C, placed in a light-tight container, with the possibility of shining in a small light source. A flat region on the wide ridge of the light distribution was selected to do some first gain evaluations, while testing various clockings and operation temperatures. We also obtained bias frames and darks. Unfortunately the darks were showing some residual light entering the system. The detector appeared to be in order and the decision was made to go to the next step: installing it at the telescope.

In September 2010, EulerCam arrived at La Silla observatory, together with a group of eight astronomers and technicians making the Swiss Telescope a place bustling with activity. On 12 September, we re-did the sanity check on the bench. Everything appeared in order and the instrument was put on the telescope on 14 September 2011, to be cooled and ready for it's first light during the following night. After a few hectic hours, the very first on sky image of EulerCam was rater an anticlimax, a blurry image of the 8th magnitude star HD204941 (see Figure 3.3), hardly visible above a strangely high background. To our relief we noticed that someone had left the lights on in the dome. From this point on, we performed a great many of tests, going from initially mainly debugging and tuning work to more dedicated sequences aiming at the instrument characterization during the last few nights. Here, I will only highlight a few aspects that can be summarized in a concise fashion.

Table 3.1: The readout noise values measured for EulerCam, using the EulerCam and C2 controller, as well as the values obtained after the reparations to the upper two quadrants in March 2011.

Quadrant	EulerCam Controller	C2 Contoller	since March 2011
		Readout noise $[e^-]$	
upper left	77.2 ± 4.8	20.0 ± 1.1	5.0 ± 0.1
upper right	20.8 ± 0.1	17.7 ± 1.3	4.6 ± 0.1
lower left	12.9 ± 0.1	4.7 ± 0.3	7.6 ± 0.5
lower right	13.7 ± 0.1	5.2 ± 0.2	5.3 ± 0.1

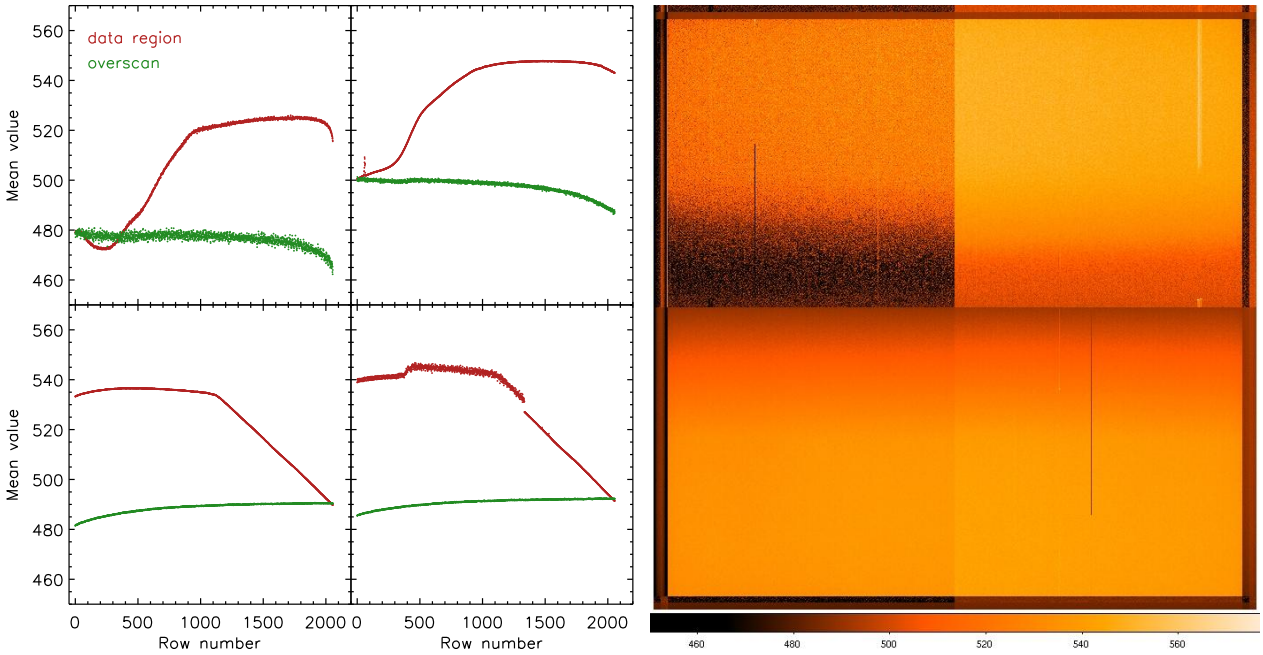

Figure 3.4 : Left: the trends in y-direction for each quadrant of the same image. Green are the trends in the overscan regions and red those in the data regions. At this time there was an evident disagreement in these trends. Right: A combined bias image obtained from the first observing night (14 September), it is clearly visible that the upper left quadrant is showing an elevated noise level.

The Noisy Quadrant

From the very first images on it was evident that the upper two quadrants showed a higher noise than the others, especially so the upper left quadrant. From a series of bias images (see Figure 3.4 for an example), I estimated the readout noises for all quadrants, obtaining the values in Table 3.1. The old controller of the C2 instrument was still at hand, and on 20 September we performed some tests to compare its performance to the performance of the new piece of hardware. With this old controller the readout noise of the upper left quadrant turned out to be reduced. As a consequence the C2 controller was left in place, yet with the upper two quadrants still showing elevated noise levels compared to the lower ones.

The Inverted Overscans

The overscans are created by performing additional charge shifts of each line, and saving the collected electrons in extra pixels next to the actual image. This way they provide a direct estimation of the bias level of a particular exposure. For bias images, the overscan must reproduce any trends along the direction normal to that of the charge shifts. At the initial installation of EulerCam at the telescope, it

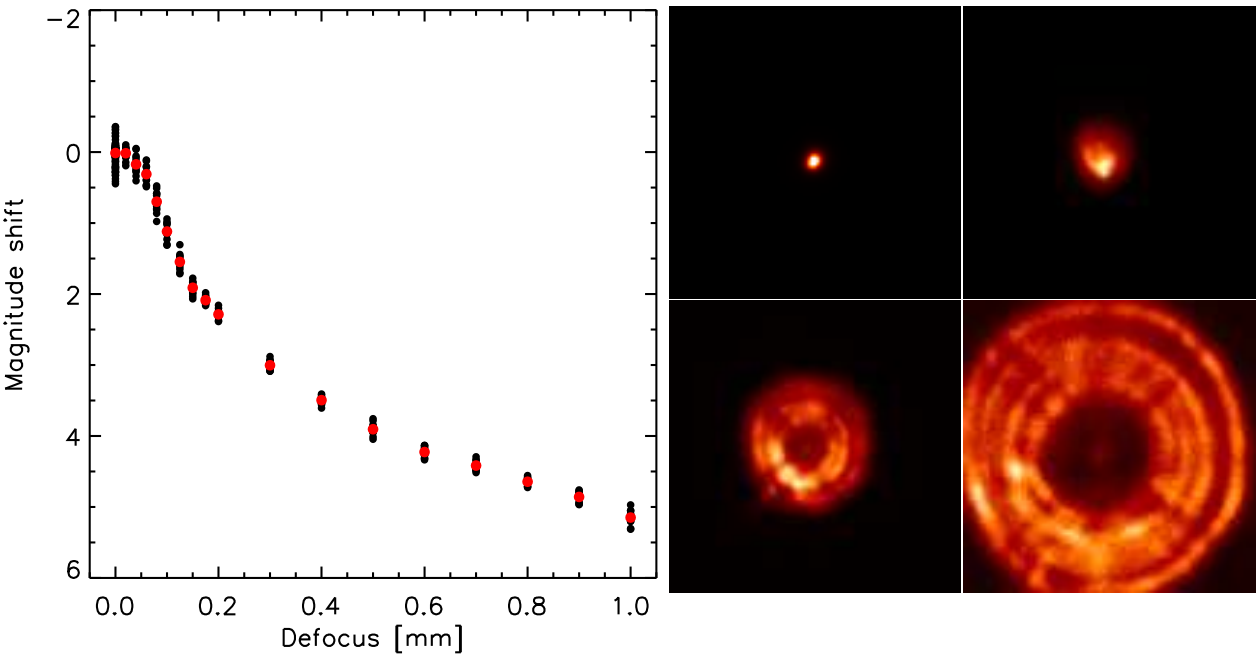

Figure 3.5 : Left: the decease of peak flux for increasing defocus expressed in units of relative magnitude. Right: example PSFs at defocus (i.e. M2 displacements) of 0.0 mm, 0.15 mm, 0.4 mm, and 1.0 mm.

was easy to notice that something was wrong with the overscan areas of the images. The slope of the overscan was opposed in direction to the slope in the bias images, and the shape was quite different (see Figure 3.4 for an example). Finally the problem identified as an error in the readout procedure and solved on 22 September.

The Defocus Effect

It is very common to defocus the telescope to improve the quality of photometric time-series observations. For the planning of observations it is important to know what flux levels are expected at which level of defocus. For this reason, and to be able to focus the telescope before the automatic focus procedures became available, several sequences were performed where the position of the M2 mirror was altered slightly (up to 0.3 mm) between exposures. By measuring the PSF of several stars in the field, and determining the FWHM and maximum count values, the position of the best focus, and the decrease in peak flux can be found. To well characterize the gain in accessible stellar magnitude on the bright side when defocusing, I expanded the sequence obtained during the commissioning at a later time to M2 deplacements up to 1 mm. These measurements are shown in Figure 3.5 together with characteristic PSF shapes at various defocus values. Note how the shape of the PSF goes from almost symmetrical to asymmetrical and finally to a distorted doughnut shape.

Gain Measurements

An integral part was the determination of the final detector gain values once all hardware changes had been carried out. For this purpose two gain sequences were carried out on the evening of the last commissioning night, using LEDs installed at the telescope. The two sequences were obtained using two different filters (V and B2), giving different count rates on the detector and thus different sampling in terms of flux and exposure times. The sequences consisted of 21 (V) and 16 (B2) pairs of exposures with exposure times ranging from 0.25 s to 45 s (V) and 1 s to 46 s (B2). Owing to the difference in filter transmission, the B2 sequence probed count levels below 10000 only while the V sequence probed the whole dynamic range. The resulting $N_{\mathrm{ADU}} - \sigma^2_{\mathrm{ADU}}$ is shown in Figure 3.7 together with

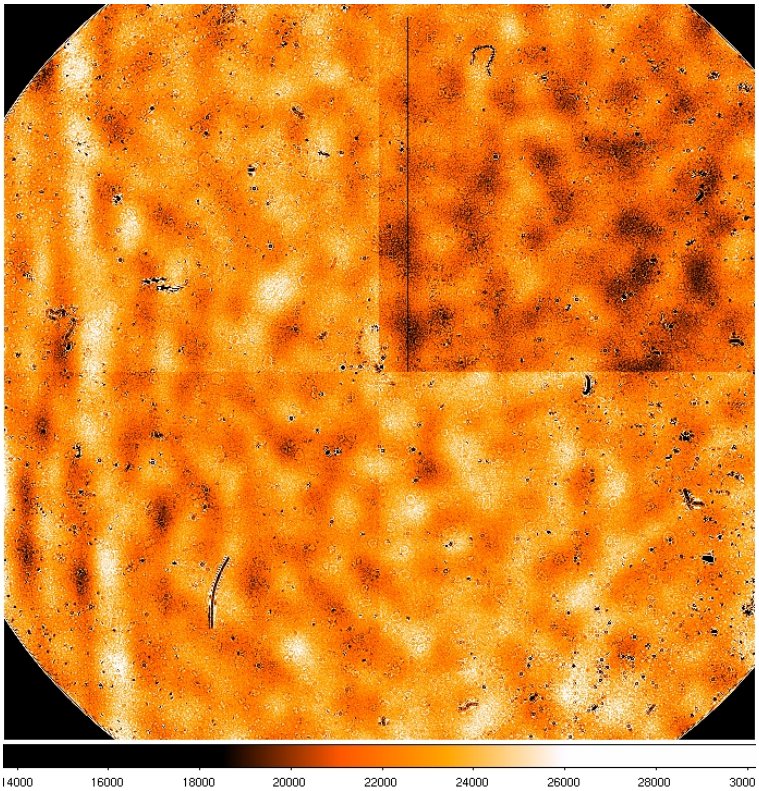

Figure 3.6 : An example image obtained with the LED installed at the telescope together with the V-filter. The LED does not show a smooth brightness distribution, with a both a wavy pattern and many sharp dark shapes.

Table 3.2: The gain values of the four EulerCam readout ports. I quote the values for calculations based on the full dynamic range (up to 55000 ADU) and up to 20000 ADUs.

Quadrant	$<$ 55000 ADU	$<$ 20000 ADU
	Gain $[e^-/ADU]$	
upper left	2.69 ± 0.02	2.60 ± 0.03
upper right	2.70 ± 0.02	2.69 ± 0.03
lower left	2.64 ± 0.02	2.59 ± 0.03
lower right	2.62 ± 0.02	2.56 ± 0.03

linear regressions made for different subsets of the data. It is visible that the slope of the regression, and consequently the gain value depends slightly on whether the dynamic range up to 55000 ADU is uses or whether the fit is limited to count values below 20000 ADU. The resulting values for the gain are shown in Table 3.2.

Linearity Tests

We performed additional tests of the detector linearity both on-sky and from the gain sequence described above. In both cases, the measured flux is predicted to be proportional to the exposure time used, i.e. a doubling of the exposure time should yield a doubling in flux. For this purpose we performed measurements of standard stars while increasing the exposure time, and used the LED sequences obtained for the gain measurement. From both the LED and the on-sky sequences I derived that the linear regime of the detector reaches out to approx. 55000 counts. I carried out a more thorough investigation on the linearity during the March 2011 mission (see Section 3.2.4).

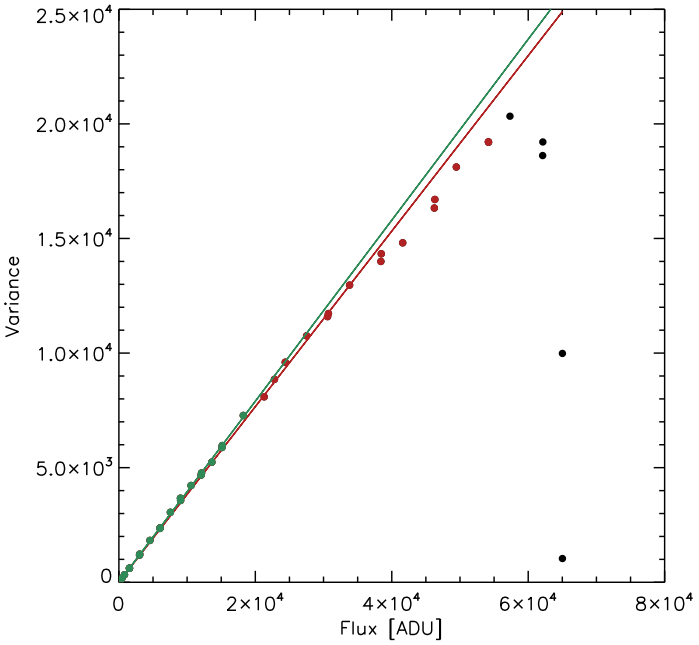

Figure 3.7 : An example of a variance – count level plot used to derive the gain values. The green line represents a linear fit based only on the datapoints below 20000 ADU (green points), while the linear fit shown in red has been calculated using all datapoints below 55000 counts (red and green points).

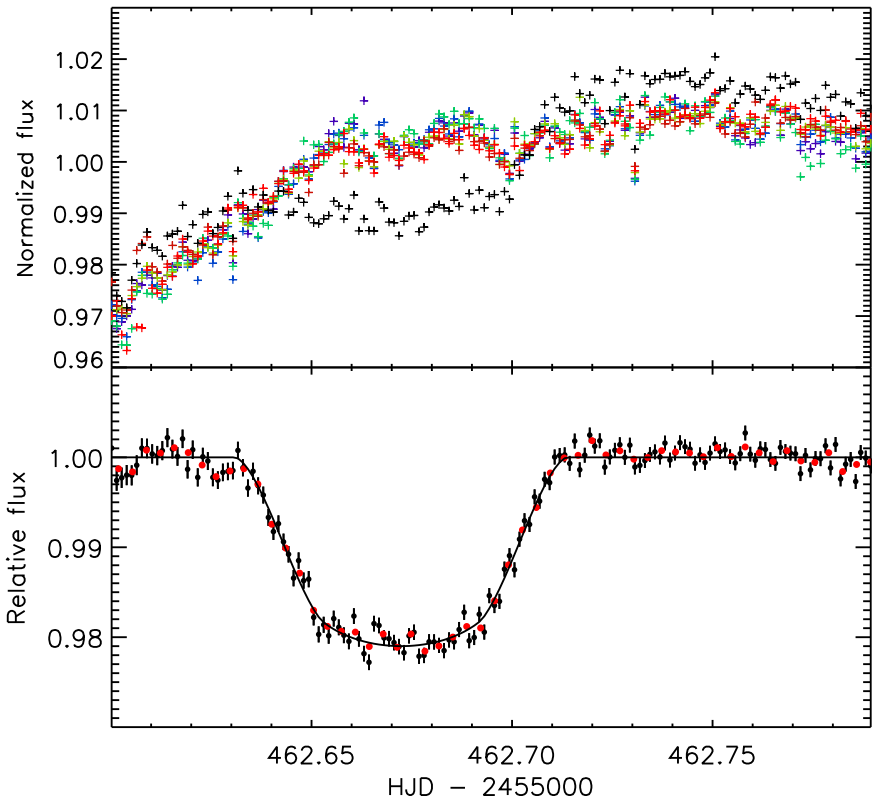

Figure 3.8 : The first scientific photometric time series obtained with EulerCam: an lightcurve of the WASP candidate SW01473.49-184952.8, later determined to be a blended eclipsing binary. The top panel shows the normalized raw lightcurves of the target (black) and six reference stars (colored). In the lower panel the relative lightcurve together with a transit model is shown.

Long Sequences

Of course one of the tests was to obtain a sequence matching the prime science goal of the instrument: a time-series spanning several hours. For this purpose we observed SW014731.49-184952.8, at that point in time a promising WASP planet candidate, throughout 4.7 hours on 22 September. The resulting lightcurves for all stars, and the relative target lightcurve are shown in Figure 3.8 . The RMS of the target lightcurve is 950 ppm, combined with a cadence of 110 s, a very encouraging value for a young instrument.

Pretty Pictures

Finally, no commissioning is complete without some beautiful pictures to show off at home. During the last night of the EulerCam commissioning, we observed the Eagle Nebula (M16) in three colors (B, V, R), and the result (see Figure 3.9) is certainly a reward for several weeks of hard work!

3.2.4 The 2011 Upgrade

After the commissioning in September 2010, a small number of defects were still limiting the performance of the new instrument. First, the upper two quadrants showed elevated noise levels including variable structures. These defects decreased the photometric performance in the affected areas and thus halved the "good" field of view while using the four-quadrant readout. Second, a lot of small particles had been deposited on the surface of the detector, creating many small insensitive spots in the field.

To remove these two defects, another technical mission was scheduled at the Euler telescope for early March 2011, involving myself, Dominique Naef and Michel Fleury. At this point, the detector was unmounted, moved to a clean room, opened and the little particles were carefully removed from the detector surface. The problem of the noisy quadrants was identified as defect cabling, and repaired. After the instrument was put back in place, the two upper quadrants were back to nominal noise levels. However the readout electronics for the lower left quadrant had been damaged in a similar way, leading to a higher noise level in that quadrant. As the opening of the detector is a very delicate procedure with high risk for the instrument, it was decided to operate with this configuration from that time on.

We used this opportunity to redo some of the measurements performed during the commissioning, obtaining refined values for readout noise, gain and linearity.

Linearity and the Shutter

One of these measurements occupied me for a considerable amount of time. We modified the gain sequence slightly, adding an exposure of 15s after each image pair. This way, any variation in the LED brightness could be corrected. The electron detection rate (in ADU/s) can be computed for each image. As we compensate for any variation in the light source, this quantity should be constant. However, images with short exposure times showed excess flux, as shown in Figure 3.10 . The effect was confirmed to be related to the quantity of the exposure time instead of count levels, as it is equally present in sequences obtained with other filters and thus different count rates. Finally, the culprit was identified to be a small inaccuracy in the true exposure time. There is a short delay between the command to close the shutter and the actual execution of this command (due to the charging of a condensator), and so the true exposure times are approx. 64 ms larger than those given in the FITS header.

Darks

At around this time, we also obtained some good-quality dark frames, and for completeness, the values are reproduced in Table 3.3. The noisy lower-left quadrant shows some structures with an amplitude of $\sim$8 e^- on 1800s exposures. Given the long exposure time of darks, the dark current is below $5 \times 10^{-3} e^- s^{-1}$, and thus completely negligible for the scientific data usage.

Figure 3.9 : The official first-light image of EulerCam, the Eagle Nebula, a composit of images in BG, VG and RG. The raw images have been obtained during the last light of the EulerCam commissioning and the color composit has been created by Malte Tewes.

3.2.5 The Exposure Time Calculator

For the planning of observations it is essential to have a way of estimating the flux and signal to noise (S/N) registered from a particular source for a certain exposure time and filter. For this purpose, I created the Exposure Time Calculator (ETC) for C2 and then adapted it to be used for EulerCam. The software has since its creation in 2010 been adapted to work in conjunction with the telescope interface and the EulerCam observation preparation software. Here, I will briefly take reader through the signal calculation.

First, a number of key quantities need to be known: the filter transmission $T_i(\lambda)$ and detector

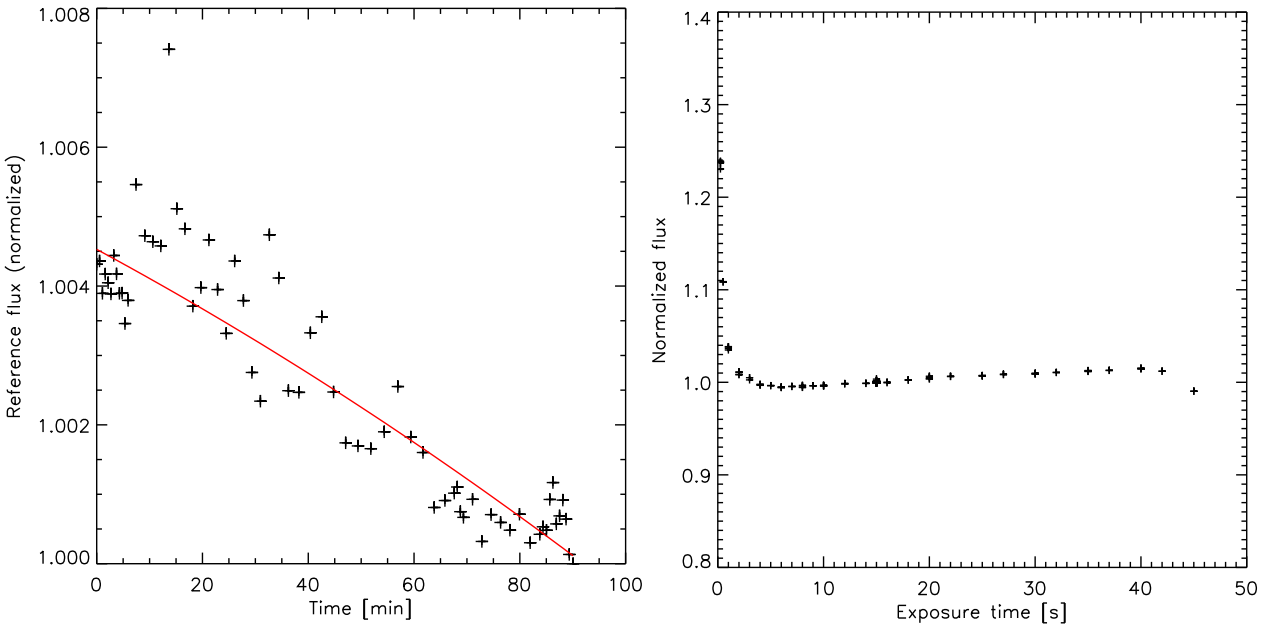

Figure 3.10 : The linearity measurement based on a sequence of LED images. Left panel: the reference flux of the LED, showing very little variation. Right panel: the incident flux in units of flux per second, corrected for the variation in the reference flux. Note the non-linearity at short exposure times.

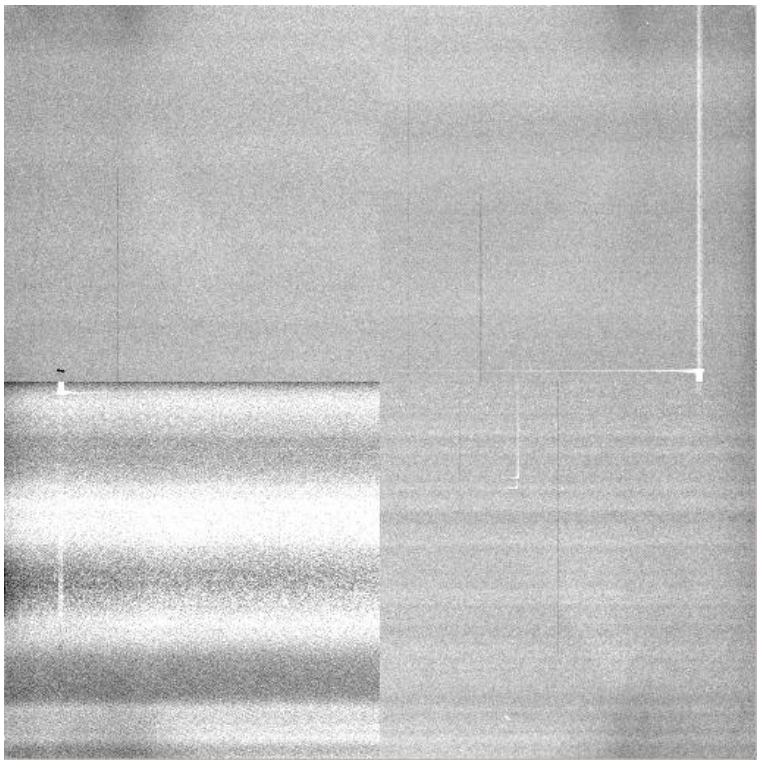

Figure 3.11 : The combined four-quadrant dark image obtained in March 2011. The lower left quadrant shows some structure, however the overall values are very low.

Table 3.3: The total dark current measured from darks with an exposure time of 1800s obtained during the March 2011 mission.

Quadrant	1800s dark (average) $[e^-]$	1800s dark (structure amplitude) $[e^-]$
upper left	2.4	1.3
upper right	2.5	0.8
lower left	2.0	7.8
lower right	2.6	0.8

quantum efficiency curves, the detector pixel size, gain, readout noise and dynamic range, but also the telescope and instrument throughput. The latter two parameters are not known to a great precision and I therefore set them both to 0.7. For each filter, both the effective wavelength

$$\lambda_{\mathrm{eff},i} = \frac{\int T_i(\lambda)\,\lambda\,d\lambda}{\int T_i(\lambda)\,d\lambda} \tag{3.8}$$

and the effective width

$$\lambda_{w,i} = \int T_i(\lambda) d\lambda \tag{3.9}$$

need to be calculated. In case of the transparent and z' filters, the edge of the sensitivity is given by the detector quantum efficiency. Before calculating $\lambda_{\mathrm{eff},i}$ and $\lambda_{w,i}$ for these filters I first multiplied the filter transmission with the detector quantum efficiency. Consequently the quantum efficiency factors QE_i are set to unity for these filters. Also, for each filter the flux density of a 0th-magnitude star $I_{\lambda,i}$ needs to be known or estimated, which has been done by Rufener & Nicolet (1988) for the *Geneva* system, Bessell (1979) for the *Johnson-Cousins* system, and Schneider et al. (1983) for the *Gunn* system. The flux densities are then converted to the number of photons n_{phot} reaching the detector in the absence of an atmosphere and with a perfect telescope via

$$n_{\mathrm{phot}} = \left[\frac{I_{\lambda,i}}{6.626\times10^{-4}}\frac{\lambda_{w,i}}{\lambda_{\mathrm{eff},i}}\right]\left[\left(\frac{D_{\mathrm{tel}}}{2}\right)^2 \pi 10^{\frac{-mag_i}{2.5}}\right] \tag{3.10}$$

where D_{tel} is the telescope diameter in cm, and mag_i is the object magnitude in filter i. Here, the first term stems from the conversion of energy flux density to photons and the second term scales the photon number to the telescope size and object magnitude.

This value needs to be converted to detected electrons, accounting for flux losses incurred in the atmosphere, and at the telescope. Atmospheric extinction is relatively well understood, and I make use of the same values as ESO[1], partially stemming from data of the old Swiss telescope (Burki et al. 1995). The detected electrons n_e are calculated as

$$n_e = n_{\mathrm{phot}}\,T_{\mathrm{tel}}\,T_{\mathrm{ins}}\,QE_i\,g\,10^{\frac{-ext_i}{2.5}AM}\,CF, \tag{3.11}$$

where T_{tel} and T_{ins} are the telescope and instrument throughputs, g is the gain, QE_i and ext_i are the detector quantum efficiency and the extinction coefficient in filter i and AM is the airmass at which the observation is carried out. CF is a correction factor determined from the calibration against real data.

The sky brightness has been measured by ESO[2], and its impact on the CCD image is computed in the same way as was done for stellar light, giving the sky electrons per pixel n_{sky}

$$n_{\mathrm{sky}} = \frac{1}{6.626\times10^{-4}}\frac{I_{\lambda,i}}{\lambda_{\mathrm{eff},i}}\lambda_{w,i}\left(\frac{D_{\mathrm{tel}}}{2}\right)^2 \pi 10^{\frac{-mag_{\mathrm{sky},i}}{2.5}}\,T_{\mathrm{tel}}\,T_{\mathrm{ins}}\,QE_i\,g\,10^{\frac{-ext_i}{2.5}AM}\,p^2\,CF, \tag{3.12}$$

[1]Extinction coefficients can be found at `https://www.eso.org/sci/observing/tools/Extinction.html`
[2]See table at `http://www.eso.org/observing/etc/doc/formulabook/node20.html`

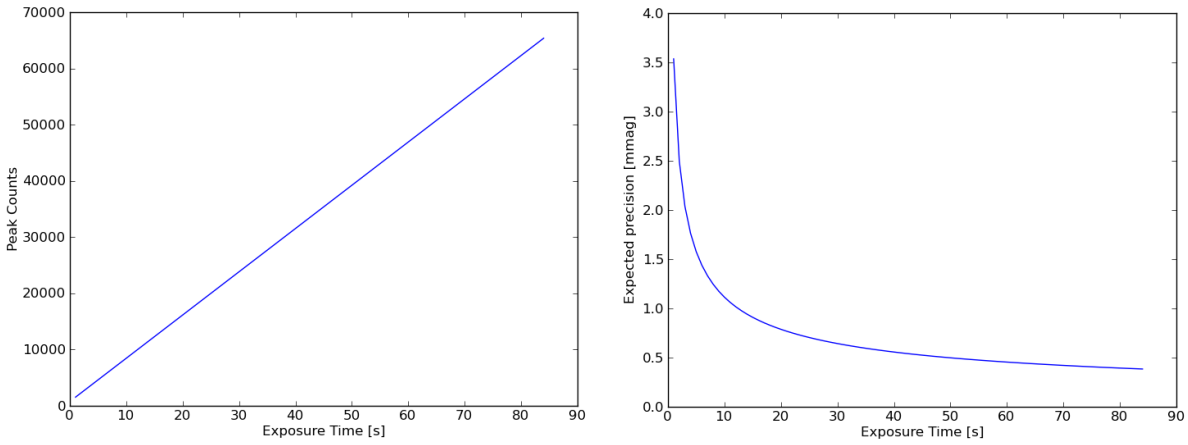

Figure 3.12 : Example outputs from the EulerCam ETC. The plots have been created for an R=11 mag star, observed with a focused telescope through an *r'-Gunn* filter.

where $mag_{\mathrm{sky},i}$ denotes the sky brightness in filter i and p is the detector pixel scale and CF is a correction factor determined from the calibration against real data. Assuming a Gaussian, the peak flux (in ADU) of the stellar PSF is then given by

$$Peak = \frac{1}{g}\left(n_{\mathrm{sky}} + \frac{n_e\, p^2}{1.33\, S^2}\right), \tag{3.13}$$

where S refers to the seeing, i.e. the stellar FWHM in arcsec.

The signal to noise is

$$S/N = \frac{n_e}{\sqrt{n_e + \left(\frac{S}{2p}\right)^2 \pi \left(n_{\mathrm{sky}} + \sigma_{\mathrm{RON}}\right)^2}} \tag{3.14}$$

where σ_{RON} is the detector readout noise. An estimate for the photometric precision is given simply by the inverse of the S/N value.

In order to account for a defocus, the measurements shown in Figure 3.5 are used to adapt the input brightness of the target. For a good photometric performance, the user is suggested to use exposure times producing a peak near 30000 ADU. This leaves room for seeing improvements without causing a rapid saturation of the target.

As I mentioned before, the telescope and instrument throughputs are not known precisely. Also, the sky transparency of the La Silla site needs to be accounted for. For this reason, I performed observations of standard stars and included a correction factor CF in Equations 3.12 and 3.11. This value (found to be near 0.7 for most filters) is a combination of the uncertainties in the knowledge of the telescope and instrument throughputs and the photometric quality of the La Silla site.

3.3 Data Reduction Procedures

The full potential of any instrument can only be reached once one has the capability to efficiently make use of the data. For EulerCam, this means that photometry needs to be extracted for the target and other bright stars, and then the best possible relative lightcurve needs to be created. I devised a set of procedures that perform these processes, and optimized them to run with little human interaction. The reduction pipeline consists of three major parts, image correction, photometric extraction and lightcurve creation, which I will describe in the following sections. These three processing steps together make up the `ECAM_PHOT` data reduction.

3.3.1 Image Correction

The first step of the reduction consists in correcting image cosmetics. For this purpose, I devised the CALEULER set of routines. It can either be launched on its own on a set of images, but is also the first procedure to be called in ECAM_PHOT. CALEULER is again composed of a set of several subroutines, carrying out the overscan, bias and flat field corrections. In detail, these routines are:

- OSCAN_IMAGE and OSCAN_IMAGE_NOFIT: These routines correct any raw input image for the overall bias level and vertical slopes present in the overscans, and thus in the image. These effects are temporally variable, and are best removed for each image individually. This is done by fitting a seventh order polynomial to each overscan and then removing the fitted values form each row in the respective image area. The procedure OSCAN_IMAGE_NOFIT works similarly but does not fit the overscan and instead subtracts the sigma-clipped mean value in each row. As OSCAN_IMAGE produces a smoother image, this is the standard setting.

- MAKE_MASTERBIAS: To remove the 2D bias structures from the images, a masterbias is created from a set of bias images, preferably obtained the same night as the science frames. First, each bias images is overscan-corrected with OSCAN_IMAGE, leaving a bias image with an overall level close to zero, yet some spatial variations. Out of the set of overscan-corrected bias frames, a masterbias, i.e. an averaged bias frame, is created. If more than four bias frames are available, for each pixel the highest and lowest values are discarded to remove outliers before calculating the mean.

- MAKE_MASTERFLAT and MAKE_MASTERFLAT_SCALED The masterflat, i.e. an average and normalized flat field, is produced from the flat field images in the same filter and readout mode. Ideally the flat fields stem from the same night or, if no good flat fields were obtained, the night before or after. Each flat field is first overscan and bias corrected using the above procedures. Then, for each frame and quadrant, a sigma-clipped mean value is calculated based on a region excluding the shaded image corners. The flat fields are the individually normalized by dividing each quadrant by its mean value. Now the images are combined with sigma clipping to remove any stars or cosmics producing the normalized flat. This procedure is implemented in the subroutine MAKE_MASTERFLAT. For reasons I will lay out below, I found it useful to, instead of normalizing each quadrant separately, select only a region in the lower left quadrant for the normalization of the whole image. The resulting flat field is thus not completely flat, but differs from the true flatfield by factors (f_i), $i \in (LL, LR, UL, UR)$ related to the difference in gain of the quadrants:

  $$f_i = \frac{g_{LL}}{g_i}. \tag{3.15}$$

  This procedure is implemented in the subroutine MAKE_MASTERFLAT_SCALED.

- MAKE_IMCOR and MAKE_IMCOR_CONSGAIN Finally we can proceed to correcting the science frames. To do so, the image is first overscan corrected, and then bias and flat field are removed via

  $$\text{redImage} = \frac{\text{rawImage} - \text{masterbias}}{\text{normflat}}. \tag{3.16}$$

  Now, if MAKE_MASTERFLAT_SCALED had been used to compute the flat field, the whole image is multiplied by the gain of the lower left quadrant, and the differences in gain of the other quadrants are automatically corrected for by the factors incorporated in the flat field. This is implemented in MAKE_IMCOR_CONSGAIN. If MAKE_MASTERFLAT was used, MAKE_IMCOR must be used, and the quadrants are individually multiplied with the gain values determined from LED sequences. In practice it has turned out that the reduction sequence MAKE_MASTERFLAT_SCALED

+ `MAKE_IMCOR_CONSGAIN` produces smoother images, most likely due to the uncertainties in the gain values obtained form the LED sequences (see Section 3.2.3).

Finally, the values in the image corners that are obscured by the filter wheel are replaced by the median value of a region in the unobstructed area.

Each of the above routines has a counterpart for one-quadrant readout, that uses the analogous procedures and shall therefore not be discussed separately. The readout mode is stored in the FITS header keyword "`HIERARCH OGE DET OUT RNAME`", which is read by `CALEULER` before launching the appropriate reduction pathway.

3.3.2 Photometric Extraction

Once the corrected images are available, the extraction of fluxes for target and reference stars has to be performed. For this purpose I built upon pre-existing C2 reduction scripts, adapting and expanding them to the needs of a flexible photometry extraction for EulerCam.

- `TRANSIT_CONFIG_ECAM`: First the position of the target and a number of reference stars need to be defined. In this routine, a reference image is displayed and the user indicates the rough position of the stars by clicking on them on the image. These positions are then refined by finding the peak of a Gaussian fit in a 80×80 pixel region centered on the clicked coordinates of each star.

- `PHOTEXTRACT`: This routine is carrying out the photometric extraction. This procedure is equipped with several options to adapt its performance to the properties of the observation in question: `binary`, `gaussian_fit`, `superfoc`, `recenter`, and `visu`.

  The radii used for the centering algorithm, the photometric apertures, and the sky apertures can be altered from their standard values are set in `ECAM_PHOT`. The outline of the `PHOTEXTRACT` procedure is as follows:

  For each star, a region of 250×250 pixels centered on the input coordinates is used for calculations. As there are always small coordinate shifts from one image to the next, it is important to redefine the exact center of the stellar PSF and thus the center for the photometric apertures. To do so, a first estimate of the center (x_1, y_1) is obtained by calculating the centroid of a circular region with a radius R_1 located at the region center. Using (x_1, y_1), a preliminary value for the sky flux is calculated in an annulus around this position. This sky value is removed from the data and another centroiding iteration is performed, with a smaller radius R_2, yielding the coordinates (x_2, y_2) for the star center. Another sky estimate is calculated and removed before all data outside a region with radius R_3 around (x_2, y_2) is set to zero, and a Gaussian is fit to the star. The parameters of this fit are saved and, if the option `gaussian_fit` is set, the centers of the Gaussian become the center coordinates for the photometric apertures. Otherwise (x_2, y_2) are used. If the option `superfoc` is set, the center coordinates can be refined once more by fitting an additional Gaussian to a smaller region. This option has proven be useful for close binaries.

  Now, with the precise stellar position known, the sky flux F_S (per pixel) is calculated as the sigma-clipped mean of all pixel values located in the sky annulus. A list of several apertures ap_i is defined for the photometric extraction and for each of them the total flux F_i in aperture i is calculated via

$$F_i = \sum_{j=1}^{N_{\mathrm{pix},i}} \left(F_j - F_S \right) \tag{3.17}$$

  where F_j is the flux in pixel j, where $j \in \{1, \ldots, N_{\mathrm{pix},i}\}$ denotes pixels in aperture i. The standard aperture radii range 18 to 50 pixel but they can be modified in `ECAM_PHOT`. At this point, if the

option `binary` is set, it is possible to place an additional photometric aperture near the target. This can be useful for visual binaries, where the photometric variation of the fainter component needs to be judged.

Finally, visualizations of the target PSF, apertures and sky determination can be displayed if the option `visu` is activated. Several supplementary parameters for the observation (PSF parameters, maximum target flux, coordinate shifts, ABTR performance, DIMM seeing, sky values ...) are saved at this point.

Pointing drifts larger than a few pixels (e.g. due to an ABTR malfunction) can be dealt with by using the `recenter` option. If it is activated, the center coordinates of the window on which the photometric extraction is carried out are adapted from one image to the next. This is done by setting these coordinates to the coordinates of the stellar center found on the previous image.

3.3.3 Lightcurve Creation

For the creation of the best possible photometric lightcurve, the best aperture and combination of reference stars needs to be found. Looping through the apertures, all stellar (target and reference) flux measurements get passed on to the routine `REFSTAR_ECAM`, which determines the best reference star combination. Then, the lightcurves and several additional plots are output. The best aperture is determined as the aperture yielding the lowest residual RMS to a transit fit.

- `REFSTAR_ECAM`: To save calculation time, noisy stars need to be rejected first. For this purpose, relative lightcurves ($\frac{\text{target}}{\text{refstar}_i}$) are created for each star and then, one by one, a transit model is fit. As the model fitting is time intensive, this process is stopped if a star (star_1) is found to have a residual RMS below 0.003 in flux. Then, for all other reference stars, the relative lightcurves with respect to star_1 are calculated. Theses are expected to be flat for the good reference stars. Stars yielding lightcurves with a scatter above 0.009 are discarded as noisy or unstable. Relative target lightcurves are created for all remaining reference stars and transit models are fit. The best (lowest residual RMS) lightcurve is identified and the respective reference star acts as the first element of the final reference source (FRS). Now, an iterative process begins. Each of the remaining reference stars is added to the FRS and the residual RMS of the resulting lightcurve is calculated. The star producing the best RMS is added to the FRS, if there is an improvement with respect to the previous iteration. The process stops once no improvement in residual RMS can be gained by adding stars to the FRS. The lightcurve is normalized by the mean out-of-transit flux and the photometric errors are calculated (see Section 5.2 for details). Finally, a number of plots and data output files are produced, allowing a straight forward check on the system performance during the observation. A sample of these outputs are shown in Figure 3.13 .

- `ECLIPSE`: Since not all time-series photometry from EulerCam are exoplanet transits, a different routine must be available to produce lightcurves, even if the transit model may not be used to evaluate the goodness of reference stars. During my PhD, I repeatedly had to reduce photometric data of eclipsing binaries, hence the name of the routine. Here, the selection of reference stars requires only a flat part of the lightcurve, and the reference star combination is optimized to minimize the scatter in this part. Should even this approach not produce satisfying results, the `give` option in `ECLIPSE` allows to specify which reference stars are to be used.

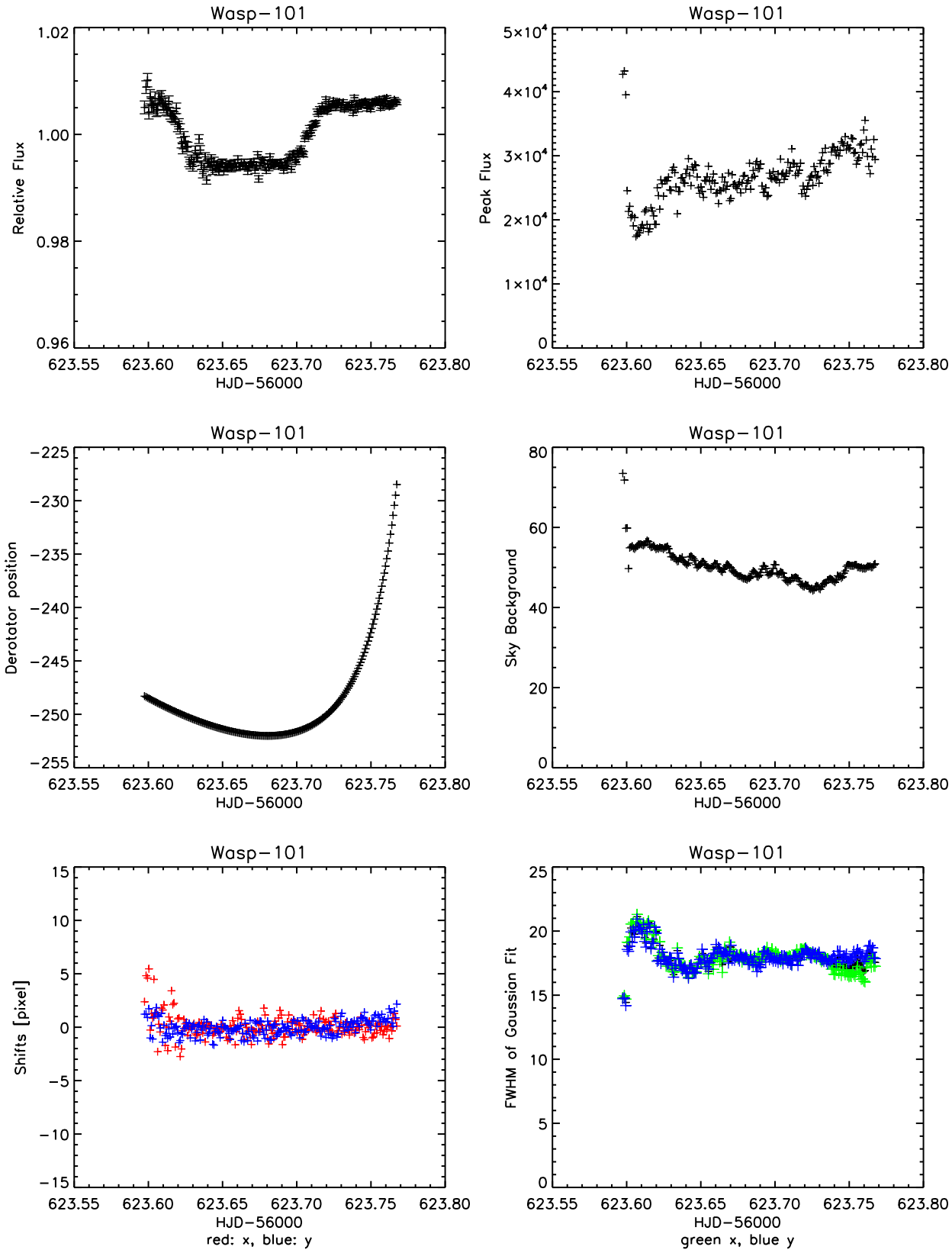

Figure 3.13 : Examples outputs from an `ECAM_PHOT` reduction of a transit data set. The data are that of a transit of WASP-101 b and were obtained on 26 November 2013. The transit lightcurve is shown in the upper right plot, the others plots represent peak flux, derotator position, sky background, coordinate shifts, and stellar FWHM.

The explorer who will not come back or send back his ships to tell his tale is not an explorer, only an adventurer.

Ursula K. Le Guin

4

WASP: A SEARCH FOR TRANSITING PLANETS

With a total of over 100 planets found (some 70 public and several tens awaiting publication), the Wide Angle Search for Planets has been the most productive ground-based transit survey to date. The success of WASP is in great parts due to finely tuned machinery in terms of candidate detection, distribution of information and extensive follow-up efforts. In this chapter I briefly describe the overall planet discovery process and give some more detailed insights in the efforts of photometric follow-up that I have been involved in.

4.1 Science Case

At the time of planning of the first steps towards the WASP survey (Kane et al. 2003, 2004, Street et al. 2003), very little was known about the overall planet frequency. HD209458b had been found to transit (Charbonneau et al. 2000, Henry et al. 2000), and RV were just about able to detect sub-Saturn mass planets. Yet, it was clear that a non-negligible fraction of Solar-type stars were orbited by close-in giant planets with reasonable transit probabilities and periods short enough to show a sufficient number of transits for solid detections in a reasonable time frame. WASP has thus been designed with the capability to detect periodic dips in the stellar brightness of $\sim$1%.

4.2 Telescopes and Observing Strategy

The WASP survey is composed of two sites. The initial SuperWASP-North site at the Observatorio del Roque de los Muchachos at La Palma (Canary Islands, Spain) that was installed in 2003, and the WASP-South site at the South Africa Astronomical Observatory at Southerland (South Africa), that has become operational in 2006.

The SuperWASP cameras (Pollacco et al. 2006) consist of 8 small 11 cm lenses paired with back-illuminated *e2v* CCDs cooled to -75°C by a Peltier system. They are mounted together on an equatorial fork mount, as shown in Figure 4.1 . They have been equipped with broad 300-700 nm filters to provide a maximum transparency. The field of view of each detector is 64 deg^2, and the detector pixel size is 13.5 μm, giving a resolution of 13.7 arcsec/pixel. The exposure time used for the survey is 30s, and the fields are usually observed with a cadence of $\sim$6 minutes, in a repetitive sequence of 7-8 fields, depending on visibility constraints (Collier Cameron et al. 2006). At the time of writing, WASP has obtained more than 420×10^9 data points of more than 31×10^6 individual objects. In Figure 4.2 all the SuperWASP fields are shown, color coded by the amount of observing time dedicated to them. The photometry has a precision of 4-10mmag for stars of magnitudes between V = 9 and V = 13.

4.3 Candidate Selection and RV Follow-up

Photometry is extracted from the WASP data by means of aperture photometry based on an input mask of stellar positions. The input catalog includes stars up to $V = 13$, and apertures of 2.5, 3.5 and 4.5 pixels are used. Given the large pixel size, this leads to a relatively large number of stars that are blended with their neighbors. The typical relative photometric precision ranges from 4 to 10 mmag, depending

Figure 4.1 : The eight SuperWASP cameras are installed together on one equatorial mount. Image credit D.R.Anderson.

on the host star magnitude. The lightcurves are then searched for transit-like signatures using the procedures described in (Collier Cameron et al. 2006), which are based on the SysRem (Tamuz et al. 2005) and Box-Least Square (Kovács et al. 2002) algorithms.

The promising candidates are then passed to spectroscopic and photometric follow-up for a confirmation of their planetary nature. I will limit my descriptions to WASP-South, where the follow-up facilities are the high-precision echelle spectrograph CORALIE for RVs, as well as TRAPPIST (TRansiting Planets and PlanetesImals Small Telescope, (Gillon et al. 2011b, Jehin et al. 2011), and EulerCam (see Section 3 for details).

The CORALIE RV follow-up observations usually consist of a first spectrum of 30 minutes exposure time, obtained at the predicted times of quadrature where the expected RV offset would be largest. An inspection of the CCF allows to immediately discard spectroscopic binaries. Provided the CCF is clean, the RV observations continue at the second quadrature allowing to estimate the amplitude of the variation. Here high mass-ratio binaries show a variation incompatible with the planetary hypothesis and can be discarded. Having passed both tests, the targets remain scheduled for further RV observations, with the hope of identifying a planetary signal as the origin of the periodic dimming of the star. Once a planet has been identified, a number of transit lightcurves are obtained in order to precisely measure its parameters, and determine where it fits in among the known planet sample.

4.4 Photometric Follow-up

Often, the path to discovering a planet is not quite as straight forward as described above. The angular resolution of the WASP images is low, with an on-sky pixel size of 13.7 arcsec, and a minimal photometric aperture of ∼34 arcsec. This means that often several stars fall in the aperture and it is not clear which one is responsible for the dips in the lightcurve. Or, even after a series of RV measurements, no significant variation is visible. In this case it is necessary to obtain photometric observations aiming to understand the system in question.

4.4.1 False Positive Scenarios

Several astrophysical constellations or instrumental effects can cause transit-like signals in the WASP photometric data. The following scenarios need to be excluded in order for the planet to be validated:

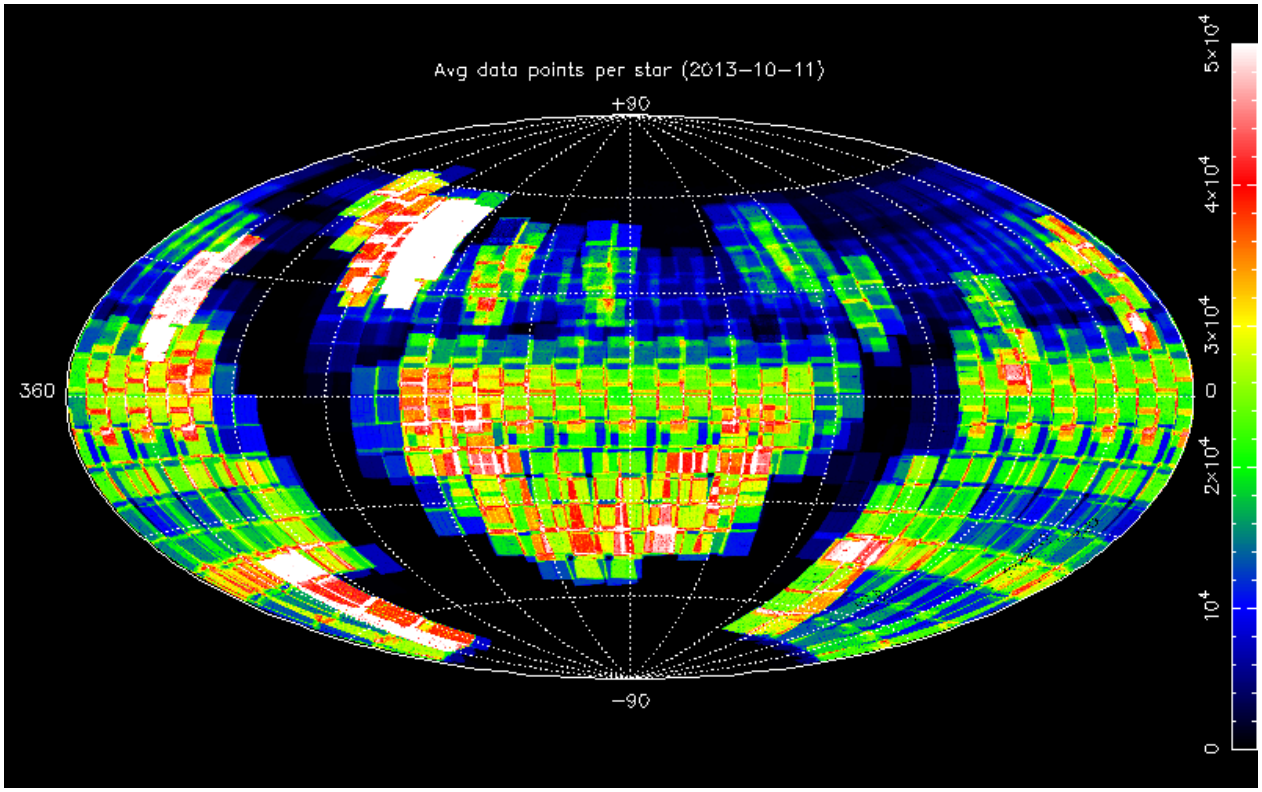

Figure 4.2 : The average number of WASP data points per star. The more frequently observed fields are easily identified, while the areas of the Milky Way have not been observed as crowded fields cause large amount of blends in the photometry. This map is corresponds to the data obtained by 11 October 2013.

- **Blended Eclipsing Binaries:** Just like transiting planets, eclipsing binaries produce periodic flux drops, however usually with amplitudes of a few to a few tens of percent. If such an object is blended with another star, the observed eclipse amplitude decreases, resembling exoplanet transits. By obtaining photometric measurements in and outside the eclipses, these cases can usually be resolved by idenifying which star in the WASP aperture is showing the eclipses, and giving a measurement of the real eclipse depth.

- **Grazing Eclipsing Binaries:** If the inclination of an eclipsing binary is sufficiently low, the system shows grazing eclipses. As only a small area of the stars is obscured, the amplitude of grazing eclipses is lower, and can be compatible with that of a planetary transit. These false-positives can be best identified with RV measurements, as these objects have large RV amplitudes and often are SB2s. Photometric observations can contribute to identifying these objects by providing full-transit lightcurves. For grazing binaries, the lightcurves are distinctively V-shaped and deep compared to grazing planetary transits.

- **High Mass Ratio Binaries:** Eclipsing binaries that are composed of two stars with very different masses can efficiently mimic planetary transits. In particular systems with M-type secondaries produce shallow eclipses and have been found to contribute a significant fraction of WASP candidates. These systems can only be identified from RV observations.

- **Instrumental False Positives:** Sometimes flux drops resembling transits are caused by instrumental effects. Such is the case if the stellar PSF drifts across a flat-field feature or bad pixel during the observations. These candidates do not show any sign of transits or RV variations in follow-up observations, and often can be explained by a more detailed inspection of the initial photometry.

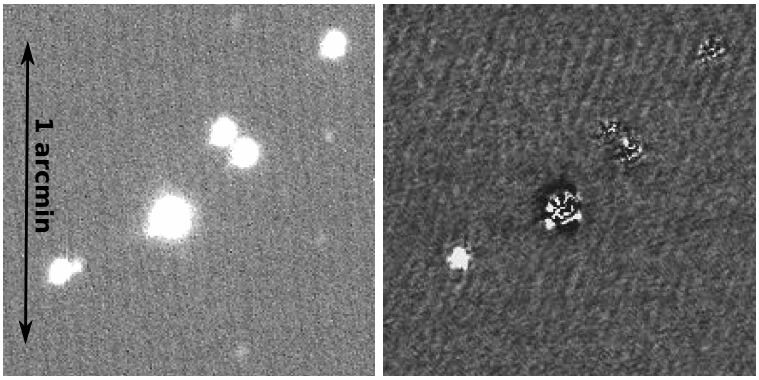

Figure 4.3 : An example of a SuperWASP candidate resolved by difference imaging. The target 1SWASPJ090128.77-185404.0 showed periodic brightness dips in the SuperWASP aperture. However the field is crowded (see left image). The difference image (right) of data obtained out-of and in-transit showes excess flux on a nearby star.

4.4.2 On-Offs, with Aperture Photometry and Difference Imaging

The most simple cases to resolve are those where there are two or three blended stars in the SuperWASP images, yet they are far enough from each other to be resolved by EulerCam without any significant overlap in their PSFs. In this case the situation can often be resolved by obtaining either several well-focused images in transit and out of transit. The effects of color-dependent extinction can be excluded by repeating the same sequence during one of the following nights at the same airmass. Then either by the use of aperture photometry or image subtraction, one can identify which star is the variable one. To obtain aperture photometry of a nearby star, the option `binary` has been added to the `ECAM_RED` pipeline, allowing to define a second aperture next to the target. The photometry is then extracted for this neighboring star as well as for the target, but the identical sky annulus is used.

For the difference imaging approach, I made use of the ISIS (Alard & Lupton 1998, Alard 2000) package. It first aligns the images interpolating them to the same coordinate grid, and then convolves the images and combines them to on in- and one out-of-transit frame. Then, the in-transit image is subtracted from the out-of transit image. The star undergoing the drop in brightness is now visible as a bright spot in the difference image (see Figure 4.3 for an example).

PSF Fitting for Lightcurves

More tricky systems to sort out are those where the two components are blended with each other and one actually needs to separate them by means of PSF photometry. In particularly if the two components have similar brightness the relative precision needed is high[1].

To do so I used the DAOPHOT package (Stetson 1987). I made use of the process `nedaphot` that performs a combination of aperture and PSF photometry to extract flux measurements of blended sources. It does so by subtracting the stellar PSF of one component before performing aperture photometry on the remaining star, and then, inverting the roles, repeats the same process for the other star. As these procedures require quite a large amount of human interaction slowing down the analysis of large datasets, I wrote several procedures to make the process a semi-automatic one, requiring only a very limited amount of input from the user. Below, I briefly describe the steps in this `ECAMDAO` routine.

Before starting `ECAMDAO`, all images are calibrated using the `CALEULER` routines described in Section 3.3.1. Then the process is as follows.

1. First, the best image of the sequence needs to be determined. This image will serve as a reference in terms of coordinate shifts throughout the sequence. Also the stars used for the creation of the PSF, and the target list for all object of interest will be chosen based on this image. As a parameter indicating the best image, I chose the stellar FWHM, extracted with the Sextractor (Bertin & Arnouts 1996) package. At this point, Sextractor is run on all images, bad objects are

[1]For example, let us assume that we have two stars of the same brightness and an overall flux decrease is 1%. The real depth on one of the stars then is 2%.

discarded and the median PSF is saved. Finally the images are sorted by their FWHM values and the best one is displayed.

2. Now some manual input is needed: on the best image, the list of stars of interest is created using the `find` routine of daophot. The result needs to be verified, input parameters adapted if necessary, and finally the list of targets can be cleaned of duplicates or spurious detections.

   The target list, given in pixel coordinates (x,y), is now saved and will be used in the subsequent analysis of all images.

3. One more sequence of manual commands (the daophot routines `ap`, `pick`, `psf`) allow to perform aperture photometry on the best image, select several good reference stars and then calculate the stellar point spread function. The result is checked by using `fallstar`. The selection of reference stars, as well as the PSF fitting options are optimized until a satisfactory result is found.

   The list of PSF stars, given in pixel coordinates (x,y), is now saved and will be used in the subsequent analysis of all images.

4. From now the rest of the reduction runs automatically. First, the reference image is astrometrically calibrated using the `astrometry.net` (Lang et al. 2010) routines. The image coordiantes in both star lists are converted to real coordinates using DS9 in command-line mode.

   The steps 5 to 8 are now performed on each image.

5. The image is calibrated astrometrically using the `astrometry.net` routines.

6. The psf and target coordinate lists are converted to pixel coordinates of the current image.

7. Aperture photometry, psf photometry and the combination of PSF and aperture photometry are run on the image using appropriate input files.

8. The output is saved.

9. Finally, a separate procedure can be launched to bring the output into an easily readable format and several plots can be created.

A good example for an astrophysical false positive identified with `ECAMDAO` is SW123235. On 24 January 2013 we observed a "transit" of this system using an EulerCam with a z'-Gunn filter and a well-focused telescope. The seeing was below 0.8 arcsec for the major part of the observation, but rose to 1.3 arcsec at the very end, resulting in an image quality between 1.1 and 2 arcsec. The two components are separated by 2.7 arcsec and show a flux ratio of 5.4. The relative photometry, shown in Figure 4.4 , clearly shows a 7 % dip on the fainter component, indicative of an eclipsing binary.

4.4.3 Transits

The vast majority of EulerCam time has been invested in the follow-up of confirmed transiting planets. An average of 5.2 eclipse lightcurves are obtained per month, giving a total of 233 transits and occultations between the installation of EulerCam and December 2013. The aim of these observations has been either to supply high-quality lightcurves for initial publication papers, which are essential to give an accurate characterization, or to support several follow-up campaigns. Follow up campaigns include photometry-heavy campaigns measuring the planet's transmission or emission spectrum, or campaigns measuring the systems projected spin-orbit angle via the Rossiter McLaughlin effect. These observations require a precise knowledge of the transit geometry and timing. The lightcurves are analyzed with the standard EulerCam reduction pipeline `ECAM_PHOT` described in Section 3.3.

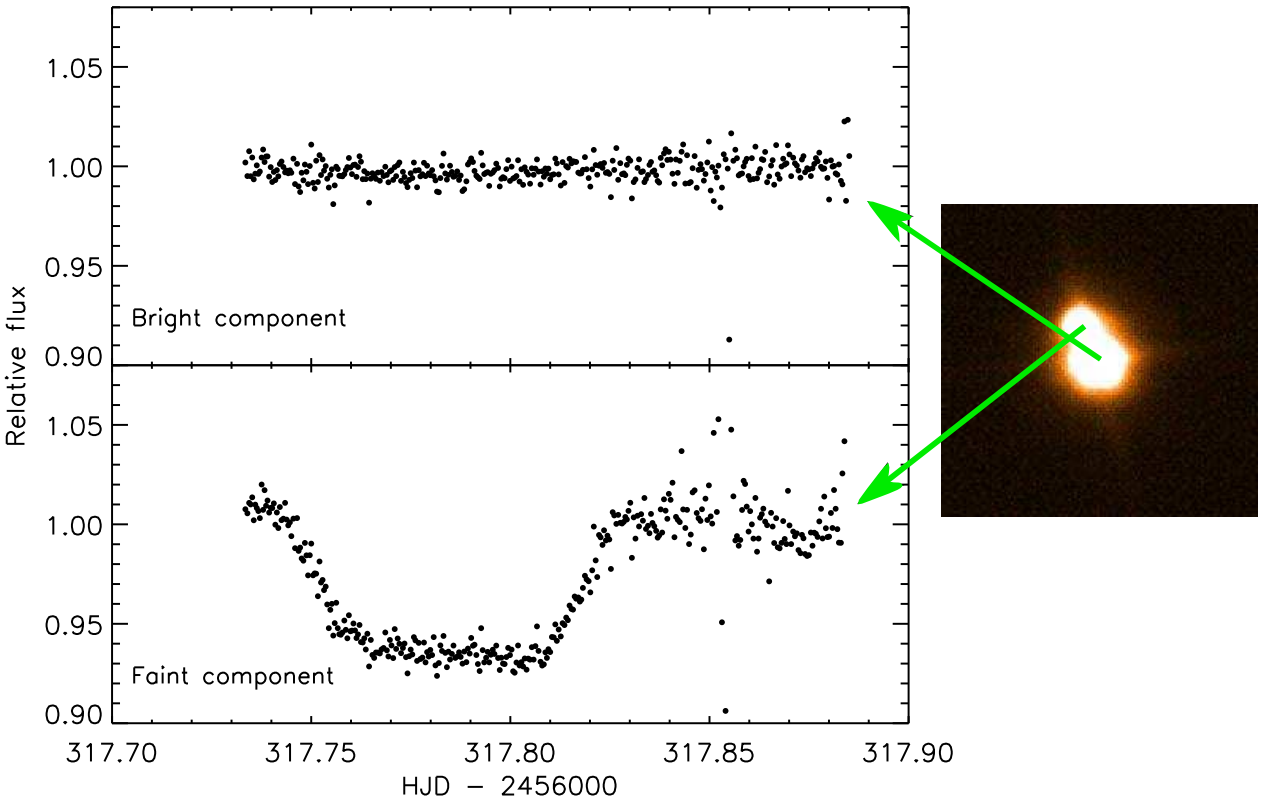

Figure 4.4 : Right: a screenshot showing the two components of the SW123235 blend. The separation is 2.7 arcsec and the upper (southern) component is 5.4 times fainter than the lower one. Left: The lightcurves of both components are shown. The bright component is stable, while the faint component is showing a deep transit-like feature, probably the eclipse of a late-type star.

4.5 WASP-42 b and WASP-49 b

I had the pleasure of taking in charge the analysis and publication of two planetary systems: WASP-42 and WASP-49. At first glance both planets seem like typical hot Jupiters, but as I was working on their announcement paper each of them captivated my interest, as such as it is often the case if one takes the time and tries to understand the details of a new discovery. First, both planets have a clearly sub-Jovian masses, 0.5 M_J and 0.38 M_J, and are thus below the bulk of WASP planets in terms of mass.

WASP-42 b has a 5 day orbit, rather long for a hot Jupiter found by a ground-based transit survey such as WASP. Initially, the first follow-up transits were planned for the 2010 season, but unfortunately could not be carried out. As the target reappeared in the sky, the ephemeris had become quite uncertain. With a first EulerCam observation on 22 February 2011 we caught the end of an egress at the beginning of the time series. Adapting the ephemeris we observed six more transits with EulerCam and TRAPPIST, enough to provide a solid dataset for the final analysis. Unfortunately the HARPS observations scheduled for 4 April 2011 were not adapted to this refined ephemeris and thus took place after the transit. Albeit of not much scientific use, the time-series nicely show the stability of HARPS over a timescale of several hours. Still having HARPS data available for WASP-42 has proven to be a feat. Next to the series aiming at detecting the Rossiter-McLaughlin effect, several other data points have been obtained at other orbital phases. As HARPS data are very precise, an analysis allowing for non-zero eccentricities shows that an eccentric model fits the data better than a purely circular orbit. As has been pointed out by Lucy & Sweeney (1971) small eccentricities need to be carefully verified, as they might be due to noise in the data. Carrying out several tests, including the very test proposed by Lucy & Sweeney (1971), we find that the eccentricity in fact is significant. Yet, data with the quality of HARPS are needed to detect it (see Section 4.1 in Lendl et al. 2012). In Figure 9 of Lendl et al. (2012), I

visualize the posterior probability density for the argument of periastron and eccentricity. Note that the argument of periastron is near $\omega = 180°$, which means that the offset of the transit time and the time of zero RV is maximized. Using the derived values of $e = 0.060 \pm 0.013$ and $\omega = 167° \pm 26$, the RV at the time of mid-transit (neglecting the Rositter-McLaughlin effect) can be calculated using Equation 1.19. For WASP-42, this value is $V_\gamma - 3.79 \pm 0.92$ m s^{-1}. As the values in Lendl et al. (2012) rely on a global analysis, this offset of the times of mid-transit and zero RV is taken into account in the parameter estimation. An additional measurement of the time of occultation of WASP-42 b would confirm its orbital eccentricity, as the time offset of the occultation from phase 0.5 is maximized for this orbital orientation (see Section 1.2.4). Yet, given the low planetary temperature, the predicted occultation depth is small, between 100 ppm and 300 ppm in K-band. The eccentric orbit of WASP-42 b can be interpreted as an indication of not yet finalized orbital circularization.

WASP-49 b has proven to be an easier nut to crack in terms of observation and parameter estimation. The object is a prime target for observations with EulerCam due to its brightness (V = 11.36) and abundance of bright reference stars nearby. Consequently the EulerCam transit lightcurves are of very good quality, with 2-minute residual RMSs of 500 ppm and 700 ppm. The object is located near the 3 day pileup (see Section 2.1.1), and is thus quite a bit hotter ($T_{\rm eq} = 1369 \pm 39$ K) than WASP-42 b. What makes WASP-49 b interesting is its very low ($\rho = 0.3\ \rho_J$) density, paired with a calm, old, main-sequence G6 V host star. As the target has a relatively low mass and density, but is well-irradiated, it should possess a large extended atmosphere making it an excellent target for transmission spectroscopy. Using a mean molecular weight of 2, a variation of one atmospheric scale height equals a variation of 330 ppm in transit depth. Naturally this property has prompted follow-up observations, and I will describe my part in them in Chapter 6.

4.5.1 Paper: WASP-42 b and WASP-49 b: Two New Transiting Sub-Jupiters

A&A 544, A72 (2012)
DOI: 10.1051/0004-6361/201219585

Astronomy & Astrophysics

WASP-42 b and WASP-49 b: two new transiting sub-Jupiters⋆,⋆⋆

M. Lendl[1], D. R. Anderson[2], A. Collier-Cameron[3], A. P. Doyle[2], M. Gillon[4], C. Hellier[2], E. Jehin[4], T. A. Lister[5], P. F. L. Maxted[2], F. Pepe[1], D. Pollacco[6], D. Queloz[1], B. Smalley[2], D. Ségransan[1], A. M. S. Smith[2], A. H. M. J. Triaud[1], S. Udry[1], R. G. West[7], and P. J. Wheatley[8]

[1] Observatoire de Genève, Université de Genève, Chemin des maillettes 51, 1290 Sauverny, Switzerland
e-mail: monika.lendl@unige.ch
[2] Astrophysics Group, Keele University, Staffordshire, ST5 5BG, UK
[3] School of Physics and Astronomy, University of St. Andrews, North Haugh, Fife, KY16 9SS, UK
[4] Université de Liège, Allée du 6 août 17, Sart Tilman, Liège 1, Belgium
[5] Las Cumbres Observatory, 6740 Cortona Drive Suite 102, Goleta, CA 93117, USA
[6] Astrophysics Research Centre, School of Mathematics & Physics, Queen's University, University Road, Belfast BT7 1NN, UK
[7] Department of Physics and Astronomy, University of Leicester, Leicester, LE1 7RH, UK
[8] Department of Physics, University of Warwick, Coventry CV4 7AL, UK

Received 11 May 2012 / Accepted 29 June 2012

ABSTRACT

We report the discovery of two new transiting planets from the WASP survey. WASP-42 b is a 0.500 ± 0.035 M_J planet orbiting a K1 star at a separation of 0.0548 ± 0.0017 AU with a period of $4.9816872 \pm 7.3 \times 10^{-6}$ days. The radius of WASP-42 b is 1.080 ± 0.057 R_J while its equilibrium temperature is $T_{eq} = 995 \pm 34$ K. We detect some evidence for a small but non-zero eccentricity of $e = 0.060 \pm 0.013$. WASP-49 b is a 0.378 ± 0.027 M_J planet around an old G6 star. It has a period of $2.7817387 \pm 5.6 \times 10^{-6}$ days and a separation of 0.0379 ± 0.0011 AU. This planet is slightly bloated, having a radius of 1.115 ± 0.047 R_J and an equilibrium temperature of $T_{eq} = 1369 \pm 39$ K. Both planets have been followed up photometrically, and in total we have obtained 5 full and one partial transit light curves of WASP-42 and 4 full and one partial light curves of WASP-49 using the Euler-Swiss, TRAPPIST and Faulkes South telescopes.

Key words. planetary systems – methods: observational – techniques: photometric – techniques: spectroscopic – stars: individual: WASP-42 – stars: individual: WASP-49

1. Introduction

Since the discovery of the first extrasolar planet around a Solar-type star by Mayor & Queloz (1995) over 700 exoplanets have been found. In recent years an increasingly large number of planets have been discovered by transit surveys, i.e. surveys that search for planets that pass in front of their host stars producing characteristic photometric signals. At the time of writing, the two most prominent ground-based transit surveys are HATnet (Bakos et al. 2004) and WASP (Pollacco et al. 2006).

From ground-based transit surveys, a population of hot close-in giant planets has been explored. These Hot Jupiters are located at small separations, having periods of typically 2 to 5 days. While the formation of gas giants is accepted to take place in cooler regions of the protoplanetary disc at several AU from the star, the process by which the planets have migrated to the proximity of the star has been a matter of debate. Migration can occur from interactions with the disc itself (Goldreich & Tremaine 1980; Lin et al. 1996), or due to dynamical interactions between massive bodies in the system, namely scattering between planets (Rasio & Ford 1996) and Kozai migration (Kozai 1962; Eggleton & Kiseleva-Eggleton 2001; Wu & Murray 2003), which put the planet on a highly eccentric orbit that then becomes tidally circularized. Recent measurements of the sky-projected spin-orbit angles have revealed several misaligned systems (Hébrard et al. 2008; Triaud et al. 2010; Winn et al. 2010), a fact which could be caused by planets undergoing Kozai migration (Fabrycky & Tremaine 2007; Wu et al. 2007; Triaud et al. 2010).

Many of these planets have been shown to posses radii which are larger than expected from models of irradiated planets (e.g. Fortney et al. 2007). Low densities appear to be common for Saturn-mass planets (e.g. WASP-39 b, Faedi et al. 2011) and up to planets of the mass of Jupiter (e.g. HAT-P-32 b, Hartman et al. 2011). The most striking examples are WASP-17 b having a density of $\rho = 0.06\,\rho_J$ (Anderson et al. 2010, 2011) and Kepler-12 b with a density of $\rho = 0.09\,\rho_J$ (Fortney et al. 2011). It appears that there is a mechanism depositing energy into the planet and thus inflating it or slowing the contraction of the planet since its formation. A variety of mechanisms have been proposed to account for this effect: the deposition of kinetic energy stemming from strong winds driven by large day/night temperature contrasts (Showman & Guillot 2002); enhanced opacities due to higher planetary metallicity causing a slow-down in contraction (Burrows et al. 2007); heating by tidal forces from the

⋆ Based on photometric observations made with WASP-South, EulerCam on the Euler-Swiss telescope, the Belgian TRAPPIST telescope, the Faulkes South Telescope and spectroscopic observations obtained with CORALIE on the Euler-Swiss telescope and HARPS on the ESO 3.6 m telescope (Prog. ID: 087.C-0649).

⋆⋆ The photometric time series and radial velocity data in this work are only available at the CDS via anonymous ftp to cdsarc.u-strasbg.fr (130.79.128.5) or via http://cdsarc.u-strasbg.fr/viz-bin/qcat?J/A+A/544/A72

circularization, synchronization and re-alignment of the planetary orbit (Bodenheimer et al. 2001); reduced heat transport efficiency by layered convection inside the planet (Chabrier & Baraffe 2007), and Ohmic heating from currents induced through winds in the planetary atmosphere (Batygin & Stevenson 2010). It has been found that the degree to which the planet is bloated is correlated with the incident stellar flux (Demory & Seager 2011; Enoch et al. 2011, 2012; Laughlin et al. 2011), favouring models which incorporate the absorption of stellar radiation as a cause of the planetary bloating.

In this paper, we announce the discovery of two additional transiting planets from the WASP-South survey. WASP-42 b is a 0.5 M_J planet in a 5 day orbit around a K1 star, and WASP-49 b, a bloated 0.4 M_J planet, is orbiting a metal poor G6 star every 2.8 days. In Sect. 2 we present the discovery and follow-up observations of WASP-42 and WASP-49, leading to their identification as harbouring transiting extrasolar planets. In Sect. 3 we describe the analysis of our data before putting the two planets into context in Sect. 4.

2. Observations

2.1. WASP-photometry

The objects WASP-42 (2MASS 12515557–4204249) and WASP-49 (2MASS 06042146–1657550) were observed using the WASP survey telescopes. The WASP survey is operated from two sites, one in each hemisphere: the Observatorio del Roque de los Muchachos in the Canary Islands in the North, and the Sutherland Station of the South African Astronomical Observatory (SAAO) in the South. Each site is equipped with eight commercial 11 cm, f = 200 mm Canon lenses on a single mount. Details of the WASP survey, its photometric reduction and candidate selection process can be found in Pollacco et al. (2006) and Collier Cameron et al. (2007). Both targets presented in this work were observed exclusively from the southern WASP site. In total 25 880 data points were obtained for WASP-42 between May 2006 and April 2008, while 18461 data points were obtained for WASP-49 between October 2006 and March 2010. The data obtained for both targets are shown in Fig. 1. In both cases a periodically occurring transit-like signal was detected in the data using the transit-search algorithms of Collier Cameron et al. (2006), triggering a closer inspection of the targets and their selection for further study.

2.2. Spectroscopic observations

WASP-42 and WASP-49 were observed with the CORALIE spectrograph mounted on the 1.2 m Euler-Swiss telescope at the La Silla site (Chile). For WASP-42 and WASP-49, 27 and 25 data points were obtained from April 2010 to March 2011, and from August 2009 to October 2011, respectively. For all spectroscopic observations we obtained radial velocities using the weighted Cross-Correlation technique (Baranne et al. 1996) as implemented in the CORALIE and HARPS reduction pipelines. The radial velocities folded on the transit ephemeris are shown in Figs. 2 and 3. In order to ensure that the radial-velocity variations are not caused by star spots we checked the CCF bisector spans (shown in Fig. 4) according to the method described by Queloz et al. (2001). After the planetary nature of the signal had been confirmed, WASP-42 was also observed with the HARPS spectrograph (Mayor et al. 2003) which is located at the ESO 3.6 m telescope at La Silla observatory. 35 data points were obtained with HARPS, 25 of which were observed nearly consecutively on 4 April 2011 (UT) in order to measure the Rossiter-McLaughlin effect (Rossiter 1924; McLaughlin 1924) and thus determine the projected spin-orbit angle of the WASP-42 system. However, due to an inaccurate

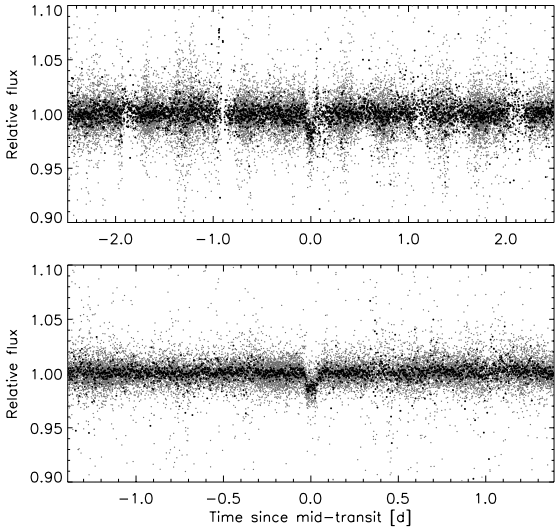

Fig. 1. Phase-folded WASP photometry of WASP-42 (*top*) and WASP-49 (*bottom*). The unbinned data are depicted in gray; the black points represent the same data set binned to 2 min.

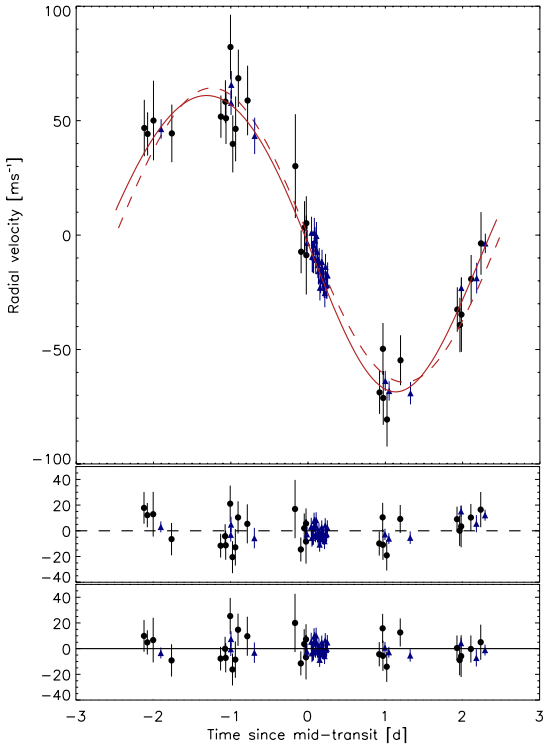

Fig. 2. *Upper panel*: radial velocity observations of WASP-42 together with the circular (dashed line) and eccentric (solid line) models. Black dots denote CORALIE data, while blue triangles denote HARPS data. *Middle panel*: residuals of the circular model. *Lower panel*: residuals of the eccentric model.

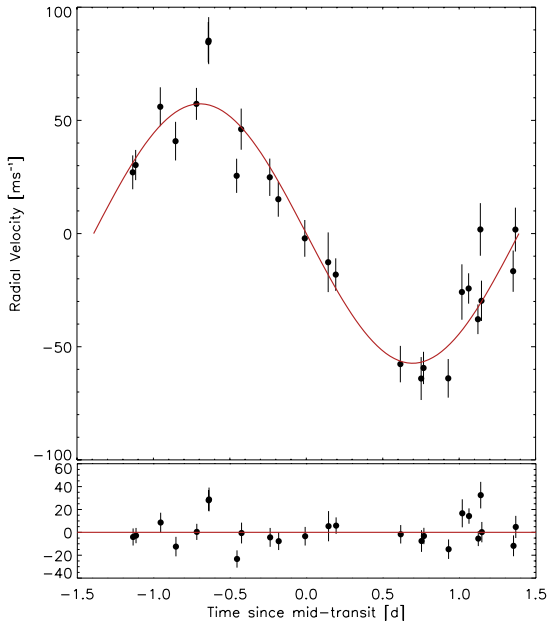

Fig. 3. Radial velocity observations of WASP-49 together with the respective model and residuals. All data have been obtained with CORALIE.

ephemeris at the time of planning of these observations, the continuous observations began only during the egress of the planet (see Fig. 6) and thus the Rossiter-McLaughlin effect was not measured.

2.3. Follow-up photometry

Two transits each of both WASP-42 b and WASP-49 b were observed using EulerCam between January and March 2011. EulerCam is an *e2v* 4k × 4k back-illuminated deep-depletion silicon CCD detector which was installed at the Cassegrain focus of the 1.2 m Euler-Swiss telescope in September 2010. The field of view of EulerCam is 15.68 × 15.73 arcmin, producing a resolution of 0.23 arcsec per pixel. The instrument is operated at a temperature of −115 °C, cool enough to make dark current negligible (measured at less than 2.6 e^- in 30 min). EulerCam can be read out using either one or four ports, giving readout times of 6.5 s and 25 s. For single-port readout the readout noise is ∼5 e^-/pixel. For four-port readout the readout noise is the same except that the lower-left port shows a slightly elevated noise of ∼8 e^-/pixel. As flat-field uncertainties are often a limiting factor in high-precision photometry, EulerCam uses a feedback scheme for the telescope guiding to keep the stars on the same locations on the detector during the observations. This system, dubbed "Absolute Tracking" is based on a combination of the *SCAMP* (Bertin 2006) and *Sextractor* (Bertin & Arnouts 1996) software packages. After recording an image, the positions of the stars on the image are extracted and then matched with a catalogue. From this match, the offset of the telescope from the nominal position is calculated using a PID algorithm and the telescope pointing is adjusted between exposures in order to compensate for drifts. Due to technical problems the 4-port readout mode was not available during the first transit of WASP-49, leading to a slightly degraded time sampling. All EulerCam observations were done with a defocus of 0.1 mm in order to improve the duty cycle and spread the light over more pixels and thereby improve the sampling of the PSF.

Four transits of WASP-42 b and two transits of WASP-49 b were observed with the automated Belgian TRAPPIST telescope, also located at La Silla. For details of TRAPPIST see Gillon et al. (2011) and Jehin et al. (2011). Again, the telescope was defocused giving a *FWHM* of 3.2 arcsec on the images.

Finally, one partial transit of WASP-49 b was observed with the Faulkes Telescope South (FTS) which is based at Siding Spring, Australia. Details of all observations are summarized in Table 1 and the light curves are depicted in Fig. 5.

All follow-up light curves were obtained from bias- and flat-field-corrected images using relative Aperture Photometry where several apertures were tested and reference stars were chosen with great care. In the case of TRAPPIST, IRAF[1] was used in the reduction process. For EulerCam, the standard reduction procedure is as follows. After overscan, bias and flat-field correction, the photometry is extracted from the images for several circular apertures with radii ranging from 12 to 50 pixels placed on the target and all other bright stars in the field. The optimal combination of reference stars is found by using the target itself to measure the quality of the references. We start the process with the reference star with which we obtain the lowest RMS transit light curve and iteratively add those other references which yield the best improvement at any given step. Typically, the final reference sources is made of between three and ten stable stars of similar brightness and color to the target and which are not affected by any short-term variations (caused, e.g., by proximity to bad pixels).

During the observations of WASP-49 with EulerCam we noticed a faint source, 9.2 arcsec North of the target. It is outside the smaller apertures for which we extracted photometry in the analysis of the EulerCam data. As the transit is present in light curves created using these apertures (while the data are noisier than for larger apertures), we are certain the transit is on the main target. However, in order to evaluate the contamination for larger apertures, we re-observed WASP-49 on 15 January 2012 with EulerCam without defocusing the telescope. The observations were performed outside of transit, a total of 8 images were obtained over 10 min using an r' Gunn filter. We find the brightness ratio between the target and the contaminant to be $1 : 0.00343 \pm (5 \times 10^{-5})$, and, as its impact on the observed transit depth is much smaller (4×10^{-5}) than the 1-σ-error quoted in Table 3, we neglect it in the analysis presented below.

3. Determination of system parameters

3.1. Stellar parameters

3.1.1. Rotation period

We have analyzed the WASP lightcurves of WASP-42 and WASP-49 to determine whether they show periodic modulation due to the combination of magnetic activity and the rotation of the star. We used the sine-wave fitting method described in Maxted et al. (2011) to calculate periodograms for both stars over 4096 uniformly spaced frequencies from 0 to 2.5 cycles/day. The false alarm probability (FAP) for the strongest peak in these periodograms was calculated using the boot-strap Monte Carlo method also described in Maxted et al. (2011).

[1] IRAF is distributed by the National Optical Astronomy Observatories, which are operated by the Association of Universities for Research in Astronomy, Inc., under cooperative agreement with the National Science Foundation.

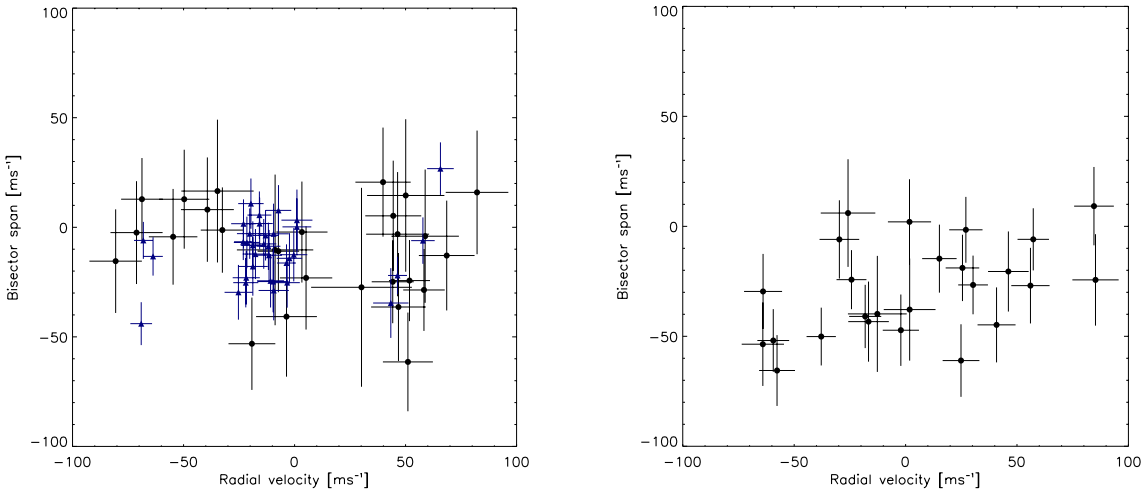

(a) Bisector measurements of WASP-42 against the measured radial velocity. Black dots denote data points from CORALIE while blue triangles denote points obtained with HARPS.

(b) Bisector measurements of WASP-49 against the measured radial velocity. All data have been obtained with CORALIE.

Fig. 4. Bisector spans measured for WASP-42 *(left)* and WASP-49 *(right)*.

Table 1. Summary of follow-up photometry.

target	Date (UT)	Telescope/instrument	Filter	T_c [HJD$_{TBD}$ − 2 450 000]	β_{red}[1]	rms [relative flux, per 2 min]
WASP-42	05-03-2011	TRAPPIST	$I+z'$	5625.65821 ± 0.00044	1.13	1.2×10^{-3}
WASP-42	10-03-2011	TRAPPIST	$I+z'$	5630.64098 ± 0.00055	1.45	1.4×10^{-3}
WASP-42	20-03-2011	EulerCam	r' Gunn	5640.60221 ± 0.0040	1.43	0.9×10^{-3}
WASP-42	25-03-2011	EulerCam	r' Gunn	5645.58600 ± 0.00057	1.06	1.9×10^{-3}
WASP-42	30-03-2011	TRAPPIST	$I+z'$	5650.56771 ± 0.00066	1.18	1.4×10^{-3}
WASP-42	04-04-2011	TRAPPIST	$I+z'$	5655.54921 ± 0.00056	1.15	1.2×10^{-3}
WASP-49	19-01-2011	EulerCam	r' Gunn	5580.59412 ± 0.00041	1.26	0.5×10^{-3}
WASP-49	19-01-2011	TRAPPIST	$I+z'$	5580.59523 ± 0.00074	1.00	1.5×10^{-3}
WASP-49	21-02-2011	FTS	z' Gunn	5613.976 ± 0.011	1.00	0.7×10^{-3}
WASP-49	24-03-2011	EulerCam	r' Gunn	5644.57521 ± 0.00035	1.00	0.7×10^{-3}
WASP-49	24-10-2011	TRAPPIST	$I+z'$	5858.76832 ± 0.00048	1.08	1.4×10^{-3}

Notes. Target, date, telescope and filter are given for each observation together with the mid-transit time, red noise amplitude and the rms of the binned (2 min) residuals. [(1)] As defined in Winn et al. (2010).

Variability due to star spots is not expected to be coherent on long timescales as a consequence of the finite lifetime of star-spots and differential rotation in the photosphere, and so for both stars we analyzed the data from each observing season independently.

We did not find any significant periodic signals (FAP < 0.05) in our data apart from frequencies near 1 cycle/day and its harmonics. We examined the distribution of amplitudes for the most significant frequency in each Monte Carlo trial and used these results to estimate a 95% upper confidence limit of 1 milli-magnitude for the amplitude of any periodic signal in the lightcurves for both WASP-42 and WASP-49.

3.1.2. Spectroscopic analysis

For each star a total of 11 (WASP-42) and 23 (WASP-49) individual CORALIE spectra were co-added to produce single spectra with typical *S/N* values of 60:1 (WASP-42) and 100:1 (WASP-49). The standard pipeline reduction products were used in the analysis.

The analyses were performed using the methods given in Gillon et al. (2009). The H_α line was used to determine the effective temperature ($T_{\rm eff}$), while the Na I D and Mg I b lines were used as surface gravity ($\log g$) diagnostics. The parameters obtained from the analysis are listed in Table 2. The elemental abundances were determined from equivalent width measurements of several clean and unblended lines. Values for microturbulence (ξ_t) were determined from Fe I using the method of Magain (1984). The quoted error estimates include those given by the uncertainties in $T_{\rm eff}$, $\log g$ and ξ_t, as well as the scatter due to measurement and atomic data uncertainties.

The projected stellar rotation velocities ($v \sin i_*$) were determined by fitting the profiles of several unblended Fe I lines. Values for macroturbulence ($v_{\rm mac}$) of 1.4 ± 0.3 km s^{-1} (WASP-42) and 2.9 ± 0.3 km s^{-1} (WASP-49) were assumed, based on the tabulation by Gray (2008). For both cases, an instrumental *FWHM* of 0.11 ± 0.01 Å was determined from the telluric lines around 6300 Å. Best fitting values of $v \sin i_* = 2.7 \pm 0.4$ km s^{-1} (WASP-42) and $v \sin i_* = 0.9 \pm 0.3$ km s^{-1} (WASP-49) were obtained.

There is no significant detection of lithium in the spectra of either star, with equivalent width upper limits of 4 mÅ, corresponding to an abundance upper limit of $\log A(\mathrm{Li}) < 0.5 \pm 0.2$

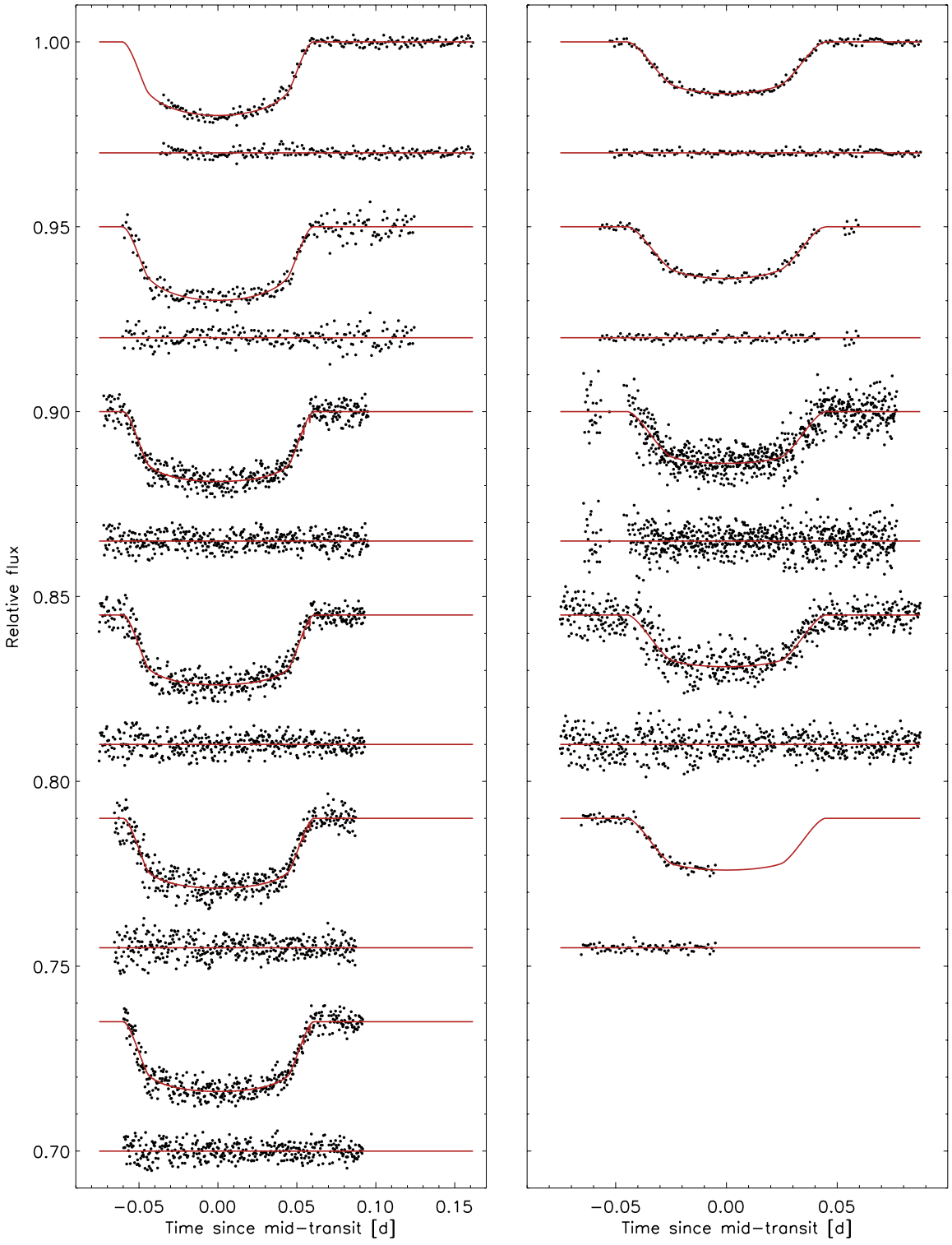

Fig. 5. Follow-up photometry of WASP-42 (*left*) and WASP-49 (*right*) together with the respective model and residuals. Each light curve has been divided by the respective photometric baseline model as described in Sect. 3.2. The light curves of WASP-42 are (from top to bottom) EulerCam on March 20 and 25, 2011, and TRAPPIST on March 5, 10, 30 and April 4, 2011 (UT). The light curves of WASP-49 are (from top to bottom) EulerCam on January 19 and March 24, 2011, TRAPPIST on January 19 and 24 October 2011, and FTS on 21 March 2011 (UT).

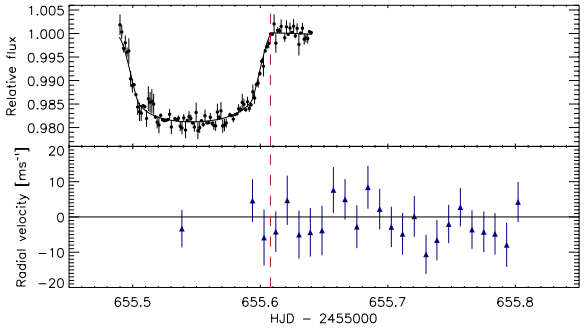

Fig. 6. Photometric and radial velocity observations obtained on April 4, 2011 (UT). *Upper panel*: TRAPPIST transit light curve binned in 2 min intervals. *Lower panel*: the the HARPS time series observation aiming at measuring the Rossiter-McLaughlin effect. Depicted are the residual values from a purely Keplerian model. The dashed red line indicates the time of fourth contact.

Table 2. Stellar parameters of WASP-42 and WASP-49 from spectroscopic analysis.

Parameter	WASP-42	WASP-49
RA	$12^h51^m55.62^s$	$06^h04^m21.47^s$
Dec	$-42°04'25.2''$	$-16°57'55.1''$
V mag	12.57	11.36
$T_{\rm eff}$	5200 ± 150 K	5600 ± 150 K
log g	4.5 ± 0.1	4.5 ± 0.1
ξ_t	0.8 ± 0.2 km s^{-1}	0.9 ± 0.2 km s^{-1}
$v \sin i_*$	2.7 ± 0.4 km s^{-1}	0.9 ± 0.3 km s^{-1}
[Fe/H]	0.05 ± 0.13	−0.23 ± 0.07
[Na/H]	0.23 ± 0.10	−0.10 ± 0.08
[Mg/H]	0.21 ± 0.10	−0.09 ± 0.06
[Si/H]	0.18 ± 0.06	−0.04 ± 0.05
[Ca/H]	0.11 ± 0.12	−0.06 ± 0.11
[Sc/H]	0.13 ± 0.09	0.06 ± 0.05
[Ti/H]	0.27 ± 0.15	0.05 ± 0.06
[V/H]	0.59 ± 0.13	0.02 ± 0.16
[Cr/H]	0.12 ± 0.12	−0.16 ± 0.03
[Co/H]	0.30 ± 0.06	−0.03 ± 0.09
[Ni/H]	0.14 ± 0.09	−0.14 ± 0.06
log A(Li)	<0.5 ± 0.2	<0.7 ± 0.1
Mass	0.89 ± 0.08 $M_\odot$	0.94 ± 0.07 $M_\odot$
Radius	0.87 ± 0.11 $R_\odot$	0.90 ± 0.11 $R_\odot$
Sp. type	K1	G6
Distance	160 ± 40 pc	170 ± 20 pc

Notes. Mass and radius estimates using the Torres et al. (2010) calibration. Spectral type estimated from $T_{\rm eff}$ using the table in Gray (2008).

(WASP-42) and 8 mÅ, corresponding to an abundance upper limit of log A(Li) < 0.7 ± 0.1 (WASP-49).

3.2. Combined analysis

The combined analysis of discovery and follow-up photometry and spectroscopic data was performed in several steps with the Markov Chain Monte Carlo (MCMC) code described in Gillon et al. (2010, 2012). The code makes use of the transit light curve models by Mandel & Agol (2002) and uses a Keplerian model to fit the radial-velocity measurements. For radial-velocity measurements obtained during transit, the prescription of the Rossiter-McLaughlin effect provided by Giménez (2006) is used. Various models for the photometric baseline (e.g. 0th to 4th order polynomials with respect to time and external variables such as pixel shifts) can be included in the fit of the transit light curves via minimization of the model coefficients at each MCMC step. The basic jump parameters are transit depth dF, impact parameter b, transit duration d, epoch of mid-transit T_0, period P and $K_2 = K\sqrt{1-e^2}P^{1/3}$ (where K and e denote the radial velocity semi-amplitude and eccentricity, respectively). For these parameters we assume a uniform prior distribution. In order to take into account the stellar limb-darkening, we adopt a quadratic law interpolating the coefficients tabulated by Claret & Bloemen (2011). However, we chose their combination $c_1 = 2u_1 + u_2$ and $c_2 = u_1 - 2u_2$ as jump parameters as introduced by Holman et al. (2006). The physical basis of these parameters leads us to assume a normal prior distribution with a width equal to the errors of these parameters. Where eccentricity is not set to $e = 0$, it is included in the analysis via including the jump parameters $\sqrt{e}\cos\omega$ and $\sqrt{e}\sin\omega$ (where ω denotes the argument of periastron). We use the calibration technique devised by Enoch et al. (2010) which uses a fit to a set of well studied main-sequence eclipsing binaries in order to infer the stellar mass and radius from the mean stellar density (measured directly from the transit light curves, Seager & Mallén-Ornelas (2003), temperature and metallicity. This technique is based on a similar relation by Torres et al. (2010) where the stellar surface gravity is used in the place of the stellar density. A minimum of two chains is run in order to check their convergence using the Gelman & Rubin test (Gelman & Rubin 1992).

As a first step, the photometric data obtained by the WASP-South cameras were analyzed with the aim of finding a mean mid-transit time and period estimate from these long-term data. As the light curves from WASP contain many large outliers (i.e. points deviating by more than 10 times the transit depth), we discarded points deviating by more than 5σ before running two MCMC chains of 10^4 points each. Here the only parameters left to vary were the time of mid-transit and the period, while all other parameters were kept fixed at their approximate values. The period derived here was used as a starting point in the subsequent analysis of the high-precision follow-up data, while the mid-transit time was included as an extra constraint on the period.

Then, for each follow-up lightcurve we performed MCMC analyses including only the light curve itself and the CORALIE radial velocity measurements. We tested various models for the photometric baseline, using chains of 10^5 points. A second-order polynomial in time was assumed as a minimal baseline model to take care of stellar variability, airmass and other time-dependent effects. More complicated models (i.e. polynomials up to the fourth degree with respect to time, position shifts, sky background, and FWHM) were tested with the Bayesian Information Criterion (Schwarz 1978). Only for the EulerCam light curve obtained on 19 January 2011 (WASP-49) was a more complicated model (a linear fit to position plus the quadratic fit to time) found to be justified.

Finally, we performed a global analysis in order to find a single solution using all available follow-up data together with the mid-transit time obtained from the discovery photometry. The dependencies and orders in the photometric baseline models were set to those found before. For each planet we ran three sets of two chains of 10^5 points. From the first set, we determined correction factors for our photometric errors based on the calculation of the red noise (Pont et al. 2006) as described in Winn et al. (2008). In the further analysis, the photometric errors were multiplied by these factors. For the RV data, we determined

Table 3. Planetary and stellar parameters for WASP-42 and WASP-49, as well as the radial-velocity rms.

	WASP-42		WASP-49
	$e = 0$	$e \neq 0$	$e = 0$
Jump parameters			
$\Delta F = (R_p/R_*)^2$	0.01650 ± 0.00039	0.01650 ± 0.00037	0.01376 ± 0.00038
$b' = a * \cos(i_p)$ $[R_*]$	$0.410^{+0.045}_{-0.055}$	$0.418^{+0.043}_{-0.056}$	0.745 ± 0.014
T_{14} [d]	$0.12042^{+0.00099}_{-0.00095}$	0.12043 ± 0.00093	0.08832 ± 0.00080
$T_{[0]} - 2\,450\,000$ [HJD]	5650.56723 ± 0.00024	5650.56720 ± 0.00023	5580.59436 ± 0.00029
P [d]	$4.9816877^{+0.0000068}_{-0.0000073}$	4.9816872 ± 0.0000073	2.7817387 ± 0.0000056
K_2 [km s^{-1} $a^{1/3}$]	109.8 ± 2.9	110.4 ± 2.9	79.9 ± 3.3
$c_{1,r'}$	1.271 ± 0.056	1.270 ± 0.055	$1.124^{+0.058}_{-0.061}$
$c_{2,r'}$	0.122 ± 0.063	0.120 ± 0.065	-0.130 ± 0.048
$c_{1,I+z'}$	0.908 ± 50.00	0.907 ± -0.049	0.835 ± 0.043
$c_{2,I+z'}$	-0.234 ± 0.033	-0.234 ± 0.032	-0.241 ± 0.046
$c_{1,z'}$	–	–	0.786 ± 0.042
$c_{2,z'}$	–	–	-0.257 ± 0.027
Deduced parameters			
K [km s^{-1}]	64.3 ± 1.7	64.8 ± 1.7	56.8 ± 2.4
R_p $[R_J]$	1.063 ± 0.051	1.080 ± 0.057	1.115 ± 0.047
M_p $[M_J]$	0.497 ± 0.035	0.500 ± 0.035	0.378 ± 0.027
e	0	0.060 ± 0.013	0
ω [deg]	-	167 ± 26	-
a [AU]	0.0547 ± 0.0017	0.0548 ± 0.0017	0.0379 ± 0.0011
a/R_*	13.84 ± 0.34	13.65 ± 0.46	8.35 ± 0.16
i_p [deg]	$88.30^{+0.26}_{-0.23}$	$88.25^{+0.27}_{-0.23}$	84.89 ± 0.19
b_{tr}	$0.410^{+0.045}_{-0.055}$	$0.411^{+0.041}_{-0.054}$	0.745 ± 0.014
$T_{occ} - 2\,450\,000$ [HJD][a]	5658.03977 ± 0.00024	5652.889 ± 0.035	5584.76697 ± 0.00028
ρ_p $[\rho_J]$	$0.412^{+0.049}_{-0.042}$	$0.397^{+0.054}_{-0.047}$	$0.273^{+0.030}_{-0.026}$
T_{eq} [K][b]	988 ± 31	995 ± 34	1369 ± 39
M_* $[M_\odot]$	$0.881^{+0.086}_{-0.081}$	$0.884^{+0.086}_{-0.080}$	$0.938^{+0.080}_{-0.076}$
R_* $[R_\odot]$	0.850 ± 0.035	$0.863^{+0.041}_{-0.034}$	0.976 ± 0.034
ρ_* $[\rho_\odot]$	1.43 ± 0.11	1.37 ± 0.14	1.0098 ± 0.06
$u_{1,r'}$	0.533 ± 0.029	0.532 ± 0.029	0.424 ± 0.029
$u_{2,r'}$	0.205 ± 0.025	0.206 ± 0.025	0.277 ± 0.017
$u_{1,I+z'}$	0.317 ± 0.024	0.316 ± 0.024	0.286 ± 0.020
$u_{2,I+z'}$	0.275 ± 0.010	0.275 ± 0.010	0.263 ± 0.020
$u_{1,z'}$	–	–	0.263 ± 0.020
$u_{2,z'}$	–	–	0.260 ± 0.010
Radial velocity rms			
CORALIE	12.12	10.7	13.53
HARPS	5.76	4.62	-
RMS/error HARPS	1.00	0.80	-
RMS/error CORALIE	0.96	0.85	1.56

Notes. For WASP-42 we show both the circular and the (preferred) eccentric model. [a] Predicted. [b] Assuming $A = 0$ and $F = 1$.

"jitter" factors which serve to scale the measurement errors to the standard deviation of the best-fit model. These factors are added quadratically to the RV errors and compensate both instrumental and astrophysical effects (such as stellar activity) that are not included in the initial error calculation. The values for the RV jitter are 0 m s^{-1} (WASP-42, CORALIE), 2.4 m s^{-1} (WASP-42, HARPS) and 10 m s^{-1} (WASP-49, CORALIE).

The second and third sets of chains were run with the adapted errors, first setting the eccentricity to $e = 0$ and then leaving it free. For WASP-49, no significant deviation from a circular orbit is detected ($e = 0.018^{+0.023}_{-0.013}$), and all parameters agree well within one sigma for circular and eccentric case. The eccentric solution for WASP-42 yields $e = 0.060^{+0.013}_{-0.011}$ and will be further discussed in Sect. 4 while the planetary and stellar parameters of both objects are presented in Table 3.

4. Discussion

We announce the discovery of two new transiting extrasolar planets in the southern hemisphere from the WASP-South survey.

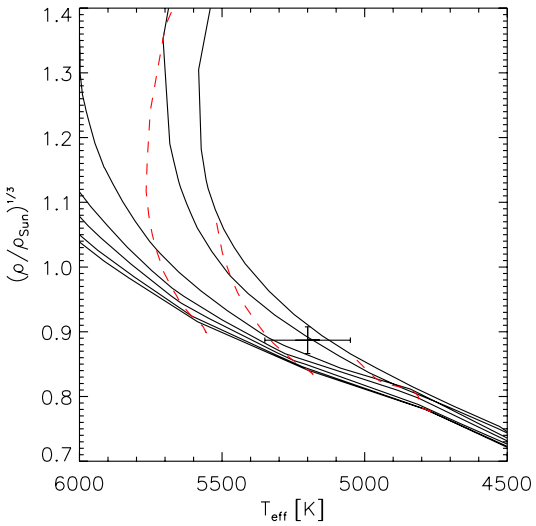

(a) Modified Hertzsprung-Russell diagram showing the location of WASP-42 together with isochrones for ages of (from bottom to top) 0.5, 1.0, 2.0, 3.0, 5.0, 10.0 and 13.0 Gyr. The red dashed lines indicate evolutionary paths for (from left to right) 1.0, 0.9 and 0.8 $M_{\odot}$. Isochrones and evolutionary paths have been interpolated from Marigo et al. (2008) using $z = 0.021$.

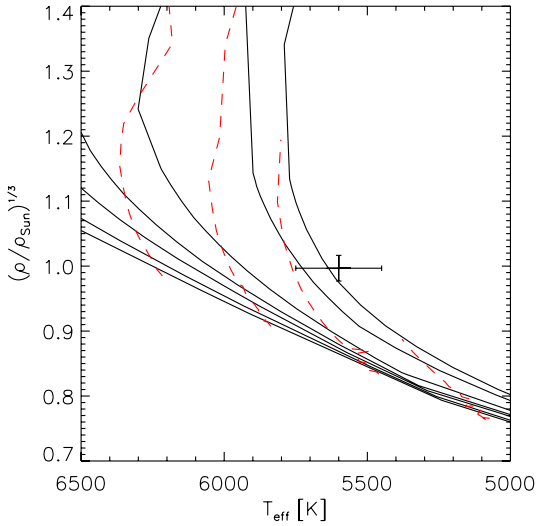

(b) Modified Hertzsprung-Russell diagram showing the location of WASP-49 together with isochrones for ages of (from bottom to top) 0.5, 1.0, 2.0, 3.0, 5.0, 10.0 and 13.0 Gyr. The red dashed lines indicate evolutionary paths for (from left to right) 1.1, 1.0, 0.9 and 0.8 $M_{\odot}$. Isochrones and evolutionary paths have been interpolated from Marigo et al. (2008) using $z = 0.011$.

Fig. 7. The locations of WASP-42 and WASP-49 in the modified Hertzsprung-Russell diagram.

4.1. WASP-42 b

WASP-42 b is a 0.5 M_J planet orbiting the K1 star 2MASS 12515557–4204249 every 5 days. The host-star metallicity is near the solar value.

Based on the $v \sin i_*$ and stellar radius of WASP-42, we deduce a maximal rotation period of $P = 16.1 \pm 3.2$ d. Using the Barnes (2007) relation, this gives an upper age limit of $\sim 0.84^{+0.51}_{-0.35}$ Gy from gyrochronology. We derived a second estimate based on the R'_{HK} activity indices (Noyes et al. 1984) from the HARPS spectra following the procedures of Lovis et al. (2011). We find $\log(R'_{HK}) = -4.9 \pm 0.7$, indicative of a rather quiet star. Using the Mamajek & Hillenbrand (2008) relation we derive a rotation period of $P = 40.1 \pm 4.7$ d and an age of 6.1 ± 1.2 Gy. We also interpolated the isochrones of Marigo et al. (2008) using $z = 0.021$ and compared them to the location of WASP-42 in the modified ($(\rho_*/\rho_\odot)^{1/3}$ vs. T_{eff}) Hertzsprung-Russell diagram (Fig. 7a). Here we used the temperature determined from the spectroscopic analysis together with the stellar density determined from the global analysis described in Sect. 3.2. It should be noted that in the analysis of the spectra a degeneracy exists between macroturbulence v_{mac} and stellar rotation $v \sin i_*$. As the value for v_{mac} is not directly measured but taken from tables, it might not be accurate for WASP-42. For example, a higher v_{mac} would produce a lower $v \sin i_*$, and thus a slower rotation and older gyrochronological age. Together with the absence of periodic brightness modulations (although we can not exclude non-periodic photometric variations of a few millimagnitudes), the evidence points towards an older age of several Gyrs for WASP-42.

The planet's position in the mass-radius diagram (see Fig. 8) is at the low-mass end of the Hot Jupiters. We used the tabulated radii of Fortney et al. (2007) in order to check whether the planetary radius is within predictions using the values for 0.1 AU = 875 K, and interpolating for a planetary mass of 0.5 M_J. Assuming the gyrochronologically determined age of 1 Gyr, we obtain a core mass of slightly above 10 $M_\oplus$, while using values for 4.5 Gyr would suggest a core mass close to 0 $M_\oplus$. Compared to other planets of similar mass, WASP-42 b is no outlier in terms of density, but with $\rho_p = 0.40 \pm 0.05\,\rho_J$ falls into the well-populated region between 0.25 ρ_J and 0.5 ρ_J. We also compared the planet's radius to the radius predicted from the

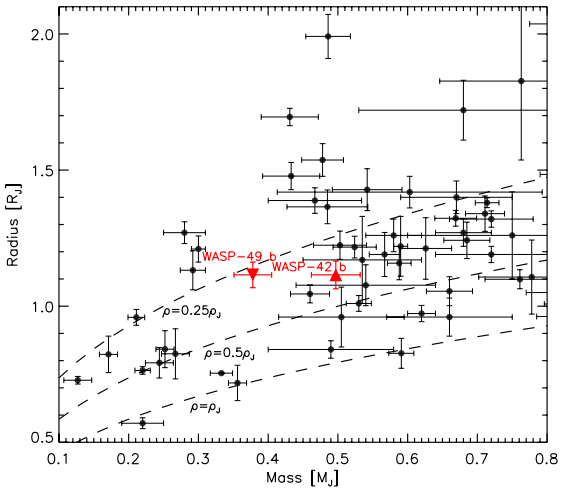

Fig. 8. Mass-radius diagram of transiting exoplanets. WASP-42 b and WASP-49 b are depicted using upward and downward facing triangles, respectively. The dotted lines represent curves of equal density at (from top to bottom) $\rho = 0.25\ \rho_J$, $\rho = 0.5\ \rho_J$ and $\rho = \rho_J$. The planet parameters were taken from `www.exoplanet.eu`.

Table 4. Eccentricities, χ^2 values and LS-test results of the eccentric and circular models for WASP-42 b found from all RV data and the datasets from the two instruments separately.

Dataset	e	$\chi^2_{\mathrm{red,\ e\neq0}}$	$\chi^2_{\mathrm{red,\ e=0}}$	LS test[a]
HARPS + CORALIE	$0.060^{+0.013}_{-0.011}$	0.82 ± 0.18	1.33 ± 0.22	0.010
HARPS + CORALIE (no RM sequence)	$0.061^{+0.014}_{-0.013}$	0.87 ± 0.23	1.53 ± 0.30	0.024
CORALIE	$0.068^{+0.029}_{-0.027}$	1.13 ± 0.34	1.33 ± 0.34	0.24
HARPS	$0.059^{+0.016}_{-0.013}$	0.90 ± 0.26	1.58 ± 0.33	0.005

Notes. [(a)] Probability of the circular model to be accurate, as defined by Lucy & Sweeney (1971).

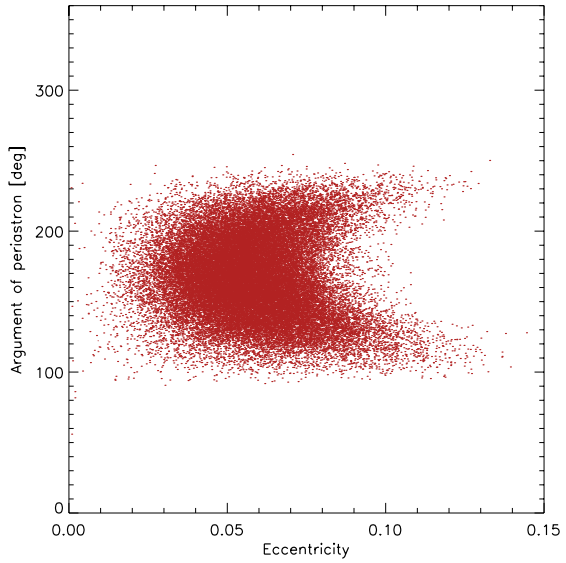

Fig. 9. The distribution of eccentricity and argument of periastron for WASP-42 b obtained from the global analysis while adding a jitter of 5 m s^{-1} to the HARPS and 15 m s^{-1} to the CORALIE data.

fits describing the Saturn-mass population presented in Enoch et al. (2012). Using Eq. (8) of Enoch et al. (2012) together with our uncertainties on stellar and planet parameters, we obtain a predicted radius of $1.31 \pm 0.03\ R_{\mathrm{J}}$, which is within the scatter around the model (Fig. 14 in Enoch et al. 2012).

Adopting an eccentric orbit for WASP-42 b allows for a small (0.060 ± 0.013) but non-zero eccentricity, while the argument of periastron is found to be $\omega = 167 \pm 26$ deg. We checked any dependence of the derived eccentricity on the jitter values assumed by re-running the analysis adding jitters of 3 m s^{-1} and 15 m s^{-1} quadratically to the CORALIE errors as well as a jitters of 5 m s^{-1} to the HARPS data. In all cases, the significance of the derived eccentricity remained above 3σ. To illustrate, the distribution of the argument of periastron and eccentricity found from the analysis including a jitter of 5 m s^{-1} for HARPS and 15 m s^{-1} for CORALIE is depicted in Fig. 9. In order to evaluate the robustness of this detection we computed the Bayes Factor (e.g. Carlin & Louis 2009) of the two models, resulting in a value of $B_{\mathrm{ec}} = 2440$. This is a very strong indication that the eccentric model is a better representation of the data. To provide a second evaluation we compared the reduced chi-squared values χ^2_{red} of the radial-velocity models, for datasets including all data (CORALIE and HARPS), as well as all data but leaving out the radial-velocity sequence obtained on April 4, 2011, and the HARPS or CORALIE data separately. For the latter cases we re-ran the MCMC analyses and found eccentricities compatible with the one derived from the complete dataset. We also used the prescription of Lucy & Sweeney (1971) (LS test) in order to test each of the above for the significance of the circular solution. The results are summarized in Table 4. In short, in all cases, the non-circular model gives a better fit to the data, and the values found for the eccentricity agree from all subsets. The LS test indicates a probability of 99.5% for the eccentric model to be required if the HARPS data are considered alone, and a 99% probability if the entire dataset is considered, both above the 5% limit suggested by Lucy & Sweeney (1971). The CORALIE data alone do not justify the eccentric model. Considering that there are only 10 HARPS points outside the consecutive time series, more data would be highly desirable in order to secure the detection. Based on these arguments, we conclude that there is considerable evidence for an eccentric orbit of WASP-42 b and we present the eccentric as well as the circular solution in Table 3.

The planet is located on the outer edge of the known Hot-Jupiter pileup, at a separation of 4.05 times the Roche limit, well above the 2 R_{RL} cutoff identified by Ford & Rasio (2006), below which planets are thought to be unable to attain that location by the circularization of previously eccentric orbits. This means WASP-42 b is compatible with the evolutionary scenario described by, for example, Matsumura et al. (2010): formation at farther orbital separations, scattering via planet-planet or Kozai interactions to an eccentric orbit, and subsequent tidal circularization.

4.2. WASP-49 b

WASP-49 b is a near Saturn-mass ($M = 0.38 \pm 0.03\ M_{\mathrm{J}}$) planet in a 2.8-day orbit around the G6 star 2MASS 06042146–1657550. In WASP-49, lack of lithium would suggest an age of several Gy (Sestito & Randich 2005) and the low $v \sin i_*$ implies a long rotation period of around 50 d. The gyrochronological relation of Barnes (2007) gives an age of $\sim 13^{+15}_{-8}$ Gy. Hence, we conclude that WASP-49 is a relatively old main-sequence star. We performed an isochrone analysis the same way as for WASP-42 with $z = 0.011$ (Fig. 7b), finding an age above 10 Gyr, in good agreement with the age found from gyrochronology.

In the period-mass plane WASP-49 b lies clearly below the bulk of Hot Jupiters and is nearly a twin of the well known HD 149026 b (Sato et al. 2005), a planet known for its high density. While the two planets have almost identical mass and period, they show very different radii and orbit two very different stars – while WASP-49 is remarkable for having one of the lowest metallicities known for planet host stars (-0.23 ± 0.07), HD 149026 is one of the most metal-rich planet hosts. In contrast to HD 149026 b, WASP-49 b has a low density ($0.27 \pm 0.03\ \rho_{\mathrm{J}}$). WASP-49 b fills a gap between 0.32 and 0.42 M_{J} in the

mass-radius plane (see Fig. 8), being the first low-density planet in this mass range. Using the tabulated values from Fortney et al. (2007) for system ages of 4.5 Gyr, an equilibrium temperature of 1300 K and interpolating for a planet mass of 0.38 M_J, we find a predicted maximal planet radius of 1.08 R_J (the case of a zero core mass). As with WASP-42 b, we employed Eq. (8) of Enoch et al. (2012) to obtain a predicted radius of $1.26 \pm 0.02\,R_J$. Again, this value is within the scatter around the fit (Fig. 14 in Enoch et al. 2012). We conclude that WASP-49 b, while larger than predicted from models, is not an outlier in the set of known planets.

There is no evidence for a non-zero eccentricity of WASP-49 b, and we determine a 3-σ upper limit of $e = 0.09$. WASP-49 b is separated from its host star by 2.4 times the Roche Limit, a rather low value which, together with the planet's old age, might indicate that orbital decay has occurred since the arrival of the planet at short orbital distances.

To summarize, WASP-42 b and WASP-49 b are two newly discovered close-in transiting planets with masses in the range 1–2 times that of Saturn. While WASP-49 b is old, inflated and orbiting close to a metal-poor G6 star, WASP-42 b is orbiting a cooler K1 star at the outer edge of the well-known planet pile-up, probably on a slightly eccentric orbit.

Acknowledgements. WASP-South is hosted by the South African Astronomical Observatory and we are grateful for their ongoing support and assistance. Funding for WASP comes from consortium universities and from the UK's Science and Technology Facilities Council. TRAPPIST is funded by the Belgian Fund for Scientific Research (Fond National de la Recherche Scientifique, FNRS) under the grant FRFC 2.5.594.09.F, with the participation of the Swiss National Science Fundation (SNF). M. Gillon and E. Jehin are FNRS Research Associates. We would also like to thank the Geneva Stellar Variability group, particularly Richard I. Anderson, for continuing flexible and short-notice time exchanges on the Euler-Swiss telescope and carefully conducted observations.

References

Anderson, D. R., Hellier, C., Gillon, M., et al. 2010, ApJ, 709, 159
Anderson, D. R., Smith, A. M. S., Lanotte, A. A., et al. 2011, MNRAS, 416, 2108
Bakos, G., Noyes, R. W., Kovács, G., et al. 2004, PASP, 116, 266
Baranne, A., Queloz, D., Mayor, M., et al. 1996, A&AS, 119, 373
Barnes, S. A. 2007, ApJ, 669, 1167
Batygin, K., & Stevenson, D. J. 2010, ApJ, 714, L238
Bertin, E. 2006, in Astronomical Data Analysis Software and Systems XV, eds. C. Gabriel, C. Arviset, D. Ponz, & S. Enrique, ASP Conf. Ser., 351, 112
Bertin, E., & Arnouts, S. 1996, A&AS, 117, 393
Bodenheimer, P., Lin, D. N. C., & Mardling, R. A. 2001, ApJ, 548, 466
Burrows, A., Hubeny, I., Budaj, J., & Hubbard, W. B. 2007, ApJ, 661, 502
Carlin, B., & Louis, T. 2009, Bayesian methods for data analysis, Texts in statistical science (CRC Press)
Chabrier, G., & Baraffe, I. 2007, ApJ, 661, L81
Claret, A., & Bloemen, S. 2011, A&A, 529, A75
Collier Cameron, A., Pollacco, D., Street, R. A., et al. 2006, MNRAS, 373, 799
Collier Cameron, A., Wilson, D. M., West, R. G., et al. 2007, MNRAS, 380, 1230
Demory, B.-O., & Seager, S. 2011, ApJS, 197, 12
Eggleton, P. P., & Kiseleva-Eggleton, L. 2001, ApJ, 562, 1012
Enoch, B., Collier Cameron, A., Parley, N. R., & Hebb, L. 2010, A&A, 516, A33
Enoch, B., Cameron, A. C., Anderson, D. R., et al. 2011, MNRAS, 410, 1631
Enoch, B., Collier Cameron, A., & Horne, K. 2012, A&A, 540, A99
Fabrycky, D., & Tremaine, S. 2007, ApJ, 669, 1298
Faedi, F., Barros, S. C. C., Anderson, D. R., et al. 2011, A&A, 531, A40
Ford, E. B., & Rasio, F. A. 2006, ApJ, 638, L45
Fortney, J. J., Marley, M. S., & Barnes, J. W. 2007, ApJ, 659, 1661
Fortney, J. J., Demory, B.-O., Désert, J.-M., et al. 2011, ApJS, 197, 9
Gelman, A., & Rubin, D. 1992, Statist. Sci., 7, 457
Gillon, M., Smalley, B., Hebb, L., et al. 2009, A&A, 496, 259
Gillon, M., Lanotte, A. A., Barman, T., et al. 2010, A&A, 511, A3
Gillon, M., Jehin, E., Magain, P., et al. 2011, Detection and Dynamics of Transiting Exoplanets, St. Michel l'Observatoire, France, eds. F. Bouchy, R. Díaz, & C. Moutou, EpJ Web Conf., 11, 6002
Gillon, M., Triaud, A. H. M. J., Fortney, J. J., et al. 2012, A&A, 542, A4
Giménez, A. 2006, ApJ, 650, 408
Goldreich, P., & Tremaine, S. 1980, ApJ, 241, 425
Gray, D. F. 2008, The Observation and Analysis of Stellar Photospheres
Hartman, J. D., Bakos, G. Á., Torres, G., et al. 2011, ApJ, 742, 59
Hébrard, G., Bouchy, F., Pont, F., et al. 2008, A&A, 488, 763
Holman, M. J., Winn, J. N., Latham, D. W., et al. 2006, ApJ, 652, 1715
Jehin, E., Gillon, M., Queloz, D., et al. 2011, The Messenger, 145, 2
Kozai, Y. 1962, AJ, 67, 591
Laughlin, G., Crismani, M., & Adams, F. C. 2011, ApJ, 729, L7
Lin, D. N. C., Bodenheimer, P., & Richardson, D. C. 1996, Nature, 380, 606
Lovis, C., Dumusque, X., Santos, N. C., et al. 2011 [arXiv:1107.5325]
Lucy, L. B., & Sweeney, M. A. 1971, AJ, 76, 544
Magain, P. 1984, A&A, 134, 189
Mamajek, E. E., & Hillenbrand, L. A. 2008, ApJ, 687, 1264
Mandel, K., & Agol, E. 2002, ApJ, 580, L171
Marigo, P., Girardi, L., Bressan, A., et al. 2008, A&A, 482, 883
Matsumura, S., Peale, S. J., & Rasio, F. A. 2010, ApJ, 725, 1995
Maxted, P. F. L., Anderson, D. R., Collier Cameron, A., et al. 2011, PASP, 123, 547
Mayor, M., & Queloz, D. 1995, Nature, 378, 355
Mayor, M., Pepe, F., Queloz, D., et al. 2003, The Messenger, 114, 20
McLaughlin, D. B. 1924, ApJ, 60, 22
Noyes, R. W., Hartmann, L. W., Baliunas, S. L., Duncan, D. K., & Vaughan, A. H. 1984, ApJ, 279, 763
Pollacco, D. L., Skillen, I., Collier Cameron, A., et al. 2006, PASP, 118, 1407
Pont, F., Zucker, S., & Queloz, D. 2006, MNRAS, 373, 231
Queloz, D., Henry, G. W., Sivan, J. P., et al. 2001, A&A, 379, 279
Rasio, F. A., & Ford, E. B. 1996, Science, 274, 954
Rossiter, R. A. 1924, ApJ, 60, 15
Sato, B., Fischer, D. A., Henry, G. W., et al. 2005, ApJ, 633, 465
Schwarz. 1978, Ann. Stat., 6, 461
Seager, S., & Mallén-Ornelas, G. 2003, ApJ, 585, 1038
Sestito, P., & Randich, S. 2005, A&A, 442, 615
Showman, A. P., & Guillot, T. 2002, A&A, 385, 166
Torres, G., Andersen, J., & Giménez, A. 2010, A&ARv, 18, 67
Triaud, A. H. M. J., Collier Cameron, A., Queloz, D., et al. 2010, A&A, 524, A25
Winn, J. N., Holman, M. J., Torres, G., et al. 2008, ApJ, 683, 1076
Winn, J. N., Johnson, J. A., Howard, A. W., et al. 2010, ApJ, 723, L223
Wu, Y., & Murray, N. 2003, ApJ, 589, 605
Wu, Y., Murray, N. W., & Ramsahai, J. M. 2007, ApJ, 670, 820

4.6 Other Planets

During my participation in the last four years, the WASP survey has been very productive. Among the highlights of the last four years have been:

- WASP-43 b: A massive ($M_P = 2.03M_J$) Jupiter-size planet ($R_P = 1.04R_J$) orbiting an active main-sequence K7 dwarf every 0.81 days (Hellier et al. 2011a). Owing the favorable planet/star size ratios the system is ideal for follow-up observations.
- WASP-49 b: A hot Saturn-mass planet with a low density (Lendl et al. 2012). This object is described in detail in Section 4.5.
- WASP-70 b and WASP-77b: These are planets in close binaries (Anderson et al. 2013a, Maxted et al. 2013)
- WASP-79 b: One of the largest ($M_P = 1.16M_J$, $R_P \geq 1.7R_J$) planets yet discovered, orbiting a F5 star (Smalley et al. 2012).
- WASP-80 b: A ($M_P = 0.55M_J$, $R_P = 0.95R_J$) planet in a 3.07-day orbit around a late K7 dwarf. This target is one of the coolest systems that can be efficiently characterized (Triaud et al. 2013).
- WASP-103 b: This $M_P = 1.22M_J$, $R_P = 1.53R_J$ planet is orbiting a F8 host star with an orbital period of only 22.2 hours (Gillon et al. 2014). It is one of the most irradiated planets known to date and its large predicted occultation signature makes it a prime target for emission spectroscopy.

I had the pleasure of contributing to many other planet discoveries by providing transit lightcurves from EulerCam. The observing methods and data analysis are essentially the same as I described them for the WASP-42 b and WASP-49 b discoveries. For more details on these discoveries the interested reader is referred to the individual publications (see Appendix A) that I prefer not to reproduce in their full length in this work. However, to give an idea of the sheer immense success of WASP, the first pages of these discovery papers are shown in Appendix B.

4.7 Other Projects

Lightcurves from EulerCam have also entered in several other follow-up projects. Several lightcurves have been observed simultaneously (or spaced only by a few orbits) with EulerCam and HARPS to measure spin-orbit alignments. Such was the case for the well-aligned WASP-22 system, (Anderson et al. 2011), and for WASP-32 (Brown et al. 2012), a system also having a low obliquity.

Lightcurves were also added to photometric follow-up observations of WASP-43 b helping in the characterization of this benchmark system (Gillon et al. 2012). Albeit not a WASP discovery, EulerCam had a part in the identification of transits of the hot Uranus GJ3470 (Bonfils et al. 2012).

Mental fight means thinking against the current, not with it. It is our business to puncture gas bags and discover the seeds of truth.

Virginia Woolf

5 High Precision Photometry

5.1 Motivation

A great part of the information obtainable about the planet-star system hinge on the ability to measure photometric lightcurves with a high precision from the ground.

In this context, very little interest lies in obtaining absolute photometry, since the effects we measure manifest themselves as relative effects in observed brightness variations of the combined flux of planet and star. The most prominent features, transit and occultation, have durations of a few hours, depending on the sizes of star and planet, the orbital inclination and the size of the star. For the hot close-in planets orbiting main sequence or slightly evolved stars that are the subject of most recent studies, the events rarely take longer than 4 hours. About two hours of observation need to be added to the eclipse duration, as we need a good measurement of both, the in-eclipse flux and the out-of-eclipse flux to calculate a precise eclipse depth. This means that a total of $\lesssim 6$ hours are needed for a typical eclipse observation. As a consequence, transits and occultations can be observed easily as one continuous sequence within a single night. The advantages of this situation are clear: no long-term stability of reference stars needs to be assured, and parameters such exposure time, telescope defocus and readout mode can be adapted to their optimal combination for the conditions of each single night.

In this chapter I will treat the different sources of photometric noise, and evaluate how they can be combated either by adapting observing strategies or data analysis procedures. I will then present the extensive follow-up campaign performed on the ultra-short period planet WASP-19 b.

5.2 Noise in Time-Series Photometry

There are several sources of noise affecting relative lightcurves. The most prominent effect stems from the Earth's atmosphere that leaves its traces in whatever observation we undertake from the ground. Much can be gained by choosing the best possible observing sites, as the effects are strongly dependent on the stability and dryness of the atmospheric layers above the telescope. The two sites used for data presented in this thesis are La Silla and Paranal, both located at altitudes of approx. 2400 m at very dry locations in the Atacama desert.

When discussing noise in photometric data, it is useful to differentiate between correlated "*red*" and uncorrelated "*white*" noise.

5.2.1 White Noise

White noise affects each point individually, i.e. the offset of a certain point N does not depend on the offset of the points $(N - i)$ observed in a short time interval t_i before or after. As the offset of each point is random (given a respective probability distribution, ideally a Gaussian), this noise contribution can be reduced by e.g. phase-folding a large number of transits and binning them to a common time interval. If the real white noise in the data, evaluated from the standard deviation of the residuals $\sigma_{w,mes}$, is higher than the the predicted photometric error including the factors described below, σ_w,

one may define a scaling factor

$$\beta_w = \frac{\sigma_{w,mes}}{\sigma_w}. \tag{5.1}$$

5.2.2 Red Noise

Red noise is noise that adds structure to the photometric time series, and in order to obtain precise transit parameters, it needs to bee included in the error estimation (Pont et al. 2006). The effects can have a range of timescales, from slow modulation due to stellar variability or differential airmass effects, to timescales of a few minutes related to telescope and detector performances. A good measurement for the red noise can be obtained by comparing the standard deviation of the residuals of the entire dataset to the standard deviation of the residuals binned into bins of several minutes. The bins size chosen should reflect a characteristic red noise timescale (Gillon et al. 2006). With σ_1 as the standard deviation of the entire dataset, one would expect the standard deviation of the binned residuals to be

$$\sigma_{N,ideal} = \frac{\sigma_1}{\sqrt{N}}\sqrt{\frac{M}{M-1}}, \tag{5.2}$$

where N is the number of bins and M is the number of points per bin (Winn et al. 2008, Gillon et al. 2010). Consequently one may define a factor β_r which is simply the factor by which the measured standard deviations of the binned residuals σ_N are larger than the theoretical ones

$$\beta_r = \frac{\sigma_N}{\sigma_{N,ideal}}. \tag{5.3}$$

This factor can vary depending on the choice of time bin, therefore several bin sizes should be tested and the maximum β_r found adopted as the adequate value. The effects of red and white noise on lightcurves are illustrated in Figure 5.1 , where I show the individual noise components for an artificially created example.

5.2.3 Noise Sources

Photon Noise

The most prominent source of noise is *photon noise*, intrinsic to any observation. Photon noise is shot noise stemming from the quantization of photons registered by the CCD detector. The shot noise for a measurement of N events (e.g. N registered photons on the detector) is simply expressed as

$$\sigma_p = \sqrt{N}. \tag{5.4}$$

Thus for increasing counts the S/N ratio of the observations increases with $\sqrt{N}$. As a consequence, photon noise is a limitation for faint objects, or if the light of bright objects is strongly dispersed in wavelength. For the transit targets usually observed with EulerCam, photon noise is in the range of several 10^2 ppm, depending on target brightness, instrument defocus and cadence. As an example, for the observation of WASP-101 shown in Figure 3.13 , the mean photon noise is 207 ppm.

Detector Noise

Every detector is affected by the noise introduced by the CCD and readout components. Two noise sources are prominent here. First *readout noise* is incurred during the transformation of the registered photons in each pixel to the final count values on the image. Readout noise makes a very small contribution to the overall noise budget, with typical values around $RON_{\rm pix} = 5e^-$ per pixel. Using $N_{\rm pix}$ as the number of co-added pixels, it is calculated as

$$\sigma_{\rm RON} = \sqrt{N_{\rm pix}}RON_{\rm pix}. \tag{5.5}$$

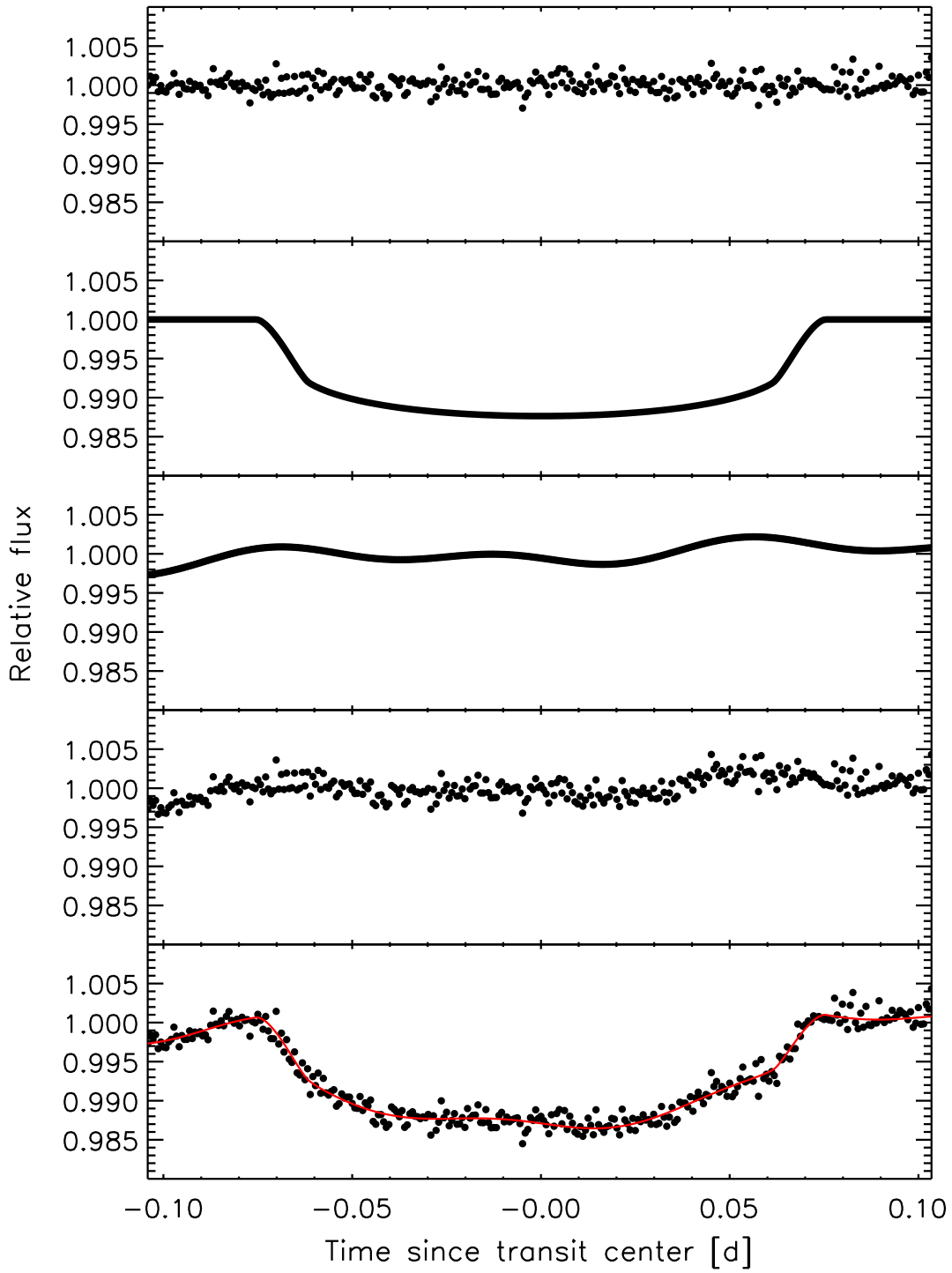

Figure 5.1 : An artificial data set to illustrate the contributions of white and red noise to the final lightcurves. The data were created with a cadence of 60s, and a Gaussian white noise amplitude of 1000 ppm. For the red noise, an arbitrary combination of polynomials and trigonometric functions was adopted. The transit shape is that of a hypothetical planet with a star/planet radius ratio of 0.1, a period of 3 days, and an inclination of 90°. The limb-darkening is that of a G6 V star, observed in r'-band. The panels represent (from top to bottom): white noise only, transit shape only, red noise only, red and white noise, and finally the lightcurve containing the combined effects of white noise and red noise on top of the transit shape.

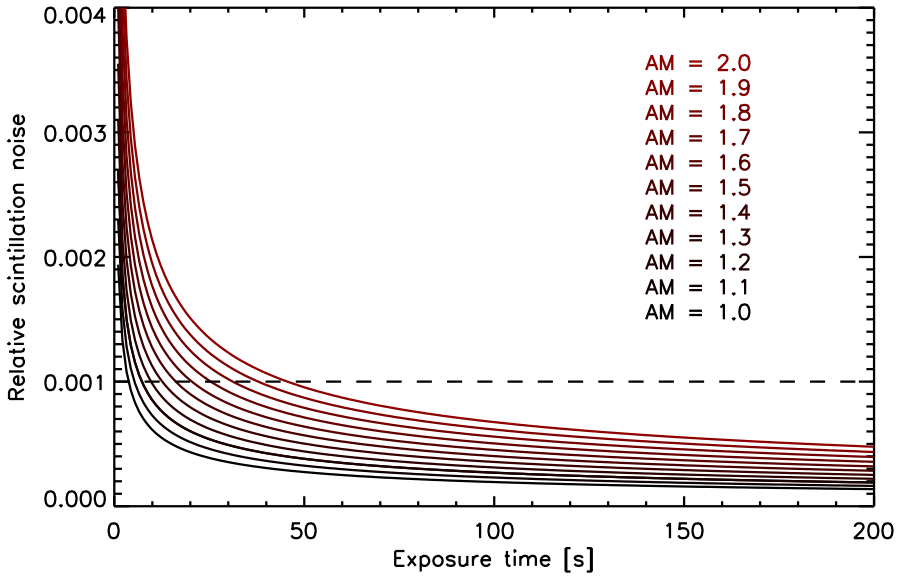

Figure 5.2 : The contribution in relative flux error ($\sigma_{\rm sci}/F_*$) of the scintillation noise to the EulerCam noise budget, calculated for airmass values between 1 and 2 (from bottom to top). As can be seen from Equation 5.6, the magnitude of the effect depends on exposure time and airmass for any given instrument. The dashed line indicates a scintillation effect of 0.001 in relative flux.

Readout noise is very small for most modern CCDs such as EulerCam. As an example, for the observation of WASP-101 shown in Figure 3.13 , the mean readout noise affecting the target photometry is 14 ppm.

Second, the *dark current* is caused by the thermally generated electrons in the CCD, which are then processed just as electrons created by the incident photons. The reader is referred to Chapter 3 for a more detailed description of these noise sources and their presence in EulerCam data. In terms of data analysis, it suffices to state here that the dark current is negligible for most optical light detectors.

Atmospheric Noise

As the light passes through the atmosphere a large fraction of the final error budget is added. The atmosphere is temporally variable introducing flux drops, and changes in the size of the stellar point spread functions. For the moment, let us assume that the atmospheric conditions are stable throughout the observation. Still, two noise factors will affect our observations. First, the *Scintillation Noise* is caused by variations of the refractive index along the light path through the atmosphere. These variations distort the wavefront of the stellar light and cause variations in the flux observed through a telescope of aperture D on the ground. Using the airmass AM, the target flux F_*, the height of the observatory in meters h, and the exposure time $t_{\rm exp}$, the following expression allows to calculate its impact on the noise budget (Young 1967, 1993):

$$\sigma_{\rm sci} = F_* \, 0.09 \, D^{-2/3} \, AM^{1.8} \, e^{-h/8000} \frac{1}{\sqrt{2 t_{\rm exp}}} . \tag{5.6}$$

Scintillation is a non-negligible noise source for photometric observations, in particular at high airmass. The effect as calculated for the Euler telescope is illustrated in Figure 5.2 . As an example, at airmass 1.5 and exposure times of 60 s, scintillation contributes ∼520 ppm to the error budget. For the observation shown in Figure 3.13 , the scintillation contribution (with a mean value of 430 ppm) exceeded the photon noise.

Sky Noise is caused by the non-zero brightness of the sky, which the target signal is added on. Given the presence of the moon and the observed wavelength of observation, the sky noise can range from being nearly negligible to being a serious nuisance. To estimate its impact on the photometry, we simply treat it as extra photon noise stemming from the average sky flux $F_{\rm sky}$ in each pixel:

$$\sigma_{\rm sky} = \sqrt{N_{\rm pix} F_{\rm sky}} . \tag{5.7}$$

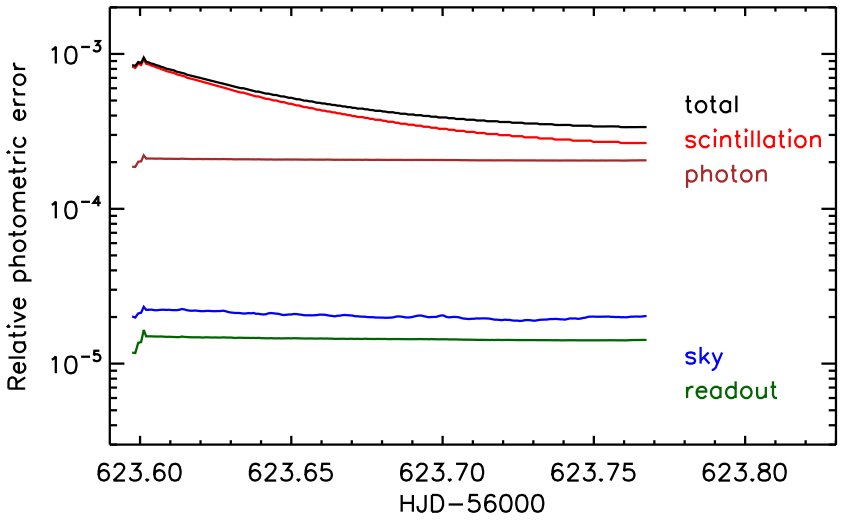

Figure 5.3 : The white noise contributions for a typical EulerCam observation, a transit of WASP-101 b on 26 November 2013 (the same data as Figure 3.13). The noise given is that calculated for the target alone. Scintillation and photon noise dominate over sky and readout noise.

Thus, the overall sky noise depends both on the sky brightness and the PSF size. As an example, for the observations shown in Figure 3.13 , the noise contribution from the sky background is 20 ppm. These observations were obtained with a PSF having a FWHM of ∼18 pixels while the moon was 36% illuminated and low in the sky.

Error Combination and Adaptation

The above noise sources make up the photometric noise estimate for each measurement, and they are added in quadrature for the final value:

$$\sigma_w = \sqrt{\sigma_p^2 + \sigma_{\rm RON}^2 + \sigma_{\rm sci}^2 + \sigma_{\rm sky}^2}\,. \tag{5.8}$$

The two dominant components are usually photon and scintillation noise, as is illustrated in Figure 5.3 for a typical EulerCam observation.

Several other factors can introduce scatter in the photometric lightcurves, and I describe the most common effects below. Using the ratio of the observed white noise to the predicted white noise β_w (see Equation 5.1), and the amplitude of the red noise β_r (see Equation 5.3), one may derive an error correction factor

$$CF = \beta_w \times \beta_r\,, \tag{5.9}$$

by which all error bars need to be scaled up to warrant accurate error bars on the derived parameters.

Flat Field

Flat field imperfections can have a very deteriorating effect on the quality of the photometric lightcurves, as they affect each area on the detector differently, and can not be removed by differential photometry. The typical flat field is composed of several components; smooth illumination gradients across the field, shadowing from dust grains located on the filters or other surfaces in the optical path, transmission inhomogeneities of components in the optical path, small grains located on the detector itself, and finally sensitivity variations of the CCD pixels. The correction of these effects can be achieved with varying efficiency. An important aspect is the temporal stability of these features throughout the night required for the correction via flat field frames. The standard procedure of removing flat field effects is described in Section 3.3.1.

Stellar FWHM Variations

The seeing, together with the telescope defocus determine the size of the stellar PSF on the detector, and consequently also the peak flux at the center of the PSF. As usually the defocus is not changed during an observation, the major part of the PSF variability is introduced by changes in the weather conditions and outside the observer's control. A secondary impact can come from the telescopes, which are usually equipped with an "autofocus" procedure that slightly adapts the position of the secondary mirror to compensate for temperature dependencies of the focus. A defect autofocus, or a defect temperature sensor can lead to undesired focus drifts during the observations.

The impact of seeing variations on the final photometry comes through several secondary effects. For crowded fields, seeing changes lead to variable contamination from faint sources. For single stars, variable seeing can lead to flux losses at the edge of the photometric aperture, or larger-than-necessary sky noise for episodes of small seeing. This can be partially compensated by using a variable aperture width. For the sky calculation, faint stars may be clipped for images of good seeing but remain undetected and thus contaminate the measurements for bad seeing. The most prominent effect of variable seeing however is that some stars can enter the non-linear regime of the detector and even saturate if the seeing decreases drastically.

Guiding

Closely connected to the effects of flat field variations is the efficiency of the telescope guiding. If there are drifts of more than a few stellar FWHMs in the telescope guiding, the stars move across an uneven flat field, perhaps even across bad pixels or detector defects. Generally a well-working guiding or tracking keeps the stars at the same position, with some variations of $\lesssim 1$ stellar FWHM. In that case, the effects can be kept small by good positioning the stars of interest on the detector.

Detector Effects

The most prominent detector effects, non-linearity at high counts and CCD defects have already been mentioned above as they are closely connected to weather dependent flux variations and guiding precision. An effect not yet discussed is the shutter. For EulerCam, the shutter has a non-negligible opening and closing time, and imprints its pattern on images with short exposure times. The pattern can be isolated from dedicated sequences, and removed from the images.

Differential Extinction

As eclipse observations span several hours and have clear timing constraints, one often is required to observe to relatively high airmass (AM$\sim$2). As the extinction of stellar light in the atmosphere is a color-dependent effect, differential extinction can introduce trends in relative lightcurves if the target and reference stars have different spectral types.

Stellar Effects

Next to all instrumental noise, also the stars themselves contribute to the total photometric noise. First, if no bright reference stars are available, the precision will be limited by the reference stars' photon noise. Then, reference stars variable on timescales similar or smaller than the transit (e.g. δ Scuti stars, Fath 1935) heavily impact the relative photometry.

Many exoplanet host stars are known to be active (e.g. WASP-19, Hebb et al. 2010, Abe et al. 2013), and the transits are overlaid on the stellar rotation curve. However, rotation periods are in the order of several days, and thus the impact of the transit lightcurve is small. A clear photometric signal is produced if planets pass across star spots during transit, leading to a short increase in brightness. This is illustrated in Figure 5.4 for the case of HAT-P-11 as observed by Kepler (Sanchis-Ojeda & Winn 2011).

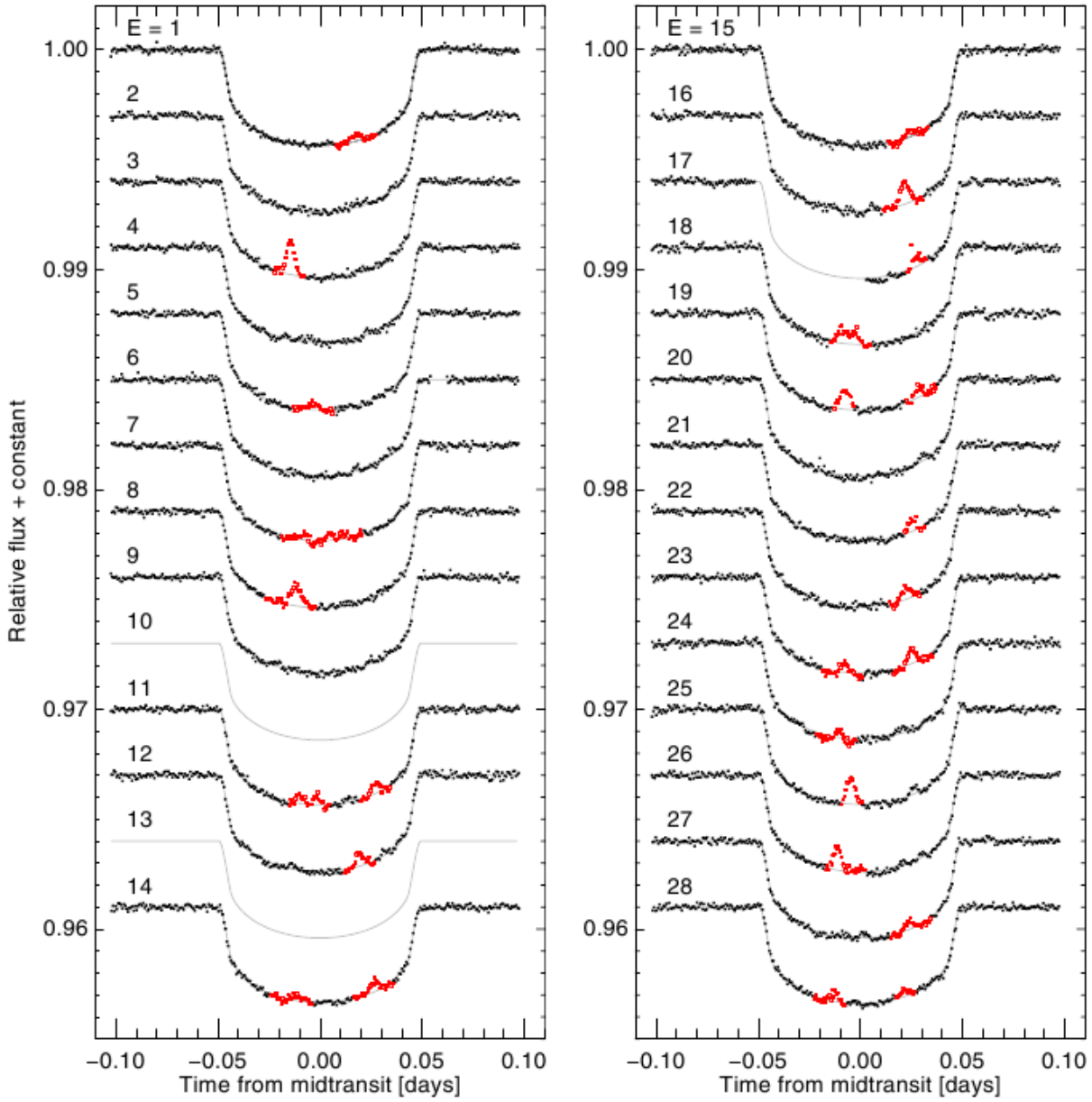

Figure 5.4 : 28 separate transits of HAT-P-11b are shown, observed by Kepler. The transit lightcurves are not smooth but show short brightness increases caused by star spots (marked in red). Figure credit: Sanchis-Ojeda & Winn (2011).

5.2.4 Observing Tricks and Data Analysis Procedures

To limit the impact of these noise sources, a number of approaches are used during observation and data reduction.

Observations

First, one should optimize the duty cycle to maximize the photons obtained from the star. This can be done by using faster readout modes (in case of EulerCam, readout through 4 amplifiers), or windowing the detector. If the target is too bright and thus exposure times would be short compared to the readout times, defocusing widens the PSF and decreases the maximum flux. Small-scale flat field inhomogeneities are also averaged out across a larger PSF. However, the best means to limit the effects

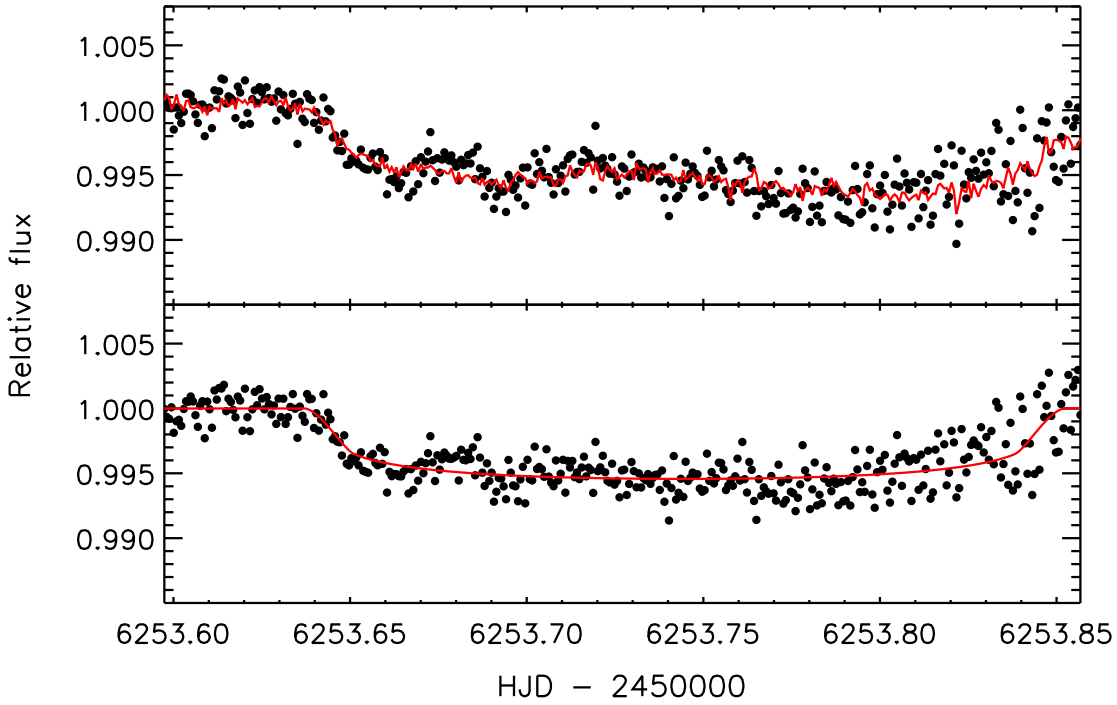

Figure 5.5 : An EulerCam lightcurve of WASP-99 (Hellier et al. 2013), heavily affected by red noise. The upper panel shows the raw data together with the transit and noise model including second order polynomials with respect to time and stellar FWHM. The lower panel shows the lightcurve corrected for the noise model together with the transit model.

of flat field imperfections, especially if there are structures that move across the field of view during the night, is simply to keep the optical components as clean as possible. For EulerCam, this means that the entrance window to the detector needs to be cleaned at least every 4 months. On top of that, a precise guiding greatly decreases the effect of flat field systematics on light curves. Seeing variations can not be avoided, but their impact on the photometry can be limited by choosing an exposure time that allows for the conditions to improve without causing the target to exceed the linear range of the detector.

Data Analysis

Once some data affected by correlated noise has been recorded, one can try to model the systematics. As they are usually overlaid on either a transit or an occultation curve, the best way to do this is to perform a simultaneous fit to the astrophysical and instrumental effects. Neglecting to do so, and instead assuming a fixed instrumental model will lead to underestimated error bars, unless the model is previously known to a very high precision. In the analyses presented in this thesis, I have made use of a Markov chain Monte Carlo approach as implemented in the routines by Gillon et al. (2010, 2012). At the start of a chain, the user can select a model to be applied to the data, a wide variety of combinations of variables are possible, but usually a good result is obtained by using time, FWHM, Sky, coordinate shifts, or any other external parameter one suspects to be correlated with the data red noise. The model parameters are not MCMC jump parameters but are calculated at each step via minimization of the residuals. Finally care must be taken not to over-fit the data with complicated photometric baseline models. The Bayesian Information Criterion (BIC, e.g. Schwarz 1978) can be a great help to decide which model to adopt. An example of a lightcurve with a large correlated noise that can be modeled is shown in Figure 5.5 . On occasions of large FWHM variability, I also found that the overall precision of the photometry can be improved by using a variable aperture size for the extraction of the photometry.

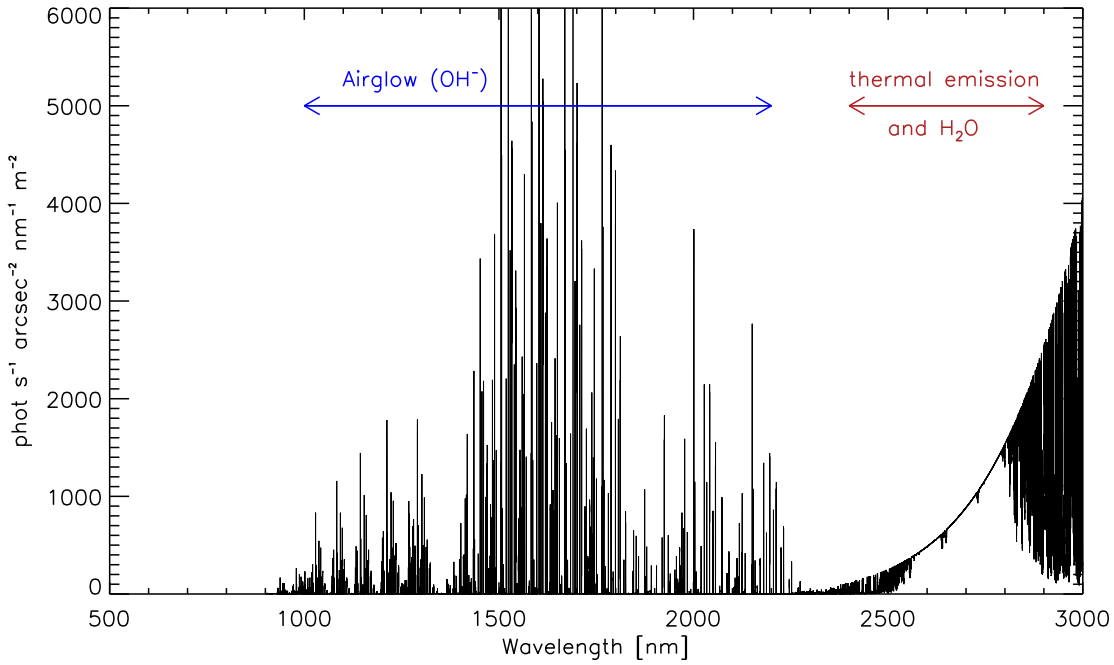

Figure 5.6 : The sky emission spectrum observed from Manua Kea (data from `http://www.gemini.edu/?q=node/10787`). The main component at wavelengths between 1 μm and 2.4 μm is "airglow": emission from OH^- that was exited during the day. Beyond 2.4 μm, thermal emission and water dominate the spectrum.

5.2.5 Near-IR

In the near IR the situation is somewhat more difficult as the incoming photons have energies below the band gap in the Si crystal. Thus, elements with lower band gaps must be used to absorb IR photons. The most widely used IR detectors operating at wavelengths up to ~10 μm consist of Indium and Antimony (InSb), or Mercury, Cadmium and Tellurium ($Hg_{1-x}Cd_xTe$). For the latter the ratio of Hg and Cd (denoted by the parameter x) can be varied tuning the detecter response range. For detectors operating between 10 and 300 μm, the charge carriers are not freed from elements in the semiconductor crystal, but stem from interactions of the photons with the impurity atoms the semiconductor is doped with. As the level of impurity can not be arbitrarily increased, quantum efficiency is an issue for these detectors.

The detectors need to be cooled down to suppress thermal dark current, as well as additional noise caused by the Brownian motion of the charge carriers (Johnson 1928). The longer the desired wavelength, the cooler the system must be. Instruments such as HAWK-I operating in the near IR temperatures operate at temperatures of $\lesssim$ 100 K, while the *Spitzer* space telescope observed out to 120 μm and thus needed to be cooled to 3 K.

At low temperatures the buried channel technology used in CCD readout does not operate. Thus a different readout mechanism involving MOSFETSs (metal–oxide–semiconductor field-effect transistors) has been developed. This technology uses transistors to measure the charge collected at any given pixel in a non-destructive way. The signal of each pixel can be individually read or reset. The manufacturing of these components, as well as the detector components is a complex process, and thus the price range of IR detectors is well above that of optical-light CCDs. For more details on IR detectors, the interested reader is referred to Rieke (2007) and references therein.

Overall, IR detectors have higher noise levels, and more defects than their optical counterparts.

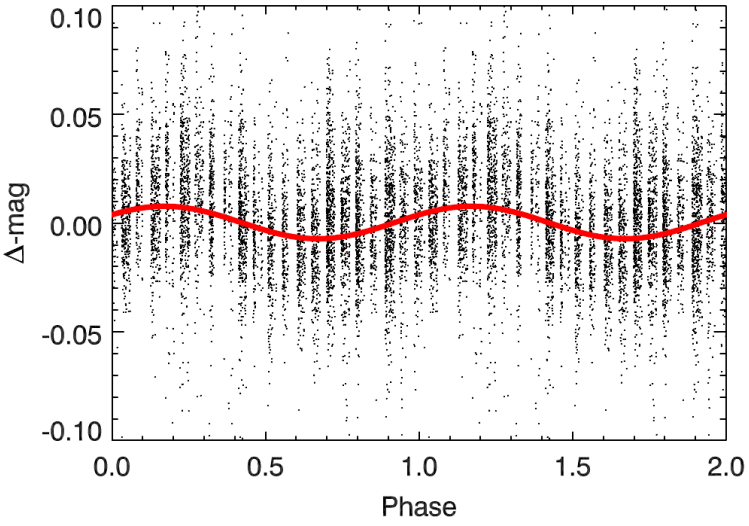

Figure 5.7 : The rotational modulation observed in the initial WASP photometry (Hebb et al. 2010), indicative of the high activity level of WASP-19. Figure credit: Hebb et al. (2010)

Thus it can be a great asset to carefully choose the positioning of the targets on the detector to make sure they do not fall on any defects.

Non-linearity is a crucial issue for IR detectors, and overexposed pixels are known to show persistence effects (e.g. Carraro 2013). The best remedy here is to keep exposure times short, and count levels below or around 10^4 ADU.

In the IR *dark current* is no longer negligible, even though the detectors are cooled down to $T < 100\ K$ (80 K for HAWK-I). To account for the dark current it is necessary to obtain dark frames, i.e. images with a closed shutter and non-zero exposure time (preferably the same as used for the science observations). The darks are then subtracted from the images as usually the bias frames would be.

On top of that, the *sky background* becomes a critical element. Below 2.4 μm the sky is dominated by a dense forest of emission lines of mainly Hydroxyl (OH^-) with smaller components of molecular Oxygen O_2 and water. Beyond the K-band, the sky background is dominated by the thermal emission of the atmosphere together with water signatures. These effects are illustrated in Figure 5.6 . The IR sky is highly variable, both spatially (typical scale 1 arcmin), and temporally (typical scale 10 minutes).

Although the standard procedure to compensate for the variable IR sky is to dither the observations, this is not as critical for relative time-series photometry which does not require a good sky determination across the whole image, but rather a precise measurement of the momentary sky next to target and reference stars. Consequently time-series observation are usually carried out in *staring* mode without dithering.

5.3 WASP-19 b

On the following pages I will introduce WASP-19 b, one of the planets I followed most closely during my PhD. WASP-19 is also one of the best studied planetary systems in existence, owing to its observationally very favorable properties. I obtained a large amount of photometric observations of this target, which were published in Lendl et al. (2013), included here in Section 5.3.3.

5.3.1 The WASP-19 System

As WASP-19 b was discovered by the WASP Survey (Hebb et al. 2010) it was immediately clear this new planet would prompt a wealth of follow-up observations. The planet is orbiting a main-sequence G8 star with an orbital period of 0.79 d, making it one of the shortest-period planets known to date. The host star is highly active, with a 10.5 d photometric modulation seen in the discovery WASP photometry

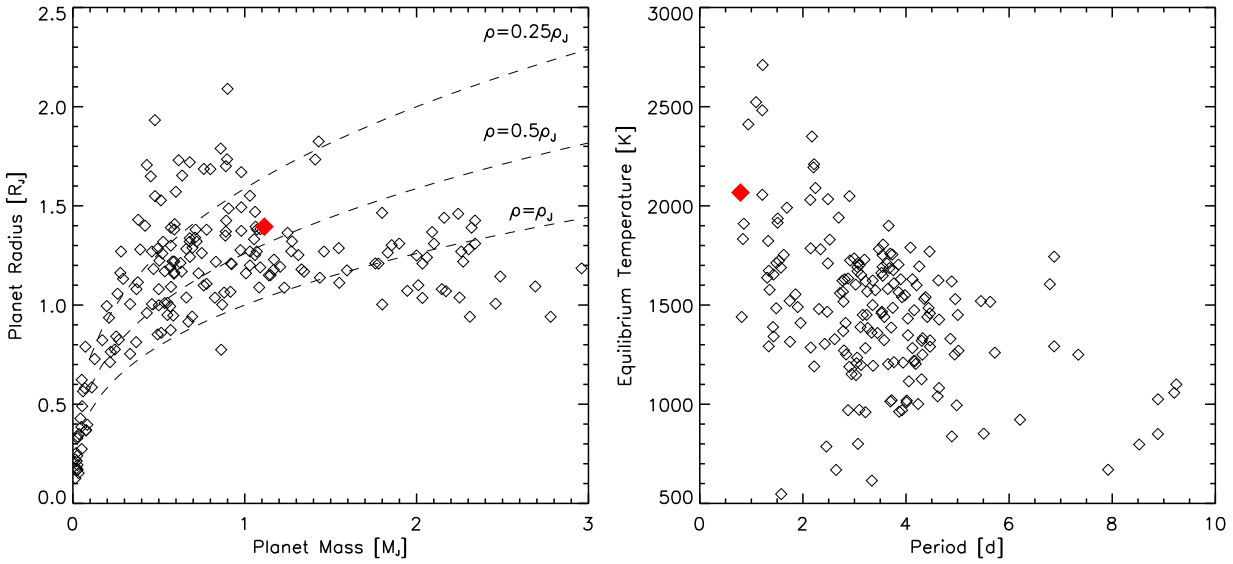

Figure 5.8 : WASP-19 b compared to other hot close-in planets. *Left panel:* The mass-radius diagram of (transiting) exoplanets out to 3 M_J. The dashed lines indicate densities of (from top to bottom) 0.25, 0.5 and 1 ρ_J. The position of WASP-19 b is shown in red. *Right panel:* The temperatures of close-in exoplanets against their orbital periods. WASP-19 b is shown in red at the very inner edge of the distribution. The equilibrium temperatures here have been calculated with full energy redistribution an albedo of zero.

(see Figure 5.7) and in the nearly-continuous 24 day follow-up from Antarctica (Abe et al. 2013). The amplitude of this variability is in the order of a few milli-magnitudes, variable from season to season.

The planet is highly irradiated, receiving a flux of 4.3×10^9ergs $s^{-1}cm^{-2}$. The planets mass (1.4 M_J), and radius (1.2 R_J) show that its density is only about half that of Jupiter, meaning the planet is slightly bloated but no outlier with respect to other close-in transiting planets. Although there has been some doubt (Anderson et al. 2010), there is no evidence for a non-zero eccentricity of WASP-19 b's orbit. The position of this planet in the mass–radius diagram as well as a comparison to other planets in terms of period and temperature is shown in Figure 5.8 . Rossiter McLaughlin observations have been obtained for WASP-19, measuring an orbital plane aligned with the stellar equator. It has been argued that the planet has been undergoing orbital decay to its current separation of 0.017 au or 1.2 times the Roche limit (Hebb et al. 2010, Hellier et al. 2011b).

Observations of WASP-19

The planetary equilibrium temperature (given ineffective atmospheric recirculation) is ~2600 K, and together with a transit depth of ~2%, the occultations may be as deep as 1200 and 4000 ppm at 1 and 2 μm, respectively. Naturally, several teams have observed WASP-19 during occultation. Anderson et al. (2010) and Gibson et al. (2010) obtained ground-based observations with HAWK-I at 2.09 μm and in J-band shortly after the planets announcement. Another narrow-band HAWK-I measurement at 1.19 μm was added later by myself, as described in Lendl et al. (2013). Anderson et al. (2013b) used Spitzer to obtain occultation measurements at 3.6, 4.5, 5.8, and 8 μm. Several occultations have been observed at shorter wavelengths, Burton et al. (2012), myself (Lendl et al. 2013), and more recently Zhou et al. (2013) have produced values in z'-band, and Abe et al. (2013) and Mancini et al. (2013) show values in a wide filter (420-950 μm) and i'-band, respectively. Spectro-photometric observations during occultation have been added by Bean et al. (2013) from data obtained with MMIRS on the Magellan II telescope spanning the range 1.25 to 2.36 μm. All occultation measurements are shown together in Figure 5.9 .

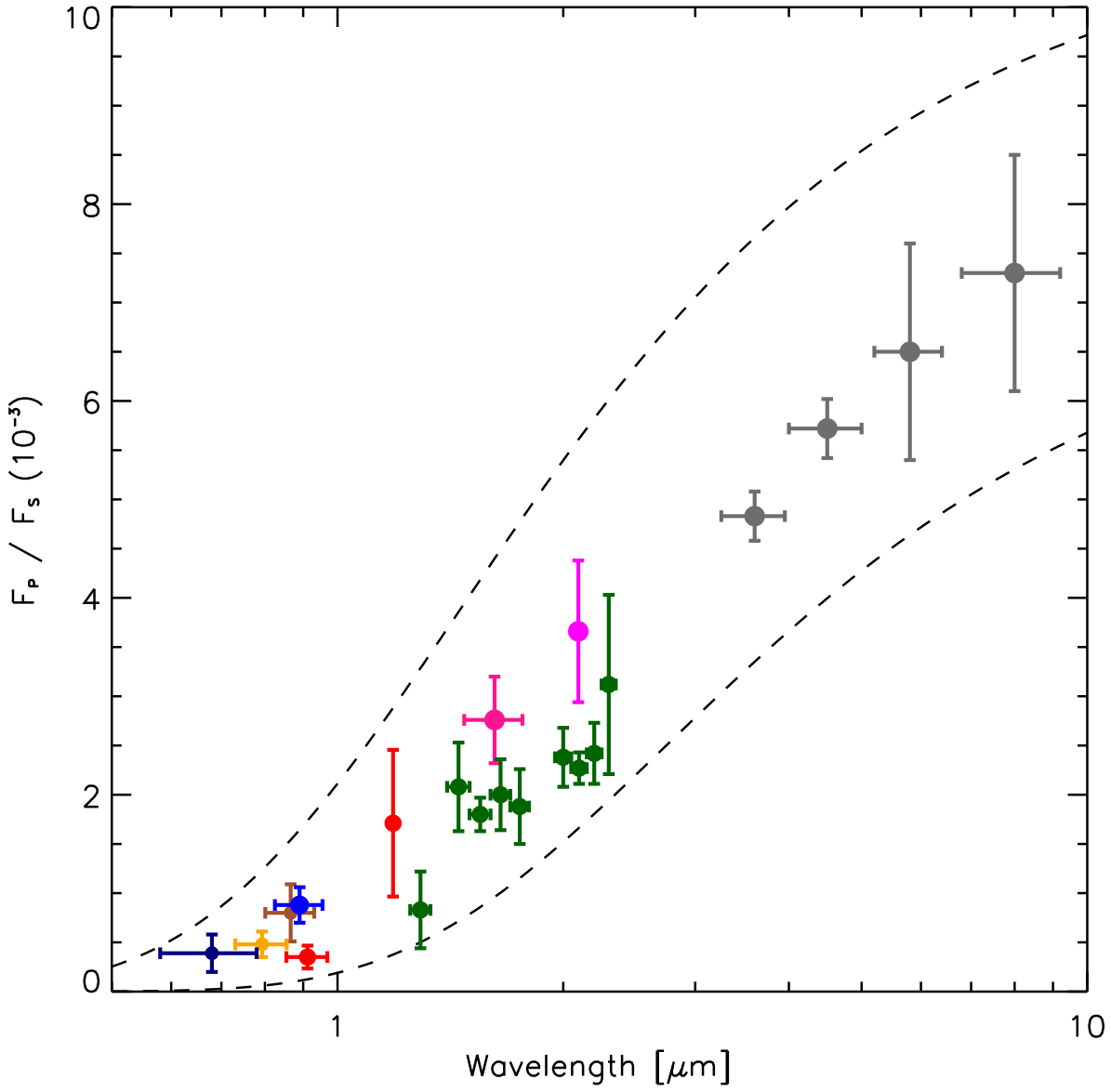

Figure 5.9 : All occultation measurements of WASP-19 b available at the time of writing of this document. The color coding is as follows: pink the H-band point of Anderson et al. (2010), gray the four *Spitzer* values of Anderson et al. (2013b), magenta the 2 µm point of Gibson et al. (2010), brown the z'-band measurement by Zhou et al. (2013), blue the z'-band value of Burton et al. (2012), and the optical point by Abe et al. (2013), orange the Ic measurement of Mancini et al. (2013), green the simultaneous spectrophotometric measurements by Bean et al. (2013), and finally red stands for my own EulerCam and TRAPPIST z'-band value (Lendl et al. 2013). To aid the eye the two dashed lines are emission curves for planetary black bodies of 3000 K (upper) and 2000 K (lower). For the stellar emission, a black body with a temperature of 5500 K was used.

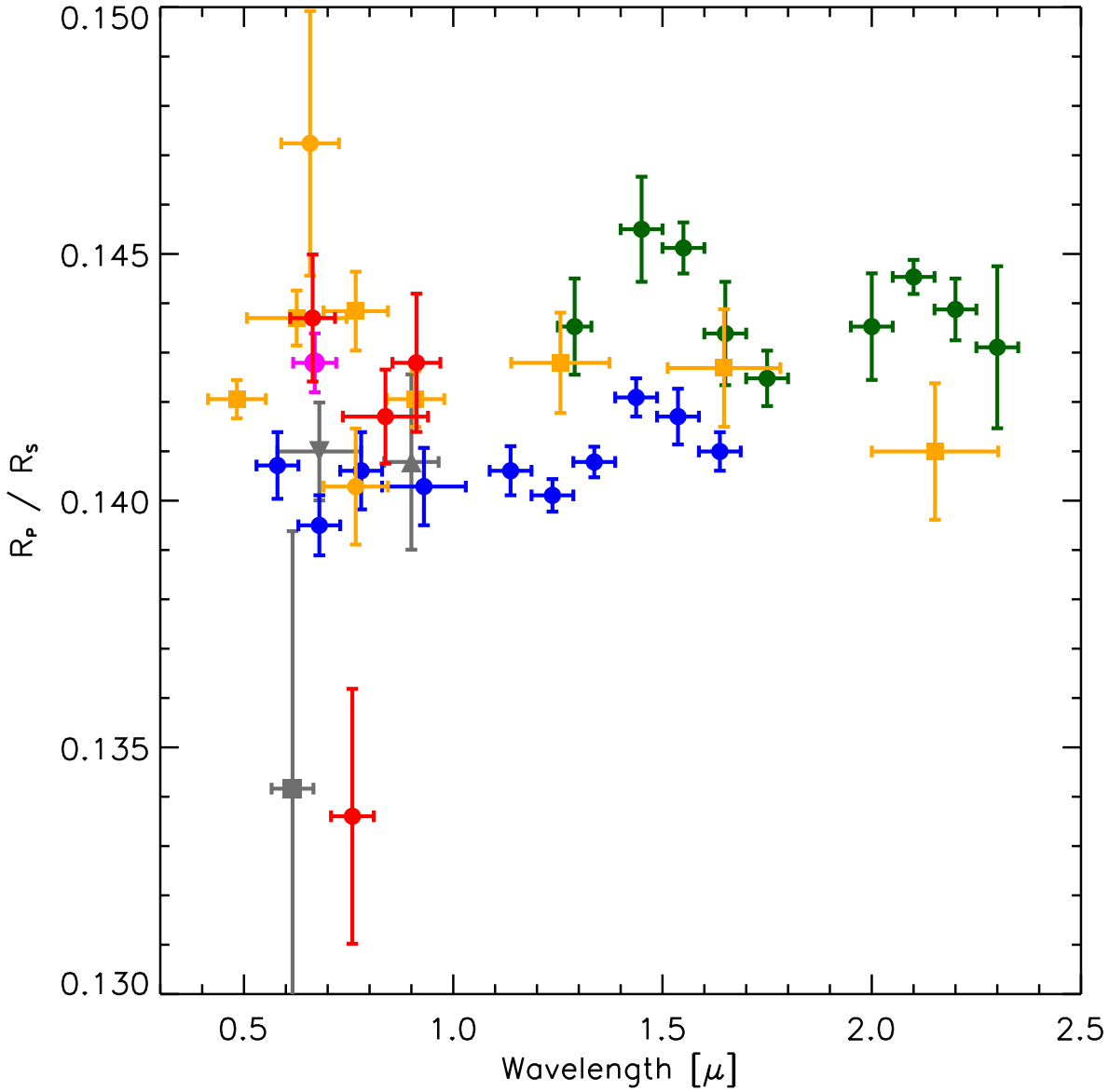

Figure 5.10 : All transits of WASP-19 b observed at the time of writing. The color coding is as follows: a gray upward facing triangle is the analysis of the z'-band lightcurve of Hebb et al. (2010) by Anderson et al. (2010), magenta is the r'-band measurement of Tregloan-Reed et al. (2013), a gray downward facing triangle is the broadband optical measurement by (Abe et al. 2013), the gray square denotes the measurement by Dragomir et al. (2011). Blue is the HST data by Huitson et al. (2013), green is the near-IR spectrophotometry of Bean et al. (2013). The data presented in Mancini et al. (2013) is shown in orange, with the filled squares denoting simultaneous GROND measurements. Finally the measurements obtained with EulerCam and TRAPPIST are shown in red.

Transit observations of WASP-19 b have been equally plentiful, and ground-based broadband photometry has been obtained in essentially all broadband filters (excluding U and B) by Abe et al. (2013) (420-950 μm), Dragomir et al. (2011) (R), Mancini et al. (2013) (g', r', R, i', z', J, H, K), Tregloan-Reed et al. (2013) (r'), and our team (r', Ic, I+z', z'). Bean et al. (2013) obtained spectrophotometric observations spanning the range of 1.25 to 2.36 μm with MMIRS on the Magellan II telescope. Using the STIS on the Hubble Space Telescope, Huitson et al. (2013) obtained low-resolution transmission spectrophotometry in the optical covering 0.5 – 1 μm in four bins, and HST/WFC3 was used by Huitson et al. (2013) and Mandell et al. (2013) to obtain spectrophotometric measurements out to 1.6 μm. To put these observations into context with each other, they are shown in Figure 5.10 . From inspecting the three series of simultaneous measurements (orange squares, blue and green dots) it is telling to note that there are relative offsets between them. A variation in R_P/R_* of 0.002 as seen between the HST (blue) and the MMIRS data (green) would, if only stellar variability were the cause, require a 2.9 % variation of the host star. Given the observed rotational amplitude of WASP-19 is $\lesssim$ 1 % in the optical where the signature of rotation is more pronounced, it is unlikely that un-occulted spots are the sole reason for the offset. On the other hand we must not discard the possibility that the variation is due to a change in the planetary atmosphere. If the stellar brightness and radius are assumed to be invariant, the offset of 0.002 in the radius ratio translates into a radius variation of 1383 km, or 2.02 times the atmospheric scale height. This is in the range of atmospheric signatures such as the appearence and disappearence of a haze layer. Thus, the effects of planetary weather can not be rejected a priori. Instrumental systematics, third light, or badly corrected lightcurve trends could equally well be the culprit of this discrepancy. This example illustrates that simultaneous observations at various epochs and a homogeneous analysis of all lightcurves is the way to go to obtain precise measurements of planetary transmission spectra.

The Atmosphere of WASP-19 b

There has been a great deal of debate about the atmospheric properties of WASP-19 b, particularly so as more and more data points become available. While the single measurements are not inconsistent with each other at more than 3 σ, the variation in the complete set of observations does not allow for precise conclusions on the atmospheric composition. However, it can be stated with large confidence that WASP-19 b does not possess a thermal inversion in its atmosphere. This inference relies on the flux in the *Spitzer* bands together with the flux in the near-IR, and has been supported by all authors presenting atmospheric models of WASP-19 b (Anderson et al. 2013b, Bean et al. 2013, Line et al. 2013a, Madhusudhan 2012, Mancini et al. 2013). Given that WASP-19 b is among the most irradiated planets, the inexistence of a temperature inversion is a challenge to explain. If thermal inversions are indeed caused by the presence of TiO and VO at high altitudes in the planetary atmosphere, then, for one reason or another, these molecules are depleted in the dayside of WASP-19 b. As the star is very active, the absence of an inversion is in line with the theory by Knutson et al. (2010), who suggested that the elevated UV flux breaks up TiO and VO in the upper atmosphere. Following Spiegel et al. (2009), gravitational settling might have depleted TiO and VO in the upper atmosphere. Madhusudhan (2012) argue that at high temperatures gravitational settling is not able to remove sufficient amounts of these molecules but propose that a super-solar C/O abundance might be to blame. In a carbon-rich atmosphere, the abundance of Oxygen bearing compounds is reduced and thus the absorption of Solar flux by TiO and VO is diminished. In line with emission spectra, Huitson et al. (2013) and Mancini et al. (2013) report no detection of TiO in the optical transmission spectra. At IR wavelengths, Huitson et al. (2013) report the detection of water at the terminator of WASP-19 b, indicating that the atmosphere is relatively clear (as the structures are not obscured by clouds or haze) and that the C/O abundance ratio can not be very high. Mandell et al. (2013) however use the same data to produce a transmission spectrum with a higher resolution which is fit better by a carbon-rich atmosphere.

In short, the available data support the absence of a stratosphere but do not allow to make inferences on the C/O ratio in the atmosphere of WASP-19 b.

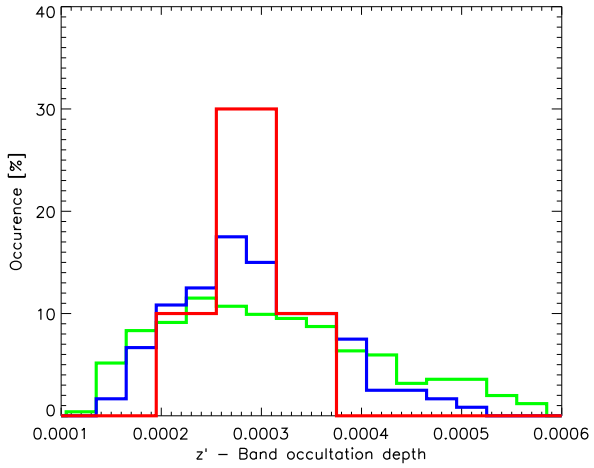

Figure 5.11 : Figure 10 of Lendl et al. (2013). The histogram of the occultation depth inferred from analyses of subsets of the EulerCam and TRAPPIST occultation data. Combinations of five (green), seven (blue) and nine (red) lightcurves are shown.

5.3.2 The EulerCam and TRAPPIST Campaign on WASP-19

Occultation Measurements in z'-band

WASP-19 b is one of the few planets for which several occultation measurements have been obtained blue-wards of 1 µm. The high depth (∼1 mmag) predicted for the occultation in z'-band puts its detection in reach of ground-based optical instrumentation. This promoted the observation of occultations of WASP-19 b with EulerCam, TRAPPIST and FORS2. The FORS2 data were affected by heavy systematics caused by bright columns and patches on the detector. After discussion with ESO about this issue, the most likely reason was that an error occurred during the swap of the red and blue detectors, as in later observations the data quality was restored. A much greater investment of observing time, a total of 10 occultations, has gone into the detection of the occultation with EulerCam and TRAPPIST. During the time of writing of the paper shown in Section 5.3.3, another z'-band measurement using ULTRACAM was made public (Burton et al. 2012), and at the time of preparation of this manuscript, a third z'-band value from the AAT has been announced (Zhou et al. 2013).

It should be discussed that the two other z'-band measurements both show larger occultation depths (880 ± 190 ppm by Burton et al. 2012 and 800 ± 290 ppm by Zhou et al. 2013) than my measurement at 352 ± 116 ppm. Both measurements are based on single observations, and trends were removed without the uncertainties of such a process being carried over to the final error estimation. As described in Section 4.3 of Lendl et al. (2013), I have tried to reproduce these results from the EulerCam / TRAPPIST measurements by including them as a prior in the MCMC analysis. I could not find a signature of that large an amplitude in the EulerCam / TRAPPIST data. In Figure 5.11 (or Figure 10 in Lendl et al. (2013)), the results obtained from smaller subsets of occultation data sets are shown. The results from five instead of ten lightcurves are shown in green, and it is easily visible that this distribution has a pronounced tail towards larger occultation depths. In fact it is combinations that contain more TRAPPIST lightcurves, that make up this tail. As the TRAPPIST light curves are showing a higher noise, this indicates that higher noise levels prompt larger deduced amplitudes. Together with showing a greater depth, also the errors on the occultation depth determined from five lightcurves are larger, and thus there is no contradiction to the final measurement.

This leads to two possible reasons for the observed discrepancy between the 350 ppm and 800 ppm measurements. Either there is variability in the planetary atmosphere, and/or (and this may well be the dominant factor) there is poor understanding of how to interpret low-significance signals in the presence of correlated noise, particularly so if one obtains only a single lightcurve of the event. I believe the solution to this mystery can be delivered by means of larger datasets of occultations, obtained with high-performance instruments optimized for photometry. The two ESO instruments which would present themselves for this job are FORS2 at the VLT/UT1, and EFOSC at the NTT. Unfortunately both

suffer from large systematics, due to inhomogeneities in the LADC transparency (FORS2) and fringing in z'-band (NTT).

At the time of writing of Lendl et al. (2013), the available models for the emission spectra of WASP-19 b (Madhusudhan 2012) were showing a clear difference in z'-band, depending on the atmospheric C/O abundance ratio. Thus the measurement of a shallow occultation prompted the inference of an oxygen-rich planetary atmosphere (see Figure 11 in Lendl et al. 2013). More recent atmospheric models however, e.g as shown in Bean et al. (2013) are able to reproduce this low a value equally well with carbon-rich atmospheres.

Occultation Measurements in the near IR

Included in the data set which I had at my disposition were two occultations observed with HAWK-I at 1.19 and 2.09 μm. Unfortunately, in the latter data set the target exceeded the linearity range of the detector. This means that the data do not have sufficient precision to detect signatures as small as a few milli-magnitudes. The 1.19 μm data are good to be analyzed, yet only half the images contain the target, as WASP-19 fell in the gap between the detectors for two out of four dithering positions. Had the full series been available, the occultation certainly would have been measured with a higher significance. I tested several approaches to best deal with the infra-red data, including sky subtraction based on the other dither positions, various cutoffs for the removal of bad pixels, variable and stable aperture sizes. Finally the best result was obtained with a variable aperture size, and using an annulus around the target for sky subtraction of each image. As the lightcurves obtained from the two dither positions require different baseline models and a small offset, I treated them separately in the MCMC analysis.

Transit Observations

To complement the occultation measurements, a number of transit lightcurves were obtained from EulerCam and TRAPPIST. The EulerCam observations were conducted in a series of filters (r', Ic and z'), while the TRAPPIST observations form a homogeneous set of nine I+z' lightcurves.

From this homogeneous set, I experimented with analyzing all possible subsets (from single lightcurves to a combined analysis of all lightcurves). The results, depicted in Figure 4 of Lendl et al. (2013), show the convergence of the obtained planetary parameters. Here a correlation is visible between the transit depth and duration, solutions finding longer transits also find larger depths. The root of this is probably the presence of star spots, which act to decrease the transit depth but also blur the in/egress.

In Figure 5.10 , the resulting planet/star radius ratios are given compared to all other data published to date. The single transit observed in Ic shows an anomalously low radius, probably due to spot crossings during transit, that is not confirmed by more recent measurements. See Figure 2 of Lendl et al. (2013) for both lightcurves and the respective photometric models.

5.3.3 Paper: A photometric study of the Hot Exoplanet WASP-19 b

A&A 552, A2 (2013)
DOI: 10.1051/0004-6361/201220924

Astronomy & Astrophysics

A photometric study of the hot exoplanet WASP-19b⋆,⋆⋆

M. Lendl[1], M. Gillon[2], D. Queloz[1], R. Alonso[3,4], A. Fumel[2], E. Jehin[2], and D. Naef[1]

[1] Observatoire de Genève, Université de Genève, 51 chemin des maillettes, 1290 Sauverny, Switzerland
e-mail: monika.lendl@unige.ch
[2] Université de Liège, Allée du 6 août 17, Sart Tilman, Liège 1, Belgium
[3] Instituto de Astrofísica de Canarias, C/Vía Lactéa s/n, 38205 La Laguna, Spain
[4] Universidad de La Laguna, Departamento de Astrofísica, 38200 La Laguna, Spain

Received 14 December 2012 / Accepted 27 January 2013

ABSTRACT

Context. The sample of hot Jupiters that have been studied in great detail is still growing. In particular, when the planet transits its host star, it is possible to measure the planetary radius and the planet mass (with radial velocity data). For the study of planetary atmospheres, it is essential to obtain transit and occultation measurements at multiple wavelengths.
Aims. We aim to characterize the transiting hot Jupiter WASP-19b by deriving accurate and precise planetary parameters from a dedicated observing campaign of transits and occultations.
Methods. We have obtained a total of 14 transit lightcurves in the r'-*Gunn*, *I-Cousins*, z'-*Gunn*, and $I + z'$ filters and 10 occultation lightcurves in z'-*Gunn* using EulerCam on the Euler-Swiss telescope and TRAPPIST. We also obtained one lightcurve through the narrow-band NB1190 filter of HAWK-I on the VLT measuring an occultation at 1.19 μm. We performed a global MCMC analysis of all new data, together with some archive data in order to refine the planetary parameters and to measure the occultation depths in z'-band and at 1.19 μm.
Results. We measure a planetary radius of $R_p = 1.376 \pm 0.046\ R_J$, a planetary mass of $M_p = 1.165 \pm 0.068\ M_J$, and find a very low eccentricity of $e = 0.0077^{+0.0068}_{-0.0032}$, compatible with a circular orbit. We have detected the z'-band occultation at 3σ significance and measure it to be $\delta F_{\mathrm{occ},z'} = 352 \pm 116$ ppm, more than a factor of 2 smaller than previously published. The occultation at 1.19 μm is only marginally constrained at $\delta F_{\mathrm{occ},NB1190} = 1711^{+745}_{-726}$ ppm.
Conclusions. We show that the detection of occultations in the visible range is within reach, even for 1 m class telescopes if a considerable number of individual events are observed. Our results suggest an oxygen-dominated atmosphere of WASP-19b, making the planet an interesting test case for oxygen-rich planets without temperature inversion.

Key words. planetary systems – techniques: photometric – planets and satellites: atmospheres

1. Introduction

At the time of writing, about 290 planets have been confirmed as transiting in front of their parent stars[1]. Via the precise measurement of transit lightcurves, we are able to constrain the planetary radius, orbital inclination, and mass (usually with the help of radial velocity measurements), hence the planetary density.

Transiting planets open up a window onto the study of planetary atmospheres, their structure and composition. High-precision spectroscopic or spectro-photometric observations of planetary transits allow us to search for wavelength dependencies in the effective planetary radius, and from there conclude on the molecular species present in the planetary atmosphere. Also, from the transit lightcurve an independent measurement of the stellar mean density can be obtained (Seager & Mallén-Ornelas 2003), which is particularly useful since it can be used to refine the host stars' parameters, namely its radius and mass. Having more accurate knowledge of the stellar parameters directly translates into more accurate physical values for the planetary mass and radius. This has led to several campaigns that collect transit lightcurves of published planets, as done by, e.g., Holman et al. (2006) and Southworth et al. (2009). Because the parameter measured from transit lightcurves is not the planetary radius itself but, in fact, the dimming of the star by the planetary disk, these measurements are affected by the brightness distribution along the stellar disk, i.e. stellar limb darkening as well as occulted and nonocculted spots. Occulted dark spots or bright faculae lead to short-term flux variations during the transit as the planet passes areas of the star having a different temperature and thus a different brightness. Nonocculted spots alter the stellar brightness outside of the planet's path, leading to a slight increase in the observed transit depth. Depending on the spot distribution on the stellar surface, spots cause a rotational modulation of the stellar flux, with typical amplitudes of a few percent in the optical and timescales of several days. While the effect on the transit depth is weak (100 ppm for a typical brightness variation and transit depth of both 1%), it is within the precision needed to detect of elements through transmission spectroscopy. Next to these physical effects, ground-based photometric lightcurves are known to suffer from correlated noise due to airmass, seeing, or other external variations (Pont et al. 2006). These effects can be mitigated by choosing optimal observation strategies (such as staying on the same pixels during the whole observation and

⋆ Based on photometric observations made with HAWK-I on the ESO VLT/UT4 (Prog. ID 084.C-0532), EulerCam on the Euler-Swiss telescope and the Belgian TRAPPIST telescope, as well as archive data from the Faulkes South Telescope, CORALIE on the Euler-Swiss telescope, HARPS on the ESO 3.6 m telescope (Prog. ID 084-C-0185), and HAWK-I (Prog. ID 083.C-0377(A)).
⋆⋆ The photometric time series data in this work are only available at the CDS via anonymous ftp to cdsarc.u-strasbg.fr (130.79.128.5) or via http://cdsarc.u-strasbg.fr/viz-bin/qcat?J/A+A/552/A2
[1] Based on www.exoplanet.eu (Schneider et al. 2011).

defocusing in order to improve the sampling of the PSF) but can rarely be completely prevented. In this work, we collect a large number of transit lightcurves from 1 m class telescopes and combine them to find not only a very precise but also an accurate measurement of the overall transit shape.

Observing the occultation of a transiting planet (Charbonneau et al. 2005; Deming et al. 2005) allows us to measure the brightness ratio of planet and star and thus measure the flux emitted or, at shorter wavelengths reflected, by the planet. At optical wavelengths, occultations have been measured almost exclusively from space (Alonso et al. 2009; Snellen et al. 2009; Borucki et al. 2009) using the *CoRoT* and *Kepler* satellites. There have been few ground based observations (Sing & López-Morales 2009; López-Morales et al. 2010; Smith et al. 2011), and so far none of the detections has been independently confirmed. Observations of occultations in the infrared have been plentiful, both from space (starting with Charbonneau et al. 2005; Deming et al. 2005) and from the ground, e.g., de Mooij & Snellen (2009); Gillon et al. (2009), and Croll et al. (2010). These observations provide information on the composition and the temperature profile of the planetary atmospheres. Some planets, such as HD 209458, show a temperature inversion at high altitudes (Knutson et al. 2008), which is usually attributed to high abundances of TiO and VO (Hubeny et al. 2003; Fortney et al. 2008). These molecules are efficient absorbers of the stellar radiation heating up the high altitude atmosphere. However, it is not yet clear why some planets show inversions while others do not. As the number of planets with characterized atmospheres increases, the presence of inversions is turning out not to depend only on either the incident stellar flux (Fortney et al. 2008) or the host star activity level (Knutson et al. 2010). Spiegel et al. (2009) argue that TiO might be depleted in many hot Jupiters by condensation and subsequent gravitational settling. Recently, Madhusudhan et al. (2011) have suggested an additional connection between the C/O ratio and the presence of an inversion, because in atmospheres dominated by carbon, the main absorbers TiO and VO are not abundant enough to cause an inversion. It is essential to increase the sample of well-studied transiting hot Jupiters and to provide accurate values for the measured occultation depths.

WASP-19b has been identified as a hot Jupiter by Hebb et al. (2010), based on data taken by the WASP survey (Pollacco et al. 2006). The slightly bloated ($\rho = 0.44\,\rho_J$) planet with a mass near that of Jupiter ($M_P = 1.17 M_J$) is orbiting an $m_V = 12.3$ G8V dwarf with a period of 0.79 days. At this close separation, the planet is assumed to have been undergoing orbital decay moving it to its current orbital position at 1.21 times the Roche limit (Hebb et al. 2010; Hellier et al. 2011). The star is known to be active showing a rotational modulation with a period of 10.5 days in the discovery lightcurves (Hebb et al. 2010). Also, anomalies in transit lightcurves attributed to spot crossings have been reported by Tregloan-Reed et al. (2013). The projected stellar rotation axis of WASP-19 is aligned with the planet's orbit (Hellier et al. 2011; Albrecht et al. 2012; Tregloan-Reed et al. 2013).

Occultations of WASP-19b have been measured in the past by Gibson et al. (2010) and Anderson et al. (2010) using HAWK-I in the K and H bands, respectively, as well as by Anderson et al. (2011) using the *Spitzer* Space Telescope at 3.6, 4.5, 5.8, and 8.0 μm. Recently, Burton et al. (2012) have published a z'-band lightcurve obtained with ULTRACAM during one occultation of WASP-19b, claiming its detection at 880 ± 119 ppm. From the ensemble of measurements, Anderson et al. (2011) and Madhusudhan (2012) determine that WASP-19b does not possess a temperature inversion. Using the z'-band value of Burton et al. (2012), models favor a C-rich atmosphere. For the eccentricity of WASP-19b, Anderson et al. (2011) derive a 3σ upper limit of $e < 0.027$.

In this paper we present results from an intense observing campaign of transits and occultations of WASP-19 obtained in both the optical and IR light. We describe all observations and their reduction in Sect. 2 and give details on the modeling in Sect. 3. In Sects. 4 and 5 we present and discuss the results before concluding in Sect. 6.

2. Observations and data reduction

Between May 2010 and April 2012, we obtained a total of 25 lightcurves of WASP-19. Fourteen of these observations were timed to observe the transit, while 11 were performed during the occultation of the planet. We made use of three instruments: EulerCam at the 1.2 m Euler-Swiss Telescope and the automated 0.6 m TRAPPIST Telescope at ESO La Silla Observatory (Chile), as well as HAWK-I at the VLT/UT4 at ESO Paranal Observatory (Chile). We include in our analysis also the Faulkes South Telescope (FTS) lightcurve published by Hebb et al. (2010), the HAWK-I H-band observation by Anderson et al. (2010) and the radial velocity measurements presented in Hebb et al. (2010) and Hellier et al. (2011). All new observations are summarized in Table 1.

2.1. EulerCam

Five transit and six occultation lightcurves have been obtained with EulerCam, the imager of the Euler-Swiss telescope at La Silla. The instrument and the reduction of EulerCam data are described in detail by Lendl et al. (2012). The observations were done either with a focused telescope or applying a small $\leq$0.1 mm defocus yielding stellar PSFs with a typical full width at half-maximum (FWHM) between 1.1 and 2.5 arcsec, while the exposure times were between 60 s and 120 s, depending on filter and conditions. On 12 March 2011, the CCD temperature during the observations was slightly elevated, $-100°$ C instead of the nominal $-115°$ C. The lightcurves were extracted using relative aperture photometry, with the reference stars and apertures selected independently for each observation.

2.2. TRAPPIST

Nine transits and four occultations of WASP-19b were observed with the robotic 60 cm TRAPPIST (Gillon et al. 2011; Jehin et al. 2011) that is also located at the La Silla site. We defocused the telescope slightly in order to spread the light over more pixels yielding typical FWHM values between 3.6 and 6.5 arcsec on the images and used exposure times between 15 s and 40 s. Again, the lightcurves were obtained with relative aperture photometry, where IRAF[1] is used in the reduction process.

2.3. HAWK-I

We obtained photometry of WASP-19 using the HAWK-I instrument (Pirard et al. 2004; Casali et al. 2006) on VLT UT4 during two occultations of WASP-19b using the narrow band filters NB1190 and NB2090. Unfortunately, during the NB2090 observations, the target exceeded the linearity range of the detector, as a consequence the data do not have the necessary precision to

[1] IRAF is distributed by the National Optical Astronomy Observatories, which are operated by the Association of Universities for Research in Astronomy, Inc., under cooperative agreement with the National Science Foundation.

Table 1. Summary of newly obtained photometry.

Date (UT)	Instrument	Filter	Eclipse nature	Photometric model function	$\beta_{\rm red}$	rms [ppm, rel. flux, per 5 min]
2010-01-20	HAWK-I	NB1190	Occultation	$p(t^2)$ and $p(t^2) + p(FWHM^1)$	1.23 and 1.11	1820 and 1096
2010-05-21	TRAPPIST	$I + z'$	Transit	$p(t^2)$	1.17	680
2010-12-09	EulerCam	IC	Transit	$p(t^2) + p(sky^1)$	1.30	900
2011-01-08	TRAPPIST	$I + z'$	Transit	$p(t^2)$	1.62	610
2011-01-21	TRAPPIST	z'	Occultation	$p(t^2)$	1.00	720
2011-01-23	EulerCam	r'	Transit	$p(t^2)$	1.22	570
2011-01-23	TRAPPIST	$I + z'$	Transit	$p(t^2)$	1.42	730
2011-02-10	TRAPPIST	$I + z'$	Transit	$p(t^2)$	2.05	1170
2011-02-14	EulerCam	z'	Transit	$p(t^2) + p(sky^1)$	1.25	700
2011-02-15	TRAPPIST	$I + z'$	Transit	$p(t^2)$	1.00	840
2011-02-23	TRAPPIST	z'	Occultation	$p(t^2)$	1.51	960
2011-02-24	TRAPPIST	z'	Occultation	$p(t^2)$	1.00	690
2011-03-02	TRAPPIST	$I + z'$	Transit	$p(t^2)$	1.00	610
2011-03-12	EulerCam	r'	Transit	$p(t^2) + p(FWHM^2)$	1.38	690
2011-04-04	TRAPPIST	$I + z'$	Transit	$p(t^2)$	1.82	980
2011-04-19	TRAPPIST	$I + z'$	Transit	$p(t^2)$	1.80	1120
2011-04-21	TRAPPIST	z'	Occultation	$p(t^2)$	1.00	700
2011-04-28	EulerCam	z'	Occultation	$p(t^2) + p(FWHM^1)$	1.19	520
2011-05-06	EulerCam	z'	Occultation	$p(t^2)$	1.13	400
2012-02-28	EulerCam	z'	Occultation	$p(t^2)$	1.00	510
2012-03-11	EulerCam	z'	Occultation	$p(t^2)$	1.13	440
2012-03-15	EulerCam	z'	Occultation	$p(t^2) + p(xy^1)$	1.29	800
2012-03-18	EulerCam	z'	Occultation	$p(t^2) + p(FWHM^1)$	1.00	460
2012-04-12	EulerCam	r'	Transit	$p(t^2)$	1.55	940
2012-05-15	TRAPPIST	$I + z'$	Transit	$p(t^2)$	1.24	970

Notes. Date, instrument, filter, and the nature of eclipse are given for each observation together with the photometric model function, red noise amplitude $\beta_{\rm red}$ (as defined in Winn et al. 2008) and the rms of the binned (5 min) residuals. The notation $p(j^i)$ refers to a polynomial of degree i of parameter j, e.g. $p(t^2)$ denotes a polynomial of second degree with respect to time.

detect the occultation; however, the NB1190 data are good, and thus we restrict our analysis to them.

The NB1190 observations of WASP-19 took place on 20 January 2010 from 02:55 to 06:55 UT covering the predicted occultation time together with 145 min of observations outside of eclipse. The detector integration time (DIT) was kept short (3 s) so the counts of the target and a bright reference star did not exceed the linear range of the detector. The data were obtained by alternating between two jitter positions, in order to be able to correct for background variations if necessary.

The data were corrected for dark and flat field effects using standard procedures. Then, we identified bad pixels on the images and substituted their values by the mean of the neighboring pixels. Here, we experimented with different cutoffs for the identification of bad pixels and obtained the best results discarding pixels deviating by 4σ for background values and 40σ for stars. The target flux was extracted from the corrected images using aperture photometry. We tested a set of constant apertures, as well as apertures that varied from image to image as a function of the stellar FWHM. The sky annulus was kept constant for all images. The best result was obtained using a variable aperture of two times the FWHM. We tested all bright stars of the four HAWK-I chips and found the best photometry using only the single bright star located on the same chip as WASP-19. The bright stars on the other detectors showed significantly different variations, so they were not used. The lightcurves are shown in Fig. 2.

3. Modeling

We performed a combined analysis of all photometric (transit and occultation) data, together with published radial velocities. The data were modeled using the Markov chain Monte Carlo (MCMC) method in order to derive the posterior probability distributions of the parameters of interest (see Sect. 3.1 for details). Incorporated in our analysis are models for photometric correction functions, which account for photometric variations not related to the eclipse, i.e. airmass, weather, or instrumental effects. We also rescale our error bars if they show to be underestimated. Please see Sect. 3.2 for details.

3.1. MCMC

We employed the MCMC method using the implementation described in Gillon et al. (2010, 2012). In short, the radial velocities are modeled using a Keplerian orbit and with the prescription of the Rossiter-McLaughlin effect (Rossiter 1924; McLaughlin 1924) provided by Giménez (2006). The photometric model for eclipses (transits and occultations) is that of Mandel & Agol (2002), used without limb darkening for occultations. The jump parameters are transit depth $\mathrm{d}F$, impact parameter b, transit duration d, time of midtransit T_0, period P, occultation depths $\mathrm{d}F_{\rm occ}$ for each wavelength, and $K_2 = K\sqrt{1-e^2}P^{1/3}$ (where K and e denote the radial velocity semi-amplitude and eccentricity, respectively). The jump parameters $\sqrt{e}\cos\omega$ and $\sqrt{e}\sin\omega$ (where ω denotes the argument of periastron) are used to determine of the eccentricity. Limb darkening is accounted for by using the combinations $c_1 = 2u_1 + u_2$ and $c_2 = u_1 - 2u_2$ of the calculated limb-darkening coefficients of Claret & Bloemen (2011) following Holman et al. (2006). With the exception of the limb darkening parameters (for which we use a normal prior with a width equal to the error quoted by Claret & Bloemen 2011), we assume uniform prior distributions. We followed the method described by Enoch et al. (2010) using the mean stellar

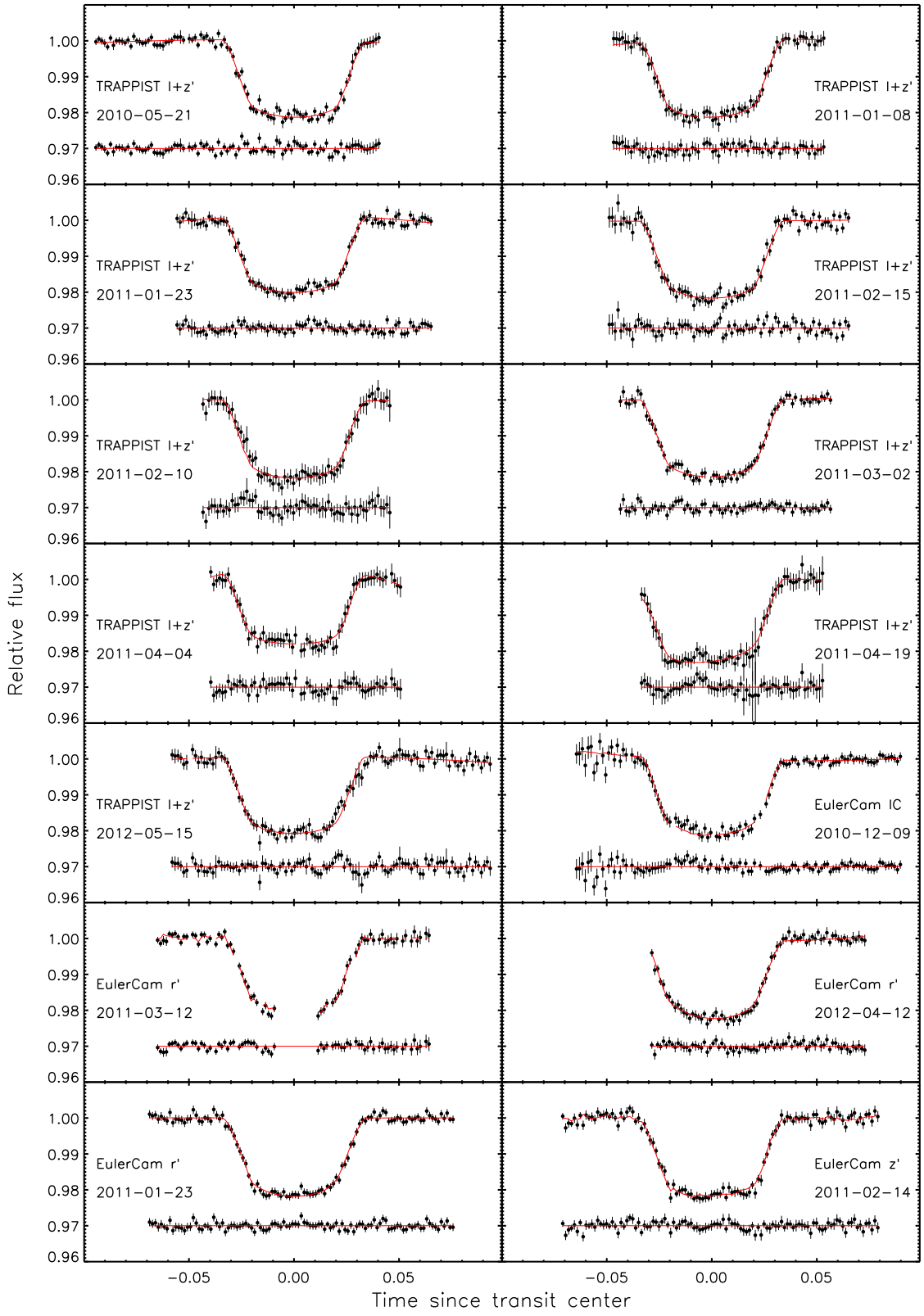

Fig. 1. All transits observed together with their models and residuals. Instrument and filter used are indicated in each frame. All data have been binned in two-minute intervals.

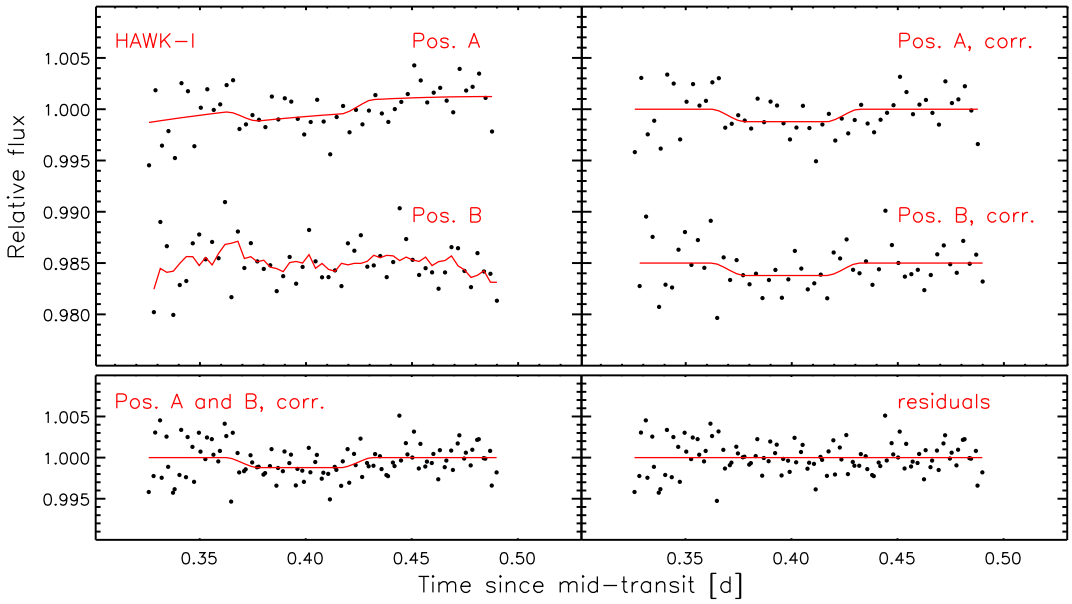

Fig. 2. Occultation observed with HAWK-I at 1.19 μm on 20 January 2010. The lightcurves obtained from the two jitter positions are shown. *Top panel*: the raw lightcurves, together with the occultation and photometric model (*left*), and divided by the photometric model (*right*). *Bottom panel*: both lightcurves corrected and normalized with the best fit (*left*) and the residuals (*right*).

density, temperature, and metallicity for determining the stellar mass and radius. In our whole analysis, we always ran at least two MCMC chains and checked convergence with the Gelman & Rubin test (Gelman & Rubin 1992). All time stamps are converted to the TDB time standard, as described by Eastman et al. (2010).

3.2. Photometric model and error adaptation

As described in Sect. 1, ground-based lightcurves are often affected by red noise correlated with external parameters. In our MCMC analysis, we have the possibility to include time, FWHM, coordinate shifts, and background variations in our model. This is done by multiplying the transit model by a polynomial (up to 4th degree) with respect to any combination of these parameters. The coefficients of the polynomial are not included as jump parameters in the MCMC but are found by minimization of the residuals at each step. In order to account for airmass and stellar variability effects, we assumed a second-order polynomial with respect to time as the minimal accurate model for ground-based photometry. We checked more complex models by running MCMC chains of 10^5 points on each lightcurve including higher orders of time dependence and additional terms in FWHM, pixel position and background. A more complex model was favored over a simple one only if the Bayes factor (Schwarz 1978) estimated from the Bayesian information criterion indicated a significantly higher probability (i.e. $B_{1,2} > 100$). The best photometric model functions are listed in Table 1 and were used in all subsequent analyses. For the H-band data, we kept the coordinate dependence described in Anderson et al. (2010), and the archive FTS lightcurve (Hebb et al. 2010) was fitted with the minimal model.

Although photometric error bars are usually derived including scintillation, readout, background, and photon noise, they are often underestimated, and we adapted them by accounting for additional white and red noise. For the white noise, we derived a scaling factor β_w from the ratio of the mean photometric error and the standard derivation of the photometric residuals. For the red noise, we obtained a scaling factor β_r by comparing the standard deviation of the binned photometric residuals to the standard deviation of the complete dataset, as described in detail by Winn et al. (2008) and Gillon et al. (2010). Finally we multiplied both scaling factors to obtain the correction factors $CF = \beta_w \times \beta_r$ for the photometric errors. In the subsequent analysis, all photometric error bars were multiplied by these factors. Analogously, we computed values for the radial velocity jitter that were added quadratically to the radial velocity errors.

3.3. Summary of tested models

Having derived the above factors, we analyzed the entire dataset. We did so by running chains of 10^5 points on all photometric and radial velocity data. Next to the global analysis, we also performed analyses of subsets of lightcurves (described in detail in Sects. 4.1 and 4.3.3). Additionally, we searched for any color dependence in the transit depths by allowing for depth offsets between the different filters (Sect. 4.3.2) and also derived individual midtransit times in order to check for transit-timing variations (Sect. 4.3.2). To verify the result of Burton et al. (2012), we performed a global analysis in which we included their value, $DF_{\mathrm{occ},z'} = 880 \pm 190$ ppm, as a Gaussian prior (Sect. 4.3.3). The results are described in detail in Sect. 4, while all newly obtained lightcurves are shown in Fig. 1 (transits), Fig. 2 (NB1190 occultation), and Fig. 3 (z'-band occultations).

4. Results

4.1. The TRAPPIST transit sequence

To investigate the benefits of combining several lightcurves, we divided our set of nine $I + z'$ TRAPPIST transit lightcurves into subsets containing all possible combinations of one to nine

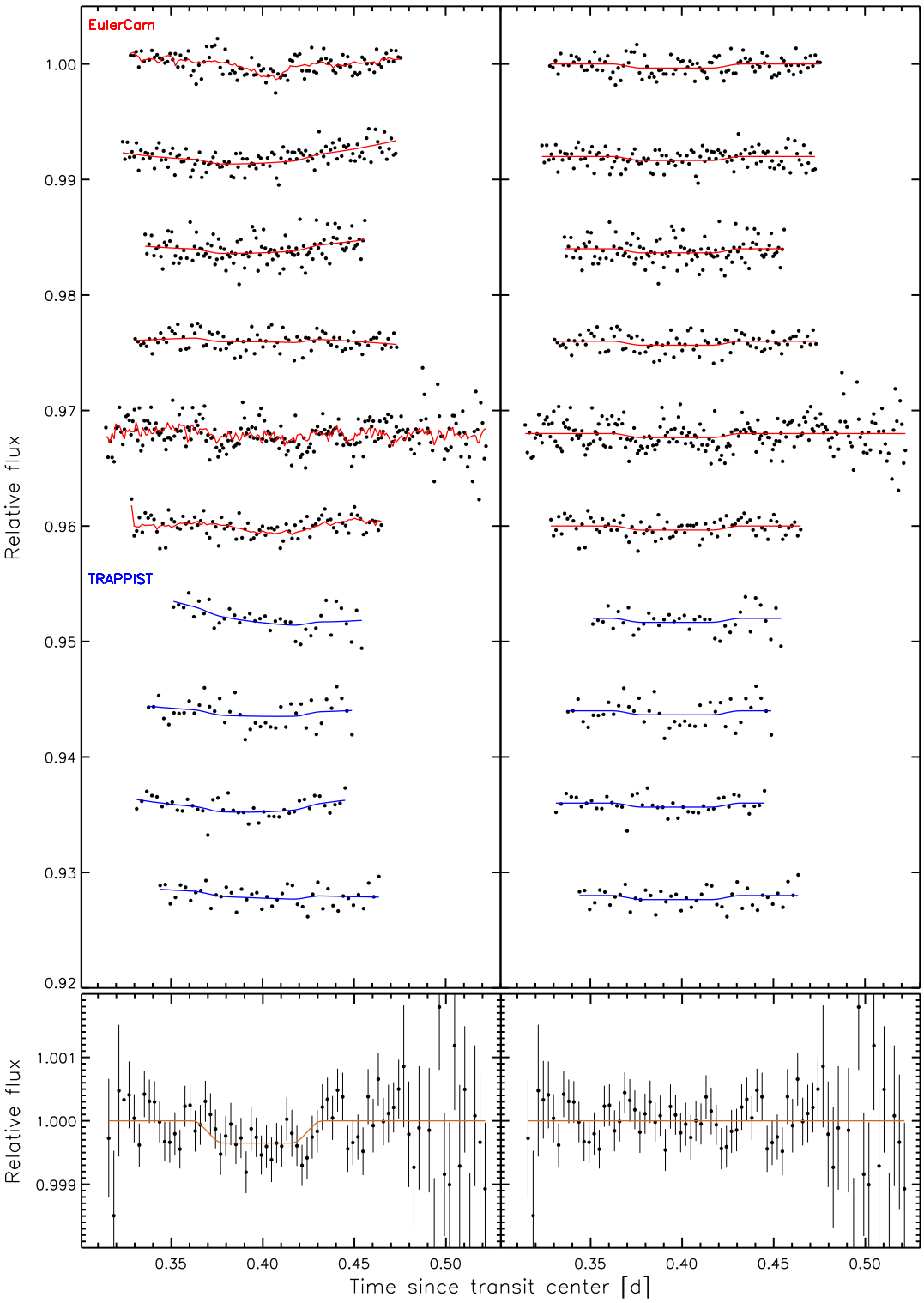

Fig. 3. All occultation lightcurves obtained in the z'-band. The upper six lightcurves were obtained with EulerCam and are unbinned, while the lower four lightcurves were obtained with TRAPPIST and binned in two-minute intervals. *Left panel*: the raw lightcurves, together with the occultation and photometric models. *Right panel*: the lightcurves and the occultation model, divided by the photometric model. The *lower panel* shows all data, corrected for the photometric model and binned in four-minute intervals. Data and model are shown on the left, while the residuals are shown on the right.

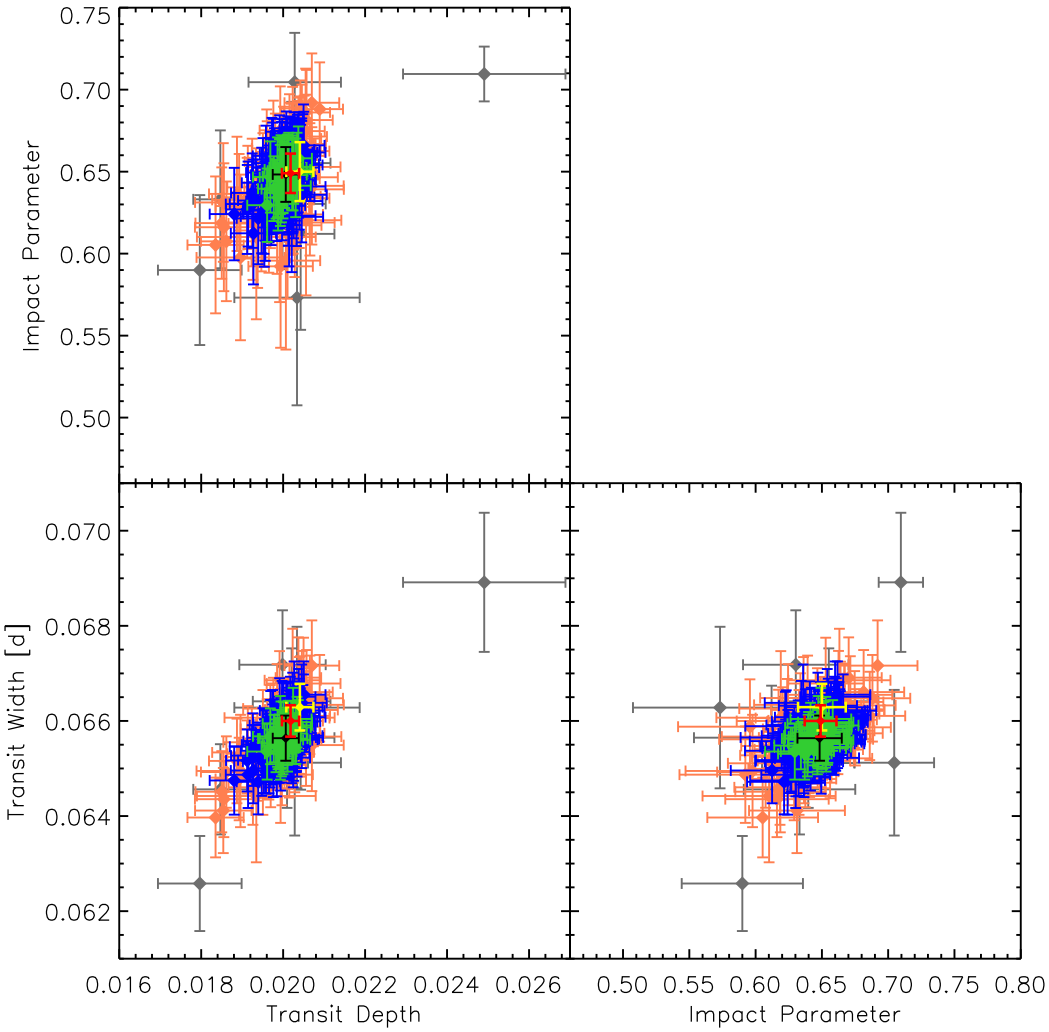

Fig. 4. Solutions found from fits to all possible subsets of TRAPPIST transits. The single transits are shown in gray, and combinations of three, five and seven transits are shown in orange, blue and green, respectively. The solution to all TRAPPIST and EulerCam lightcurves are shown in black and yellow, respectively. The global solution is shown in red.

lightcurves and performed an MCMC analysis on each of them using the procedure described in Sect. 3. We can observe how the solutions converge as we use an increasing number of transits in Fig. 4. The outlier located at high transit depth stems from the transit observed on 10 February 2011, which is showing very high red noise. It is clearly visible that combinations favoring a large transit depth also require a larger transit width. This correlation might be related to the presence of star spots occulted by the planet. While spots on the limb of the star shorten the apparent transit duration, spots closer to the center of the star will produce a flux increase leading to a decrease in the apparent transit depth. It is also possible that the overall stellar variability is not well constrained, e.g. due to little or no out-of-transit data, and thus the photometric correction model cannot be determined correctly. Figure 4 also shows the global solution and the solution obtained from the EulerCam transits alone. The results from TRAPPIST and EulerCam agree within their error bars, yet the EulerCam data find a slightly larger transit depth, width, and impact parameter.

Next to investigating the parameters obtained from combinations of transits, one can also check the photometric improvement reached by combining an increasing number of lightcurves. To measure this effect, we used each set of combinations of $n = 1$ to $n = 9$ lightcurves, folded them on the best-fit period, and binned the data. Points before −0.05 and after +0.05 days from transit center were discarded to avoid phases that are not covered by all lightcurves. In Fig. 5, we show the photometric rms against the number of combined lightcurves and compare the decrease in rms to the "best case" (decrease with $\frac{1}{\sqrt{n}}$). The increase in precision is near that value, particularly if small time bins are used. By combining all nine TRAPPIST lightcurves, we obtain an rms of 321 ppm for a moderately sized time bin of five minutes.

4.2. One simultaneous observation

The transit of 23 January 2011 was observed with EulerCam and TRAPPIST simultaneously, using an r'-*Gunn* filter on EulerCam and an $I + z'$ filter on TRAPPIST. Figure 6 depicts the two

Table 2. Median values and the 1-σ errors of the marginalized posterior PDF obtained from the MCMC analysis of all new data plus the radial velocities and lightcurves published by Hebb et al. (2010), Anderson et al. (2010) and Hellier et al. (2011).

WASP-19		
Jump parameters		
Transit depth	$\Delta F = (R_p/R_*)^2$	0.02018 ± 0.00021
	$b' = a * \cos(i_p)$ $[R_*]$	0.649 ± 0.012
Transit duration	T_{14} [d]	$0.06586^{+0.00033}_{-0.00031}$
Time of midtransit	$T_{[0]} - 2\,450\,000$ [HJD]	6029.59204 ± 0.00013
Period	P [d]	$0.7888390 \pm 2 \times 10^{-7}$
	$K_2 = K\sqrt{1-e^2}P^{1/3}$ [m s^{-1} $d^{1/3}$]	238.1 ± 2.7
z'-band occultation depth	$\Delta F_{occz'}$ [ppm]	352 ± 116
NB1190 occultation depth	$\Delta F_{occNB1190}$ [ppm]	1711^{+745}_{-726}
H-band occultation depth	ΔF_{occH} [ppm]	3216^{+473}_{-455}
	$\sqrt{e}\cos\omega$	0.053 ± 0.020
	$\sqrt{e}\sin\omega$	$0.054^{+0.057}_{-0.082}$
	$\sqrt{v_* \sin I_*}\cos\beta$	$1.85^{+0.17}_{-0.19}$
	$\sqrt{v_* \sin I_*}\sin\beta$	-0.27 ± 0.23
	$c_{1,r'} = 2u_{1,r} + u_{2,r}$	1.123 ± 0.040
	$c_{2,r'} = u_{1,r} - 2u_{2,r}$	-0.052 ± 0.037
	$c_{1,IC} = 2u_{1,IC} + u_{2,IC}$	0.903 ± 0.034
	$c_{2,IC} = u_{1,IC} - 2u_{2,IC}$	-0.173 ± 0.025
	$c_{1,I+z'} = 2u_{1,I+z'} + u_{2,I+z'}$	0.840 ± 0.050
	$c_{2,I+z'} = u_{1,I+z'} - 2u_{2,I+z'}$	-0.251 ± 0.053
	$c_{1,z'} = 2u_{1,z'} + u_{2,z'}$	0.831 ± 0.029
	$c_{2,z'} = u_{1,z'} - 2u_{2,z'}$	-0.218 ± 0.021
Deduced parameters		
Radial velocity semi-amplitude	K [m s^{-1}]	257.7 ± 2.9
Planet radius	R_p $[R_J]$	1.376 ± 0.046
Planet mass	M_p $[M_J]$	1.165 ± 0.068
Planet density	ρ_p $[\rho_J]$	$0.447^{+0.027}_{-0.025}$
Eccentricity	e	$0.0077^{+0.0068}_{-0.0032}$
Argument of periastron	ω [deg]	43^{+28}_{-67}
Semi-major axis	a [AU]	0.01653 ± 0.00046
Normalized semi-major axis	a/R_*	3.573 ± 0.046
Inclination	i_p [deg]	79.54 ± 0.33
Transit impact parameter	b_{tr}	0.645 ± 0.012
Occultation impact parameter	b_{occ}	0.652 ± 0.015
Time of midoccultation	$T_{occ} - 2\,450\,000$ [HJD]	6030.77766 ± 0.00088
Projected spin-orbit angle	β [deg]	$-8.4^{+7.0}_{-7.2}$
Planet equilibrium temperature[a]	T_{eq} [K]	2058 ± 40
Planet surface gravity	$\log g_p$ [cgs]	3.184 ± 0.015
Stellar mass	M_* $[M_\odot]$	$0.968^{+0.084}_{-0.079}$
Stellar radius	R_* $[R_\odot]$	0.994 ± 0.031
Stellar mean density	ρ_* $[\rho_\odot]$	$0.983^{+0.039}_{-0.036}$
1st quadratic LD coeff., r' band	$u_{1,r'}$	0.439 ± 0.020
2nd quadratic LD coeff., r' band	$u_{2,r'}$	0.246 ± 0.015
1st quadratic LD coeff, $I + z'$ band	$u_{1,I+z}$	0.286 ± 0.026
2nd quadratic LD coeff., $I + z'$ band	$u_{2,I+z}$	0.268 ± 0.019
1st quadratic LD coeff., IC band	$u_{1,IC}$	0.326 ± 0.016
2nd quadratic LD coeff., IC band	$u_{2,IC}$	0.2497 ± 0.0094
1st quadratic LD coeff., z' band	$u_{1,z'}$	0.289 ± 0.014
2nd quadratic LD coeff., z' band	$u_{2,z'}$	0.2536 ± 0.0077

Notes. [(a)] Assuming an Albedo of $A = 0$ and full redistribution from the planets day to night side, $F = 1$.

lightcurves superimposed. It is obvious that the TRAPPIST data are showing an anomalously small transit depth and a short-term brightening during the second half of the transit. With only one lightcurve, one might conclude that the planet crossed a star spot during transit. Since the EulerCam light curve was observed at shorter wavelengths and given the cooler temperature of the spot, we would expect the effect to be more pronounced here. However, the feature is absent in the r'-band, excluding the spot-hypothesis. We tried to account for it by adopting photometric correction models including backgound, sky, and FWHM parameters, yet were not able to find a model that reproduced the lightcurve shape. Removing the points during the second half of the transit in the TRAPPIST lightcurve, we obtain a value within 1σ of the EulerCam result.

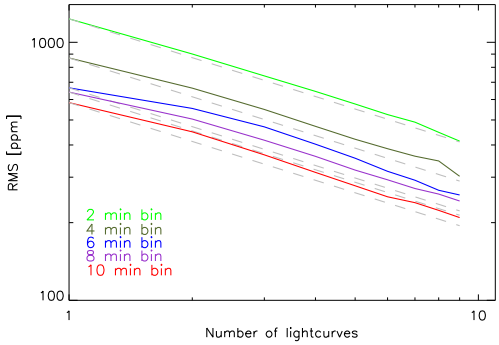

Fig. 5. Increase in photometric precision by combining up to nine lightcurves from TRAPPIST. The rms in bin sizes of (from top to bottom) two, four, six, eight and ten minutes are shown. The gray dashed lines show the expected $1/\sqrt{n_{lc}}$ decrease for each time bin.

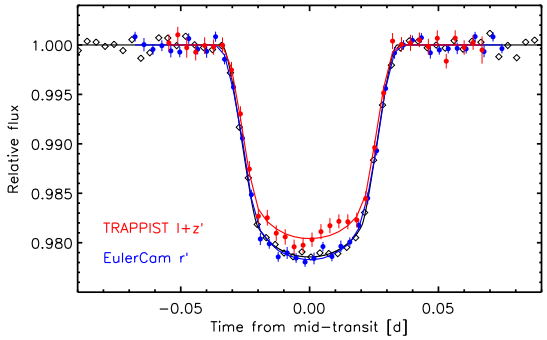

Fig. 6. Simultaneous transit observation performed with TRAPPIST (red) and EulerCam (blue). For clarity, the data are binned into 5-min bins, and the models of the individual transits are shown as solid lines. The binned data from the combination of all $I + z'$ lightcurves (same as in Fig. 8) are shown in black for comparison.

4.3. Global analysis

We performed a global MCMC analysis using all available radial velocity and photometric data including transits and occultations (described in detail in Sect. 3). The results are shown in Table 2.

4.3.1. Eccentricity

While Hebb et al. (2010) and Hellier et al. (2011) did not measure a significant nonzero eccentricity from the analysis of radial velocity and transit data, Anderson et al. (2010) presented for WASP-19b a value of $e = 0.016^{+0.015}_{-0.007}$ from the timing of their H-band occultation. When including their data in our analysis, we derived a lower value for the eccentricity with a similar significance $0.0077^{+0.0068}_{-0.0032}$. Removing the H-band data, we obtained $0.0061^{+0.0063}_{-0.0043}$, clearly not significant. We therefore do not see any evidence for a nonzero eccentricity of the WASP-19 system.

4.3.2. Transit depth and timing variations

One of the checks we performed on the data was letting the transit depth vary for different filters, in order to search for any wavelength dependencies in the star/planet radii ratio which can be used to constrain models of the atmospheric transmission. The phase-folded and binned lightcurves for each filter are shown in Fig. 8, and the respective radii ratios are shown in Fig. 9 and listed in Table 3. The r', $I + z'$, and z' band values match very

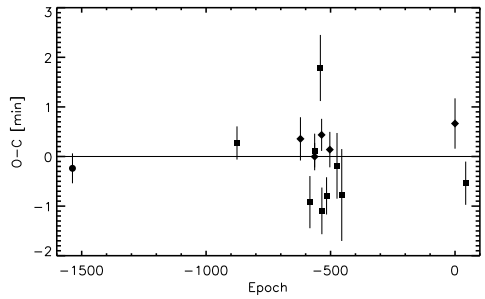

Fig. 7. O–C deviations of the individual transits from the ephemeris given in Table 2. The filled circle represents the FTS transit of Hebb et al. (2010), the squares represent data obtained with EulerCam, and the diamonds represent data from TRAPPIST.

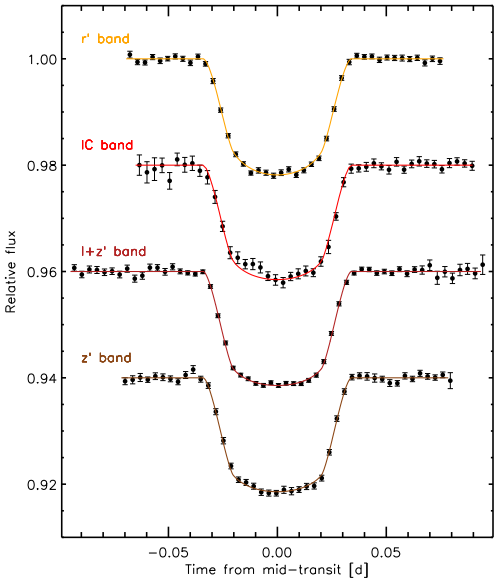

Fig. 8. Combined lightcurves in each of the observed bands binned in five-minute intervals. The lightcurves are a combination of (from top to bottom) three, one, nine, and two observations. Using the displayed five-minute intervals, the rms of the residuals in the interval $[-0.05, 0.05]$ days are (from top to bottom) 432, 1021, 321, and 487 ppm.

well, only the IC value is slightly lower, 2.6σ below the global solution.

We also searched for any deviation from a linear ephemeris by performing a global analysis while fixing the ephemeris to the ephemeris derived from the global analysis but letting the individual midtransit times vary. The results are shown in Fig. 7 and listed in Table 4. While there is some (expected) scatter around the linear ephemeris, none of the deviations exceed 2.7σ, so we find no evidence of TTVs in the WASP-19 system.

4.3.3. z'-band and 1.19 μm occultations

We measure a z'-band occultation depth of 352 ± 116 ppm from the combined analysis of the ten z'-band occultation lightcurves in our dataset. For individual lightcurves the occultation is well buried in the noise. To verify that our nonzero occultation depth is not caused by a systematic effect present in a single or a small number of lightcurves, we proceeded in a similar way to what we did with the set of TRAPPIST transits (Sect. 4.1). We created all

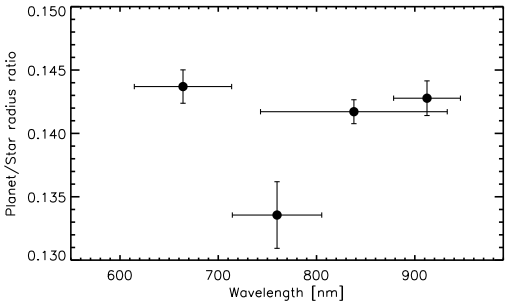

Fig. 9. Planet/star radius ratios obtained from an MCMC analysis of all data, while allowing for filter-dependent transit depths. The errorbars in wavelength span the filters effective width. The deviation IC lightcurve is based on only a single observation.

Table 3. Planet/star radius ratios obtained from a global MCMC analysis, while allowing for filter-dependent transit depths.

Filter	Wavelength (width) [nm]	R_p/R_*
r'-Gunn	664 (99)	0.1437 ± 0.0013
IC	760 (91)	0.1336 ± 0.0026
$I + z'$	838 (190)	0.14171 ± 0.00094
z'-Gunn	912.4 (68)	0.1428 ± 0.0014

Notes. For the $I + z'$ and z' filters, the widths given here have been determined from the combination of the filter transmission and detector response curves. For the r' and IC filters we give the equivalent widths.

possible subsets containing at least five occultation lightcurves and analyzed them while fixing all parameters except the occultation depth to the values derived above. Histograms of the derived occultation depths are shown in Fig. 10. The results obtained from fits of fewer light curves are consistent with the presented value, although they have lower significance. Recently, Burton et al. (2012) have presented an occultation depth for WASP-19b of 880 ± 190 ppm based on one lightcurve obtained with ULTRACAM mounted at the NTT telescope at ESO La Silla observatory. We tried to reproduce this value by using it as a Gaussian prior (with a width equal the error bar on the measurement) in our MCMC. Even with this prior, the resulting occultation depth is 466 ± 97 ppm. We are thus not confirming the measurement of Burton et al. (2012) but conclude that the occultation of WASP-19b in z' band is significantly smaller.

In our global analysis we include the occultation observed with HAWK-I using the narrow-band $NB1190$ filter. From our data we measure the occultation depth at 1.19 μm to be 1711^{+750}_{-730} ppm.

5. Discussion

From the homogeneous set of TRAPPIST $I + z'$ lightcurves, we can evaluate the photometric improvement obtained from combining lightcurves. As presented in Fig. 5, we are not far from the ideal case of only white noise. Even if combining as many as nine lightcurves, we are still gaining in photometric precision by adding additional transits.

Following our observation strategy of deriving the most accurate measurement of the overall transit shape and thus the planetary parameters, we can reduce correlated noise, which can drastically affect single lightcurves. This is most evident if the same transit is observed simultaneously using different instruments. In the case of a combination of nine TRAPPIST lightcurves, we measured the planet/star radius ratio with a

Table 4. Midtransit times and their deviation from a linear ephemeris.

Epoch	Mid-transit time [HJD_{TDB} − 2 450 000]	O−C [min]	Deviation in σ
−1537	4817.14633 ± 0.00021	−0.24 ± 0.30	0.8
−876	5338.56927 ± 0.00023	0.27 ± 0.33	0.8
−621	5539.72327 ± 0.00030	0.36 ± 0.44	0.8
−583	5569.69826 ± 0.00036	−0.92 ± 0.53	1.8
−564[a]	5584.68693 ± 0.00024	0.12 ± 0.34	0.4
−564[b]	5584.68684 ± 0.00019	−0.00 ± 0.28	0.0
−541	5602.83138 ± 0.00046	1.78 ± 0.67	2.7
−536	5606.77464 ± 0.00022	0.44 ± 0.32	1.4
−535	5607.56241 ± 0.00033	−1.10 ± 0.47	2.3
−516	5622.55057 ± 0.00026	−0.79 ± 0.38	2.1
−503	5632.80612 ± 0.00025	0.14 ± 0.36	0.4
−474	5655.68222 ± 0.00045	−0.19 ± 0.66	0.3
−455	5670.66976 ± 0.00064	−0.78 ± 0.93	0.8
0	6029.59250 ± 0.00035	0.67 ± 0.51	1.3
43	6063.51174 ± 0.00030	−0.54 ± 0.44	1.2

Notes. The values were obtained from the combined analysis of all transits while the ephemeris was fixed to the one quoted in Table 2. [a] TRAPPIST lightcurve. [b] EulerCam lightcurve.

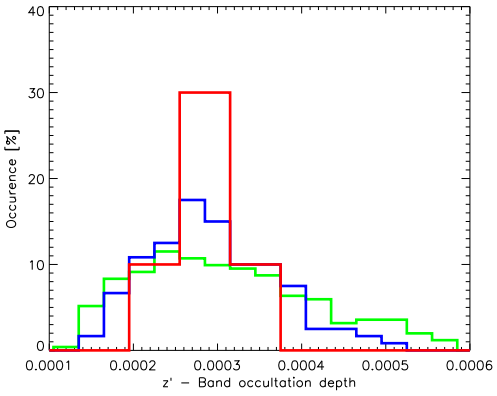

Fig. 10. Histogram of the results obtained from modeling combinations of five (green), seven (blue), and nine (red) occultations.

precision of 0.7% in $I + z'$-band, while three observations with EulerCam in r'-band and a combination of two EulerCam lightcurves and an FTS yield slightly larger errors, giving a precision of 0.9 and 1.0%. While these values agree well within their error bars, a single lightcurve obtained in IC-band gives a 2.6σ lower value. This lightcurve shows a small flux increase during transit (possibly the signature of a star spot), and we suggest that this possible radius variation be verified with additional data. Discarding this point, we see a flat optical transmission spectrum of WASP-19b. Overall, the values derived from our analysis are in good agreement with the values previously derived.

With two new occultation measurements, we can proceed to constrain the chemical composition and structure of the planetary atmosphere. For this purpose, we use the model spectra calculated by Madhusudhan (2012). In their work, they show models of WASP-19b for a carbon-dominated C/O = 1.1 and an oxygen-dominated C/O = 0.4 atmosphere. For oxygen-rich models, a strong absorption around 0.9 μm is expected from the TiO and VO leading to a smaller z'-band occultation depth. Following the occultation measurement by Burton et al. (2012), Madhusudhan (2012) tentatively classified WASP-19b as having a carbon-dominated atmosphere.

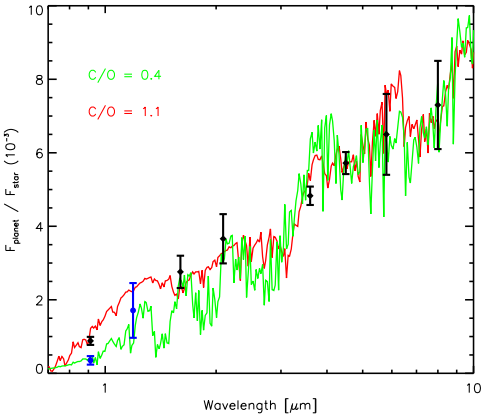

Fig. 11. Model spectra of the dayside atmosphere of WASP-19b computed by Madhusudhan (2012) compared to observations. The z'-band and 1.19 μm observations presented in this work are shown in blue, while the data of Anderson et al. (2010, 2011); Burton et al. (2012) and Gibson et al. (2010) are shown in black. The two model atmospheres shown have been computed for the carbon-dominated (C/O = 1.1, red) and oxygen-dominated (C/O = 0.4, green) case and are reproduced here with kind permission of N. Madhusudhan.

Comparing our values to these models (see Fig. 11), we find our measurement of the z'-band matches the oxygen-rich model extremely well, showing higher absorption, indicative of higher abundances in TiO and VO. These elements require a higher concentration of oxygen in the planetary atmosphere in order to contribute measurably to the planetary spectrum. The 1.19 μm value matches the oxygen- and carbon-rich models equally well. Thus, we suggest WASP-19b is a highly irradiated oxygen-dominated planet, fitting the *O2* or upper *O1* Class defined by Madhusudhan (2012). This should be confirmed by a joint analysis of the previously published data and the measurements added in this work since the models of planetary emission are not unique.

From the *Spitzer* data on WASP-19b (Anderson et al. 2011), we know that WASP-19b does not show any temperature inversion. At first glance, this might seem unexpected for an oxygen-dominated atmosphere, because it is precisely the molecules of which we measure higher concentrations that are presumed to be causing temperature inversions. Still, as different wavelengths probe different depths in the planetary atmosphere, the z'-band observations probe a deeper atmospheric layer, which is below the expected temperature inversion. In this context it would be interesting to evaluate the effects of gravitational settling and stellar UV radiation on the presence and distribution of TiO and VO in the planetary atmosphere. TiO and VO might be destroyed or depleted from the upper atmosphere, thus inhibiting a temperature inversion, while lower in the atmosphere the intact TiO and VO could be causing the measured absorption in the z' band.

6. Conclusion

We have carried out an in-depth observing campaign on WASP-19 collecting a total of 14 transit and 10 occultation lightcurves with EulerCam and TRAPPIST, as well as one 1.19 μm lightcurve with HAWK-I. From the large homogeneous set of nine TRAPPIST lightcurves, we demonstrate how both the attainable photometric precision and the accuracy of the derived parameters can be greatly improved by combining an increasing number of lightcurves.

We have detected the z'-band occultation of WASP-19b using 1 m class telescopes by the combined analysis of our lightcurves. We measure it at 352 ± 116 ppm, more than a factor of two smaller than previously published. From our HAWK-I data we obtain an occultation depth of 1711^{+750}_{-730} ppm at 1.19 μm. These results shed new light on the chemical composition of the planetary atmosphere, indicating a C/O ratio of C/O < 1, i.e. an oxygen-dominated atmosphere.

Acknowledgements. We would like to thank Nikku Madhusudhan for sharing with us the model spectra of WASP-19b. TRAPPIST is a project funded by the Belgian Fund for Scientific Research (Fond National de la Recherche Scientique, F.R.SFNRS) under grant FRFC 2.5.594.09.F, with the participation of the Swiss National Science Foundation (SNF). M. Gillon and E. Jehin are FNRS Research Associates.

References

Albrecht, S., Winn, J. N., Johnson, J. A., et al. 2012, ApJ, 757, 18
Alonso, R., Guillot, T., Mazeh, T., et al. 2009, A&A, 501, L23
Anderson, D. R., Gillon, M., Maxted, P. F. L., et al. 2010, A&A, 513, L3
Anderson, D. R., Smith, A. M. S., Madhusudhan, N., et al. 2011 [arXiv:1112.5145]
Borucki, W. J., Koch, D., Jenkins, J., et al. 2009, Science, 325, 709
Burton, J. R., Watson, C. A., Littlefair, S. P., et al. 2012, ApJS, 201, 36
Casali, M., Pirard, J.-F., Kissler-Patig, M., et al. 2006, in SPIE Conf. Ser., 6269
Charbonneau, D., Allen, L. E., Megeath, S. T., et al. 2005, ApJ, 626, 523
Claret, A., & Bloemen, S. 2011, A&A, 529, A75
Croll, B., Albert, L., Lafreniere, D., Jayawardhana, R., & Fortney, J. J. 2010, ApJ, 717, 1084
de Mooij, E. J. W., & Snellen, I. A. G. 2009, A&A, 493, L35
Deming, D., Seager, S., Richardson, L. J., & Harrington, J. 2005, Nature, 434, 740
Eastman, J., Siverd, R., & Gaudi, B. S. 2010, PASP, 122, 935
Enoch, B., Collier Cameron, A., Parley, N. R., & Hebb, L. 2010, A&A, 516, A33
Fortney, J. J., Lodders, K., Marley, M. S., & Freedman, R. S. 2008, ApJ, 678, 1419
Gelman, A., & Rubin, D. 1992, Statist. Sci., 7, 457
Gibson, N. P., Aigrain, S., Pollacco, D. L., et al. 2010, MNRAS, 404, L114
Gillon, M., Smalley, B., Hebb, L., et al. 2009, A&A, 496, 259
Gillon, M., Lanotte, A. A., Barman, T., et al. 2010, A&A, 511, A3
Gillon, M., Jehin, E., Magain, P., et al. 2011, Detection and Dynamics of Transiting Exoplanets, St. Michel l'Observatoire, France, eds. F. Bouchy, R. Díaz, & C. Moutou, EPJ Web Conf., 11, 6002
Gillon, M., Triaud, A. H. M. J., Fortney, J. J., et al. 2012, A&A, 542, A4
Giménez, A. 2006, ApJ, 650, 408
Hebb, L., Collier-Cameron, A., Triaud, A. H. M. J., et al. 2010, ApJ, 708, 224
Hellier, C., Anderson, D. R., Collier-Cameron, A., et al. 2011, ApJ, 730, L31
Holman, M. J., Winn, J. N., Latham, D. W., et al. 2006, ApJ, 652, 1715
Hubeny, I., Burrows, A., & Sudarsky, D. 2003, ApJ, 594, 1011
Jehin, E., Gillon, M., Queloz, D., et al. 2011, The Messenger, 145, 2
Knutson, H. A., Charbonneau, D., Allen, L. E., Burrows, A., & Megeath, S. T. 2008, ApJ, 673, 526
Knutson, H. A., Howard, A. W., & Isaacson, H. 2010, ApJ, 720, 1569
Lendl, M., Anderson, D. R., Collier-Cameron, A., et al. 2012, A&A, 544, A72
López-Morales, M., Coughlin, J. L., Sing, D. K., et al. 2010, ApJ, 716, L36
Madhusudhan, N. 2012, ApJ, 758, 36
Madhusudhan, N., Harrington, J., Stevenson, K. B., et al. 2011, Nature, 469, 64
Mandel, K., & Agol, E. 2002, ApJ, 580, L171
McLaughlin, D. B. 1924, ApJ, 60, 22
Pirard, J.-F., Kissler-Patig, M., Moorwood, A., et al. 2004, in SPIE Conf. Ser. 5492, eds. A. F. M. Moorwood, & M. Iye, 1763
Pollacco, D. L., Skillen, I., Collier Cameron, A., et al. 2006, PASP, 118, 1407
Pont, F., Zucker, S., & Queloz, D. 2006, MNRAS, 373, 231
Rossiter, R. A. 1924, ApJ, 60, 15
Schneider, J., Dedieu, C., Le Sidaner, P., Savalle, R., & Zolotukhin, I. 2011, A&A, 532, A79
Schwarz. 1978, Ann. Statist., 6, 461
Seager, S., & Mallén-Ornelas, G. 2003, ApJ, 585, 1038
Sing, D. K., & López-Morales, M. 2009, A&A, 493, L31
Smith, A. M. S., Anderson, D. R., Skillen, I., Collier Cameron, A., & Smalley, B. 2011, MNRAS, 416, 2096
Snellen, I. A. G., de Mooij, E. J. W., & Albrecht, S. 2009, Nature, 459, 543
Southworth, J., Hinse, T. C., Jørgensen, U. G., et al. 2009, MNRAS, 396, 1023
Spiegel, D. S., Silverio, K., & Burrows, A. 2009, ApJ, 699, 1487
Tregloan-Reed, J., Southworth, J., & Tappert, C. 2013, MNRAS, 428, 3671
Winn, J. N., Holman, M. J., Torres, G., et al. 2008, ApJ, 683, 1076

The most effective way to do it, is to do it.
Amelia Earhart

6 SPECTRO-PHOTOMETRY

6.1 Motivation

The final stop in the scientific journey of my PhD was to move to the latest techniques for the study of exoplanet atmospheres: spectrophotometry. This technique has been introduced previously in Sections 2.3 and 1.2.6, but let it be briefly rediscribed here.

During transit, the planetary atmosphere imprints its signature on the stellar light passing through it. Depending on the atmospheric composition and scale height, wavelength-dependent variations are seen in the observed absorption and consequently the inferred planetary radius. The planet's transmission spectrum is therefore obtained from transit lightcurves at different wavelengths. When constructing an exoplanet transmission or emission spectrum, simultaneous observations at different wavelengths are of a great advantage. They capture the star-planet system during one instant in time, eliminating systematic effects both due to changes in the host star (e.g. activity) and variations in the planetary atmosphere (e.g. cloud structures). The first effect, stellar activity, can have a non-negligible effect on the transmission spectrum, as a variation of 1% in the stellar brightness induces variations comparable in size to the signal one intends to measure. In practice, spectrophotometry is obtained in a similar way as traditional relative photometry, but by dispersing the light of target and reference stars instead of defining the wavelength region via filters. Before dispersion, the field of view is obscured, and only the light of the desired stars is selected either by movable slits or a specifically created mask. The dispersed spectra of each star are then binned in wavelength, and lightcurves are created for each wavelength bin via relative photometry of target and reference stars. The resolution of the resulting transmission or emission spectrum is given by the wavelength coverage and bin size. Here it is useful to find the best compromise between spectral resolution and noise level.

We have already met WASP-49 b as one of the planets I had the privilege of announcing in Lendl et al. (2012). WASP-49 b is a hot Saturn with a low density and hence its atmosphere is predicted to have a large scale height. The host star is a calm G6 V star with a visual magnitude of $V_{mag} = 11.36$, a good value for ground-based follow-up observations. These two advantages make WASP-49 b one of the best targets for transmission spectroscopy.

In this chapter I describe my efforts in creating a ground-based transmission spectrum of WASP-49 b, based on an observing campaign using the *FORS2* instrument at the ESO Very Large Telescope (VLT).

6.2 FORS2 – the Instrument

The FORS2 (**FO**cal **R**educer and low dispersion **S**pectrograph) instrument (Appenzeller et al. 1998) is installed at the VLT/UT1. FORS2 can be used with two detectors, the standard red-sensitive *MIT* and a more blue-sensitive *e2v* detector that was previously part of the now decomissioned FORS1 twin instrument. The instrument can be used in imaging, polarimetry, and low-resolution spectroscopy mode including multi-object spectroscopy. The latter is the mode used for spectrophotometry.

Spectrophotometric observations of exoplanets have been first carried out with FORS2 by Bean et al. (2010) to measure the transmission spectrum of the hot SuperEarth GJ1214 b. Several other targets have been observed since then by various groups, but results have not been published in refereed jour-

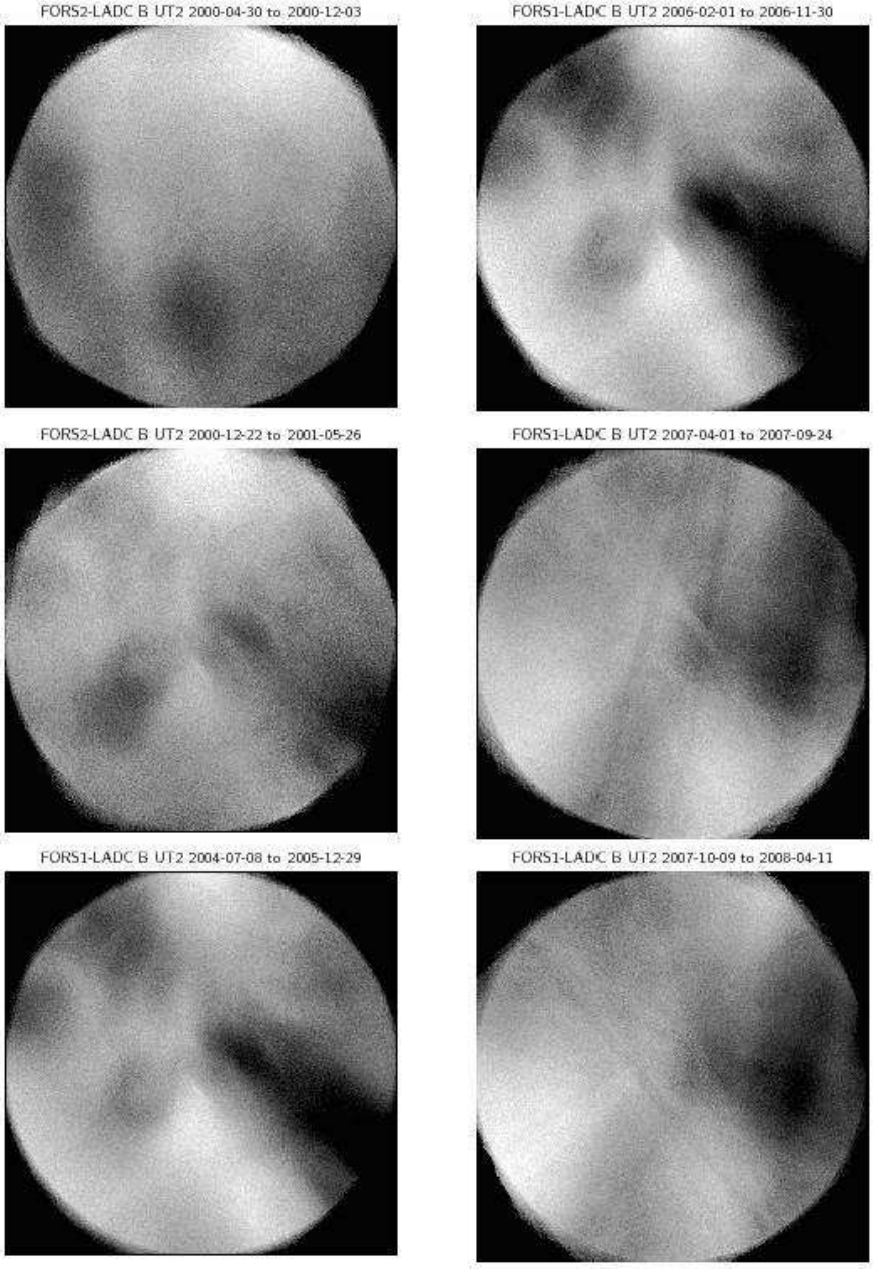

Figure 6.1 : The LADC component of the FORS flatfield, extracted from a large set of archival data by Moehler et al. (2010). The different images represent the component at different times.

nals. The major limitation of FORS2 is given by inhomogeneities in transmission of its atmospheric dispersion corrector (**L**inear **A**tmospheric **D**ispersion **C**orrector, **LADC**). The LADC is composed of two prisms that change their separation to compensate the elongation and spectral dispersion of astronomical objects at high airmass. The prisms are located in the optical path above the image derotator and thus the field rotates with respect to the LADC during the observing sequence. This means that the inhomogeneities in the LADC add a rotation dependent flat field component to the images. This effect has been studied in detail by Moehler et al. (2010), who identified the LADC as the noise source hence the orientation of the structures scales with the parallactic angle. They also found that the structures are temporally variable. Their measurements spanning flat fields from 2000 to 2008 are shown in Figure 6.1 .

Another effect that might affect spectrophotometric observations are flux losses at the edges of the slits. If the slits are too narrow, PSF or guiding variations can cause the wings of the stellar PSFs to fall outside the slit, and so flux is lost to the observation. Very slight differences in these losses between target and reference stars then introduce systematics in the lightcurves. For this reason it is beneficial

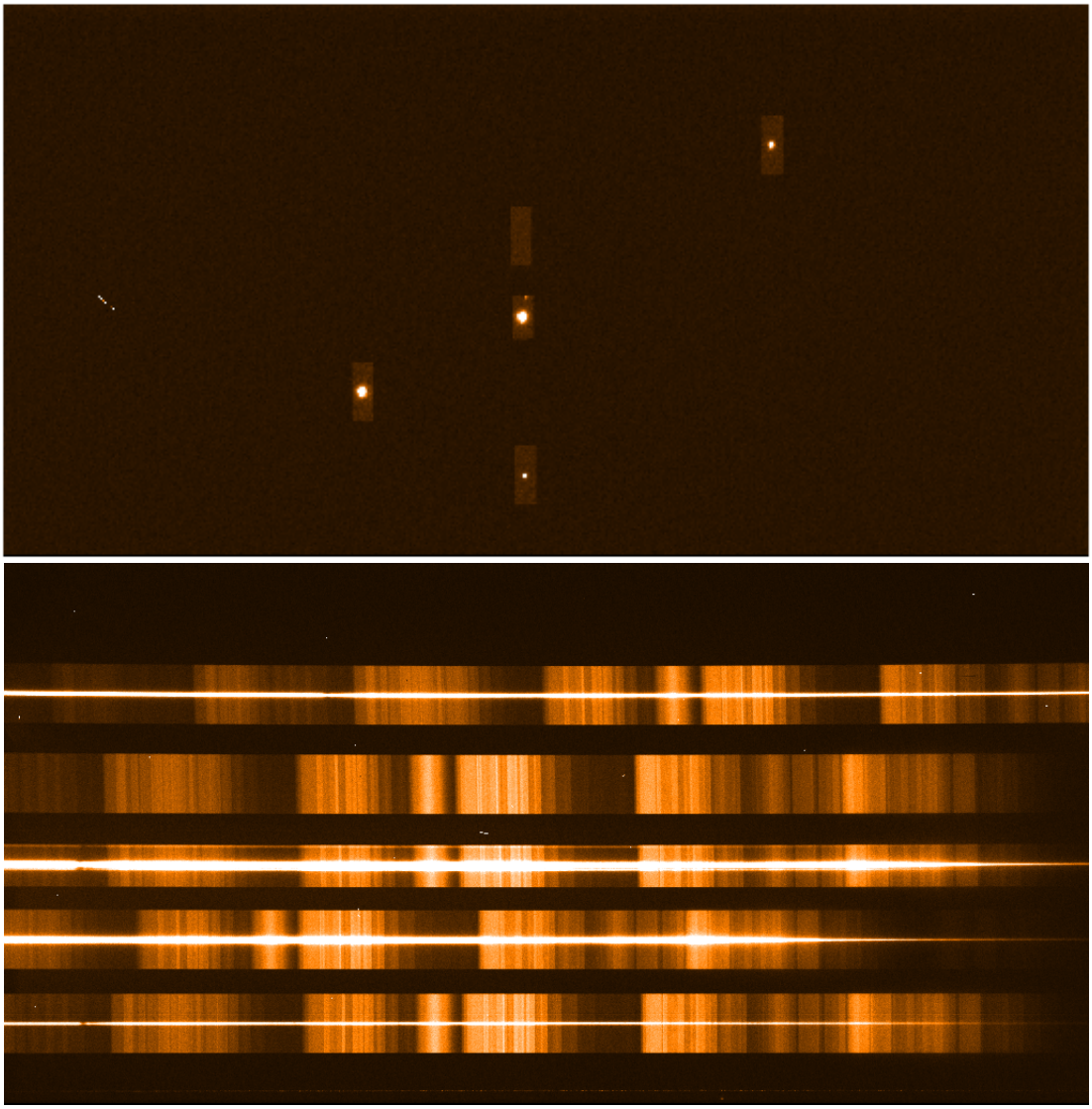

Figure 6.2 : Top: An acquisition image for the WASP-49 FORS2 observations. The mask with five slits is visible, four of the slits are placed on stars, while one is placed on the sky. Bottom: The same field and instrument setup but the dispersive element has been introduced, converting the slits imaged above into spectra.

to use the largest possible slits. Neighboring stars need to be excluded from the aperture if they are located in the dispersion direction as their spectra would blend with that of the target.

6.3 Observations and Data Reduction

6.3.1 FORS2 Spectrophotometry

Observations

Three transits of WASP-49 b were observed (in service mode) with FORS2 (Appenzeller et al. 1998) at the VLT/UT1 during the nights of 05 December 2012, 14 January 2013 and 07 February 2013, under program no. 090.C-0758 (PI Gillon). The instrument was used in MXU mode, which allows to obtain ($R \sim 1000$) spectra of several objects in the field of view by placing a laser cut mask in the focal plane and then disperse the selected objects with a grism. We placed slits of 10 by 28 arcsec (in one case 10 by

20 arcsec) on the target and three reference stars, and used grism GRIS_600z together with the order selection filter OG590. The resulting wavelength range is $738-1026$ nm for WASP-49. The wavelength range of the reference stars is slightly different owing to their position on the detector and thus the displacement of their spectra on the chip (see Figures 6.3 and 6.2).

To reduce systematic noise stemming from the LADC, the LADC prism separation was set to a constant value throughout each transit observation. For the first two nights this value was set by the previous instrument configuration, 155.0 mm for 05 December 2012, and 898.1 mm for 14 January 2013. The observation obtained with the smaller prism separation showed superior photometric quality and less correlated noise. Consequently, the LADC was set to a minimum separation of 30 mm for the third (14 February 2013) observation. The conditions during the first two observations were good, with stable seeing around 0.9 arcsec (05 December 2012) and seeing between 0.8 and 1.5 arcsec (14 January 2013). The data obtained on 07 February 2013 were affected by variable and bad seeing, between 1.0 and 2.5 arcsec. The exposure times used were 30 s (adapted down to 25 s after the end of the transit) for the first observation, and 20 s for the other observations. The third observation was interrupted by a technical malfunction before the beginning of the transit.

For the wavelength calibration a HeArNe lamp spectrum was used but with only 0.5 arcsec wide slits in order to provide well defined non-saturated emission lines to match with the database.

During the pre-imaging of the target field we discovered the presence of a faint star ($\Delta \mathrm{mag}_z = 4.303 \pm 0.12$) at a distance of 2.5 arcsec from WASP-49. See Figure 6.4 for a 3D representation of the PSFs. This star was blended with WASP-49 in previous observations.

Data Reduction

The ESO pipeline was used for the production of the master calibration frames, as well as for the first determination of the wavelength solution (a 3rd order polynomial based on the lamp frames). The wavelength solution was later refined by matching prominent absorption lines in the mean stellar spectra. For the extraction of spectrophotometric measurements, I proceeded using custom-built routines. For each pixel, the PSF in the spatial direction was determined iteratively via a Moffat function (Moffat 1969) using the `mpfit` routines (Markwardt 2009). Outliers (typically cosmics) were rejected at this step and then replaced by the fit values. For the background removal, a first order polynomial was fit in the spatial dimension of the spectra to regions well outside the stellar PSF and then this fit was subtracted at each pixel. This compensated slight variations in the background due to bends in the spectra with respect to the CCD pixel grid. The spectra were extracted for several one dimensional "apertures", i.e. regions of different widths centered on the PSF peak. For each of these "apertures", the one-dimensional spectra were created by summing up the flux inside it at each spectral pixel. At this point data affected by saturation of the detector during the 05 December 2012 observation were identified and removed from further analysis.

To derive the contamination of the spectrum of WASP-49, the PSF was subtracted from the data and then the contaminant flux falling inside the "aperture" was measured. To get a second estimate of the target/contaminant flux ratio, the PSF of the contaminant was fitted in the same way as that of the target, and the peaks compared. The resulting values averaged for all three transits and for each spectral bin are shown in Figure 6.4 .

Once the spectra of all exposures were extracted, outliers were removed once more, this time based on the temporal domain. For each spectral pixel, the extracted flux values were fit with a 4th order polynomial with respect to time, outliers were identified and replaced by the values of the fit at the same position.

Then the relative lightcurves displayed in Figures 6.6 , 6.7 and 6.8 were produced by binning the spectra in the 10 nm bins indicated in blue in Figure 6.3 . All combinations of references were tested; the best lightcurves were obtained using all references available in each wavelength bin.

For all further analysis, the lightcurves obtained from large extraction windows were used: 32 pixels for the 05 December 2012 and 14 January 2013 transits, and 36 pixels for the 07 February 2013 transit.

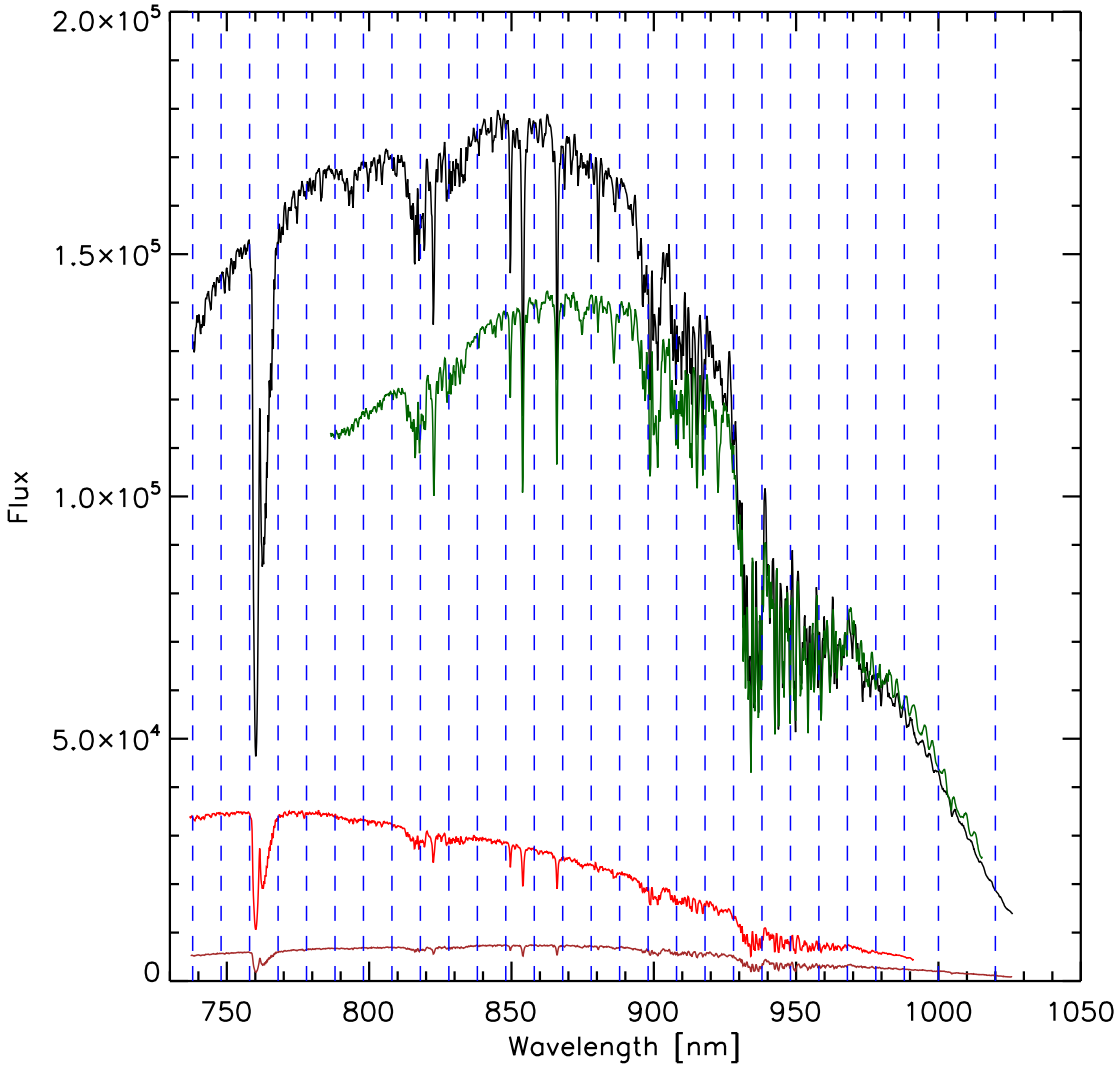

Figure 6.3 : An example of the spectra of WASP-49 (black), and the three reference stars (green, red, brown). The blue dashed lines indicate the bins used for spectrophotometry. Note that for the five shortest-wavelength bins only the two faint reference stars are available.

This way the contaminating star was contained in the aperture and its contribution to the lightcurve kept as stable as possible.

6.3.2 EulerCam and TRAPPIST Photometry

Two additional transit lightcurves of WASP-49 were obtained using EulerCam at the 1.2 m Euler-Swiss telescope at the La Silla site (Chile). During the night of 5 December 2012 a wide (520 nm to 880 nm) filter designed for the upcoming *NGTS* survey (Wheatley et al. 2013) was used, while during the night of 30 December 2012, an r'-Gunn filter was used. The telescope was slightly defocused for both observations, and exposure times were between 35s and 60s (December 5), and 90s (December 30). The data were reduced using relative aperture photometry. More details on instrument and reduction can be found in Chapter 3.

The TRAnsiting Planets and PlanetesImals Small Telescope (TRAPPIST, Gillon et al. (2011b), Jehin et al. (2011)) is also located at the La Silla site. It was used to observe four more transits through an

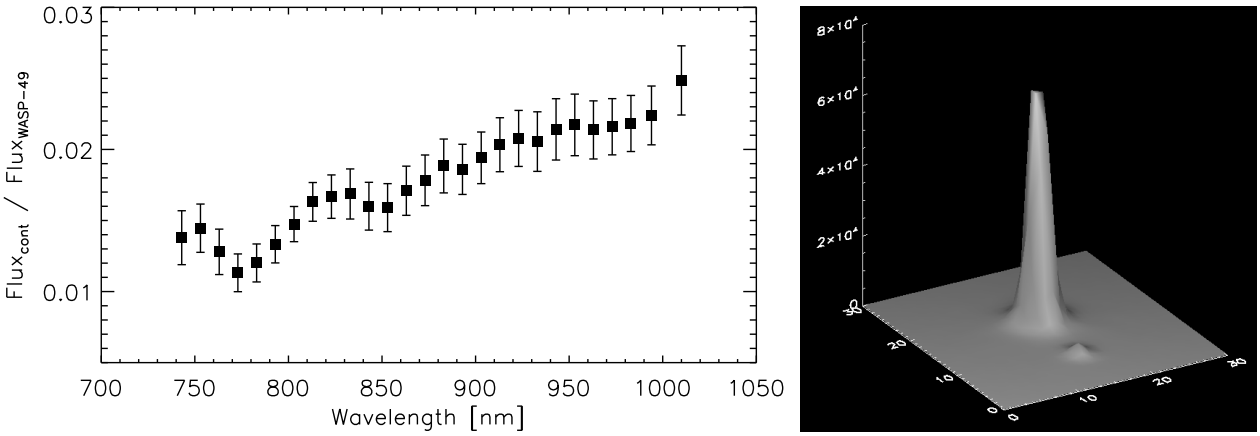

Figure 6.4 : Left: the contamination on WASP-49 b from the blended star, as a function of wavelength. The contamination increases with wavelength indicating that it stems from a redder source than WASP-49. Right: the PSF of WASP-49 (saturated) and the contaminant as seen in the pre-imaging data. The image size is 3.75 × 3.75 arcsec.

I+z' filter during the nights of 5, 16, and 30 December 2012, and 21 February 2013. The exposure times used were 6 s (first two transits) and 10 s (last two transits). The lightcurves were produced using relative aperture photometry, where several apertures were tested and the ideal combination of reference stars was found. IRAF [1] was used in the reduction process.

Included in the analysis are also the two full transit lightcurves of each EulerCam and TRAPPIST that have been already described in Lendl et al. (2012). All broadband lightcurves are shown in Figure 6.5 .

6.4 Modeling

6.4.1 Modeling Procedure

To derive the transmission spectrum of the planet and find improved measurements of the planetary and stellar parameters a Markov Chain Monte Carlo (MCMC) approach was used. Included in the analysis were all available photometric data as described in Section 6.3 (FORS2, EulerCam and TRAPPIST).

I made use of the adaptive MCMC code described in detail in Gillon et al. (2012). In this code, a Keplerian is used to model the radial velocity measurements while the prescription of Mandel & Agol (2002) is applied for the transit lightcurves. The jump parameters are: $b' = a\cos(i_p)/R_*$ (where R_p and R_* denote the planetary and stellar radii, a the semi-major axis of the planetary orbit, and i_p the orbital inclination), the transit duration d, the time of midtransit T_0, the orbital period P, the transit depth $dF_i = (R_p/R_*)_i^2$ for each wavelength band i, the stellar parameters effective temperature $T_{\rm eff}$ and metallicity [Fe/H]. The value for the RV amplitude K was set to that of the discovery paper.

Uniform prior distributions were assumed for most parameters. For the stellar effective temperature $T_{\rm eff}$ and metallicity [Fe/H] a normal prior distribution was used centered on the values of Lendl et al. (2012) with the width corresponding to their 1- σ errors.

The eccentricity was set to zero as there has been no evidence for an eccentric orbit of WASP-49b. A quadratic model was used to account for the effect of stellar limb-darkening on the transit lightcurves, and I interpolated the limb darkening coefficients from those tabulated by Claret & Bloemen (2011) to match the wavelength bands of this observations. The limb darkening parameters are kept fixed in the analysis. The method described in Enoch et al. (2010) and Gillon et al. (2011a) was used to

[1] IRAF is distributed by the National Optical Astronomy Observatories, which are operated by the Association of Universities for Research in Astronomy, Inc., under cooperative agreement with the National Science Foundation.

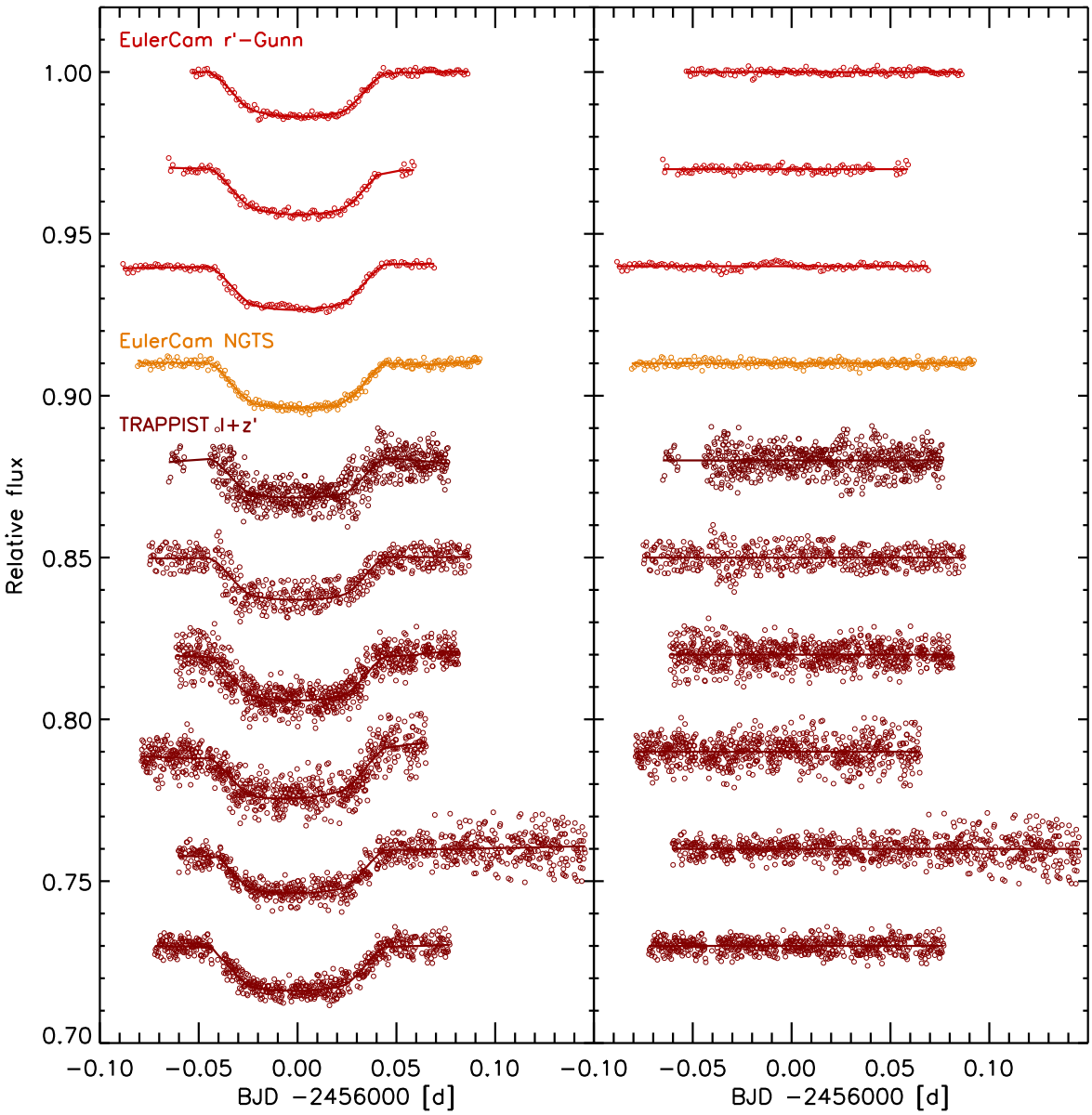

Figure 6.5 : The WASP-49 transit lightcurves from EulerCam and TRAPPIST included in the analysis. The instrument and filters are color coded, and are (from top to bottom) EulerCam using an r'-Gunn filter (top three), EulerCam using the NGTS filter (fourth), and TRAPPIST using an I+z' filter (all remaining lightcurves).

derive the stellar radius and mass from the transit lightcurve, the stellar temperature and metallicity. The contribution (and its error) from the neighboring star was included in the analysis and the transit depths were adapted.

To compensate for correlated noise in the lightcurves, several external parameters can be included in the MCMC as a baseline model for the photometric time series. This is done via polynomials of up to fourth order that are multiplied with the theoretical transit lightcurve, and the coefficients of which are found by minimization at every MCMC step. As the FORS2 data are clearly affected by the rotation of the LADC across the field of view (or, more precisely, the rotation of the detector with respect to the optical components), I tested the parallactic angle *par*, the change in parallactic angle *dpar* (i.e. the derotator speed), and the functions sin(*par*) and cos(*par*) next to the sky background, FWHM, time and (for the EulerCam and TRAPPIST data) coordinate shifts. Including either *par* or sin(*par*) lead to a much better fit of the overall lightcurve shape as a simple time dependence does, especially for those lightcurves that show large systematics caused by the LADC. A variety of parameter combinations were tested in order to find the best model, always preferring a simple model over a more complicated one unless the Bayes factor (e.g. Schwarz 1978) estimated from the Bayesian information criterion indicated significantly highter probability.

The photometric error bars were rescaled by calculating the white β_w and red β_r noise scale factors from a first MCMC chain. β_w is given by the ratio of the mean photometric error and the standard deviation of the final photometric residuals, and β_r (Winn et al. 2008, Gillon et al. 2010) is derived by comparing the standard deviations of the binned and unbinned residuals. I multiplied the errors with their product $CF = \beta_r \times \beta_w$ for the final analysis. These values together with the final baseline models are given in Table 6.1. Red noise and white noise are described in more details in Section 5.2 together with the definition of β_w and β_r.

6.4.2 Individual Observations

The analysis of the additional EulerCam and TRAPPIST data did not require any additional fine-tuning or unusual baseline functions. The resulting lightcurves are depicted in Figure 6.5 , and the baseline functions are given in Table 6.1. The FORS2 data however showed a very high level of correlated noise and some anomalies occurred during the observation process. Therefore these data are discussed in detail here.

FORS2 5 December 2012

The FORS2 observations of 5 December 2012 were carried out throughout the transit using an exposure time of 30 s, however the peak of the target spectrum exceeded the non-linear range of the detector from ∼05:15 UT on, until the exposure time was adapted down to 25 s at 06:14 UT. Points affected by this episode of saturation were excluded from the analysis, together with a handful of points obtained with a larger exposure time at the very beginning of the sequence. I carried out MCMC analyses for the complete (30 and 25 s exposures) series as well as only for the 30 s part. Analyzing the entire sequence required more complex baseline models including an offset at the change of exposure time. As only a short part of the data were obtained with the shorter exposure time, and all of these data are outside transit, I decided to use only the 30 s part for the definitive analysis. The five bluest lightcurves show a very particular wave-like pattern around meridian passage. These are the same lightcurves that were created using only two reference stars, as the brightest one does not cover those wavelengths. A probable explanation for this effect is the rotation of a dark spot on the LADC across one of the fainter reference stars. The effect can be modeled using 4th order polynomials in $\cos(par)$, while the overall lightcurve shape in all other bins is best fit by using a second order polynomial in $\cos(par)$. The use of $\cos(par)$ reproduces the lightcurve shapes more efficiently than a time-dependent term. An additional term in the FWHM is beneficial for some lightcurves. The final baseline models for each lightcurve are given in Table 6.1, and the lightcurves are displayed in Figure 6.6 .

FORS2 14 January 2013

The bluest five lightcurves obtained with FORS2 on 14 January 2013 also show a wave-like pattern around meridian passage, presumably for the same reason as for the 5 December 2012 data. For this transit, it can be modeled best with a 4th order polynomial in the change of position angle *dpar*. The overall shapes of the lightcurves of this date show strong trends, that vary in shape and amplitude. As for the 05 December 2012 observations, these are fit very well by a 2nd order polynomial in $\sin(par)$. After the removal of these large-scale trends, a few lightcurves still show unexplained trends at the very beginning of the observation. If unaccounted for, these points affect the measured transit depths by biasing the pre-transit flux, while if they are fit by third-order time polynomials, the introduced uncertainty on the transit depth increases due to the complex baseline. To avoid both effects, I excluded the most diverging lightcurve parts from the analysis, and add a 1st-order polynomial in time where warranted by a significant BIC improvement. The final baseline models for each lightcurve are given in Table 6.1, and the lightcurves are displayed in Figure 6.7 .

FORS2 7 February 2013

The FORS2 data taken on 7 February 2013 were affected by less favorable conditions than the other transit observations. The seeing was variable and very large at the beginning and end of the time series. The observations were interrupted due to a technical problem between 02:08 UT and 02:29 UT. The data obtained before the interruption show large variations, related to unfavorable seeing as well as the passage of meridian, and I thus decided to exclude them from the fit rather than complicate the models to fit for them. A small number of points heavily affected by a short-term increase in seeing after the transit are also excluded. Some lightcurves show an unexplained short-term increase in flux during egress. MCMCs were ran for the 07 January 2013 data alone, both including and excluding these points, the results agreeing well within 0.5 σ. For the global analysis I opt to discard these points as the effect is most likely instrumental instead of astrophysical. All lightcurves were modeled with a 2nd order polynomial in the parallactic angle par together with a 1st order polynomial in FWHM. The final baseline models for each lightcurve are given in Table 6.1, and the lightcurves are displayed in Figure 6.6 .

Table 6.1: Details on the observations: date, wavelength band, baseline parameters and noise statistics of all data included in the global analysis of WASP-49 b. The baseline functions of the form $p(i)^j$ denote a polynomial of order j in parameter i, where i can be time t, parallactic angle par, it's sine or cosine $\sin(par)$, $\cos(par)$, the differential parallactic angle from one exposure to the next *dpar*, and the PSF or spectra full-width at half maximum *fwhm*. *off* refers to an offset in some TRAPPIST lightcurves caused by a meridian flip of the telescope. The red- and white noise amplitudes β_r and β_w, and the error adaptation factor CF are those defined in Section 5.2, and the RMS is given for a data binned in bins of two minutes. For the FORS2 data, the four data quality parameters are given for the global fit (left) and for a fits restricted to single transit events (right).

Wavelength [nm]	date	Baseline function	β_r		β_w		CF		RMS_{120s} [%]	
FORS2										
738 - 748	05 Dec 2012	$p(\cos(par)^4)$	1.67	1.24	1.04	1.08	1.74	1.34	0.086	0.082
	14 Jan 2013	$p(\sin(par)^2)+p(dpar^4)$	1.30	1.26	1.03	1.06	1.34	1.34	0.091	0.091
	07 Feb 2013	$p(fwhm^1)+p(par^2)$	1.44	1.34	0.92	0.97	1.33	1.30	0.108	0.106
748 - 758	05 Dec 2012	$p(fwhm^1)+p(\cos(par)^4)$	1.53	1.39	1.06	1.12	1.62	1.55	0.100	0.097
	14 Jan 2013	$p(\sin(par)^2)+p(dpar^4)$	1.48	1.45	0.98	1.00	1.45	1.45	0.096	0.094
	07 Feb 2013	$p(fwhm^1)+p(par^2)$	1.67	1.55	0.78	0.81	1.31	1.25	0.090	0.086
758 - 768	05 Dec 2012	$p(fwhm^1)+p(\cos(par)^4)$	1.67	1.24	0.78	1.04	1.31	1.29	0.104	0.099
	14 Jan 2013	$p(\sin(par)^2)+p(dpar^4)$	1.69	1.69	1.05	1.05	1.78	1.78	0.104	0.102
	07 Feb 2013	$p(fwhm^1)+p(par^2)$	2.91	2.47	0.69	0.79	2.02	1.94	0.135	0.133
768 - 778	05 Dec 2012	$p(\cos(par)^4)$	1.53	1.42	1.17	1.19	1.79	1.70	0.098	0.096
	14 Jan 2013	$p(\sin(par)^2)+p(dpar^4)$	2.15	1.52	1.05	1.48	2.25	2.25	0.108	0.102
	07 Feb 2013	$p(fwhm^1)+p(par^2)$	1.55	1.28	0.87	1.03	1.35	1.31	0.119	0.118
778 - 788	05 Dec 2012	$p(fwhm^1)+p(\cos(par)^4)$	1.42	1.23	0.92	1.15	1.31	1.41	0.080	0.079
	14 Jan 2013	$p(\sin(par)^2)+p(dpar^4)$	1.76	1.50	0.90	1.05	1.58	1.58	0.080	0.078

	07 Feb 2013	$p(fwhm^1)+p(par^2)$	2.98	2.68	0.85	1.16	2.54	3.10	0.099	0.094
788 - 798	05 Dec 2012	$p(\cos(par)^4)$	1.20	1.44	0.83	0.84	1.00	1.21	0.057	0.058
	14 Jan 2013	$p(\sin(par)^2)+p(dpar^4)$	1.20	1.16	0.83	0.86	1.00	1.00	0.056	0.057
	07 Feb 2013	$p(fwhm^1)+p(par^2)$	2.86	1.55	0.40	1.08	1.13	1.67	0.070	0.062
798 - 808	05 Dec 2012	$p(\cos(par)^2)$	1.47	1.02	0.68	0.98	1.00	1.00	0.047	0.046
	14 Jan 2013	$p(\sin(par)^2)$	2.80	1.69	0.48	0.79	1.34	1.34	0.053	0.048
	07 Feb 2013	$p(fwhm^1)+p(par^2)$	1.78	1.08	0.56	0.93	1.00	1.00	0.067	0.064
808 - 818	05 Dec 2012	$p(\cos(par)^2)$	1.62	1.46	0.67	0.73	1.08	1.07	0.053	0.055
	14 Jan 2013	$p(\sin(par)^2)$	1.50	1.45	0.75	0.78	1.13	1.13	0.051	0.051
	07 Feb 2013	$p(fwhm^1)+p(par^2)$	2.21	1.46	0.48	0.69	1.06	1.01	0.056	0.054
818 - 828	05 Dec 2012	$p(fwhm^1)+p(\cos(par)^2)$	2.12	2.03	0.69	0.73	1.46	1.49	0.054	0.053
	14 Jan 2013	$p(\sin(par)^2)$	2.50	1.94	0.65	0.84	1.63	1.63	0.060	0.056
	07 Feb 2013	$p(fwhm^1)+p(par^2)$	1.99	1.35	0.50	0.74	1.00	1.00	0.059	0.054
828 - 838	05 Dec 2012	$p(fwhm^1)+p(\cos(par)^2)$	1.20	1.32	0.83	0.76	1.00	1.00	0.053	0.054
	14 Jan 2013	$p(\sin(par)^2)$	1.88	1.68	0.68	0.76	1.28	1.28	0.057	0.055
	07 Feb 2013	$p(fwhm^1)+p(par^2)$	2.58	1.25	0.59	0.80	1.53	1.00	0.064	0.059
838 - 848	05 Dec 2012	$p(\cos(par)^2)$	1.15	1.03	0.87	0.97	1.00	1.00	0.051	0.052
	14 Jan 2013	$p(\sin(par)^2)$	1.75	1.41	0.63	0.78	1.10	1.10	0.049	0.047
	07 Feb 2013	$p(fwhm^1)+p(par^2)$	2.58	1.72	0.53	0.78	1.38	1.34	0.067	0.062
848 - 858	05 Dec 2012	$p(fwhm^1)+p(\cos(par)^2)$	2.33	1.14	0.43	0.88	1.00	1.00	0.058	0.050
	14 Jan 2013	$p(\sin(par)^2)$	2.07	1.45	0.63	0.90	1.30	1.30	0.054	0.052
	07 Feb 2013	$p(fwhm^1)+p(par^2)$	2.43	1.64	0.49	0.75	1.19	1.24	0.068	0.063
858 - 868	05 Dec 2012	$p(fwhm^1)+p(\cos(par)^2)$	3.13	2.22	0.82	0.64	2.57	1.41	0.051	0.049
	14 Jan 2013	$p(\sin(par)^2)$	1.89	1.44	0.69	0.90	1.30	1.30	0.051	0.050
	07 Feb 2013	$p(fwhm^1)+p(par^2)$	1.51	1.40	0.68	0.71	1.03	1.00	0.062	0.062
868 - 878	05 Dec 2012	$p(fwhm^1)+p(\cos(par)^2)$	1.14	1.15	0.88	0.87	1.00	1.00	0.062	0.062
	14 Jan 2013	$p(\sin(par)^2)$	1.85	1.36	0.64	0.88	1.19	1.19	0.055	0.053
	07 Feb 2013	$p(fwhm^1)+p(par^2)$	2.07	1.55	0.51	0.86	1.06	1.34	0.064	0.062
878 - 888	05 Dec 2012	$p(\cos(par)^2)$	1.98	1.60	0.78	0.95	1.55	1.51	0.055	0.054
	14 Jan 2013	$p(\sin(par)^2)$	2.00	1.38	0.57	0.83	1.14	1.14	0.053	0.050
	07 Feb 2013	$p(fwhm^1)+p(par^2)$	2.27	1.58	0.55	0.81	1.25	1.27	0.073	0.072
888 - 898	05 Dec 2012	$p(fwhm^1)+p(\cos(par)^2)$	1.50	1.40	0.79	1.01	1.18	1.42	0.063	0.063
	14 Jan 2013	$p(\sin(par)^2)$	1.19	1.24	0.93	0.90	1.11	1.11	0.060	0.060
	07 Feb 2013	$p(fwhm^1)+p(par^2)$	1.43	1.65	1.01	0.90	1.45	1.48	0.089	0.089
898 - 908	05 Dec 2012	$p(\cos(par)^2)$	1.30	1.23	0.85	0.90	1.10	1.11	0.063	0.061
	14 Jan 2013	$p(\sin(par)^2)$	1.37	1.36	0.85	0.86	1.17	1.17	0.062	0.062
	07 Feb 2013	$p(fwhm^1)+p(par^2)$	2.60	1.97	0.63	0.94	1.64	1.85	0.093	0.086
908 - 918	05 Dec 2012	$p(\cos(par)^2)$	1.36	1.41	0.93	0.89	1.26	1.25	0.062	0.062
	14 Jan 2013	$p(\sin(par)^2)$	1.21	1.86	1.40	0.91	1.69	1.69	0.056	0.060
	07 Feb 2013	$p(fwhm^1)+p(par^2)$	1.74	1.80	0.80	0.80	1.39	1.45	0.078	0.080
918 - 928	05 Dec 2012	$p(\cos(par)^2)$	2.09	1.40	0.58	0.92	1.22	1.28	0.063	0.058
	14 Jan 2013	$p(\sin(par)^2)$	2.45	2.10	0.71	0.83	1.74	1.74	0.064	0.062
	07 Feb 2013	$p(fwhm^1)+p(par^2)$	2.40	1.46	0.49	0.86	1.18	1.26	0.085	0.083
928 - 938	05 Dec 2012	$p(\cos(par)^2)$	1.38	1.41	1.15	1.14	1.59	1.61	0.084	0.083
	14 Jan 2013	$p(\sin(par)^2)$	1.16	1.33	1.35	1.18	1.57	1.57	0.092	0.093
	07 Feb 2013	$p(fwhm^1)+p(par^2)$	3.22	1.95	0.76	1.58	2.44	3.07	0.139	0.129
938 - 948	05 Dec 2012	$p(fwhm^1)+p(\cos(par)^2)$	1.27	1.30	1.07	1.05	1.36	1.36	0.081	0.080
	14 Jan 2013	$p(\sin(par)^2)$	1.06	1.13	1.21	1.13	1.28	1.28	0.080	0.082
	07 Feb 2013	$p(fwhm^1)+p(par^2)$	1.45	1.10	0.77	1.10	1.12	1.21	0.101	0.099
948 - 958	05 Dec 2012	$p(fwhm^1)+p(\cos(par)^2)$	2.22	1.43	0.71	1.10	1.57	1.57	0.085	0.082
	14 Jan 2013	$p(\sin(par)^2)$	1.00	1.00	1.16	1.16	1.16	1.16	0.085	0.085
	07 Feb 2013	$p(fwhm^1)+p(par^2)$	2.25	1.62	0.73	1.06	1.64	1.72	0.113	0.111
958 - 968	05 Dec 2012	$p(fwhm^1)+p(\cos(par)^2)$	2.11	1.26	0.61	1.00	1.28	1.25	0.079	0.077
	14 Jan 2013	$p(\sin(par)^2)$	1.16	1.52	1.63	1.24	1.89	1.89	0.083	0.088
	07 Feb 2013	$p(fwhm^1)+p(par^2)$	1.73	1.12	0.58	0.89	1.00	1.00	0.090	0.082
968 - 978	05 Dec 2012	$p(fwhm^1)+p(\cos(par)^2)$	1.46	1.37	0.95	1.11	1.39	1.51	0.082	0.081
	14 Jan 2013	$p(\sin(par)^2)$	1.33	1.13	0.83	0.97	1.10	1.10	0.081	0.080
	07 Feb 2013	$p(fwhm^1)+p(par^2)$	1.46	1.33	0.86	0.98	1.25	1.30	0.103	0.102
978 - 988	05 Dec 2012	$p(fwhm^1)+p(\cos(par)^2)$	1.17	1.07	0.97	1.05	1.13	1.12	0.090	0.090
	14 Jan 2013	$p(t^1)+p(\sin(par)^2)$	2.35	1.50	0.72	1.13	1.70	1.70	0.097	0.089
	07 Feb 2013	$p(fwhm^1)+p(par^2)$	1.71	1.64	0.86	0.92	1.47	1.51	0.120	0.118
988 - 1000	05 Dec 2012	$p(fwhm^1)+p(\cos(par)^2)$	2.11	1.18	0.64	1.14	1.34	1.34	0.091	0.088
	14 Jan 2013	$p(t^1)+p(\sin(par)^2)$	2.09	1.27	0.68	1.12	1.42	1.42	0.102	0.097
	07 Feb 2013	$p(fwhm^1)+p(par^2)$	1.91	1.59	1.03	1.23	1.96	1.95	0.132	0.126
1000 - 1020	05 Dec 2012	$p(fwhm^1)+p(\cos(par)^2)$	1.42	1.82	1.40	0.85	1.99	1.55	0.101	0.100
	14 Jan 2013	$p(t^1)+p(\sin(par)^2)$	2.33	1.43	0.77	1.25	1.79	1.79	0.119	0.113
	07 Feb 2013	$p(fwhm^1)+p(par^2)$	1.37	1.56	1.23	1.16	1.68	1.81	0.128	0.128
EulerCam										
r'-Gunn	19 Mar 2011	$p(t^2)+p(sky^1)$	1.28	-	1.41	-	1.81	-	0.065	-

r'-Gunn	24 Mar 2011	$p(t^2)$	1.45	-	1.47	-	2.13	-	0.088	-		
r'-Gunn	30 Dec 2012	$p(t^2)$	2.85	-	1.15	-	3.28	-	0.078	-		
NGTS	05 Dec 2012	$p(t^2)+p(fwhm^1)$	1.11	-	1.51	-	1.68	-	0.062	-		
TRAPPIST												
I+z'	19 Jan 2011	$p(t^2)$	1.17	-	1.10	-	1.29	-	0.151	-		
I+z'	24 Oct 2011	$p(t^2)$	2.02	-	1.03	-	2.09	-	0.161	-		
I+z'	05 Dec 2012	$p(t^2)+off$	1.04	-	1.12	-	1.17	-	0.131	-		
I+z'	16 Dec 2012	$p(t^2)$	2.49	-	0.92	-	2.30	-	0.165	-		
I+z'	30 Dec 2012	$p(t^2)+off$	1.19	-	1.15	-	1.37	-	0.167	-		
I+z'	21 Feb 2013	$p(t^2)+off$	1.15	-	1.00	-	1.15	-	0.113	-		

6.5 Results

6.5.1 Individual Transits

From the analysis of the FORS2, EulerCam and TRAPPIST transit data of WASP-49 b measurements of the planetary radius at a series of wavelengths are obtained. The values obtained from fits to each FORS2 data set separately are shown in the upper panel of Figure 6.9 . From the instrumental point of view two things can be noted:

- The five shortest-wavelength FORS2 bins have larger error bars and larger offsets between the data obtained at different dates. The origin of the increased noise is twofold: first, only two reference stars are available at these wavelengths and second, the lightcurves show large correlated noise, clearly visible in Figures 6.6 , 6.7 , and 6.8 . These systematics are most probably related to the LADC inhomogeneities described in Section 6.2, as the noise structures are occurring near zenith where the image derotator is fastest and hence the effect of LADC structures in the image changes fastest. The data of 07 February 2013, which are least affected by LADC noise, are least divergent at these wavelengths. Both the 05 December 2012 and the 14 January 2013 data require complex baseline functions including 4th order polynomials with respect to the cosine of the parallactic angle and the derotator speed. The uncertainties in these baseline models additionally inflate the error bars. By performing a global fit, constraints from three times the amount of data are imposed on the lightcurve shapes and the rather complex baseline functions adapt to find a solution matching well with other wavelengths.
- Overall the results from the three observations are in good agreement with each other, and no two single points diverge by more than 2.4 σ. When comparing the results from the 6th bin onwards, one finds that there are slight systematic offsets from one date to the next. In particular the 14 January 2013 data are overall lower than the other dates, with an average offset of $\Delta R_P/R_* = 0.0020$ and 0.0016 to the December and February data, respectively. Should these offsets be stemming from unocculted starspots during the transit of 14 January 2013 data, this would require the star to vary by 3.4% on timescales of the rotation period (i.e. several days). This kind of variability is not seen in the WASP discovery photometry from which a limit of 1 mmag is placed on rotational modulation (Lendl et al. 2012). The second possible source of an offset in measured radius can be contamination. In fact there is a small difference ($\Delta dF = 0.0035$) in the measured contamination of the 14 January 2013 and the 07 February 2013 data. This difference translates into a difference in radius ratio of $\Delta R_P/R_* = 0.0002$, and can thus not explain the observed offset. This leads me to conclude that again the correlated noise is the source of this offset, as the 14 January 2013 data is the data most drastically affected by LADC noise (both on short and long timescales).

6.5.2 The WASP-49 b Transmission Spectrum

The transmission spectrum obtained from the global analysis including all FORS2 and broadband data together is given in Table 6.2 and shown in the lower panel of Figure 6.9 . Of course, this spectrum

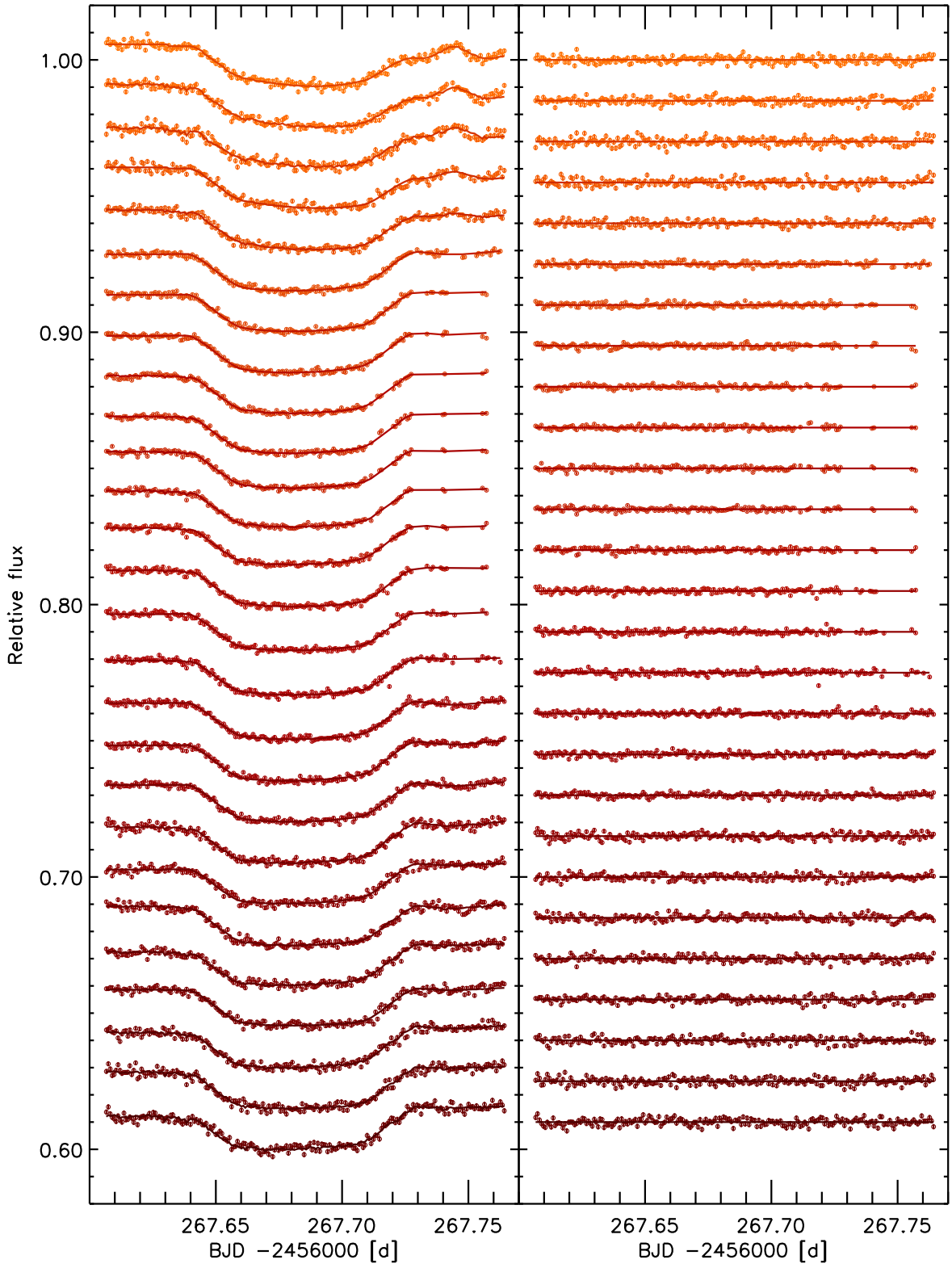

Figure 6.6 : The spectro-photometric transit lightcurves of WASP-49, obtained from the observations on 05 December 2012 with FORS2. The lightcurves and residuals are shown in the left and right panel, respectively. The wavelength of the individual lightcurves increases from top to bottom, centered on: 743, 753, 763, 773, 783, 793, 803, 813, 823, 833, 843, 853, 863, 873, 883, 893, 903, 913, 923, 933, 943, 953, 963, 973, 983, 994, and 1010 nm.

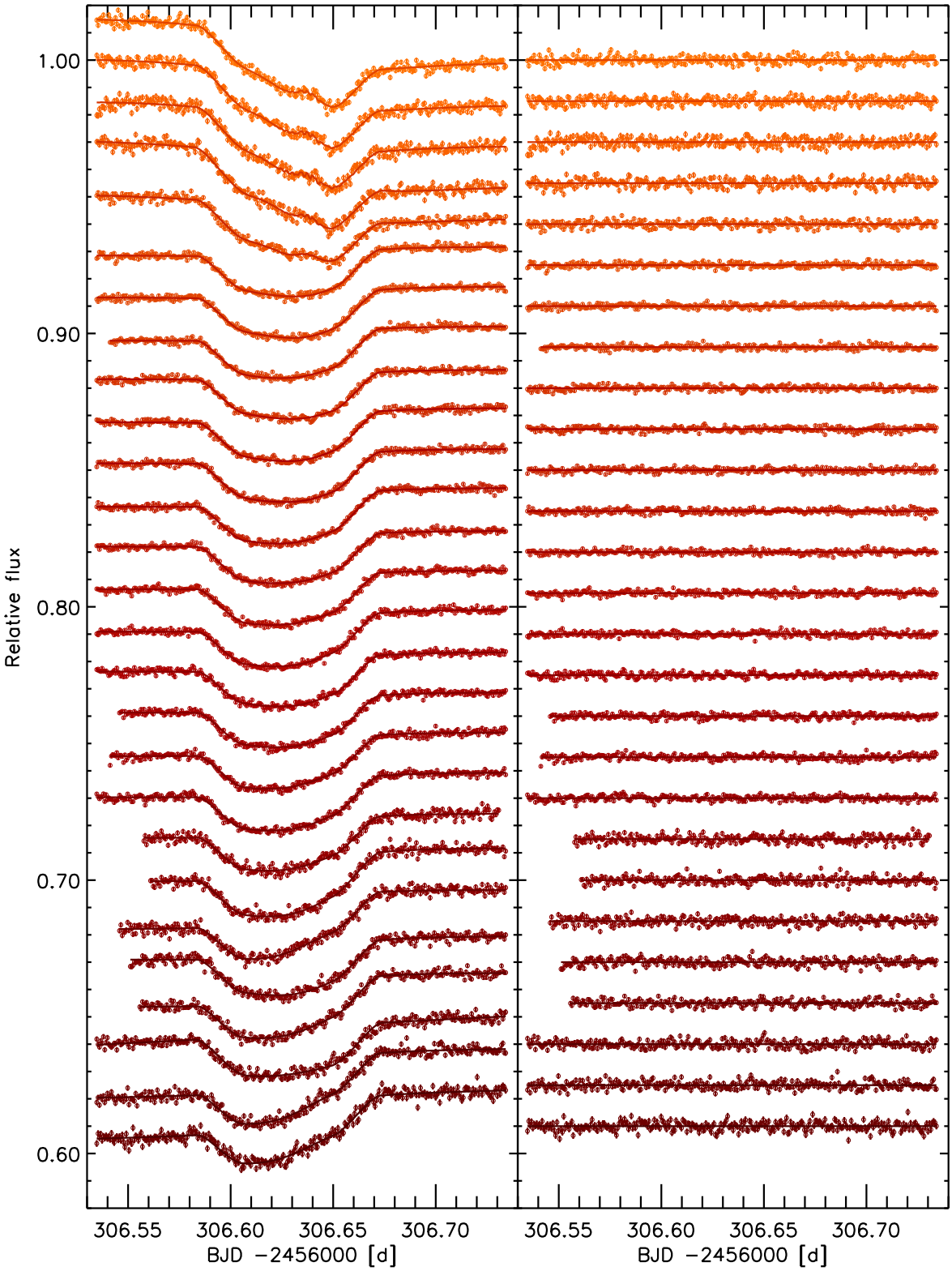

Figure 6.7 : The spectro-photometric transit lightcurves of WASP-49, obtained from the observations on 14 January 2013 with FORS2. The lightcurves and residuals are shown in the left and right panel, respectively. The wavelength of the individual lightcurves increases from top to bottom, centered on: 743, 753, 763, 773, 783, 793, 803, 813, 823, 833, 843, 853, 863, 873, 883, 893, 903, 913, 923, 933, 943, 953, 963, 973, 983, 994, and 1010 nm.

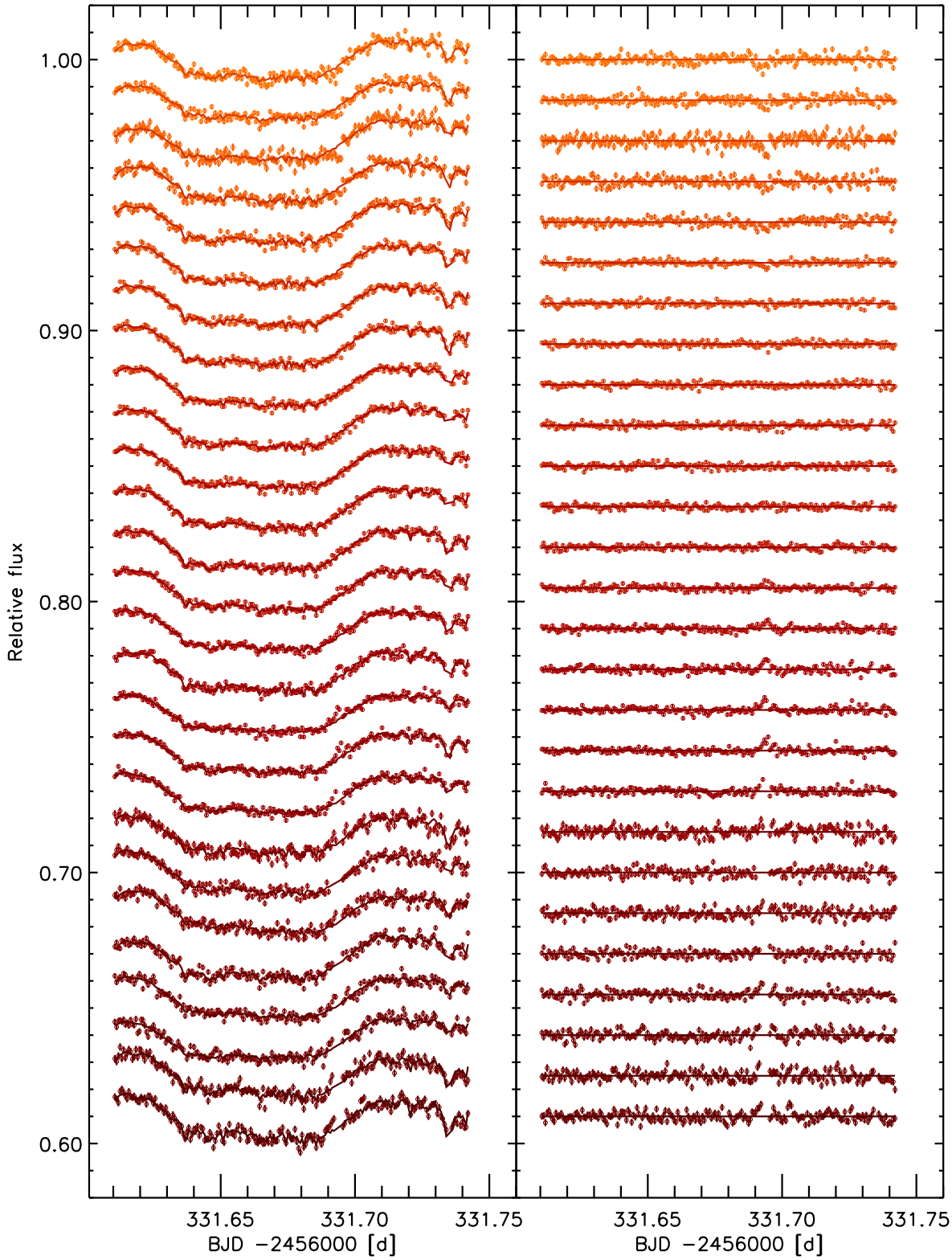

Figure 6.8 : The spectro-photometric transit lightcurves of WASP-49, obtained from the observations on 07 February 2013 with FORS2. The lightcurves and residuals are shown in the left and right panel, respectively. The wavelength of the individual lightcurves increases from top to bottom, centered on: 743, 753, 763, 773, 783, 793, 803, 813, 823, 833, 843, 853, 863, 873, 883, 893, 903, 913, 923, 933, 943, 953, 963, 973, 983, 994, and 1010 nm

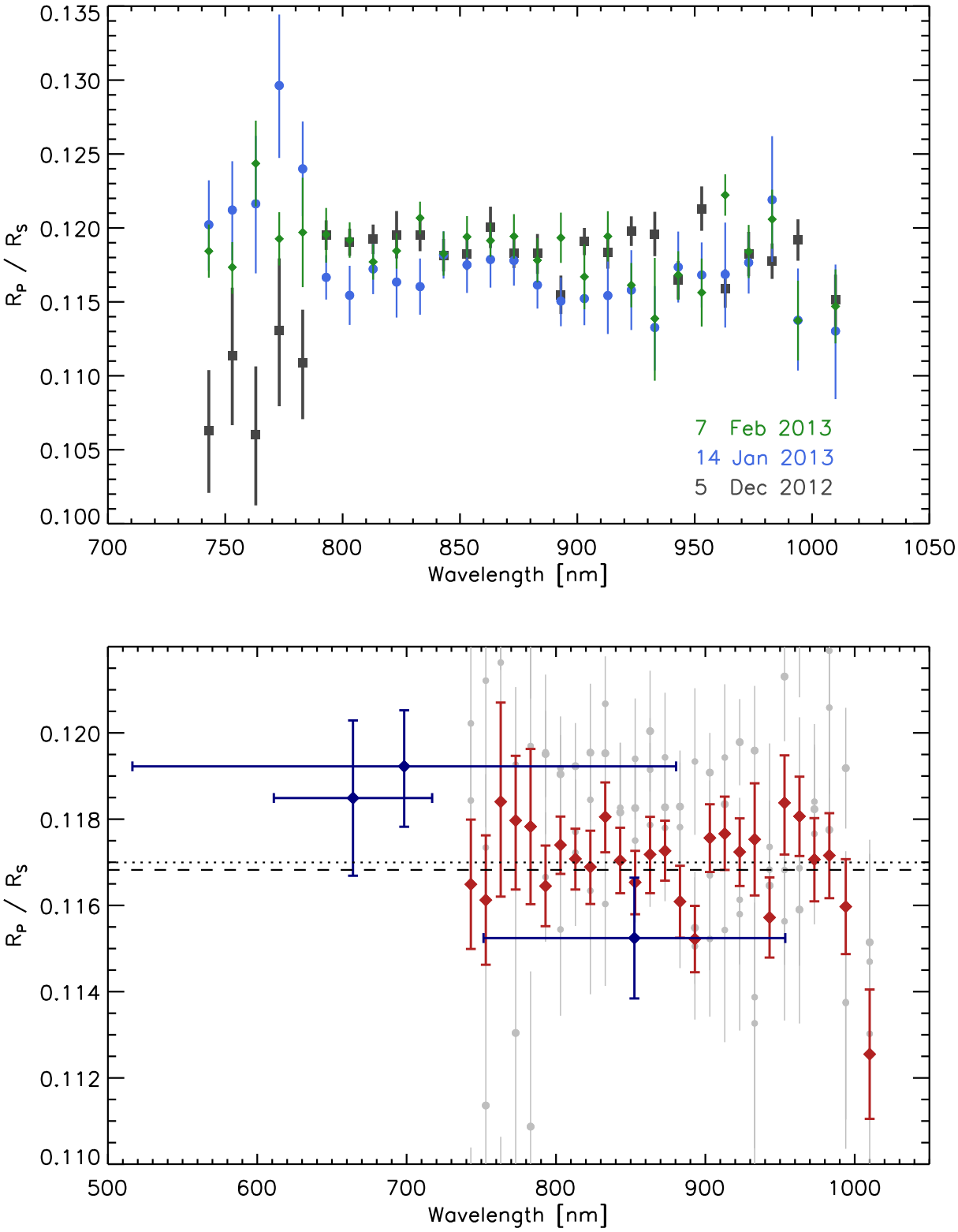

Figure 6.9 : The transmission spectrum of WASP-49 b as observed with FORS2, EulerCam and TRAPPIST. Top: the FORS2 data are shown for each date separately. Black squares refer to data of 05 December 2012, blue filled circles to data of 14 January 2013, and green diamonds to data of 07 February 2013. Bottom: the results of the global analysis are shown, the FORS2 data are shown as red diamonds, and the broadband EulerCam and TRAPPIST data are shown as blue squares. The grey filled circles denote the FORS2 results from separate dates, as shown in the upper panel. The two horizontal lines indicate fits of a constant radius to all data (dotted line) and to the FORS2 data only (dashed line).

Table 6.2: The transmission spectrum of WASP-49 b as found by the global analysis of all *FORS2*, EulerCam, and TRAPPIST data.

Wavelength [nm]	R_p/R_*
738 - 748	0.1164 ± 0.0015
748 - 758	0.1161 ± 0.0015
758 - 768	0.1184 ± 0.0023
768 - 778	0.1180 ± 0.0015
778 - 788	0.1178 ± 0.0018
788 - 798	0.11639 ± 0.00091
798 - 808	0.11738 ± 0.00066
808 - 818	0.11705 ± 0.00071
818 - 828	0.11687 ± 0.00085
828 - 838	0.11802 ± 0.00082
838 - 848	0.11698 ± 0.00077
848 - 858	$0.11650^{+0.00073}_{-0.00075}$
858 - 868	0.11714 ± 0.00092
868 - 878	$0.11726^{+0.00066}_{-0.00068}$
878 - 888	0.11607 ± 0.00082
888 - 898	$0.11519^{+0.00080}_{-0.00078}$
898 - 908	$0.11740^{+0.00076}_{-0.00079}$
908 - 918	0.11773 ± 0.00087
918 - 928	$0.11723^{+0.00080}_{-0.00078}$
928 - 938	0.11726 ± 0.0013
938 - 948	0.11532 ± 0.00092
948 - 958	0.1183 ± 0.0011
958 - 968	$0.11789^{+0.00093}_{-0.00091}$
968 - 978	0.11708 ± 0.00097
978 - 988	0.11709 ± 0.00097
988 - 1000	0.1160 ± 0.0011
1000 - 1020	0.1125 ± 0.0015
611 - 717[a]	0.1186 ± 0.0018
516 - 880[b]	0.1191 ± 0.0013
751 - 953[c]	0.1152 ± 0.0014

[(a)] *r'-Gunn* filter, [(b)] *NGTS* filter, [(c)] *Ic+z'-Gunn* filter

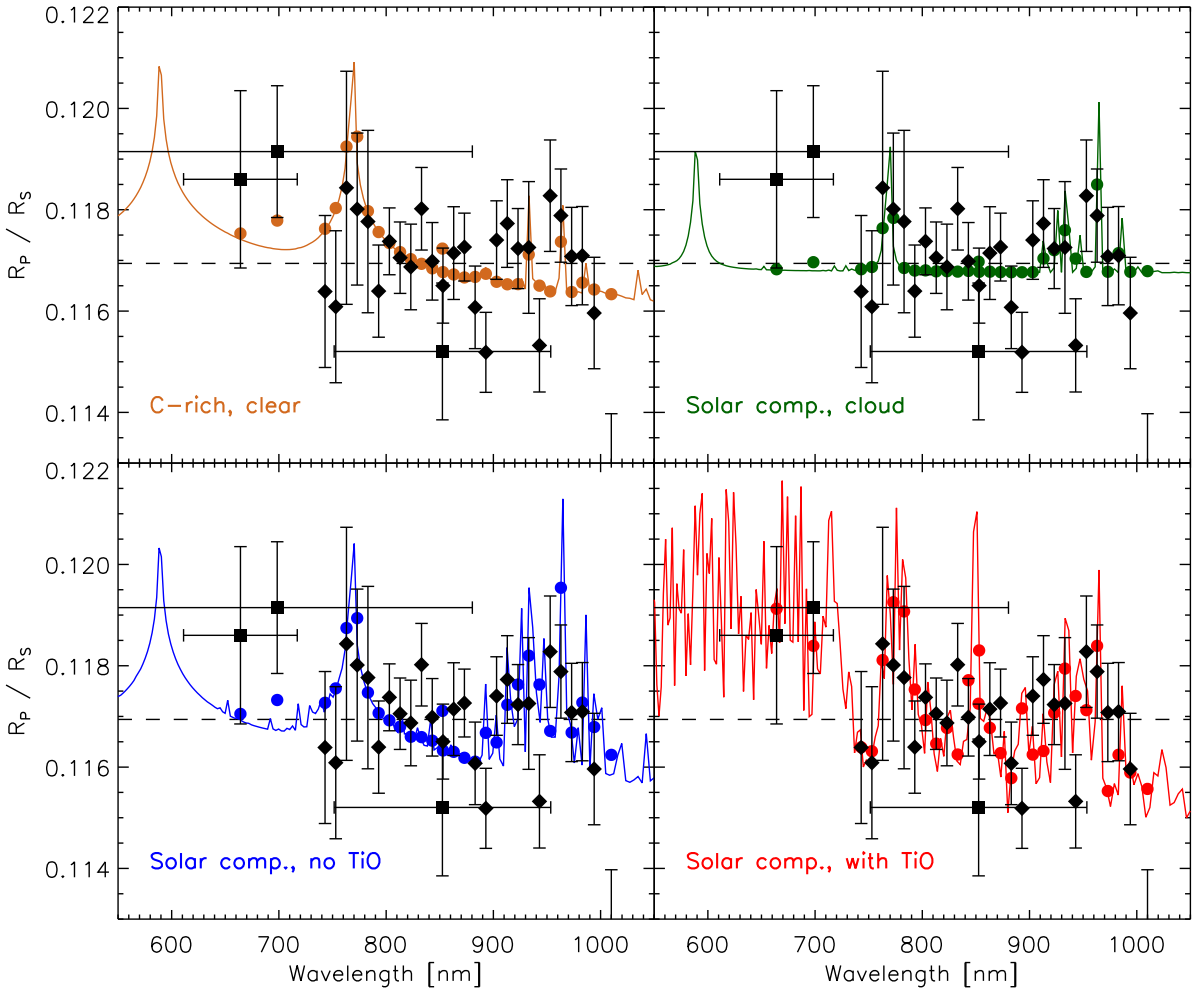

Figure 6.10 : The observed transmission spectrum compared to predictions from atmosphere models. Models atmospheres were calculated for a clear C-rich atmosphere (top left), a Solar-composition atmosphere with a cloud deck at 10 mbar pressure (top right), a clear Solar-composition atmosphere without contributions from TiO (lower left), and a clear Solar-composition atmosphere with TiO (lower right). In all plots, the dashed line is a straight-line fitted to all data points, representative of a high-altitude cloud deck.

needs to be compared to model transmission spectra for WASP-49 b, and the models used were calculated for:

- a clear Solar-composition atmosphere, without TiO
- a clear Solar-composition atmosphere, with TiO
- a clear carbon-rich atmosphere
- a Solar-composition atmosphere, without TiO, but a cloud-deck at a pressure level of 10 mbar.

The fit of these models to the observed transmission spectrum are shown in Figure 6.10 . Also a straight line was fit to the data, such as expected if a high-altitude cloud deck obscuring all features. All models fit the data relatively well, and the χ^2 values considering all points, or the FORS2 points only, are given in Table 6.3. Based on these values, the best fit to the data is given by the Solar-composition model without TiO and with a cloud deck, while the C-rich model, and the high-altitude cloud deck (straight horizontal line) produce comparably good matches to the data. For the straight horizontal

Table 6.3: The χ^2 values calculated from the data and the various atmosphere models for WASP-49 b.

Model	χ^2
All data	
Solar (TiO, cloud)	31.4 ± 7.9
Carbon-rich	32.6 ± 8.1
Horizontal line	33.0 ± 8.1
Solar (no TiO)	39.4 ± 8.9
Solar (with TiO)	46.3 ± 9.6
FORS2 data only	
Solar (TiO, cloud)	25.9 ± 7.2
Carbon-rich	28.9 ± 7.6
Horizontal line	27.6 ± 7.4
Solar (no TiO)	34.6 ± 8.3
Solar (with TiO)	43.5 ± 9.3

line, a reduced χ^2 is readily computed to be $\chi^2_{red} = 1.11$ for all data and $\chi^2_{red} = 1.06$ for the FORS2 data alone with, indicating a good fit. The two models involving clear Solar-abundance atmospheres show the worst fit to the data. In particular the model including TiO is incompatible in χ^2 with the best model at the 1-σ level.

This leads me to conclude that models showing smaller-amplitude signatures give a slightly better fit to the data, than models with clear Solar-composition atmospheres. This indicates that clouds are likely to play a role in the atmosphere of WASP-49 b, or that the atmosphere may be enhanced in carbon compared to oxygen.

Reserve your right to think, for even to think wrongly is better than not to think at all.

Hypatia of Alexandria

7

SUMMARY AND OUTLOOK

7.1 Summary

During my PhD I was involved in a wide spectrum of activities related to exoplanet detection and characterization. Right from the start, I was involved in the WASP survey for transiting planets, which was at it's peak performance at that moment. My job was to provide high-precision photometry to identify false positives and measure the properties of confirmed planets. To maximize the Genevan contribution on the photometry side, the CCD imager EulerCam was in development when I joined the team and I quickly became very active in the instrument's installation and characterization process and finally became one of the main users of it's scientific output. Time and energy consuming as it was, the process of getting the maximal scientific performance from a new instrument has been a highly gratifying and educative experience. At the time of writing, data from EulerCam have been used for the characterization of 55 new (published and yet unpublished) planetary systems. Among them are several planets that are prime targets for follow-up studies aiming at the characterization of the planets' atmospheric properties, such as composition and thermal structure.

With an instrument such as EulerCam at my disposal, the next step was to move to smaller signals and go from transits to occultations. Even for the most favorable objects, occultations are 10-100 times shallower than transits and hence a challenge to instrumentation, observation and data reduction. Instead of relying on data from a single observation, a combination of 10 occultation lightcurves in z'-band were obtained of WASP-19. All data were analyzed at once while using an approach that allows to include correlated noise. The operation was successful and for the first time, an occultation had been detected with 1 m class telescopes. The depth, 352 ± 116 ppm, is smaller than what has been found by other teams who measure values near 900 ppm. For the resolution of this discrepancy, whether astrophysical variability or instrumental noise, I recommend to proceed with coordinated (ideally simultaneous) observations and a homogeneous data analysis. Next to the z'-band data, I was provided with a set of occultation data at 1.19 μm from HAWK-I. The reduction of these data were a challenge on its own as IR detectors are not up to the level of Silicon CCDs in terms of noise properties and linearity. My efforts to make the most of these data yielded a 2.3 σ detection that only loosely constrains the atmospheric parameters of WASP-19 b.

The third and last step in my PhD work was to move to the *spectrophotometry* technique to study the transmission spectrum of WASP-49 b. The data were obtained with the FORS2 instrument at three different epochs. I devised my own procedures to extract the spectra and produce lightcurves from the FORS2 data. Although the data were affected by varying levels of systematic noise, the overall results show good agreement between the three dates. An extensive global analysis finally allowed me to produce a transmission spectrum for WASP-49 b between 0.73 and 1.02 μm. The results are well-matched by a variety of atmospheric models. The best fits are obtained from models with low-amplitude spectral features, such as those including clouds and super-Solar carbon abundances.

7.2 Looking Forward

The field of exoplanet atmospheres is one of the youngest areas of study in astronomy and has seen significant advances during the four years of my PhD. Yet, fundamental aspects of the atmospheres of hot giant planets remain little understood. Among the most pressing questions at this point are: What process is responsible for the inflated radii of irradiated hot Jupiters? What compositional diversity exists in the sample of hot Jupiters and what is the link between composition, migration and formation? What is the origin of the stratospheres observed on hot Jupiters, and why do some planets possess them while others do not? What fraction of hot Jupiters is covered by clouds, and are the cloud properties related to any of the underlying system parameters such as irradiation or metallicity? And finally, what are the temporal variability and 3D properties of these planets?

If we wish to answer these questions major investments in time, technology and brainpower will need to be made. Without highest-quality data and a good understanding of instrumental effects these answers will ever elude us. The instruments that are currently available have been devised with other science goals in mind and the exoplanet community is in the process of learning how to best use them four our purposes. There is still a lot of room for improvement on observing and data reduction techniques, in particular using ground-based telescopes. The recent experiences with FORS2 have taught us that the limitation of this instrument are the LADC inhomogeneities, a problem that is well-understood and that can be resolved. Also other observatories are equipped with multi-object spectrographs and have started producing transmission and emission spectra. At ESO, the new *KMOS* instrument has been commissioned recently. An IFU with good spatial resolution and a field large enough to provide suitable reference stars, this instrument has great potential for the study of exoplanet atmospheres. It can be used with different wavelength resolutions in the spectral range between I and K band that will allow the construction of near-complete exoplanet eclipse spectra. With the efficient use of ground-based instrumentation, momentum is being gained at this moment towards a comprehensive study of the most observationally favorable planets.

Finally we will need to turn away from studying only the most extreme exoplanet worlds but aim at characterizing a large sample of planets. Only by understanding the *standard* type of hot Jupiter, the reasons why some objects diverge from this standard can become clear. Several promising instruments are currently in the planning or construction phase and will hopefully provide a more profound understanding of planets. Operating from space, *CHEOPS* is an ESA S-class mission dedicated to high-precision photometry of exoplanet transits and occultations. The satellite is scheduled for launch in 2017 and will soon produce precise optical-light occultation measurements and phase curves of several hot Jupiters. Further along, the James Webb Space Telescope will provide high resolution transmission and emission spectra for a selected number of systems. A wider sample of planets are targeted by the proposed ESA M-class mission *ECHO*, dedicated to exoplanet transmission and emission spectra. If selected, this instrument will resolve the signatures of several molecules in the atmospheres of a range of planets and provide a broad view on exoplanetary atmospheres.

It will be critical to have the best targets available in order to make full use of these future capabilities. While a good sample of transiting hot Jupiters are known, characterizable Neptunes and (super-)Earths are in high demand. As the size of atmospheric signatures scales inversely with the host star's size and brightness, the only characterizable small planets are those in orbit around late-type stars. The planned survey NGTS will extend the work of WASP towards hot Neptunes, providing a number of low-mass planets around predominantly bright K-type hosts. For M-type host stars, targeted searches such as M-Earth are capable of discovering low-mass planets. The lowest-mass planets amenable for characterization will be searched for by the SPECULOOS project that is directed at M5 and cooler host stars.

It is this synergy of discovery and characterization that will shape the next fifteen years of exoplanet research. The work currently undertaken to study a handful of favorable planets is paving the way towards the future study of cooler, more Earth-like planets. At the moment all we can tell is that these planets are plentiful. Only by unlocking the secrets of their atmospheres we will know if there is truly

one of them out there resembling our Earth, with it's oceans, continents, and, perhaps, bustling with life.

ACKNOWLEDGMENTS

I have made extensive use of the Centre de Données astronomiques de Strasbourg (CDS) databases, in particular SIMBAD and VIZIR, as well as NASA's Astrophysics Data System Service (ADS). I acknowledge the use of the exoplanet archives `www.exoplanets.eu`, `www.exoplanets.org`, and `TepCat`.

This work includes data obtained with the HARPS, HAWK-I, and FORS2 instruments that are operated by the European Southern Observatory (ESO). Further data of the WASP survey, TRAPPIST and the Euler-Swiss telescope have been used.

This work was funded by the Swiss National Science Foundation, Geneva University, and the canton of Geneva.

A
PUBLICATIONS

During my PhD I was priviledged to be part of a number of collaborations. In particular the WASP project has been a highly producitve endeavour. The publications to which I contributed are presented here.

A.1 Refereed Articles

WASP-29B: A SATURN-SIZED TRANSITING EXOPLANET.
Hellier C, Anderson D R, Collier Cameron A, Gillon M, **Lendl M**, Maxted P F L, Queloz D, Smalley B, Triaud A H M J, West R G, Brown D J A, Enoch B, Lister T A, Pepe F, Pollacco D, Ségransan D, and Udry S.
ApJ, **723**, pp. L60–L63, (2010).

WASP-40B: INDEPENDENT DISCOVERY OF THE 0.6 M TRANSITING EXOPLANET HAT-P-27B.
Anderson D R, Barros S C C, Boisse I, Bouchy F, Collier Cameron A, Faedi F, Hebrard G, Hellier C, **Lendl M**, Moutou C, Pollacco D, Santerne A, Smalley B, Smith A M S, Todd I, Triaud A H M J, West R G, Wheatley P J, Bento J, Enoch B, Gillon M, Maxted P F L, McCormac J, Queloz D, Simpson E K, and Skillen I.
PASP, **123**, pp. 555–560, (2011).

SPIN-ORBIT MEASUREMENTS AND REFINED PARAMETERS FOR THE EXOPLANET SYSTEMS WASP-22 AND WASP-26.
Anderson D R, Collier Cameron A, Gillon M, Hellier C, Jehin E, **Lendl M**, Queloz D, Smalley B, Triaud A H M J, and Vanhuysse M.
A&A, **534**, A16, (2011).

WASP-31B: A LOW-DENSITY PLANET TRANSITING A METAL-POOR, LATE-F-TYPE DWARF STAR.
Anderson D R, Collier Cameron A, Hellier C, **Lendl M**, Lister T A, Maxted P F L, Queloz D, Smalley B, Smith A M S, Triaud A H M J, West R G, Brown D J A, Gillon M, Pepe F, Pollacco D, Ségransan D, Street R A, and Udry S.
A&A, **531**, A60, (2011).

WASP-30B: A 61 M $_{Jup}$ BROWN DWARF TRANSITING A V = 12, F8 STAR.
Anderson D R, Collier Cameron A, Hellier C, **Lendl M**, Maxted P F L, Pollacco D, Queloz D, Smalley B, Smith A M S, Todd I, Triaud A H M J, West R G, Barros S C C, Enoch B, Gillon M, Lister T A, Pepe F, Ségransan D, Street R A, and Udry S.
ApJ, **726**, L19, (2011).

WASP-35B, WASP-48B, AND HAT-P-30B/WASP-51B: TWO NEW PLANETS AND AN INDEPENDENT DISCOVERY OF A HAT PLANET.
Enoch B, Anderson D R, Barros S C C, Brown D J A, Collier Cameron A, Faedi F, Gillon M, Hébrard G, Lister T A, Queloz D, Santerne A, Smalley B, Street R A, Triaud A H M J, West R G, Bouchy F, Bento J, Butters O, Fossati L, Haswell C A, Hellier C, Holmes S, Jehin E, **Lendl M**, Maxted P F L, McCormac J,

Miller G R M, Moulds V, Moutou C, Norton A J, Parley N, Pepe F, Pollacco D, Segransan D, Simpson E, Skillen I, Smith A M S, Udry S, and Wheatley P J.
AJ, **142**, 86, (2011).

WASP-25b: a 0.6 M_J planet in the Southern hemisphere.
Enoch B, Cameron A C, Anderson D R, Lister T A, Hellier C, Maxted P F L, Queloz D, Smalley B, Triaud A H M J, West R G, Brown D J A, Gillon M, Hebb L, **Lendl M**, Parley N, Pepe F, Pollacco D, Segransan D, Simpson E, Street R A, and Udry S.
MNRAS, **410**, pp. 1631–1636, (2011).

WASP-39b: a highly inflated Saturn-mass planet orbiting a late G-type star.
Faedi F, Barros S C C, Anderson D R, Brown D J A, Collier Cameron A, Pollacco D, Boisse I, Hébrard G, **Lendl M**, Lister T A, Smalley B, Street R A, Triaud A H M J, Bento J, Bouchy F, Butters O W, Enoch B, Haswell C A, Hellier C, Keenan F P, Miller G R M, Moulds V, Moutou C, Norton A J, Queloz D, Santerne A, Simpson E K, Skillen I, Smith A M S, Udry S, Watson C A, West R G, and Wheatley P J.
A&A, **531**, A40, (2011).

WASP-50 b: a hot Jupiter transiting a moderately active solar-type star.
Gillon M, Doyle A P, **Lendl M**, Maxted P F L, Triaud A H M J, Anderson D R, Barros S C C, Bento J, Collier-Cameron A, Enoch B, Faedi F, Hellier C, Jehin E, Magain P, Montalbán J, Pepe F, Pollacco D, Queloz D, Smalley B, Segransan D, Smith A M S, Southworth J, Udry S, West R G, and Wheatley P J.
A&A, **533**, A88, (2011).

WASP-43b: the closest-orbiting hot Jupiter.
Hellier C, Anderson D R, Collier Cameron A, Gillon M, Jehin E, **Lendl M**, Maxted P F L, Pepe F, Pollacco D, Queloz D, Ségransan D, Smalley B, Smith A M S, Southworth J, Triaud A H M J, Udry S, and West R G.
A&A, **535**, L7, (2011).

WASP-34b: a near-grazing transiting sub-Jupiter-mass exoplanet in a hierarchical triple system.
Smalley B, Anderson D R, Collier Cameron A, Hellier C, **Lendl M**, Maxted P F L, Queloz D, Triaud A H M J, West R G, Bentley S J, Enoch B, Gillon M, Lister T A, Pepe F, Pollacco D, Segransan D, Smith A M S, Southworth J, Udry S, Wheatley P J, Wood P L, and Bento J.
A&A, **526**, A130, (2011).

WASP-44b, WASP-45b and WASP-46b: three short-period, transiting extrasolar planets.
Anderson D R, Collier Cameron A, Gillon M, Hellier C, Jehin E, **Lendl M**, Maxted P F L, Queloz D, Smalley B, Smith A M S, Triaud A H M J, West R G, Pepe F, Pollacco D, Ségransan D, Todd I, and Udry S.
MNRAS, **422**, pp. 1988–1998, (2012).

A hot Uranus transiting the nearby M dwarf GJ 3470. Detected with HARPS velocimetry. Captured in transit with TRAPPIST photometry.
Bonfils X, Gillon M, Udry S, Armstrong D, Bouchy F, Delfosse X, Forveille T, Fumel A, Jehin E, **Lendl M**, Lovis C, Mayor M, McCormac J, Neves V, Pepe F, Perrier C, Pollaco D, Queloz D, and Santos N C.
A&A, **546**, A27, (2012).

Analysis of Spin-Orbit Alignment in the WASP-32, WASP-38, and HAT-P-27/WASP-40 Systems.
Brown D J A, Collier Cameron A, Díaz R F, Doyle A P, Gillon M, **Lendl M**, Smalley B, Triaud A H M J, Anderson D R, Enoch B, Hellier C, Maxted P F L, Miller G R M, Pollacco D, Queloz D, Boisse I, and Hébrard G.

ApJ, **760**, 139, (2012).

THE TRAPPIST SURVEY OF SOUTHERN TRANSITING PLANETS. I. THIRTY ECLIPSES OF THE ULTRA-SHORT PERIOD PLANET WASP-43 B.
Gillon M, Triaud A H M J, Fortney J J, Demory B O, Jehin E, **Lendl M**, Magain P, Kabath P, Queloz D, Alonso R, Anderson D R, Collier Cameron A, Fumel A, Hebb L, Hellier C, Lanotte A, Maxted P F L, Mowlavi N, and Smalley B.
A&A, **542**, A4, (2012).

SEVEN TRANSITING HOT JUPITERS FROM WASP-SOUTH, EULER AND TRAPPIST: WASP-47B, WASP-55B, WASP-61B, WASP-62B, WASP-63B, WASP-66B AND WASP-67B.
Hellier C, Anderson D R, Collier Cameron A, Doyle A P, Fumel A, Gillon M, Jehin E, **Lendl M**, Maxted P F L, Pepe F, Pollacco D, Queloz D, Ségransan D, Smalley B, Smith A M S, Southworth J, Triaud A H M J, Udry S, and West R G.
MNRAS, **426**, pp. 739–750, (2012).

WASP-42 B AND WASP-49 B: TWO NEW TRANSITING SUB-JUPITERS.
Lendl M, Anderson D R, Collier-Cameron A, Doyle A P, Gillon M, Hellier C, Jehin E, Lister T A, Maxted P F L, Pepe F, Pollacco D, Queloz D, Smalley B, Ségransan D, Smith A M S, Triaud A H M J, Udry S, West R G, and Wheatley P J.
A&A, **544**, A72, (2012).

WASP-4B TRANSIT OBSERVATIONS WITH GROND.
Nikolov N, Henning T, Koppenhoefer J, **Lendl M**, Maciejewski G, and Greiner J.
A&A, **539**, A159, (2012).

WASP-78B AND WASP-79B: TWO HIGHLY-BLOATED HOT JUPITER-MASS EXOPLANETS ORBITING F-TYPE STARS IN ERIDANUS.
Smalley B, Anderson D R, Collier-Cameron A, Doyle A P, Fumel A, Gillon M, Hellier C, Jehin E, **Lendl M**, Maxted P F L, Pepe F, Pollacco D, Queloz D, Ségransan D, Smith A M S, Southworth J, Triaud A H M J, Udry S, and West R G.
A&A, **547**, A61, (2012).

WASP-36B: A NEW TRANSITING PLANET AROUND A METAL-POOR G-DWARF, AND AN INVESTIGATION INTO ANALYSES BASED ON A SINGLE TRANSIT LIGHT CURVE.
Smith A M S, Anderson D R, Collier Cameron A, Gillon M, Hellier C, **Lendl M**, Maxted P F L, Queloz D, Smalley B, Triaud A H M J, West R G, Barros S C C, Jehin E, Pepe F, Pollacco D, Segransan D, Southworth J, Street R A, and Udry S.
AJ, **143**, 81, (2012).

WASP-54B, WASP-56B, AND WASP-57B: THREE NEW SUB-JUPITER MASS PLANETS FROM SUPERWASP.
Faedi F, Pollacco D, Barros S C C, Brown D, Collier Cameron A, Doyle A P, Enoch R, Gillon M, Gómez Maqueo Chew Y, Hébrard G, **Lendl M**, Liebig C, Smalley B, Triaud A H M J, West R G, Wheatley P J, Alsubai K A, Anderson D R, Armstrong D, Bento J, Bochinski J, Bouchy F, Busuttil R, Fossati L, Fumel A, Haswell C A, Hellier C, Holmes S, Jehin E, Kolb U, McCormac J, Miller G R M, Moutou C, Norton A J, Parley N, Queloz D, Santerne A, Skillen I, Smith A M S, Udry S, and Watson C.
A&A, **551**, A73, (2013).

WASP-64 B AND WASP-72 B: TWO NEW TRANSITING HIGHLY IRRADIATED GIANT PLANETS.
Gillon M, Anderson D R, Collier-Cameron A, Doyle A P, Fumel A, Hellier C, Jehin E, **Lendl M**, Maxted P F L, Montalbán J, Pepe F, Pollacco D, Queloz D, Ségransan D, Smith A M S, Smalley B, Southworth J,

Triaud A H M J, Udry S, and West R G.
A&A, **552**, A82, (2013).

Fast-evolving weather for the coolest of our two new substellar neighbours.
Gillon M, Triaud A H M J, Jehin E, Delrez L, Opitom C, Magain P, **Lendl M**, and Queloz D.
A&A, **555**, L5, (2013).

Discovery of WASP-65b and WASP-75b: Two hot Jupiters without highly inflated radii.
Gómez Maqueo Chew Y, Faedi F, Pollacco D, Brown D J A, Doyle A P, Collier Cameron A, Gillon M, **Lendl M**, Smalley B, Triaud A H M J, West R G, Wheatley P J, Busuttil R, Liebig C, Anderson D R, Armstrong D J, Barros S C C, Bento J, Bochinski J, Burwitz V, Delrez L, Enoch B, Fumel A, Haswell C A, Hébrard G, Hellier C, Holmes S, Jehin E, Kolb U, Maxted P F L, McCormac J, Miller G R M, Norton A J, Pepe F, Queloz D, Rodríguez J, Ségransan D, Skillen I, Stassun K G, Udry S, and Watson C.
A&A, **559**, A36, (2013).

WASP-52b, WASP-58b, WASP-59b, and WASP-60b: Four new transiting close-in giant planets.
Hébrard G, Collier Cameron A, Brown D J A, Díaz R F, Faedi F, Smalley B, Anderson D R, Armstrong D, Barros S C C, Bento J, Bouchy F, Doyle A P, Enoch B, Gómez Maqueo Chew Y, Hébrard É M, Hellier C, **Lendl M**, Lister T A, Maxted P F L, McCormac J, Moutou C, Pollacco D, Queloz D, Santerne A, Skillen I, Southworth J, Tregloan-Reed J, Triaud A H M J, Udry S, Vanhuysse M, Watson C A, West R G, and Wheatley P J.
A&A, **549**, A134, (2013).

A photometric study of the hot exoplanet WASP-19b.
Lendl M, Gillon M, Queloz D, Alonso R, Fumel A, Jehin E, and Naef D.
A&A, **552**, A2, (2013).

The CORALIE survey for southern extrasolar planets. XVII. New and updated long period and massive planets.
Marmier M, Ségransan D, Udry S, Mayor M, Pepe F, Queloz D, Lovis C, Naef D, Santos N C, Alonso R, Alves S, Berthet S, Chazelas B, Demory B O, Dumusque X, Eggenberger A, Figueira P, Gillon M, Hagelberg J, **Lendl M**, Mardling R A, Mégevand D, Neveu M, Sahlmann J, Sosnowska D, Tewes M, and Triaud A H M J.
A&A, **551**, A90, (2013).

WASP-77 Ab: A Transiting Hot Jupiter Planet in a Wide Binary System.
Maxted P F L, Anderson D R, Collier Cameron A, Doyle A P, Fumel A, Gillon M, Hellier C, Jehin E, **Lendl M**, Pepe F, Pollacco D L, Queloz D, Ségransan D, Smalley B, Southworth K, Smith A M S, Triaud A H M J, Udry S, and West R G.
PASP, **125**, pp. 48–55, (2013).

WASP-71b: a bloated hot Jupiter in a 2.9-day, prograde orbit around an evolved F8 star.
Smith A M S, Anderson D R, Bouchy F, Collier Cameron A, Doyle A P, Fumel A, Gillon M, Hébrard G, Hellier C, Jehin E, **Lendl M**, Maxted P F L, Moutou C, Pepe F, Pollacco D, Queloz D, Santerne A, Segransan D, Smalley B, Southworth J, Triaud A H M J, Udry S, and West R G.
A&A, **552**, A120, (2013).

WASP-80b: a gas giant transiting a cool dwarf.
Triaud A H M J, Anderson D R, Collier Cameron A, Doyle A P, Fumel A, Gillon M, Hellier C, Jehin E, **Lendl M**, Lovis C, Maxted P F L, Pepe F, Pollacco D, Queloz D, Ségransan D, Smalley B, Smith A M S, Udry S, West R G, and Wheatley P J.

A&A, **551**, A80, (2013).

A.2 Articles in Review

THREE IRRADIATED AND BLOATED HOT JUPITERS: WASP-76B, WASP-82B & WASP-90B.
West R G, Almenara J M, Anderson D R, Bouchy F, Brown D J A, Collier Cameron A, Deleuil M, Delrez L, Doyle A P, Faedi F, Fumel A, Gillon M, Hebrard G, Hellier C, Jehin E, **Lendl M**, Maxted P F L, Pepe F, Pollacco D, Queloz D, Segransan D, Smalley B, Smith A M S, Triaud A H M J, and Udry S.
ArXiv e-prints, 1310.5607 (2013).

TRANSITING HOT JUPITERS FROM WASP-SOUTH, EULER AND TRAPPIST: WASP-95B TO WASP-101B.
Hellier C, Anderson D R, Collier Cameron A, Delrez L, Gillon M, Jehin E, **Lendl M**, Maxted P F L, Pepe F, Pollacco D, Queloz D, Segransan D, Smalley B, Smith A M S, Southworth J, Triaud A H M J, Udry S, and West R G.
ArXiv e-prints, 1310.5630 (2013).

THREE SUB-JUPITER-MASS PLANETS: WASP-69B & WASP-84B TRANSIT ACTIVE K DWARFS AND WASP-70AB TRANSITS THE EVOLVED PRIMARY OF A G4+K3 BINARY.
Anderson D R, Collier Cameron A, Delrez L, Doyle A P, Faedi F, Fumel A, Gillon M, Gómez Maqueo Chew Y, Hellier C, Jehin E, **Lendl M**, Maxted P F L, Pepe F, Pollacco D, Queloz D, Ségransan D, Skillen I, Smalley B, Smith A M S, Southworth J, Triaud A H M J, Turner O D, Udry S, and West R G.
ArXiv e-prints, 1310.5654 (2013).

COROT 223992193: A NEW, LOW-MASS, PRE-MAIN SEQUENCE ECLIPSING BINARY WITH EVIDENCE OF A CIRCUMBINARY DISK.
Gillen E, Aigrain S, McQuillan A, Bouvier J, Hodgkin S, Alencar S H P, Terquem C, Southworth J, Gibson N P, Cody A M, **Lendl M**, Morales-Calderón M, Favata F, Stauffer J, and Micela G.
ArXiv e-prints, 1311.3990 (2013).

TRANSITING PLANETS FROM WASP-SOUTH, EULER AND TRAPPIST: WASP-68 B, WASP-73 B AND WASP-88 B, THREE HOT JUPITERS TRANSITING EVOLVED SOLAR-TYPE STARS.
Delrez L, Van Grootel V, Anderson D R, Collier-Cameron A, Doyle A P, Fumel A, Gillon M, Hellier C, Jehin E, **Lendl M**, Neveu-VanMalle M, Maxted P F L, Pepe F, Pollacco D, Queloz D, Ségransan D, Smalley B, Smith A M S, Southworth J, Triaud A H M J, Udry S, and West R G.
ArXiv e-prints, 1312.1827 (2013).

WASP-103B: A NEW PLANET AT THE EDGE OF TIDAL DISRUPTION.
Gillon M, Anderson D R, Collier-Cameron A, Delrez L, Hellier C, Jehin E, **Lendl M**, Maxted P F L, Pepe F, Pollacco D, Queloz D, Segransan D, Smith A M S, Smalley B, Southworth J, Triaud A H M J, Udry S, Van Grootel V, West, R G.
ArXiv e-prints, 1401.2784 (2014).

A.3 Conference Proceedings

THE WASP-SOUTH SEARCH FOR TRANSITING EXOPLANETS.
Hellier C, Anderson D R, Collier Cameron A, Gillon M, **Lendl M**, Lister T A, Maxted P F L, Pollacco D, Queloz D, Smalley B, Triaud A H M J, and West R G.
European Physical Journal Web of Conferences, **11**, p. 1004 (2011).

TRAPPIST: TRAnsiting Planets and PlanetesImals Small Telescope.
Jehin E, Gillon M, Queloz D, Magain P, Manfroid J, Chantry V, **Lendl M**, Hutsemékers D, and Udry S.
The Messenger, **145**, pp. 2–6, (2011).

Multiband Transit Light Curve Modeling of WASP-4.
Nikolov N, Koppenhoefer J, **Lendl M**, Henning T, and Greiner J.
IAU Symposium, **282**, pp. 141–142 (2012).

Towards the first transmission spectrum of a gas giant transiting an M-dwarf.
Delrez L, Gillon M, **Lendl M**, Jehin E, Anderson D, Demory B O, De Wit J, Hellier C, Triaud A, and Queloz D.
Protostars and Planets VI, Heidelberg, July 15-20, 2013, Poster #2G014, p. 14 (2013).

A new, low-mass, pre-main sequence eclipsing binary with evidence of a circumbinary disk.
Gillen E, Aigrain S, McQuillan A, Bouvier J, Hodgkin S, Alencar S, Terquem C, Southworth J, Gibson N, Cody A M, **Lendl M**, Morales-Calderón M, Favata F, Stauffer J, and Micela G.
Protostars and Planets VI, Heidelberg, July 15-20, 2013, Poster #1K074, p. 74 (2013).

Towards a Transmission Spectrum of the Hot Saturn WASP-49b.
Lendl M, Delrez L, Gillon M, Jehin E, and Queloz D.
Protostars and Planets VI, Heidelberg, July 15-20, 2013, Poster #2G009, p. 9 (2013).

Spin-orbit angles as a probe to orbital evolution.
Triaud A, Collier Cameron A, Queloz D, Anderson D, Brown D, Smalley B, Bouchy F, **Lendl M**, and Gillon M.
Protostars and Planets VI, Heidelberg, July 15-20, 2013, Poster #2H037, p. 37 (2013).

B
WASP PLANETS

The WASP survey has been described in detail in Section 4. Here the first pages of all WASP discoveries that I have been involved in are shown.

The Astrophysical Journal Letters, 723:L60–L63, 2010 November 1 doi:10.1088/2041-8205/723/1/L60

WASP-29b: A SATURN-SIZED TRANSITING EXOPLANET

Coel Hellier[1], D. R. Anderson[1], A. Collier Cameron[2], M. Gillon[3], M. Lendl[4], P. F. L. Maxted[1], D. Queloz[4], B. Smalley[1], A. H. M. J. Triaud[4], R. G. West[5], D. J. A. Brown[2], B. Enoch[2], T. A. Lister[6], F. Pepe[4], D. Pollacco[7], D. Ségransan[4], and S. Udry[4]
[1] Astrophysics Group, Keele University, Staffordshire, ST5 5BG, UK
[2] SUPA, School of Physics and Astronomy, University of St. Andrews, North Haugh, Fife, KY16 9SS, UK
[3] Institut d'Astrophysique et de Géophysique, Université de Liège, Allée du 6 Août, 17, Bat. B5C, Liège 1, Belgium
[4] Observatoire astronomique de l'Université de Genève 51 ch. des Maillettes, 1290 Sauverny, Switzerland
[5] Department of Physics and Astronomy, University of Leicester, Leicester, LE1 7RH, UK
[6] Las Cumbres Observatory, 6740 Cortona Dr. Suite 102, Santa Barbara, CA 93117, USA
[7] Astrophysics Research Centre, School of Mathematics & Physics, Queen's University, University Road, Belfast, BT7 1NN, UK
Received 2010 March 25; accepted 2010 September 29; published 2010 October 12

ABSTRACT

We report the discovery of a Saturn-sized planet transiting a $V = 11.3$, K4 dwarf star every 3.9 days. WASP-29b has a mass of $0.24 \pm 0.02\ M_{\rm Jup}$ and a radius of $0.79 \pm 0.05\ R_{\rm Jup}$, making it the smallest planet so far discovered by the WASP survey, and the exoplanet most similar in mass and radius to Saturn. The host star WASP-29 has an above-solar metallicity and fits a possible correlation for Saturn-mass planets such that planets with higher-metallicity host stars have higher core masses and thus smaller radii.

Key words: stars: individual (WASP-29) – planetary systems

Online-only material: color figures

1. INTRODUCTION

Searches for transiting exoplanets have now found more than 50 "hot Jupiters" with masses of ∼0.5–3 Jupiters. At much smaller masses there are several transiting "Neptunes" (GJ 436b, Gillon et al. 2007; HAT-P-11b, Bakos et al. 2010; & Kepler-4b, Borucki et al. 2010) and "super-Earths" (GJ1214b, Charbonneau et al. 2009; CoRoT-7b, Léger et al. 2009).

By 2009 there were only two known transiting planets of Saturn-mass (∼0.3 $M_{\rm Jup}$), namely, HD 149026b (Sato et al. 2005) and HAT-P-12b (Hartman et al. 2009). In 2010 this number is growing fast, with near simultaneous announcements of WASP-29b (this Letter), CoRoT-8b (Bordé et al. 2010), WASP-21b (Bouchy et al. 2010), and HAT-P-18b and HAT-P-19b (Hartman et al. 2010), giving rapidly increasing insight into planets of this mass range.

2. OBSERVATIONS

WASP-South is an array of cameras based on 11.1 cm, $f/1.8$ lenses which cover a total of 450 deg^2 of sky. The typical observing pattern tiles 30 s exposures of several fields with a cadence of 8 minutes, recording stars in the range $V = 8$–15. The WASP-South survey is described in Pollacco et al. (2006) while a discussion of our planet-hunting methods can be found in Collier Cameron et al. (2007a), Pollacco et al. (2008), and references therein.

WASP-29 is a $V = 11.3$, K4V star in the constellation Phoenix. It was observed by WASP-South from May to November in both 2006 and 2007, accumulating 9161 data points. These data show periodic transits with a 3.9 day period (Figure 1). There are no other significant sources within the 48″ extraction aperture (3.5 14″ pixels) to dilute the transit depth.

We used the CORALIE spectrograph on the Euler 1.2 m telescope at La Silla to obtain fourteen radial-velocity measurements over 2009 August–December (Table 1). These show that the transiting body is a Saturn-mass planet. On 2010 September 6, we obtained a transit light curve with Euler's CCD camera, using 20 s, *R*-band exposures, resulting in a mean error of 1.5 mmag (Figure 1).

The CORALIE radial-velocity measurements were combined with the Euler and WASP-South photometry in a simultaneous Markov chain Monte Carlo (MCMC) analysis to find the parameters of the WASP-29 system (Table 2). For details of our methods see Collier Cameron et al. (2007b) and Pollacco et al. (2008). For limb darkening, we used the four parameter non-linear law of Claret (2000) with parameters fixed to the values noted in Table 2. The eccentricity was a free parameter but the data are compatible with a circular orbit.

One departure from early WASP practice is the way we determine the stellar mass. The stellar effective temperature and metallicity are treated as jump parameters in the Markov chain, and controlled by Gaussian priors derived from their spectroscopically determined values and uncertainties. At each step in the chain the stellar density is determined from the transit duration and impact parameter. The stellar mass is then determined at each step as a polynomial function of $T_{\rm eff}$, [Fe/H], and $\log \rho/\rho_\odot$, as determined by Enoch et al. (2010a). This calibration is derived from the compilation of 40 stars in eclipsing binaries with well-determined masses, radii, effective temperatures, and metallicities, published by Torres et al. (2010).

3. WASP-29 STELLAR PARAMETERS

The 14 CORALIE spectra of WASP-29 were co-added to produce a spectrum with a typical S/N of 80:1, which we analyzed using the methods described in Gillon et al. (2009). We used the Hα line to determine the effective temperature ($T_{\rm eff}$), and the Na I D and Mg I b lines as diagnostics of the surface gravity ($\log g$). The parameters obtained are listed in Table 2. The elemental abundances were determined from equivalent-width measurements of several clean and unblended lines. A value for microturbulence ($\xi_{\rm t}$) was determined from Fe I using

The Astrophysical Journal Letters, 726:L19 (5pp), 2011 January 10 doi:10.1088/2041-8205/726/2/L19

WASP-30b: A 61 $M_{\rm Jup}$ BROWN DWARF TRANSITING A $V = 12$, F8 STAR

D. R. Anderson[1], A. Collier Cameron[2], C. Hellier[1], M. Lendl[3], P. F. L. Maxted[1], D. Pollacco[4], D. Queloz[3], B. Smalley[1], A. M. S. Smith[1], I. Todd[4], A. H. M. J. Triaud[3], R. G. West[5], S. C. C. Barros[4], B. Enoch[2], M. Gillon[6], T. A. Lister[7], F. Pepe[3], D. Ségransan[3], R. A. Street[7], and S. Udry[3]
[1] Astrophysics Group, Keele University, Staffordshire, ST5 5BG, UK; dra@astro.keele.ac.uk
[2] SUPA, School of Physics and Astronomy, University of St. Andrews, North Haugh, Fife, KY16 9SS, UK
[3] Observatoire de Genève, Université de Genève, 51 Chemin des Maillettes, 1290 Sauverny, Switzerland
[4] Astrophysics Research Centre, School of Mathematics & Physics, Queen's University, University Road, Belfast, BT7 1NN, UK
[5] Department of Physics and Astronomy, University of Leicester, Leicester, LE1 7RH, UK
[6] Institut d'Astrophysique et de Géophysique, Université de Liège, Allée du 6 Août, 17, Bat. B5C, Liège 1, Belgium
[7] Las Cumbres Observatory, 6740 Cortona Dr. Suite 102, Santa Barbara, CA 93117, USA
Received 2010 October 14; accepted 2010 November 30; published 2010 December 17

ABSTRACT

We report the discovery of a 61-Jupiter-mass brown dwarf (BD), which transits its F8V host star, WASP-30, every 4.16 days. From a range of age indicators we estimate the system age to be 1–2 Gyr. We derive a radius ($0.89 \pm 0.02\ R_{\rm Jup}$) for the companion that is consistent with that predicted ($0.914\ R_{\rm Jup}$) by a model of a 1 Gyr old, non-irradiated BD with a dusty atmosphere. The location of WASP-30b in the minimum of the mass–radius relation is consistent with the quantitative prediction of Chabrier & Baraffe, thus confirming the theory.

Key words: binaries: eclipsing – brown dwarfs – stars: individual (WASP-30)

Online-only material: color figures, machine-readable table

1. INTRODUCTION

A brown dwarf (BD) is traditionally defined as an object with a mass above the deuterium-burning limit ($13\ M_{\rm Jup}$; e.g., Chabrier et al. 2000a) and below the hydrogen-burning limit ($0.07\ M_{\odot}$; e.g., Chabrier et al. 2000b). However, an alternative suggestion is that the manner in which an object forms should determine whether it is a planet or a BD. Thus, if an object formed by core accretion of dust and ices in a protoplanetary disk then it would be a planet, and if it formed by gravoturbulent collapse of a molecular cloud, as do stars, then it would be a BD.

Studies such as the Caballero et al. (2007) observations of a young open cluster core find a continuous mass function down to $\sim 6\ M_{\rm Jup}$, indicating that the star formation mechanism can produce objects with planetary masses. This is supported by theoretical studies (Padoan & Nordlund 2004; Hennebelle & Chabrier 2008) which suggest that gravoturbulent fragmentation of molecular clouds produces stars and BDs down to a few Jupiter masses in numbers comparable to the observationally determined distribution. In contrast, when taking into account planetary migration through the protoplanetary disk, the core accretion process might result in giant planets with masses of up to $10\ M_{\rm Jup}$ (Alibert et al. 2005) or even $25\ M_{\rm Jup}$ (Mordasini et al. 2008). Sahlmann et al. (2010) see evidence for a bimodal distribution in BD masses, with the less-massive group presumably representing the high-mass tail of the planetary distribution.

An accurate, precise measurement of an object's radius is therefore required to probe for the existence of a core and thus discriminate between the two formation mechanisms. For example, the radius of the $8\ M_{\rm Jup}$ body, HAT-P-2b, is consistent with an irradiated planet incorporating a 340-Earth-mass core, but is smaller than if it were coreless (Leconte et al. 2009). The $22\ M_{\rm Jup}$ CoRoT-3b (Deleuil et al. 2008) is sufficiently massive to qualify as a BD under the traditional definition, but the radius of this object is uncertain at the 7% level. This is higher than the 3% required to discriminate between the absence or the presence of a core and thus determine how it formed (Leconte et al. 2009). Irwin et al. (2010) found a $\sim 30\ M_{\rm Jup}$ BD, NLTT 41135C, which transits one member of an M-dwarf binary system. However, as the transits are grazing, it is not currently possible to accurately measure its radius.

There is less ambiguity around the upper end of the BD mass regime: if a body is sufficiently massive to fuse hydrogen then it is a star, otherwise it is a BD. High-mass BDs with precise radius measurements are useful for testing BD evolution models, as it is in the high-mass regime that models predict the greatest changes in radius with age (e.g., Baraffe et al. 2003). Stassun et al. (2006) discovered a BD eclipsing binary system in the Orion Nebula star-forming region, with masses of $57 \pm 5\ M_{\rm Jup}$ and $36 \pm 3\ M_{\rm Jup}$. With very large radii of $0.699 \pm 0.034\ R_{\odot}$ and $0.511 \pm 0.026\ R_{\odot}$, it seems that these objects are in the earliest stages of gravitational contraction. Similar to the NLTT 41135 system, LHS 6343 C (Johnson et al. 2010; J. A. Johnson 2010, private communication) is a $63\ M_{\rm Jup}$ BD that transits one member of an M-dwarf binary system. In this case, the transits are full and so the radius ($0.825 \pm 0.023\ R_{\rm Jup}$) of this object is precisely determined. CoRoT-15b (Bouchy et al. 2010) is a $63\ M_{\rm Jup}$ mass BD in a 3 day orbit around an F7V star. Due to the faintness of the host star ($V \sim 16$), the BD radius ($1.12^{+0.30}_{-0.15}\ R_{\rm Jup}$) is not yet well determined.

To test and refine models of BD formation and evolution, a population of well-characterized objects is required. In this Letter, we present the discovery of WASP-30b, a $61\ M_{\rm Jup}$ BD that transits its moderately bright host star.

2. OBSERVATIONS

WASP-30 is a $V = 11.9$, F8V star located in Aquarius, on the border with Cetus. A transit search (Collier Cameron et al. 2006) of WASP-South data from 2008 July to November found a strong, 4.16 day periodicity. Further observations in 2009 with

Monthly Notices of the ROYAL ASTRONOMICAL SOCIETY

Mon. Not. R. Astron. Soc. **410,** 1631–1636 (2011) doi:10.1111/j.1365-2966.2010.17550.x

WASP-25b: a 0.6$M_{\rm J}$ planet in the Southern hemisphere

B. Enoch,[1⋆] A. Collier Cameron,[1] D. R. Anderson,[2] T. A. Lister,[3] C. Hellier,[2] P. F. L. Maxted,[2] D. Queloz,[4] B. Smalley,[2] A. H. M. J. Triaud,[4] R. G. West,[5] D. J. A. Brown,[1] M. Gillon,[4,6] L. Hebb,[7] M. Lendl,[4] N. Parley,[1] F. Pepe,[4] D. Pollacco,[8] D. Segransan,[4] E. Simpson,[8] R. A. Street[3] and S. Udry[4]

[1]*School of Physics and Astronomy, University of St Andrews, North Haugh, St Andrews KY16 9SS*
[2]*Astrophysics Group, Keele University, Staffordshire ST5 5BG*
[3]*Las Cumbres Observatory, 6740 Cortona Drive Suite 102, Goleta, CA 93117, USA*
[4]*Observatoire astronomique de l'Universitén de Genéve, 51 Chemin des Maillettes, 1290 Sauverny, Switzerland*
[5]*Department of Physics and Astronomy, University of Leicester, Leicester LE1 7RH*
[6]*Institut d'Astrophysique et de Géophysique, Université de Liége, Allée de 6 Août, 17, Bat B5C, Liége 1, Belgium*
[7]*Vanderbilt University, Department of Physics and Astronomy, Nashville, TN 37235, USA*
[8]*Astrophysics Research Centre, School of Mathematics & Physics, Queen's University, University Road, Belfast BT7 1NN*

Accepted 2010 August 16. Received 2010 July 22; in original form 2010 April 13

ABSTRACT

We report the detection of a 0.6 $M_{\rm J}$ extrasolar planet by WASP-South, WASP-25b, transiting its solar-type host star every 3.76 d. A simultaneous analysis of the WASP, FTS and Euler photometry and CORALIE spectroscopy yields a planet of $R_{\rm p} = 1.22 R_{\rm J}$ and $M_{\rm p} = 0.58 M_{\rm J}$ around a slightly metal-poor solar-type host star, [Fe/H] $= -0.05 \pm 0.10$, of $R_* = 0.92\,{\rm R}_\odot$ and $M_* = 1.00\,{\rm M}_\odot$. WASP-25b is found to have a density of $\rho_{\rm p} = 0.32\,\rho_{\rm J}$, a low value for a sub-Jupiter mass planet. We investigate the relationship of planetary radius to planetary equilibrium temperature and host star metallicity for transiting exoplanets with a similar mass to WASP-25b, finding that these two parameters explain the radii of most low-mass planets well.

Key words: planetary systems.

1 INTRODUCTION

To date, over 440 exoplanets have been discovered, including more than 70 detected by the transit method.[1] The transit method together with follow-up radial velocity observations allow measurement of both the mass and radius of the planet, leading to a value for the planet's bulk density (Charbonneau et al. 2000). The atmospheric composition of transiting exoplanets can also be investigated through high-precision photometric and spectroscopic measurements, see e.g. Charbonneau et al. (2002).

A wide range of transiting exoplanets radii has been found and there has been much investigation into the factors that may influence a planet's radius. For example, Guillot et al. (2006) propose a negative relationship between the metallicity of a host star and the radius of an orbiting planet, caused by an increase in the amount of heavy elements in the planet, leading to a more massive core and hence smaller radius for a given mass. Alternatively, Burrows et al. (2007) consider that increasing the metallicity may increase the opacity of an exoplanet's atmosphere, retarding cooling and leading to a larger radius for a given mass. Another influence on a planet's radius may be the equilibrium temperature of the planet (Guillot & Showman 2002), determined by the stellar irradiation and the planet's distance from its host star. Tidal heating due to the circularization of the orbits of close-in exoplanets may also play a role in inflating the planetary radius (Bodenheimer, Laughlin & Lin 2003; Jackson, Greenberg & Barnes 2008). One motivation of the SuperWASP project is to detect enough transiting exoplanets, with a wide range of orbital and compositional parameters, to allow analyses that may distinguish between such differing models.

In this paper, we report the discovery of a 0.6$M_{\rm J}$ planet orbiting a solar mass star, WASP-25 (TYC6706-861-1, 1SWASP J130126.36-273120.0), in the Southern hemisphere. Analysis of photometric and spectroscopic data reveals WASP-25b to be another low-density planet, comparable to HD 209458b (Charbonneau et al. 2000). We also analyse the dependence of the radii of low-mass planets on host star metallicity and planetary equilibrium temperature, including WASP-25b and 18 other transiting planets, finding a relationship using singular value decomposition (SVD) analysis that gives an excellent agreement between observed and calibrated radii.

In Section 2 we describe the photometric and spectroscopic observations and data reduction procedures. In Section 3 we present the stellar and planetary parameters extracted from these data. Finally,

⋆E-mail: becky.enoch@st-andrews.ac.uk
[1] www.exoplanet.eu

A&A 526, A130 (2011)
DOI: 10.1051/0004-6361/201015992

Astronomy & Astrophysics

WASP-34b: a near-grazing transiting sub-Jupiter-mass exoplanet in a hierarchical triple system⋆

B. Smalley[1], D. R. Anderson[1], A. Collier Cameron[2], C. Hellier[1], M. Lendl[3], P. F. L. Maxted[1], D. Queloz[3], A. H. M. J. Triaud[3], R. G. West[4], S. J. Bentley[1], B. Enoch[2], M. Gillon[5,3], T. A. Lister[6], F. Pepe[3], D. Pollacco[7], D. Segransan[3], A. M. S. Smith[1], J. Southworth[1], S. Udry[3], P. J. Wheatley[8], P. L. Wood[1], and J. Bento[8]

[1] Astrophysics Group, Keele University, Staffordshire, ST5 5BG, UK
e-mail: bs@astro.keele.ac.uk
[2] SUPA, School of Physics and Astronomy, University of St. Andrews, North Haugh, Fife, KY16 9SS, UK
[3] Observatoire de Genève, Université de Genève, 51 chemin des Maillettes, 1290 Sauverny, Switzerland
[4] Department of Physics and Astronomy, University of Leicester, Leicester, LE1 7RH, UK
[5] Institut d'Astrophysique et de Géophysique, Université de Liège, Allée du 6 Août, 17, Bât. B5C, Liège 1, Belgium
[6] Las Cumbres Observatory, 6740 Cortona Dr. Suite 102, Santa Barbara, CA 93117, USA
[7] Astrophysics Research Centre, School of Mathematics & Physics, Queen's University, University Road, Belfast, BT7 1NN, UK
[8] Department of Physics, University of Warwick, Coventry CV4 7AL, UK

Received 25 October 2010 / Accepted 9 December 2010

ABSTRACT

We report the discovery of WASP-34b, a sub-Jupiter-mass exoplanet transiting its 10.4-magnitude solar-type host star (1SWASP J110135.89-235138.4; TYC 6636-540-1) every 4.3177 days in a slightly eccentric orbit ($e = 0.038 \pm 0.012$). We find a planetary mass of $0.59 \pm 0.01\ M_{\rm Jup}$ and radius of $1.22^{+0.11}_{-0.08}\ R_{\rm Jup}$. There is a linear trend in the radial velocities of $55 \pm 4\ {\rm m\,s^{-1}\,y^{-1}}$ indicating the presence of a long-period third body in the system with a mass $\gtrsim 0.45\ M_{\rm Jup}$ at a distance of $\gtrsim 1.2$ AU from the host star. This third-body is either a low-mass star, a white dwarf, or another planet. The transit depth ($(R_{\rm P}/R_*)^2 = 0.0126$) and high impact parameter ($b = 0.90$) suggest that this could be the first known transiting exoplanet expected to undergo grazing transits, but with a confidence of only ∼80%.

Key words. planets and satellites: general – stars: individual: WASP-34 – techniques: photometric – techniques: spectroscopic – techniques: radial velocities

1. Introduction

The majority of the known exoplanets have been discovered using the radial velocity technique (Mayor & Queloz 1995). In recent years, however, an ever increasing number have been discovered as a result of group-based and space-based transit search survey projects. Transiting exoplanets allow parameters such as the mass, radius, and density to be accurately determined, as well as their atmospheric properties to be studied during their transits and occultations (Charbonneau et al. 2005; Southworth 2009; Winn 2009).

The SuperWASP project has robotic observatories in the Canary Islands and South Africa. The wide angle survey is designed to find exoplanets around relatively bright stars in the V-magnitude range $9 \sim 13$. A detailed description of the SuperWASP project is given in Pollacco et al. (2006).

In this paper we report the discovery of WASP-34b, an exoplanet in orbit around its $V = 10.4$ mag. host star 1SWASP J110135.89-235138.4 in the constellation Crater. We present the WASP-South discovery photometry, together with Euler Telescope photometry and CORALIE radial velocity measurements.

⋆ Radial velocity and photometric data are only available in electronic form at the CDS via anonymous ftp to cdsarc.u-strasbg.fr (130.79.128.5) or via http://cdsarc.u-strasbg.fr/viz-bin/qcat?J/A+A/526/A130

2. Observations

2.1. WASP-South photometry

The host star WASP-34 (1SWASP J110135.89-235138.4; CD-23 9677; TYC 6636-540-1; GSC 06636-00540) was observed within two WASP-South camera fields during the periods 2006 May 4 to June 20 and 2007 January 4 to June 1, and in 3 fields during the period 2008 January 1 to May 28. A total of 35 351 data points were obtained. The pipeline-processed data were de-trended and searched for transits using the methods described in Collier Cameron et al. (2006), yielding a detection of a periodic, transit-like signature with a period of 4.3177 days and a depth of 0.011 mag (Fig. 1).

2.2. Spectroscopic observations with CORALIE

Spectroscopic observations were obtained with the CORALIE spectrograph on the Swiss 1.2 m telescope. The data were processed using the standard pipeline (Baranne et al. 1996; Queloz et al. 2000; Pepe et al. 2002). A total of 24 radial velocity (RV) and line bisector span ($V_{\rm span}$) measurements were made between 2009 December 1 and August 1 (Table 1). The bisector spans are a measure of the asymmetry of the cross-correlation function and, based on our experience, have standard errors of $\approx 2\sigma_{\rm RV}$.

The RV measurements show velocity variations with the same period as the transit light curve, but with a relatively

PUBLICATIONS OF THE ASTRONOMICAL SOCIETY OF THE PACIFIC, **123**:555–560, 2011 May

WASP-40b: Independent Discovery of the 0.6 $M_{\rm Jup}$ Transiting Exoplanet HAT-P-27b

D. R. ANDERSON,[1] S. C. C. BARROS,[2] I. BOISSE,[3,4] F. BOUCHY,[3,5] A. COLLIER CAMERON,[6] F. FAEDI,[2] G. HEBRARD,[3,5] C. HELLIER,[1] M. LENDL,[7] C. MOUTOU,[8] D. POLLACCO,[2] A. SANTERNE,[8] B. SMALLEY,[1] A. M. S. SMITH,[1] I. TODD,[2] A. H. M. J. TRIAUD,[7] R. G. WEST,[9] P. J. WHEATLEY,[10] J. BENTO,[10] B. ENOCH,[6] M. GILLON,[11] P. F. L. MAXTED,[1] J. MCCORMAC,[2] D. QUELOZ,[7] E. K. SIMPSON,[2] AND I. SKILLEN[12]

Received 2011 January 24; accepted 2011 March 21; published 2011 April 13

ABSTRACT. From WASP photometry and SOPHIE radial velocities we report the discovery of WASP-40b (HAT-P-27b), a 0.6 $M_{\rm Jup}$ planet that transits its 12th magnitude host star every 3.04 days. The host star is of late G-type or early K-type and likely has a metallicity greater than solar ($[{\rm Fe/H}] = 0.14 \pm 0.11$). The planet's mass and radius are typical of the known hot Jupiters, thus adding another system to the apparent pileup of transiting planets with periods near 3–4 days. Our parameters match those of the recent HATnet announcement of the same planet, thus giving confidence in the techniques used. We report a possible indication of stellar activity in the host star.

Online material: color figures

1. INTRODUCTION

While the Kepler mission is currently producing the most candidates for transiting extrasolar planets (e.g., Borucki et al. 2010), the ground-based transit-search programs continue to find more planets around stars at brighter magnitudes than those found in the space missions. Of these, Hungarian Automated Telescope Network (HATnet; Bakos et al. 2004) and Wide Angle Search for Planets (WASP; Pollacco et al. 2006) have been the most successful. Both projects are based on arrays of 200 mm f/1.8 lenses backed by CCDs, with the biggest difference being that HATnet operates at several longitudes, while WASP consists of one station in each hemisphere. The two projects look at overlapping regions of sky, which has led to some near-simultaneous discoveries, such as the planet WASP-11b (West et al. 2009) also being HAT-P-10b (Bakos et al. 2009). Reporting of such independent discoveries gives important information on the reliability of the respective techniques and on the completeness of the transit surveys.

Recently, HATnet announced the planet HAT-P-27b (Béky et al. 2011), a hot Jupiter in a 3 day orbit around a $m_V = 12.2$ star. This planet had been independently discovered by the WASP project and assigned the name WASP-40b (Hellier et al. 2011). We report here on the discovery of WASP-40b made using data from SuperWASP-North and WASP-South combined, together with radial velocities from the SOPHIE spectrograph at the Observatoire de Haute-Provence (OHP) observatory.

2. OBSERVATIONS

We observed WASP-40, an ~K0-type star located in Virgo, with the SuperWASP-North and WASP-South cameras during the three seasons of 2008–2010. A transit search (Collier Cameron et al. 2006) of the resulting 30,260 photometric measurements found a strong 3.04 day periodicity. The discovery light curve is displayed in Figure 1a, folded on this period.

Using the SOPHIE spectrograph mounted on the 1.93 m OHP telescope (Perruchot et al. 2008; Bouchy et al. 2009), we obtained eight spectra of WASP-40 during 2010 April and May. The high-efficiency mode and slow readout were

[1] Astrophysics Group, Keele University, Staffordshire, ST5 5BG, UK; dra@astro.keele.ac.uk.
[2] Astrophysics Research Centre, School of Mathematics & Physics, Queen's University, University Road, Belfast, BT7 1NN, UK.
[3] Institut d'Astrophysique de Paris, UMR7095 CNRS, Universite Pierre & Marie Curie, 75014 Paris, France.
[4] Centro de Astrofísica, Universidade do Porto, Rua das Estrelas, 4150-762 Porto, Portugal.
[5] Observatoire de Haute-Provence, CNRS/OAMP, 04870 Saint-Michel l'Observatoire, France.
[6] SUPA, School of Physics and Astronomy, University of St. Andrews, North Haugh, Fife, KY16 9SS, UK.
[7] Observatoire Astronomique de l'Université de Genève 51 ch. des Maillettes, 1290 Sauverny, Switzerland.
[8] Laboratoire d'Astrophysique de Marseille, 38 rue Fréderic Joliot-Curie, 13388 Marseille Cedex 13, France.
[9] Department of Physics and Astronomy, University of Leicester, Leicester, LE1 7RH, UK.
[10] Department of Physics, University of Warwick, Coventry CV4 7AL, UK.
[11] Institut d'Astrophysique et de Géophysique, Université de Liège, Allée du 6 Août, 17, Bat. B5C, Liège 1, Belgium.
[12] Isaac Newton Group of Telescopes, Apartado de Correos 321, E-38700 Santa Cruz de la Palma, Tenerife, Spain.

A&A 531, A40 (2011)
DOI: 10.1051/0004-6361/201116671

Astronomy & Astrophysics

WASP-39b: a highly inflated Saturn-mass planet orbiting a late G-type star⋆

F. Faedi[1], S. C. C. Barros[1], D. R. Anderson[2], D. J. A. Brown[3], A. Collier Cameron[3], D. Pollacco[1], I. Boisse[4,5], G. Hébrard[4,6], M. Lendl[7], T. A. Lister[8], B. Smalley[2], R. A. Street[8], A. H. M. J. Triaud[7], J. Bento[9], F. Bouchy[4,6], O. W. Butters[10], B. Enoch[3], C. A. Haswell[11], C. Hellier[2], F. P. Keenan[1], G. R. M. Miller[3], V. Moulds[1], C. Moutou[12], A. J. Norton[11], D. Queloz[7], A. Santerne[4,6], E. K. Simpson[1], I. Skillen[13], A. M. S. Smith[2], S. Udry[7], C. A. Watson[1], R. G. West[10], and P. J. Wheatley[9]

[1] Astrophysics Research Centre, School of Mathematics and Physics, Queen's University Belfast, University Road, Belfast BT7 1NN, UK
e-mail: f.faedi@qub.ac.uk
[2] Astrophysics Group, Keele University, Staffordshire, ST5 5BG, UK
[3] School of Physics and Astronomy, University of St Andrews, St Andrews, Fife KY16 9SS, UK
[4] Institut d'Astrophysique de Paris, UMR 7095 CNRS, Université Pierre & Marie Curie, France
[5] Centro de Astrofísica, Universidade do Porto, Rua das Estrelas, 4150-762 Porto, Portugal
[6] Observatoire de Haute-Provence, CNRS/OAMP, 04870 St Michel l'Observatoire, France
[7] Observatoire astronomique de l'Université de Genève, 51 Ch. des Maillettes, 1290 Sauverny, Switzerland
[8] Las Cumbres Observatory Global Telescope Network, 6740 Cortona Drive Suite 102, CA 93117, USA
[9] Department of Physics, University of Warwick, Coventry CV4 7AL, UK
[10] Department of Physics and Astronomy, University of Leicester, Leicester, LE1 7RH, UK
[11] Department of Physics and Astronomy, The Open University, Milton Keynes, MK7 6AA, UK
[12] Laboratoire d'Astrophysique de Marseille, 38 rue Frédéric Joliot-Curie, 13388 Marseille Cedex 13, France
[13] Isaac Newton Group of Telescopes, Apartado de Correos 321, 38700 Santa Cruz de Palma, Spain

Received 7 February 2011 / Accepted 21 April 2011

ABSTRACT

We present the discovery of WASP-39b, a highly inflated transiting Saturn-mass planet orbiting a late G-type dwarf star with a period of 4.055259 ± 0.000008 d, Transit Epoch T_0 = 2 455 342.9688 ± 0.0002 (HJD), of duration 0.1168 ± 0.0008 d. A combined analysis of the WASP photometry, high-precision follow-up transit photometry, and radial velocities yield a planetary mass of $M_{\rm pl}$ = 0.28 ± 0.03 $M_{\rm J}$ and a radius of $R_{\rm pl}$ = 1.27 ± 0.04 $R_{\rm J}$, resulting in a mean density of 0.14 ± 0.02 $\rho_{\rm J}$. The stellar parameters are mass $M_\star$ = 0.93 ± 0.03 $M_\odot$, radius $R_\star$ = 0.895 ± 0.23 $R_\odot$, and age 9^{+3}_{-4} Gyr. Only WASP-17b and WASP-31b have lower densities than WASP-39b, although they are slightly more massive and highly irradiated planets. From our spectral analysis, the metallicity of WASP-39 is measured to be [Fe/H] = −0.12 ± 0.1 dex, and we find the planet to have an equilibrium temperature of 1116^{+33}_{-32} K. Both values strengthen the observed empirical correlation between these parameters and the planetary radius for the known transiting Saturn-mass planets.

Key words. stars: individual: WASP-39 – techniques: photometric – techniques: radial velocities – planetary systems

1. Introduction

The importance of transiting extrasolar planets is related to their geometrical configuration (Sackett 1999). Transit geometry severely constrains the orbital inclination of the planet, allowing accurate measurements of its mass and radius to be derived. The inferred planet's density provides information on the system's bulk physical properties, and thus is a fundamental parameter for constraining theoretical models of planetary formation, structure, and evolution (e.g. Guillot 2005; Fortney et al. 2007; Liu et al. 2008).

To date, more than 100 transiting planets have been discovered, which show a huge range of diversity in their physical and dynamical properties. For example, their mass ranges from ~5 $M_\oplus$ (Kepler-10b, Batalha et al. 2011) to about 12 $M_{\rm J}$ (XO-3b, Johns-Krull et al. 2008; Hébrard et al. 2008). Some planets have radii that agree with models of irradiated planets (Burrows et al. 2007; Fortney et al. 2007), while others are found to be anomalously large (e.g. WASP-12b, Hebb et al. 2009, and TrES-4b, Southworth 2010; Torres et al. 2008; Mandushev et al. 2007). The diversity in exoplanet densities, hence in their internal compositions, is particularly noticeable at sub-Jupiter masses. For example, some exoplanets have very high densities and are thought to have a rocky/ice core (e.g. HD 149026b, $\rho_{\rm pl} \simeq 1\,\rho_{\rm J}$, Sato et al. 2005), while systems such as TrES-4b ($\rho_{\rm pl} = 0.17\,\rho_{\rm J}$, Mandushev et al. 2007), WASP-17b ($\rho_{\rm pl} = 0.06\,\rho_{\rm J}$, Anderson et al. 2010b, 2011b), WASP-31b ($\rho_{\rm pl} = 0.132\ \rho_{\rm J}$, Anderson et al. 2010a), and Kepler-7b ($\rho_{\rm pl} = 0.13\ \rho_{\rm J}$, Latham et al. 2010) are examples of planets with puzzlingly low densities that challenge standard evolutionary theories in reproducing their radii (Fortney et al. 2007; Burrows et al. 2007). To assess the inflation status of a system, generally planetary radii are compared to

⋆ Spectroscopic and photometric data are only available at the CDS via anonymous ftp to
cdsarc.u-strasbg.fr (130.79.128.5) or via
http://cdsarc.u-strasbg.fr/viz-bin/qcat?J/A+A/531/A40

A&A 531, A60 (2011)
DOI: 10.1051/0004-6361/201016208

Astronomy & Astrophysics

WASP-31b: a low-density planet transiting a metal-poor, late-F-type dwarf star⋆,⋆⋆

D. R. Anderson[1], A. Collier Cameron[2], C. Hellier[1], M. Lendl[3], T. A. Lister[4], P. F. L. Maxted[1], D. Queloz[3], B. Smalley[1], A. M. S. Smith[1], A. H. M. J. Triaud[3], R. G. West[5], D. J. A. Brown[2], M. Gillon[6], F. Pepe[3], D. Pollacco[7], D. Ségransan[3], R. A. Street[4], and S. Udry[3]

[1] Astrophysics Group, Keele University, Staffordshire ST5 5BG, UK
e-mail: dra@astro.keele.ac.uk
[2] SUPA, School of Physics and Astronomy, University of St. Andrews, North Haugh, Fife KY16 9SS, UK
[3] Observatoire de Genève, Université de Genève, 51 Chemin des Maillettes, 1290 Sauverny, Switzerland
[4] Las Cumbres Observatory, 6740 Cortona Dr. Suite 102, Santa Barbara, CA 93117, USA
[5] Department of Physics and Astronomy, University of Leicester, Leicester LE1 7RH, UK
[6] Institut d'Astrophysique et de Géophysique, Université de Liège, Allée du 6 Août 17, Bat. B5C, Liège 1, Belgium
[7] Astrophysics Research Centre, School of Mathematics & Physics, Queen's University, University Road, Belfast BT7 1NN, UK

Received 25 November 2010 / Accepted 18 May 2011

ABSTRACT

We report the discovery of the low-density, transiting giant planet WASP-31b. The planet is 0.48 Jupiter masses and 1.55 Jupiter radii. It is in a 3.4-day orbit around a metal-poor, late-F-type, $V = 11.7$ dwarf star, which is a member of a common proper motion pair. In terms of its low density, WASP-31b is second only to WASP-17b, which is a more highly irradiated planet of similar mass.

Key words. binaries: eclipsing – planetary systems – stars: individual: WASP-31

1. Introduction

To date, 107 transiting extrasolar planets have been discovered[1], the majority of which are gas giants in short orbits. The radii of a subset of these exoplanets are larger than predicted by standard models of irradiated gas giants (e.g., Burrows et al. 2007; Fortney et al. 2007), including TrES-4b (Mandushev et al. 2007; Sozzetti et al. 2009), WASP-12b (Hebb et al. 2009), and WASP-17b (Anderson et al. 2010, 2011b). A number of mechanisms have been proposed as potential solutions to the radius anomaly (see Fortney et al. 2010, for a review), each of which involves either injecting heat into the planet from an external source or slowing heat loss from the planet.

One such mechanism is the dissipation of energy within a planet as heat during the tidal circularisation of an eccentric orbit (Bodenheimer et al. 2001; Gu et al. 2003; Jackson et al. 2008; Ibgui & Burrows 2009). Such studies suggest that tidal heating may be sufficient to explain the large radii of even the most bloated exoplanets, though we would have to be observing some systems at very special times. A high heating rate, as suggested by Leconte et al. (2010), would mean most tidal energy is radiated away by the age typical of the very most bloated planets (a few Gyr) and so could not have played a significant role in their observed bloating. However, the current uncertainty in tidal theory allows for a wide range of heating rates (e.g. Ibgui et al. 2011). Though most studies have considered a transient phase of tidal heating, ongoing tidal heating (e.g. Ibgui et al. 2010) would occur if an additional companion continues to excite the orbital eccentricity of the bloated planet (e.g. Mardling 2007).

Burrows et al. (2007) proposed that enhanced opacities would retard the loss of internal heat and thus slow contraction of bloated planets. They suggested that enhanced opacities may arise due to the strong optical and UV irradiation of short-orbit, gas giants that could alter their atmospheres, producing thick hazes, absorbing clouds and non-equilibrium chemical species (e.g. tholins or polyacetylenes).

The bloated planets are all very strongly irradiated by their host stars, and a small fraction of stellar insolation energy would be sufficient to account for the observed degrees of bloating. Guillot & Showman (2002) suggested that the kinetic energy of strong winds, induced in the atmosphere by the large day-night temperature contrasts that result from tidal locking, may be transported downward and deposited as thermal energy in the deep interior. However, a mechanism to convert the kinetic energy into thermal energy would still be required. Li & Goodman (2010) and Youdin & Mitchell (2010) found that turbulence is efficient at dissipating kinetic energy. Magnetic drag on weakly ionized winds (Perna et al. 2010) and Ohmic heating (Batygin & Stevenson 2010) are alternative mechanisms. The non-bloated planets are also highly irradiated. Hence, such a mechanism would either have to act more efficiently on the bloated planets, or some other property must counteract its effect. One such possibility is the presence of a massive core.

⋆ Based in part on observations made with the HARPS spectrograph on the 3.6-m ESO telescope (proposal 085.C-0393) and with the CORALIE spectrograph and the Euler camera on the 1.2-m Euler Swiss telescope, both at the ESO La Silla Observatory, Chile.
⋆⋆ The photometric time-series and radial-velocity data used in this work are available at the CDS via anonymous ftp to cdsarc.u-strasbg.fr (130.79.128.5) or via http://cdsarc.u-strasbg.fr/viz-bin/qcat?J/A+A/531/A60
[1] 2010 Nov. 25, http://exoplanet.eu

A&A 533, A88 (2011)
DOI: 10.1051/0004-6361/201117198

Astronomy & Astrophysics

WASP-50 b: a hot Jupiter transiting a moderately active solar-type star⋆

M. Gillon[1], A. P. Doyle[2], M. Lendl[3], P. F. L. Maxted[2], A. H. M. J. Triaud[3], D. R. Anderson[2], S. C. C. Barros[4], J. Bento[5], A. Collier-Cameron[6], B. Enoch[6], F. Faedi[4], C. Hellier[2], E. Jehin[1], P. Magain[1], J. Montalbán[1], F. Pepe[3], D. Pollacco[4], D. Queloz[3], B. Smalley[2], D. Segransan[3], A. M. S. Smith[2], J. Southworth[2], S. Udry[3], R. G. West[7], and P. J. Wheatley[5]

[1] Université de Liège, Allée du 6 août 17, Sart Tilman, Liège 1, Belgium
e-mail: michael.gillon@ulg.ac.be
[2] Astrophysics Group, Keele University, Staffordshire, ST5 5BG, UK
[3] Observatoire de Genève, Université de Genève, 51 chemin des Maillettes, 1290 Sauverny, Switzerland
[4] Astrophysics Research Centre, School of Mathematics & Physics, Queen's University, University Road, Belfast, BT7 1NN, UK
[5] Department of Physics, University of Warwick, Coventry CV4 7AL, UK
[6] School of Physics and Astronomy, University of St. Andrews, North Haugh, Fife, KY16 9SS, UK
[7] Department of Physics and Astronomy, University of Leicester, Leicester, LE1 7RH, UK

Received 6 May 2011 / Accepted 1 August 2011

ABSTRACT

We report the discovery by the WASP transit survey of a giant planet in a close orbit (0.0295 ± 0.0009 AU) around a moderately bright (V = 11.6, K = 10) G9 dwarf (0.89 ± 0.08 $M_\odot$, 0.84 ± 0.03 $R_\odot$) in the Southern constellation Eridanus. Thanks to high-precision follow-up photometry and spectroscopy obtained by the telescopes TRAPPIST and *Euler*, the mass and size of this planet, WASP-50 b, are well constrained to 1.47 ± 0.09 $M_{\rm Jup}$ and 1.15 ± 0.05 $R_{\rm Jup}$, respectively. The transit ephemeris is 2 455 558.6120 (±0.0002) + N × 1.955096 (±0.000005) $\mathrm{HJD_{UTC}}$. The size of the planet is consistent with basic models of irradiated giant planets. The chromospheric activity ($\log R'_{HK} = -4.67$) and rotational period ($P_{\rm rot}$ = 16.3 ± 0.5 days) of the host star suggest an age of 0.8 ± 0.4 Gy that is discrepant with a stellar-evolution estimate based on the measured stellar parameters ($\rho_* = 1.48 \pm 0.10\,\rho_\odot$, $T_{\rm eff}$ = 5400 ± 100 K, [Fe/H] = −0.12 ± 0.08) which favors an age of 7 ± 3.5 Gy. This discrepancy could be explained by the tidal and magnetic influence of the planet on the star, in good agreement with the observations that stars hosting hot Jupiters tend to show faster rotation and magnetic activity. We measure a stellar inclination of 84^{+6}_{-31} deg, disfavoring a high stellar obliquity. Thanks to its large irradiation and the relatively small size of its host star, WASP-50 b is a good target for occultation spectrophotometry, making it able to constrain the relationship between hot Jupiters' atmospheric thermal profiles and the chromospheric activity of their host stars.

Key words. techniques: spectroscopic – planetary systems – techniques: radial velocities – stars: individual: WASP-50 – techniques: photometric

1. Introduction

While the *Kepler* space mission is pursuing its pioneering search for habitable terrestrial planets transiting solar-type stars (Borucki et al. 2011), ground-based, wide-field surveys continue to detect short-period (i.e. a few days, or even less) transiting giant planets at an increasing rate. These transiting "hot Jupiters" are important objects for the nascent field of comparative exoplanetology. As they could not form in situ at such short distances from their parent stars, their orbital configurations pose an interesting challenge for theories of formation and evolution of planetary systems (D'Angelo et al. 2010; Lubow & Ida 2010). Their migrational history can be further constrained by the measurement of the orientation of their orbital axis relative to the stellar spin axis (Winn 2010a), the measurements obtained so far suggesting that past dynamical interactions with a third body could be driving their migration (Triaud et al. 2010). Hot Jupiters also make it possible to study the physical response of a giant planet to an irradiation orders of magnitude larger than in solar system planets (Burrows et al. 2008; Fortney et al. 2010), and also to the strong gravitational and magnetic fields so close to their host stars (Correia & Laskar 2010; Chang et al. 2010). Furthermore, these planets could be able to influence the properties of their parent stars, notably by modifying their angular momentum budget and by inducing chromospheric activity (Lanza 2010). The atmospheres of hot Jupiters can also be studied thoroughly. Their generally large atmospheric scale heights and their frequent transits maximize the signal-to-noise ratios (SNR) achievable on short timescales in transit absorption spectrophotometry, while their large irradiation makes it possible to measure the thermal emission profile of their dayside through occultation-depth measurements at different wavelengths (Seager 2010). Such atmospheric measurements have made possible the study of the atmospheric composition of several planets (Seager & Deming 2010). They have also revealed that most "hot Jupiters" harbor a high-altitude thermal inversion

⋆ The photometric time-series used in this work are only available at the CDS via anonymous ftp to
cdsarc.u-strasbg.fr (130.79.128.5) or via
http://cdsarc.u-strasbg.fr/viz-bin/qcat?J/A+A/533/A88

The Astronomical Journal, 142:86 (9pp), 2011 September doi:10.1088/0004-6256/142/3/86

WASP-35b, WASP-48b, AND HAT-P-30b/WASP-51b: TWO NEW PLANETS AND AN INDEPENDENT DISCOVERY OF A HAT PLANET

B. Enoch[1], D. R. Anderson[2], S. C. C. Barros[3], D. J. A. Brown[1], A. Collier Cameron[1], F. Faedi[3], M. Gillon[4], G. Hébrard[5,6], T. A. Lister[7], D. Queloz[8], A. Santerne[9], B. Smalley[2], R. A. Street[7], A. H. M. J. Triaud[8], R. G. West[10], F. Bouchy[5,6], J. Bento[11], O. Butters[10], L. Fossati[12], C. A. Haswell[12], C. Hellier[2], S. Holmes[12], E. Jehen[4], M. Lendl[8], P. F. L. Maxted[2], J. McCormac[3], G. R. M. Miller[1], V. Moulds[3], C. Moutou[9], A. J. Norton[12], N. Parley[1], F. Pepe[8], D. Pollacco[3], D. Segransan[8], E. Simpson[3], I. Skillen[13], A. M. S. Smith[2], S. Udry[8], and P. J. Wheatley[11]
[1] SUPA, School of Physics and Astronomy, University of St Andrews, North Haugh, St Andrews KY16 9SS, UK
[2] Astrophysics Group, Keele University, Staffordshire ST5 5BG, UK
[3] Astrophysics Research Centre, School of Mathematics & Physics, Queen's University Belfast, University Road, Belfast BT7 1NN, UK
[4] Institut d'Astrophysique et de Géophysique, Université de Liége, Allée de 6 Août, 17, Bat B5C, Liége 1, Belgium
[5] Institut d'Astrophysique de Paris, UMR7095 CNRS, Université Pierre & Marie Curie, France
[6] Observatoire de Haute-Provence, CNRS/OAMP, 04870 St Michel l'Observatoire, France
[7] Las Cumbres Observatory, 6740 Cortona Drive Suite 102, Goleta, CA 93117, USA
[8] Observatoire Astronomique de l'Université de Genéve, 51 Chemin des Maillettes, 1290 Sauverny, Switzerland
[9] Laboratoire d'Astrophysique de Marseille, Université d'Aix-Marseille & CNRS, 38 rue Frédéric Joliot-Curie, 13388 Marseille Cedex 13, France
[10] Department of Physics and Astronomy, University of Leicester, Leicester LE1 7RH, UK
[11] Department of Physics, University of Warwick, Coventry CV4 7AL, UK
[12] Department of Physics and Astronomy, The Open University, Milton Keynes MK7 6AA, UK
[13] Isaac Newton Group of Telescopes, Apartado de Correos 321, E-38700 Santa Cruz de Palma, Spain
Received 2011 April 8; accepted 2011 July 2; published 2011 August 16

ABSTRACT

We report the detection of WASP-35b, a planet transiting a metal-poor ([Fe/H] = −0.15) star in the Southern hemisphere, WASP-48b, an inflated planet which may have spun-up its slightly evolved host star of 1.75 $R_\odot$ in the Northern hemisphere, and the independent discovery of HAT-P-30b/WASP-51b, a new planet in the Northern hemisphere. Using WASP, RISE, Faulkes Telescope South, and TRAPPIST photometry, with CORALIE, SOPHIE, and NOT spectroscopy, we determine that WASP-35b has a mass of $0.72 \pm 0.06\ M_J$ and radius of $1.32 \pm 0.05 R_J$, and orbits with a period of 3.16 days, WASP-48b has a mass of $0.98 \pm 0.09\ M_J$, radius of $1.67 \pm 0.10\ R_J$, and orbits in 2.14 days, while HAT-P-30b/WASP-51b, with an orbital period of 2.81 days, is found to have a mass of $0.76 \pm 0.05\ M_J$ and radius of $1.42 \pm 0.03\ R_J$, agreeing with values of $0.71 \pm 0.03\ M_J$ and $1.34 \pm 0.07\ R_J$ reported for HAT-P-30b.

Key words: planetary systems

Online-only material: color figures

1. INTRODUCTION

Around 120 transiting exoplanets have now been discovered,[14] having both their radii and masses known, and may be subjected to further investigations into their bulk and atmospheric composition (see, e.g., Charbonneau et al. 2002, 2005; Fortney et al. 2007; Haswell 2010; Seager & Deming 2010). They show a diverse range of densities and thus internal compositions. Over 80% of those with masses greater than 0.1 M_J have radii greater than that of Jupiter, and many have extremely low densities which even coreless models struggle to explain (Fortney et al. 2007; Burrows et al. 2007), for example TrES-4b (Mandushev et al. 2007), WASP-17b (Anderson et al. 2010, 2011), and Kepler-7b (Latham et al. 2010). More transiting exoplanets are vital to constrain the formation and evolution of such planets.

Several possible effects on planetary radii have been discussed in the literature, including inflation due to strong heating by irradiation received from the host star (Guillot et al. 1996; Guillot & Showman 2002), ohmic heating from the coupling of magnetic fields and atmospheric flows (Batygin & Stevenson 2010; Batygin et al. 2011), and tidal heating due to the circularization of close-in exoplanets (Bodenheimer et al. 2001, 2003; Jackson et al. 2008).

Most of the known transiting exoplanets orbit very close to their host star, which produces strong tidal forces between them. The tidal interactions may result in orbital circularization, synchronization, and decay (Pont 2009). An apparent relationship between period and eccentricity of non-transiting exoplanets, such that planets very close to their host stars have circular orbits while those farther from the stars show a wide range of eccentricities, seems to provide evidence for the tidal circularization of planetary orbits (Mazeh 2008). However, it had generally been assumed that the masses of planets are too small to synchronize the stellar rotation with the planetary orbit through tidal forces (Mazeh 2008). Some possible exceptions exist for planets with large masses, for example the τ Boo system with a 4 M_J planet, for which there is evidence for stellar rotation synchronization (Fares et al. 2009). Recently, CoRoT-11b has been announced to have a "peculiar tidal evolution" (Gandolfi et al. 2011), where the stellar rotation period of 1.7 days is now shorter than the planetary orbital period of 3 days, due to the strong tidal forces causing orbital expansion of the planet from a previously approximately synchronized orbital period. The possibility of perhaps unknown close-in exoplanets affecting the stellar spin rate of their host stars produces uncertainty in the use of the gyrochronological age estimate of a star, based on the normal spin-down of a star as it ages.

[14] http://www.exoplanet.eu.

A&A 535, L7 (2011)
DOI: 10.1051/0004-6361/201117081

Astronomy & Astrophysics

Letter to the Editor

WASP-43b: the closest-orbiting hot Jupiter

C. Hellier[1], D. R. Anderson[1], A. Collier Cameron[2], M. Gillon[3], E. Jehin[3], M. Lendl[4], P. F. L. Maxted[1], F. Pepe[4], D. Pollacco[5], D. Queloz[4], D. Ségransan[4], B. Smalley[1], A. M. S. Smith[1], J. Southworth[1], A. H. M. J. Triaud[4], S. Udry[4], and R. G. West[6]

[1] Astrophysics Group, Keele University, Staffordshire, ST5 5BG, UK
e-mail: ch@astro.keele.ac.uk
[2] SUPA, School of Physics and Astronomy, University of St. Andrews, North Haugh, Fife, KY16 9SS, UK
[3] Institut d'Astrophysique et de Géophysique, Université de Liège, Allée du 6 Août, 17, Bât. B5C, Liège 1, Belgium
[4] Observatoire astronomique de l'Université de Genève, 51 Ch. des Maillettes, 1290 Sauverny, Switzerland
[5] Astrophysics Research Centre, School of Mathematics & Physics, Queen's University, University Road, Belfast, BT7 1NN, UK
[6] Department of Physics and Astronomy, University of Leicester, Leicester, LE1 7RH, UK

Received 14 April 2011 / Accepted 1 November 2011

ABSTRACT

We report the discovery of WASP-43b, a hot Jupiter transiting a K7V star every 0.81 d. At 0.6-$M_{\odot}$ the host star has the lowest mass of any star currently known to host a hot Jupiter. It also shows a 15.6-d rotation period. The planet has a mass of 1.8 $M_{\rm Jup}$, a radius of 0.9 $R_{\rm Jup}$, and with a semi-major axis of only 0.014 AU has the smallest orbital distance of any known hot Jupiter. The discovery of such a planet around a K7V star shows that planets with apparently short remaining lifetimes owing to tidal decay of the orbit are also found around stars with deep convection zones.

Key words. stars: individual: WASP-43 – planetary systems

1. Introduction

As planet discoveries increase we begin to see patterns in their distribution, and to find the rarer systems that mark the edges of the envelope. The ground-based transit searches such as WASP (Pollacco et al. 2006) and HAT (Bakos et al. 2002) are particularly suitable for finding the systems that delineate the cut-off of hot Jupiters as orbital radius decreases. This distribution is expected to tell us about several processes, including disk migration and possible "stopping mechanisms" (e.g. Matsumura et al. 2007), third-body processes, such as scattering and the Kozai mechanism, that can move planets onto eccentric orbits that then circularize at short periods (e.g. Guillochon et al. 2011), and the effect of tidal interactions with the host star (e.g. Matsumura et al. 2010).

The WASP-South camera array has been monitoring stars of magnitude 9–13 since 2006, and, in conjunction with radial-velocities from the Euler/CORALIE spectrograph, is now responsible for the majority of transiting hot Jupiters currently known in the Southern hemisphere (see Hellier et al. 2011). Here we report the discovery of WASP-43b, a hot Jupiter orbiting a late-type star with a very small semi-major axis.

2. Observations

The WASP project uses 8-camera arrays that cover 450 square degrees of sky with a typical cadence of 8 min. The WASP surveys are described in Pollacco et al. (2006) while a discussion of our planet-hunting methods can be found in Collier-Cameron et al. (2007) and Pollacco et al. (2007).

WASP-43 is a $V = 12.4$, K7V star in the constellation Sextans. It was flagged as a planet candidate based on WASP-South data obtained during 2009 January–May, and has been further observed by both WASP-South and SuperWASP-North over 2010 January–May, leading to a total of 13 768 data points. A putative 0.81-d transit period led to radial-velocity followup with the CORALIE spectrograph on the Euler 1.2-m telescope at La Silla. Fourteen radial-velocity measurements over 2010 January–July (Table 1) showed that the transiting body is a 1.8-$M_{\rm Jup}$ planet. We also checked the bisectors (e.g. Queloz et al. 2001) to guard against transit mimics (Fig. 1). On 2010 December 07 we obtained a transit lightcurve with the

Table 1. CORALIE radial velocities of WASP-43.

BJD – 2 400 000 (UTC)	RV (km s^{-1})	$\sigma_{\rm RV}$ (km s^{-1})	Bisector (km s^{-1})
55 205.7594	–3.058	0.013	0.052
55 325.6232	–4.041	0.021	0.055
55 327.5745	–3.430	0.026	0.050
55 328.5441	–3.067	0.014	0.033
55 334.5030	–3.821	0.018	0.023
55 359.4824	–3.026	0.022	–0.098
55 362.5333	–3.522	0.031	0.050
55 364.4596	–3.262	0.017	0.110
55 375.4741	–3.830	0.018	0.048
55 376.4911	–3.036	0.045	0.097
55 378.4837	–3.994	0.018	–0.035
55 379.5246	–3.904	0.021	–0.003
55 380.4904	–3.282	0.021	0.017
55 391.4617	–3.869	0.028	0.036
55 392.4602	–4.086	0.021	0.072

Notes. Bisector errors are twice RV errors.

The Astronomical Journal, 143:81 (9pp), 2012 April doi:10.1088/0004-6256/143/4/81

WASP-36b: A NEW TRANSITING PLANET AROUND A METAL-POOR G-DWARF, AND AN INVESTIGATION INTO ANALYSES BASED ON A SINGLE TRANSIT LIGHT CURVE

A. M. S. Smith[1,8], D. R. Anderson[1], A. Collier Cameron[2], M. Gillon[3], C. Hellier[1], M. Lendl[4], P. F. L. Maxted[1], D. Queloz[4], B. Smalley[1], A. H. M. J. Triaud[4], R. G. West[5], S. C. C. Barros[6], E. Jehin[3], F. Pepe[4], D. Pollacco[6], D. Segransan[4], J. Southworth[1], R. A. Street[7], and S. Udry[4]

[1] Astrophysics Group, Keele University, Staffordshire, ST5 5BG, UK; amss@astro.keele.ac.uk
[2] SUPA, School of Physics & Astronomy, University of St Andrews, North Haugh, Fife, KY16 9SS, UK
[3] Institut d'Astrophysique et de Géophysique, Université de Liège, Allée du 6 Août, 17 Bât. B5C, Liège 1, Belgium
[4] Observatoire de Genève, Université de Genève, 51 Chemin des Maillettes, 1290 Sauverny, Switzerland
[5] Department of Physics & Astronomy, University of Leicester, Leicester, LE1 7RH, UK
[6] Astrophysics Research Centre, School of Mathematics & Physics, Queen's University, University Road, Belfast, BT7 1NN, UK
[7] Las Cumbres Observatory, 6740 Cortona Drive Suite 102, Goleta, CA 93117, USA
Received 2011 October 17; accepted 2012 January 25; published 2012 February 24

ABSTRACT

We report the discovery, from WASP and CORALIE, of a transiting exoplanet in a 1.54 day orbit. The host star, WASP-36, is a magnitude $V = 12.7$, metal-poor G2 dwarf ($T_{\rm eff} = 5959 \pm 134$ K), with [Fe/H] $= -0.26 \pm 0.10$. We determine the planet to have mass and radius, respectively, 2.30 ± 0.07 and 1.28 ± 0.03 times that of Jupiter. We have eight partial or complete transit light curves, from four different observatories, which allow us to investigate the potential effects on the fitted system parameters of using only a single light curve. We find that the solutions obtained by analyzing each of these light curves independently are consistent with our global fit to all the data, despite the apparent presence of correlated noise in at least two of the light curves.

Key words: planetary systems – planets and satellites: detection – planets and satellites: fundamental parameters – stars: individual (WASP-36) – techniques: photometric

1. INTRODUCTION

Of the 171 confirmed transiting planetary systems,[9] the majority have been discovered from the ground, from surveys such as WASP (Pollacco et al. 2006) and HATnet (Bakos et al. 2004). Although the *Kepler* space mission is discovering an increasing number of planets and even more candidate planets (e.g., Borucki et al. 2010, 2011), the ground-based discoveries have the advantage that the host stars are generally brighter. This allows radial velocity (RV) measurements to measure the planetary mass, and is conducive to further characterization observations, such as measuring occultations in the infrared to probe atmospheric temperature and structure.

Many of the current questions in exoplanet science are being addressed by analyzing the statistical properties of the growing ensemble of well-characterized transiting planetary systems. Here we report the discovery of a transiting planet orbiting the $V \sim 12.7$ star WASP-36 (= 2MASS J08461929−0801370) in the constellation Hydra.

2. OBSERVATIONS

2.1. WASP Photometry

WASP-36 was observed in 2009 and 2010 by WASP-South, which is located at the South African Astronomical Observatory (SAAO), near Sutherland in South Africa, and by SuperWASP at the Observatorio del Roque de los Muchachos on La Palma, Spain. Each instrument consists of eight Canon 200 mm $f/1.8$ lenses, each equipped with an Andor 2048 × 2048 e2v CCD camera, on a single robotic mount. Further details of the instrument, survey, and data reduction procedures are described in Pollacco et al. (2006), and details of the candidate selection procedure can be found in Collier Cameron et al. (2007) and Pollacco et al. (2008). A total of 13,781 measurements of WASP-36 were made between 2009 January 14 and 2010 April 21.

WASP-South 2009 data revealed the presence of a transit-like signal with a period of ∼1.5 days and a depth of ∼15 mmag. The WASP light curve is shown folded on the best-fitting orbital period in Figure 1.

2.2. Spectroscopy

Spectroscopic observations of WASP-36 were made with the CORALIE spectrograph of the 1.2 m Euler–Swiss Telescope. Simultaneous spectra of a thorium–argon emission line lamp were obtained in order to calibrate the stellar spectra. A total of 19 spectra were taken between 2010 March 11 and 2011 January 11, and processed using the standard CORALIE data reduction pipeline (Baranne et al. 1996). The resulting RV data are given in Table 1 and plotted in Figure 2. In order to rule out non-planetary causes for the RV variation, such as a blended eclipsing binary system, we examined the bisector spans (e.g., Queloz et al. 2001), which exhibit no correlation with RV (Figure 2), as expected.

2.3. Follow-up Photometry

We have a total of eight high-precision follow-up light curves of the transit of WASP-36b, summarized in Table 2. Differential aperture photometry was performed using the IRAF/DAOPHOT package for TRAPPIST and FTN data, and the ULTRACAM pipeline (Dhillon et al. 2007; Barros et al. 2011) for the LT data, with aperture radii and choice of comparison stars optimized to give the lowest rms of the out-of-transit photometry.

[8] Author to whom any correspondence should be addressed.
[9] http://www.exoplanet.eu, 2011 October 13.

Monthly Notices of the ROYAL ASTRONOMICAL SOCIETY

Mon. Not. R. Astron. Soc. **422,** 1988–1998 (2012) doi:10.1111/j.1365-2966.2012.20635.x

WASP-44b, WASP-45b and WASP-46b: three short-period, transiting extrasolar planets

D. R. Anderson,[1⋆] A. Collier Cameron,[2] M. Gillon,[3] C. Hellier,[1] E. Jehin,[3] M. Lendl,[4] P. F. L. Maxted,[1] D. Queloz,[4] B. Smalley,[1] A. M. S. Smith,[1] A. H. M. J. Triaud,[4] R. G. West,[5] F. Pepe,[4] D. Pollacco,[6] D. Ségransan,[4] I. Todd[6] and S. Udry[4]

[1]*Astrophysics Group, Keele University, Staffordshire ST5 5BG*
[2]*SUPA, School of Physics and Astronomy, University of St Andrews, North Haugh, Fife KY16 9SS*
[3]*Institut d'Astrophysique et de Géophysique, Université de Liège, Allée du 6 Août, 17, Bat. B5C, Liège 1, Belgium*
[4]*Observatoire de Genève, Université de Genève, 51 Chemin des Maillettes, 1290 Sauverny, Switzerland*
[5]*Department of Physics and Astronomy, University of Leicester, Leicester LE1 7RH*
[6]*Astrophysics Research Centre, School of Mathematics & Physics, Queen's University, University Road, Belfast BT7 1NN*

Accepted 2012 January 21. Received 2012 January 21; in original form 2011 May 15

ABSTRACT

We report the discovery of three extrasolar planets that transit their moderately bright (m_V = 12–13) host stars. WASP-44b is a 0.89-M_{Jup} planet in a 2.42-day orbit around a G8V star. WASP-45b is a 1.03-M_{Jup} planet which passes in front of the limb of its K2V host star every 3.13 days. Weak Ca II H&K emission seen in the spectra of WASP-45 suggests that the star is chromospherically active. WASP-46b is a 2.10-M_{Jup} planet in a 1.43-day orbit around a G6V star. Rotational modulation of the light curves of WASP-46 and weak Ca II H&K emission in its spectra show the star to be photospherically and chromospherically active.

We imposed circular orbits in our analyses as the radial-velocity data are consistent with (near-)circular orbits, as could be expected from both empirical and tidal-theory perspectives for such short-period, ∼Jupiter-mass planets. We discuss the impact of fitting for eccentric orbits for such planets when not supported by the data. The derived planetary and stellar radii depend on the fitted eccentricity and these parameters inform intense theoretical efforts concerning tidal circularization and heating, bulk planetary composition and the observed systematic errors in planetary and stellar radii. As such, we recommend exercising caution in fitting the orbits of short-period, ∼Jupiter-mass planets with an eccentric model when there is no evidence of non-circularity.

Key words: planets and satellites: individual: WASP-44b – planets and satellites: individual: WASP-45b – planets and satellites: individual: WASP-46b – stars: individual: WASP-44 – stars: individual: WASP-45 – stars: individual: WASP-46.

1 INTRODUCTION

The ensemble of well-characterized transiting extrasolar planets is growing at pace, with well over 100 known to date. It is important to determine the system parameters accurately so that the inferences based on them are reliable. For example, to determine the bulk composition of a planet it is necessary to measure accurately its radius (e.g. Fortney, Marley & Barnes 2007). Many short-period, giant planets (e.g. WASP-17b; Anderson et al. 2010, 2011b) are larger than predicted by standard cooling theory of irradiated, gas-giant planets (e.g. Fortney et al. 2007). One potential explanation is that energy from the tidal circularization of eccentric orbits was dissipated within the planets' interiors, causing them to bloat (e.g. Bodenheimer, Lin & Mardling 2001). To evaluate the likelihood that a planet was inflated by such tidal heating, it is necessary to have an accurate determination of both its radius and its orbital eccentricity (e.g. Ibgui, Spiegel & Burrows 2011).

A planet's orbital eccentricity can be determined by measuring the radial motion of its host star around its orbit (e.g. Queloz et al. 2010), or by observing occultations of the planet by its host star (e.g. Anderson et al. 2011b), or from a combination of the two. By combining this eccentricity measurement with high-quality transit light curves, we can measure a star's density (Seager & Mallén-Ornelas 2003). The stellar mass can be estimated using stellar evolution models (e.g. Demarque et al. 2004) or mass-calibration laws (e.g. Torres, Andersen & Giménez 2010), and the stellar radius follows. This, combined with the ratio of the radii derived from the transit depth, gives the planet radius.

⋆E-mail: dra@astro.keele.ac.uk

Monthly Notices of the ROYAL ASTRONOMICAL SOCIETY

Mon. Not. R. Astron. Soc. **426,** 739–750 (2012) doi:10.1111/j.1365-2966.2012.21780.x

Seven transiting hot Jupiters from WASP-South, Euler and TRAPPIST: WASP-47b, WASP-55b, WASP-61b, WASP-62b, WASP-63b, WASP-66b and WASP-67b

Coel Hellier,[1]★ D. R. Anderson,[1] A. Collier Cameron,[2] A. P. Doyle,[1] A. Fumel,[3] M. Gillon,[3] E. Jehin,[3] M. Lendl,[4] P. F. L. Maxted,[1] F. Pepe,[4] D. Pollacco,[5] D. Queloz,[4] D. Ségransan,[4] B. Smalley,[1] A. M. S. Smith,[1] J. Southworth,[1] A. H. M. J. Triaud,[4] S. Udry[4] and R. G. West[6]

[1]*Astrophysics Group, Keele University, Staffordshire ST5 5BG*
[2]*SUPA, School of Physics and Astronomy, University of St. Andrews, North Haugh, Fife KY16 9SS*
[3]*Institut d'Astrophysique et de Géophysique, Université de Liège, Allée du 6 Août 17, Bat. B5C, Liège 1, Belgium*
[4]*Observatoire astronomique de l'Université de Genève, 51 ch. des Maillettes, 1290 Sauverny, Switzerland*
[5]*Astrophysics Research Centre, School of Mathematics & Physics, Queen's University, University Road, Belfast BT7 1NN*
[6]*Department of Physics and Astronomy, University of Leicester, Leicester LE1 7RH*

Accepted 2012 July 23. Received 2012 July 23; in original form 2012 April 23

ABSTRACT

We present seven new transiting hot Jupiters from the WASP-South survey. The planets are all typical hot Jupiters orbiting stars from F4 to K0 with magnitudes of $V = 10.3$–12.5. The orbital periods are all in the range of 3.9–4.6 d, the planetary masses range from 0.4 to 2.3 $M_{\rm Jup}$ and the radii from 1.1 to 1.4 $R_{\rm Jup}$. In line with known hot Jupiters, the planetary densities range from Jupiter-like to inflated ($\rho = 0.13$–$1.07\rho_{\rm Jup}$). We use the increasing numbers of known hot Jupiters to investigate the distribution of their orbital periods and the 3–4 d 'pile-up'.

Key words: planetary systems.

1 INTRODUCTION

Transiting exoplanets found by the ground-based transit searches are mostly 'hot Jupiters', Jupiter-sized planets in ≈1–6 d orbits, since these are the easiest planets for such surveys to find. However, planet candidate lists from *Kepler* show that hot Jupiters are much less common than smaller planets (Batalha et al. 2012). This means that the much larger sky coverage of the ground-based surveys (e.g. HATnet, Bakos et al. 2004; WASP, Pollacco et al. 2006) is needed to produce large samples of hot Jupiters that will enable us to understand the properties of this class. In addition, hot Jupiters from these surveys orbit stars of $V \approx 9$–13, which are bright enough for radial-velocity measurements of the planetary masses and for many other types of study.

Here we present seven new transiting planets discovered by the WASP-South survey (Hellier et al. 2011a) in conjunction with the Euler/CORALIE spectrograph and the TRAPPIST robotic photometer (Jehin et al. 2011). These are all hot Jupiters with ∼4 d orbits that are compatible with being circular, and with masses and radii that are typical of the class. They all orbit relatively isolated stars of $V = 10.3$–12.5 which have metallicities and space velocities compatible with local thin-disc stars. WASP-South planets that are less typical of the class will be reported in other papers.

2 OBSERVATIONS

WASP-South uses an eight-camera array that covers 450 deg^2 of sky observing with a typical cadence of 8 min. The WASP surveys are described in Pollacco et al. (2006) while a discussion of our planet-hunting methods can be found in Collier Cameron et al. (2007a) and Pollacco et al. (2008).

WASP-South planet candidates are followed up using the TRAPPIST robotic photometer and the CORALIE spectrograph on the Euler 1.2-m telescope at La Silla. About one in 12 candidates turns out to be a planet, the remainder being blends that are unresolved in the WASP data (which uses 14 arcsec pixel) or astrophysical transit mimics, usually eclipsing binary stars. A list of observations reported in this paper is given in Table 1, while the CORALIE radial velocities are listed in Table A1 (with the online version of the paper – see Supporting Information).

3 THE HOST STARS

The CORALIE spectra of the host stars were co-added to produce spectra for analysis using the methods described in Gillon

★E-mail: ch@astro.keele.ac.uk

A&A 547, A61 (2012)
DOI: 10.1051/0004-6361/201219731

Astronomy & Astrophysics

WASP-78b and WASP-79b: two highly-bloated hot Jupiter-mass exoplanets orbiting F-type stars in Eridanus⋆,⋆⋆

B. Smalley[1], D. R. Anderson[1], A. Collier-Cameron[2], A. P. Doyle[1], A. Fumel[3], M. Gillon[3], C. Hellier,[1], E. Jehin[2], M. Lendl[4], P. F. L. Maxted[1], F. Pepe[4], D. Pollacco[5], D. Queloz[4], D. Ségransan[4], A. M. S. Smith[1], J. Southworth[1] A. H. M. J. Triaud[4], S. Udry[4], and R. G. West[6]

[1] Astrophysics Group, Keele University, Staffordshire, ST5 5BG, UK
e-mail: b.smalley@keele.ac.uk
[2] SUPA, School of Physics and Astronomy, University of St. Andrews, North Haugh, Fife, KY16 9SS, UK
[3] Université de Liège, Allée du 6 août 17, Sart Tilman, Liège 1, Belgium
[4] Observatoire de Genève, Université de Genève, Chemin des maillettes 51, 1290 Sauverny, Switzerland
[5] Astrophysics Research Centre, School of Mathematics & Physics, Queen's University Belfast, University Road, Belfast BT7 1NN, UK
[6] Department of Physics and Astronomy, University of Leicester, Leicester, LE1 7RH, UK

Received 1 June 2012 / Accepted 28 September 2012

ABSTRACT

We report the discovery of WASP-78b and WASP-79b, two highly-bloated Jupiter-mass exoplanets orbiting F-type host stars. WASP-78b orbits its $V = 12.0$ host star (TYC 5889-271-1) every 2.175 days and WASP-79b orbits its $V = 10.1$ host star (CD-30 1812) every 3.662 days. Planetary parameters have been determined using a simultaneous fit to WASP and TRAPPIST transit photometry and CORALIE radial-velocity measurements. For WASP-78b a planetary mass of $0.89 \pm 0.08\ M_{\rm Jup}$ and a radius of $1.70 \pm 0.11\ R_{\rm Jup}$ is found. The planetary equilibrium temperature of $T_{\rm P} = 2350 \pm 80$ K for WASP-78b makes it one of the hottest of the currently known exoplanets. WASP-79b its found to have a planetary mass of $0.90 \pm 0.08\ M_{\rm Jup}$, but with a somewhat uncertain radius due to lack of sufficient TRAPPIST photometry. The planetary radius is at least $1.70 \pm 0.11\ R_{\rm Jup}$, but could be as large as $2.09 \pm 0.14\ R_{\rm Jup}$, which would make WASP-79b the largest known exoplanet.

Key words. planets and satellites: general – stars: individual: WASP-78 – stars: individual: WASP-79 – techniques: spectroscopic – techniques: radial velocities – techniques: photometric

1. Introduction

The first exoplanets were discovered using the radial velocity technique (Mayor & Queloz 1995). However, following the detection of a transiting exoplanet (Charbonneau et al. 2000), several ground-based and space-based survey projects have dramatically increased the number of known systems. Transiting exoplanets allow parameters such as the mass, radius, and density to be precisely determined, as well as their atmospheric properties to be studied during their transits and occultations (Charbonneau et al. 2005; Southworth 2009; Winn 2009).

Most of the transiting exoplanets found by ground-based surveys are "hot Jupiters", with orbital periods of up to around 5 days. Many of these have radii larger than predicted by irradiated planet models (Fortney et al. 2007). Several have markedly low densities, with WASP-17b (Anderson et al. 2010, 2011), Kepler-12b (Fortney et al. 2011) and Kepler-7b (Latham et al. 2010) having a density less than 1/10 that of Jupiter. The mechanisms for producing such bloated planets are at present unclear (Fortney & Nettelmann 2010), but several have been proposed, including Ohmic heating in the planetary atmosphere (Batygin & Stevenson 2010; Perna et al. 2010) and thermal tidal effects (Arras & Socrates 2010).

In this paper we report the detection of WASP-78b and WASP-79b, two highly-bloated Jupiter-mass planets in orbit around F-type stars. We present the WASP-South discovery photometry, together with follow-up optical photometry and radial velocity measurements.

2. WASP-south photometry

The WASP project has two robotic observatories; one on La Palma in the Canary Islands and another in Sutherland in South Africa. The wide angle survey is designed to find planets around relatively bright stars in the V-magnitude range $9 \sim 13$. A detailed description is given in Pollacco et al. (2006).

The pipeline-processed data were de-trended and searched for transits using the methods described in Collier Cameron et al. (2006), yielding detections of periodic, transit-like signatures on two stars in the constellation Eridanus (Fig. 1). The $V = 12.0$ star WASP-78 (1SWASPJ041501.50-220659.0; TYC 5889-271-1) exhibited ~0.010 mag transits every 2.175 days, while the $V = 10.1$ star WASP-79 (1SWASPJ042529.01-303601.5; CD-30 1812) showed ~0.015 mag transits every 3.66 days. A total of 16489 observations of WASP-78 were obtained between 2006 August and 2009 December and 15424 observations of WASP-79 were obtained between 2006 September and 2010 February.

There is a 15th mag star, 2MASS 04150416-2207189, located 42″ away from WASP-78, which is just within the photometric extraction aperture. However, the dilution is only 2%

⋆ Photometric data is only available at the CDS via anonymous ftp to cdsarc.u-strasbg.fr (130.79.128.5) or via http://cdsarc.u-strasbg.fr/viz-bin/qcat?J/A+A/547/A61
⋆⋆ Table 1 is available in electronic form at http://www.aanda.org

A&A 549, A134 (2013)
DOI: 10.1051/0004-6361/201220363

Astronomy & Astrophysics

WASP-52b, WASP-58b, WASP-59b, and WASP-60b: Four new transiting close-in giant planets⋆

G. Hébrard[1,2], A. Collier Cameron[3], D. J. A. Brown[3], R. F. Díaz[4,1,2], F. Faedi[13], B. Smalley[5], D. R. Anderson[5], D. Armstrong[13], S. C. C. Barros[4], J. Bento[12], F. Bouchy[1,2], A. P. Doyle[5], B. Enoch[3], Y. Gómez Maqueo Chew[13,14], É. M. Hébrard[2], C. Hellier[5], M. Lendl[6], T. A. Lister[11], P. F. L. Maxted[5], J. McCormac[8], C. Moutou[4], D. Pollacco[13], D. Queloz[6], A. Santerne[4,2], I. Skillen[8], J. Southworth[5], J. Tregloan-Reed[5], A. H. M. J. Triaud[6], S. Udry[6], M. Vanhuysse[10], C. A. Watson[7], R. G. West[9], and P. J. Wheatley[13]

[1] Institut d'Astrophysique de Paris, UMR 7095 CNRS, Université Pierre & Marie Curie, 98bis boulevard Arago, 75014 Paris, France
e-mail: hebrard@iap.fr
[2] Observatoire de Haute-Provence, CNRS/OAMP, 04870 Saint-Michel-l'Observatoire, France
[3] School of Physics and Astronomy, University of St Andrews, St Andrews, Fife KY16 9SS, UK
[4] Laboratoire d'Astrophysique de Marseille, Univ. de Provence, CNRS (UMR 6110), 38 r. F. Joliot Curie, 13388 Marseille Cedex 13, France
[5] Astrophysics Group, Keele University, Staffordshire, ST5 5BG, UK
[6] Observatoire de Genève, Université de Genève, 51 chemin des Maillettes, 1290 Sauverny, Switzerland
[7] Astrophysics Research Centre, School of Mathematics and Physics, Queens University Belfast, University Road, Belfast BT7 1NN, UK
[8] Isaac Newton Group of Telescopes, Apartado de Correos 321, 38700 Santa Cruz de Palma, Spain
[9] Department of Physics and Astronomy, University of Leicester, Leicester, LE1 7RH, UK
[10] OverSky, 47 allée des Palanques, BP 12, 33127 Saint-Jean d'Illac, France
[11] Las Cumbres Observatory, 6740 Cortona Drive Suite 102, Goleta, CA 93117, USA
[12] The Open University, Walton Hall, Milton Keynes, MK7 6AA, UK
[13] Department of Physics, University of Warwick, Gibbet Hill Road, Coventry CV4 7AL, UK
[14] Department of Physics and Astronomy, Vanderbilt University, 6301 Stevenson Center, Nashville, TN 37235, USA

Received 11 September 2012 / Accepted 5 November 2012

ABSTRACT

We present the discovery of four new transiting hot Jupiters, detected mainly from SuperWASP-North and SOPHIE observations. These new planets, WASP-52b, WASP-58b, WASP-59b, and WASP-60b, have orbital periods ranging from 1.7 to 7.9 days, masses between 0.46 and 0.94 $M_{\rm Jup}$, and radii between 0.73 and 1.49 $R_{\rm Jup}$. Their G1 to K5 dwarf host stars have V magnitudes in the range 11.7−13.0. The depths of the transits are between 0.6 and 2.7%, depending on the target. With their large radii, WASP-52b and WASP-58b are new cases of low-density, inflated planets, whereas WASP-59b is likely to have a large, dense core. WASP-60 shows shallow transits. In the case of WASP-52 we also detected the Rossiter-McLaughlin anomaly via time-resolved spectroscopy of a transit. We measured the sky-projected obliquity $\lambda = 24^{\circ}{}^{+17}_{-9}$, indicating that WASP-52b orbits in the same direction as its host star is rotating and that this prograde orbit is slightly misaligned with the stellar equator. These four new planetary systems increase our statistics on hot Jupiters and provide new targets for follow-up studies.

Key words. planetary systems – techniques: polarimetric – techniques: radial velocities

1. Introduction

About 200 exoplanets are known today as transiting in front of their host stars as seen from the Earth. That population is particularly interesting since it allows numerous studies, including accurate radius, mass, and density measurements, atmospheric studies in absorption through transits and in emission through occultations, dynamic analyses through possible timing variations, and obliquity measurements. Increasing the size of that sample is essential to improve our statistical knowledge on exoplanets and to discover individual cases that are particularly well-adapted to follow-up studies. Several ground-based photometric programs are surveying large fields with that goal, including SuperWASP (Pollacco et al. 2006) and HAT (Bakos et al. 2007). More recently, the dedicated space-based missions CoRoT (Baglin et al. 2009) and *Kepler* (Borucki et al. 2010) also joined that effort and have discovered new transiting exoplanets, including ones that have longer periods and smaller radii, which is not easily detectable by ground-based surveys. Because they survey smaller fields, however, CoRoT and *Kepler* detect planets transiting mainly in front of fainter stars, typically in the magnitude range $13 < V < 16$. These faint stars make follow-up observations difficult. By comparison, the planets detected by SuperWASP or HAT transit brighter stars, typically in the range $10 < V < 13$, allowing easier and more accurate complementary studies. Thus, ground-based surveys for detection of transiting exoplanets remain pertinent and are complementary to their space-based counterparts.

We present here the discovery of four new transiting planets detected with SuperWASP-North and SOPHIE. These two instruments allowed the detection of the first three WASP planets (Collier Cameron et al. 2007a; Pollacco et al. 2008), followed by about twenty others, including inflated hot Jupiters

⋆ Radial velocities (Table 4) are only available at the CDS via anonymous ftp to cdsarc.u-strasbg.fr (130.79.128.5) or via http://cdsarc.u-strasbg.fr/viz-bin/qcat?J/A+A/549/A134

A&A 551, A73 (2013)
DOI: 10.1051/0004-6361/201220520

Astronomy & Astrophysics

WASP-54b, WASP-56b, and WASP-57b: Three new sub-Jupiter mass planets from SuperWASP⋆,⋆⋆

F. Faedi[1,2,⋆⋆⋆], D. Pollacco[1,2,⋆⋆⋆], S. C. C. Barros[3], D. Brown[4], A. Collier Cameron[4], A. P. Doyle[5], R. Enoch[4], M. Gillon[6], Y. Gómez Maqueo Chew[1,2,7,⋆⋆⋆], G. Hébrard[8,9], M. Lendl[10], C. Liebig[4], B. Smalley[5], A. H. M. J. Triaud[10], R. G. West[11], P. J. Wheatley[1], K. A. Alsubai[12], D. R. Anderson[5], D. Armstrong[1,2,⋆⋆⋆], J. Bento[1], J. Bochinski[13], F. Bouchy[8,9], R. Busuttil[13], L. Fossati[14], A. Fumel[6], C. A. Haswell[13], C. Hellier[5], S. Holmes[13], E. Jehin[6], U. Kolb[13], J. McCormac[15,2,1,⋆⋆⋆], G. R. M. Miller[4], C. Moutou[3], A. J. Norton[13], N. Parley[4], D. Queloz[10], A. Santerne[3], I. Skillen[15], A. M. S. Smith[5], S. Udry[10], and C. Watson[2]

[1] Department of Physics, University of Warwick, Coventry CV4 7AL, UK
e-mail: f.faedi@warwick.ac.uk
[2] Astrophysics Research Centre, School of Mathematics and Physics, Queen's University Belfast, University Road, Belfast BT7 1NN, UK
[3] Aix Marseille Universit, CNRS, LAM (Laboratoire d'Astrophysique de Marseille) UMR 7326, 13388 Marseille, France
[4] School of Physics and Astronomy, University of St. Andrews, St. Andrews, Fife KY16 9SS, UK
[5] Astrophysics Group, Keele University, Staffordshire, ST5 5BG, UK
[6] Université de Liège, Allée du 6 août 17, Sart Tilman, Liège 1, Belgium
[7] Physics and Astronomy Department, Vanderbilt University, Nashville, Tennessee, USA
[8] Institut d'Astrophysique de Paris, UMR7095 CNRS, Université Pierre & Marie Curie, France
[9] Observatoire de Haute-Provence, CNRS/OAMP, 04870 St Michel l'Observatoire, France
[10] Observatoire astronomique de l'Université de Genève, 51 ch. des Maillettes, 1290 Sauverny, Switzerland
[11] Department of Physics and Astronomy, University of Leicester, Leicester, LE1 7RH, UK
[12] Qatar Foundation, PO Box 5825, Doha, Qatar
[13] Department of Physical Sciences, The Open University, Milton Keynes, MK7 6AA, UK
[14] Argelander-Institut für Astronomie der Universität Bonn, Auf dem Hgel 71, 53121 Bonn, Germany
[15] Isaac Newton Group of Telescopes, Apartado de Correos 321, 38700 Santa Cruz de Palma, Spain

Received 8 October 2012 / Accepted 23 December 2012

ABSTRACT

We present three newly discovered sub-Jupiter mass planets from the SuperWASP survey: WASP-54b is a heavily bloated planet of mass $0.636^{+0.025}_{-0.024}$ M_J and radius $1.653^{+0.090}_{-0.083}$ R_J. It orbits a F9 star, evolving off the main sequence, every 3.69 days. Our MCMC fit of the system yields a slightly eccentric orbit ($e = 0.067^{+0.033}_{-0.025}$) for WASP-54b. We investigated further the veracity of our detection of the eccentric orbit for WASP-54b, and we find that it could be real. However, given the brightness of WASP-54 $V = 10.42$ mag, we encourage observations of a secondary eclipse to draw robust conclusions on both the orbital eccentricity and the thermal structure of the planet. WASP-56b and WASP-57b have masses of $0.571^{+0.034}_{-0.035}$ M_J and $0.672^{+0.049}_{-0.046}$ M_J, respectively; and radii of $1.092^{+0.035}_{-0.033}$ R_J for WASP-56b and $0.916^{+0.017}_{-0.014}$ R_J for WASP-57b. They orbit main sequence stars of spectral type G6 every 4.67 and 2.84 days, respectively. WASP-56b and WASP-57b show no radius anomaly and a high density possibly implying a large core of heavy elements; possibly as high as ∼50 $M_\oplus$ in the case of WASP-57b. However, the composition of the deep interior of exoplanets remains still undetermined. Thus, more exoplanet discoveries such as the ones presented in this paper, are needed to understand and constrain giant planets' physical properties.

Key words. techniques: photometric – techniques: radial velocities – stars: individual: WASP-54 – stars: individual: WASP-56 – stars: individual: WASP-57

1. Introduction

To date the number of extrasolar planets for which precise measurements of masses and radii are available amounts to more than a hundred. Although these systems are mostly Jupiter-like gas giants they have revealed an extraordinary variety of physical and dynamical properties that have had a profound impact on our knowledge of planetary structure, formation and evolution and unveiled the complexity of these processes (see Baraffe et al. 2010, and references there in). Transit surveys such as SuperWASP (Pollacco et al. 2006) have been extremely successful in providing great insight into the properties of extrasolar planets and their host stars (see e.g., Baraffe et al. 2010). Ground-based surveys excel in discovering systems with peculiar/exotic characteristics. Subtle differences in their observing strategies can yield unexpected selection effects impacting the emerging distributions of planetary and stellar properties such

⋆ RV data (Tables 6–9) are available in electronic form at http://www.aanda.org
⋆⋆ Photometric data are only available at the CDS via anonymous ftp to cdsarc.u-strasbg.fr (130.79.128.5) or via http://cdsarc.u-strasbg.fr/viz-bin/qcat?J/A+A/551/A73
⋆⋆⋆ Part of the work was carried out while at Queen's University Belfast.

A&A 551, A80 (2013)
DOI: 10.1051/0004-6361/201220900

Astronomy & Astrophysics

WASP-80b: a gas giant transiting a cool dwarf⋆,⋆⋆

A. H. M. J. Triaud[1], D. R. Anderson[2], A. Collier Cameron[3], A. P. Doyle[2], A. Fumel[4], M. Gillon[4], C. Hellier[2], E. Jehin[4], M. Lendl[1], C. Lovis[1], P. F. L. Maxted[2], F. Pepe[1], D. Pollacco[5], D. Queloz[1], D. Ségransan[1], B. Smalley[2], A. M. S. Smith[2,6], S. Udry[1], R. G. West[7], and P. J. Wheatley[5]

[1] Observatoire Astronomique de l'Université de Genève, Chemin des Maillettes 51, 1290 Sauverny, Switzerland
e-mail: Amaury.Triaud@unige.ch
[2] Astrophysics Group, Keele University, Staffordshire, ST55BG, UK
[3] SUPA, School of Physics & Astronomy, University of St. Andrews, North Haugh, KY16 9SS, St. Andrews, Fife, Scotland, UK
[4] Institut d'Astrophysique et de Géophysique, Université de Liège, Allée du 6 Août, 17, Bat. B5C, Liège 1, Belgium
[5] Department of Physics, University of Warwick, Coventry CV4 7AL, UK
[6] N. Copernicus Astronomical Centre, Polish Academy of Sciences, Bartycka 18, 00-716 Warsaw, Poland
[7] Department of Physics and Astronomy, University of Leicester, Leicester, LE17RH, UK

Received 13 December 2012 / Accepted 9 January 2013

ABSTRACT

We report the discovery of a planet transiting the star WASP-80 (1SWASP J201240.26-020838.2; 2MASS J20124017-0208391; TYC 5165-481-1; BPM 80815; $V = 11.9$, $K = 8.4$). Our analysis shows this is a 0.55 ± 0.04 $M_{\rm jup}$, 0.95 ± 0.03 $R_{\rm jup}$ gas giant on a circular 3.07 day orbit around a star with a spectral type between K7V and M0V. This system produces one of the largest transit depths so far reported, making it a worthwhile target for transmission spectroscopy. We find a large discrepancy between the $v \sin i_\star$ inferred from stellar line broadening and the observed amplitude of the Rossiter-McLaughlin effect. This can be understood either by an orbital plane nearly perpendicular to the stellar spin or by an additional, unaccounted for source of broadening.

Key words. planetary systems – binaries: eclipsing – stars: individual: WASP-80 – techniques: radial velocities – techniques: photometric – techniques: spectroscopic

1. Introduction

Numerous planets have been found since Mayor & Queloz (1995) and, like 51 Pegasi b, most orbit stars whose spectral type, mass, or size are similar to the Sun's. This occurs even though a few surveys have concentrated their efforts on other spectral types notably towards M dwarfs, such as the HARPS M-dwarf survey (Bonfils et al. 2013) or the M-Earth project (Nutzman & Charbonneau 2008). In their rarity, those planets nevertheless help us better understand the processes leading to planet formation.

The Wide Angle Search for Planets (WASP) survey aims to find transiting planets (Pollacco et al. 2006), and has now surveyed most of the night sky in both hemispheres. With some 70 planets now publicly announced, this is the most efficient ground-based planet discovery project. Thanks to its observation of now more than 30 million stars of magnitude between 8.5 and 13.5, it can pick up those rare planets that have avoided detection by the radial-velocity surveys or even by the space-missions *Kepler* and CoRoT, which have surveyed *only* 150 000 stars each. Amongst those rare planets found by WASP is the first gas giant around a δ Scuti (Collier Cameron et al. 2010) and the population of very short period gas giants, such as WASP-12, 18, 19, and 43 (Hebb et al. 2009, 2010; Hellier et al. 2009, 2011).

Despite their numbers and the facility of discovering them (radial velocities or transits), the occurrence rate of hot Jupiters orbiting solar-type stars is low. It has been estimated to be as high as $1.5 \pm 0.6\%$ by Cumming et al. (2008) from radial velocity surveys, and as low as $0.5 \pm 0.1\%$ by Howard et al. (2012) from the *Kepler* results. Johnson et al. (2010) have made a case that, because no hot Jupiter was known to orbit an M dwarf, their occurrence must therefore be lower. Not long afterwards, Johnson et al. (2012) announced the discovery of a transiting gas giant around a star observed by *Kepler*, KOI-254, describing it as a "*lone example [...] for some time to come*". Approximately 300 M dwarf systems have been searched for planets between the main radial velocity teams (Johnson et al. 2010). The M-Earth project is targeting about 3000 (with a geometrical detection of only 5−10%). If the rate of hot Jupiters is but a half to a third that of solar type stars, there is a significant chance that such planets have avoided detection, a point made by Bonfils et al. (2013). Knowing this rate is important since gas giant formation is perceived as less efficient because protoplanetary disc masses scale with their primary's mass as dynamical timescales do (Laughlin et al. 2004; Ida & Lin 2005; Alibert et al. 2011; Mordasini et al. 2012).

Within this context, we announce the discovery of a gas giant transiting a late K-early M dwarf. We first describe our data collection, then its analysis, and finally the results we obtain.

⋆ Using WASP-South photometric observations, from Sutherland (South Africa), confirmed with the 60 cm TRAPPIST robotic telescope, EulerCam, and the CORALIE spectrograph on the Swiss 1.2 m *Euler* Telescope, and HARPS on the ESO 3.6 m (Prog ID 089.C-0151), all three located at La Silla Observatory, Chile.

⋆⋆ Radial velocity and photometric data are available in electronic form at the CDS via anonymous ftp to cdsarc.u-strasbg.fr (130.79.128.5) or via http://cdsarc.u-strasbg.fr/viz-bin/qcat?J/A+A/551/A80

A&A 552, A82 (2013)
DOI: 10.1051/0004-6361/201220561

Astronomy & Astrophysics

WASP-64 b and WASP-72 b: two new transiting highly irradiated giant planets⋆

M. Gillon[1], D. R. Anderson[2], A. Collier-Cameron[3], A. P. Doyle[2], A. Fumel[1], C. Hellier[2], E. Jehin[1], M. Lendl[4], P. F. L. Maxted[2], J. Montalbán[1], F. Pepe[4], D. Pollacco[5], D. Queloz[4], D. Ségransan[4], A. M. S. Smith[2], B. Smalley[2], J. Southworth[2], A. H. M. J. Triaud[4], S. Udry[4], and R. G. West[6]

[1] Institut d'Astrophysique et de Géophysique, Université de Liège, Allée du 6 août 17, Sart Tilman, Liège 1, Belgium
e-mail: michael.gillon@ulg.ac.be
[2] Astrophysics Group, Keele University, Staffordshire, ST5 5BG, UK
[3] School of Physics and Astronomy, University of St. Andrews, North Haugh, Fife, KY16 9SS, UK
[4] Observatoire de Genève, Université de Genève, 51 chemin des Maillettes, 1290 Sauverny, Switzerland
[5] Department of Physics, University of Warwick, Coventry CV4 7AL, UK
[6] Department of Physics and Astronomy, University of Leicester, Leicester, LE1 7RH, UK

Received 15 October 2012 / Accepted 11 February 2013

ABSTRACT

We report the discovery by the WASP transit survey of two new highly irradiated giant planets. WASP-64 b is slightly more massive ($1.271 \pm 0.068\ M_{\rm Jup}$) and larger ($1.271 \pm 0.039\ R_{\rm Jup}$) than Jupiter, and is in very-short ($a = 0.02648 \pm 0.00024$ AU, $P = 1.5732918 \pm 0.0000015$ days) circular orbit around a $V = 12.3$ G7-type dwarf ($1.004 \pm 0.028\ M_\odot$, $1.058 \pm 0.025\ R_\odot$, $T_{\rm eff} = 5500 \pm 150$ K). Its size is typical of hot Jupiters with similar masses. WASP-72 b has also a mass a bit higher than Jupiter's ($1.461^{+0.059}_{-0.056}\ M_{\rm Jup}$) and orbits very close (0.03708 ± 0.00050 AU, $P = 2.2167421 \pm 0.0000081$ days) to a bright ($V = 9.6$) and moderately evolved F7-type star ($1.386 \pm 0.055\ M_\odot$, $1.98 \pm 0.24\ R_\odot$, $T_{\rm eff} = 6250 \pm 100$ K). Despite its extreme irradiation ($\sim 5.5 \times 10^9$ erg s^{-1} cm^{-2}), WASP-72 b has a moderate size ($1.27 \pm 0.20\ R_{\rm Jup}$) that could suggest a significant enrichment in heavy elements. Nevertheless, the errors on its physical parameters are still too high to draw any strong inference on its internal structure or its possible peculiarity.

Key words. planetary systems – stars: individual: WASP-64 – techniques: photometric – techniques: radial velocities – techniques: spectroscopic – stars: individual: WASP-72

1. Introduction

The booming study of exoplanets allow us to assess the diversity of the planetary systems of the Milky Way and to put our own solar system in perspective. Notably, ground-based transit surveys targeting relatively bright ($V < 13$) stars are detecting at an increasing rate short-period giant planets amenable for a thorough characterization (orbit, structure, atmosphere), thanks to the brightness of their host star, the favorable planet-star size ratio and their high stellar irradiation (e.g. Winn 2010). With its very high detection efficiency, the WASP transit survey (Pollacco et al. 2006) is one of the most productive projects in that domain.

In this context, we report here the detection by WASP of two new giant planets, WASP-64 b and WASP-72 b, transiting relatively bright southern stars. Section 2 presents the WASP discovery photometry, and high-precision follow-up observations obtained from La Silla ESO Observatory (Chile) by the TRAPPIST and *Euler* telescopes to confirm the transits and planetary nature of both objects and to determine precisely the systems parameters. In Sect. 3, we present the spectroscopic determination of the stellar properties and the derivation of the systems parameters through a combined analysis of the follow-up photometric and spectroscopic time-series. Finally, we discuss our results in Sect. 4.

2. Observations

2.1. WASP transit detection photometry

The stars 1SWASPJ064427.63-325130.4 (WASP-64; $V = 12.3$, $K = 11.0$) and 1SWASPJ024409.60-301008.5 (WASP-72; $V = 10.1$, $K = 9.6$) were observed by the southern station of the WASP survey (Hellier et al. 2011) between 2006 Oct. 11 and 2010 Mar. 12 and between 2006 Aug. 11 and 2007 Dec. 31, respectively. The 17981 and 6500 pipeline-processed photometric measurements were detrended and searched for transits using the methods described by Collier-Cameron et al. (2006). The selection process (Collier-Cameron et al. 2007) identified WASP-72 as a high priority candidate showing periodic low-amplitude (2–3 mmag) transit-like signatures with period of 2.217 days. For WASP-64, similar transit-like signals with a period of 1.573 days were also detected, not only on the target itself but also on a brighter star at 28″, 1SWASPJ064429.53–325129.5 (TYC7091-1288-1, $V = 12.3$, $K = 11.0$). Figure 1 presents for TYC7091-1288-1 and WASP-64 the WASP photometry folded on the deduced transit ephemeris. Figure 2 does the same for WASP-72.

A search for periodic modulation was applied to the photometry of WASP-72, using for this purpose the method described

⋆ The photometric time-series used in this work are only available at the CDS via anonymous ftp to
cdsarc.u-strasbg.fr (130.79.128.5) or via
http://cdsarc.u-strasbg.fr/viz-bin/qcat?J/A+A/552/A82

A&A 552, A120 (2013)
DOI: 10.1051/0004-6361/201220727

Astronomy & Astrophysics

WASP-71b: a bloated hot Jupiter in a 2.9-day, prograde orbit around an evolved F8 star⋆

A. M. S. Smith[1,2], D. R. Anderson[1], F. Bouchy[3,4], A. Collier Cameron[5], A. P. Doyle[1], A. Fumel[6], M. Gillon[6], G. Hébrard[3,4], C. Hellier[1], E. Jehin[6], M. Lendl[7], P. F. L. Maxted[1], C. Moutou[8], F. Pepe[7], D. Pollacco[9], D. Queloz[7], A. Santerne[8,4], D. Segransan[7], B. Smalley[1], J. Southworth[1], A. H. M. J. Triaud[7], S. Udry[7], and R. G. West[10]

[1] Astrophysics Group, Lennard-Jones Laboratories, Keele University, Keele, Staffordshire, ST5 5BG, UK
[2] N. Copernicus Astronomical Centre, Polish Academy of Sciences, Bartycka 18, 00-716 Warsaw, Poland
e-mail: amss@camk.edu.pl
[3] Institut d'Astrophysique de Paris, UMR 7095 CNRS, Université Pierre & Marie Curie, 98bis boulevard Arago, 75014 Paris, France
[4] Observatoire de Haute-Provence, CNRS/OAMP, 04870 Saint-Michel-l'Observatoire, France
[5] SUPA, School of Physics and Astronomy, University of St. Andrews, North Haugh, St. Andrews, Fife, KY16 9SS, UK
[6] Institut d'Astrophysique et de Géophysique, Université de Liège, Allée du 6 Août 17, Sart Tilman, Liège 1, Belgium
[7] Observatoire de Genève, Université de Genève, 51 chemin des Maillettes, 1290 Sauverny, Switzerland
[8] Aix Marseille Université, CNRS, LAM (Laboratoire d'Astrophysique de Marseille) UMR 7326, 13388 Marseille, France
[9] Department of Physics, University of Warwick, Coventry CV4 7AL, UK
[10] Department of Physics & Astronomy, University of Leicester, Leicester, LE1 7RH, UK

Received 12 November 2012 / Accepted 14 March 2013

ABSTRACT

We report the discovery by the WASP transit survey of a highly-irradiated, massive ($2.242 \pm 0.080\ M_{\rm Jup}$) planet which transits a bright ($V = 10.6$), evolved F8 star every 2.9 days. The planet, WASP-71b, is larger than Jupiter ($1.46 \pm 0.13\ R_{\rm Jup}$), but less dense ($0.71 \pm 0.16\ \rho_{\rm Jup}$). We also report spectroscopic observations made during transit with the CORALIE spectrograph, which allow us to make a highly-significant detection of the Rossiter-McLaughlin effect. We determine the sky-projected angle between the stellar-spin and planetary-orbit axes to be $\lambda = 20.1 \pm 9.7$ degrees, i.e. the system is "aligned", according to the widely-used alignment criteria that systems are regarded as misaligned only when λ is measured to be greater than 10 degrees with 3-σ confidence. WASP-71, with an effective temperature of 6059 ± 98 K, therefore fits the previously observed pattern that only stars hotter than 6250 K are host to planets in misaligned orbits. We emphasise, however, that λ is merely the sky-projected obliquity angle; we are unable to determine whether the stellar-spin and planetary-orbit axes are misaligned along the line-of-sight. With a mass of $1.56 \pm 0.07\ M_{\odot}$, WASP-71 was previously hotter than 6250 K, and therefore might have been significantly misaligned in the past. If so, the planetary orbit has been realigned, presumably through tidal interactions with the cooling star's growing convective zone.

Key words. planetary systems – planets and satellites: detection – planets and satellites: fundamental parameters – stars: individual: WASP-71 – planets and satellites: individual: WASP-71b

1. Introduction

The recent *Kepler* discoveries of thousands of transiting exoplanet candidates (e.g. Batalha et al. 2013) has extended the parameter space of planet discovery and made major advances in answering questions about the statistical population of planetary systems in our Galaxy (e.g. Howard et al. 2012).

The vast majority of the systems detected by *Kepler*, however, are too faint for in-depth characterisation, which is required to increase our knowledge of the range of properties exhibited by the nearby planetary population, as well as to make advances in our understanding of planetary formation and evolution. Examples of planet characterisation that require bright targets include radial velocities to measure the star-to-planet mass ratio, orbital eccentricity and spin-orbit alignment and transit and occultation spectra and photometry at a range of wavelengths to measure the planet's atmospheric properties.

Discovering relatively bright transiting systems that are amenable for characterisation measurements is where ground-based transit surveys such as WASP (Pollacco et al. 2006) and HAT (Bakos et al. 2002) are vital. Between them, these two surveys have discovered more than 100 systems around bright stars ($8.5 \lesssim V \lesssim 12.5$); a sample which comprises the majority of the systems suitable for in-depth characterisation.

One of the characterisation measurements that can be made is spectroscopic transit measurements with the aim of detecting the changes in apparent radial velocity characteristic of the Rossiter-McLaughlin (RM) effect (Holt 1893; Rossiter 1924; McLaughlin 1924). As the planet obscures a portion of the star rotating towards us, an anomalous red-shift is observed in the radial velocities of the star, and a blue shift is observed during the planet's passage across the portion of the star rotating away from us. The shape of the RM signature is therefore sensitive to the path of the planet across the stellar disk relative to the stellar spin axis. It is possible to determine the sky-projection of the obliquity angle, λ, between the stellar-rotation axis and the planetary-orbital axis.

⋆ Photometric data is only available at the CDS via anonymous ftp to cdsarc.u-strasbg.fr (130.79.128.5) or via http://cdsarc.u-strasbg.fr/viz-bin/qcat?J/A+A/552/A120

A&A 559, A36 (2013)
DOI: 10.1051/0004-6361/201322314

Astronomy & Astrophysics

Discovery of WASP-65b and WASP-75b: Two hot Jupiters without highly inflated radii⋆

Y. Gómez Maqueo Chew[1,2,3], F. Faedi[1], D. Pollacco[1], D. J. A. Brown[4], A. P. Doyle[5], A. Collier Cameron[4], M. Gillon[7], M. Lendl[6], B. Smalley[5], A. H. M. J. Triaud[6,8], R. G. West[1], P. J. Wheatley[1], R. Busuttil[13], C. Liebig[4], D. R. Anderson[5], D. J. Armstrong[1], S. C. C. Barros[9], J. Bento[1,10], J. Bochinski[13], V. Burwitz[14], L. Delrez[7], B. Enoch[4], A. Fumel[7], C. A. Haswell[13], G. Hébrard[11,12], C. Hellier[5], S. Holmes[13], E. Jehin[7], U. Kolb[13], P. F. L. Maxted[5], J. McCormac[15,1], G. R. M. Miller[4], A. J. Norton[13], F. Pepe[6], D. Queloz[6,16], J. Rodríguez[17], D. Ségransan[6], I. Skillen[15], K. G. Stassun[2,18], S. Udry[6], and C. Watson[19]

[1] Department of Physics, University of Warwick, Coventry CV4 7AL, UK
e-mail: y.gomez@warwick.ac.uk
[2] Physics and Astronomy Department, Vanderbilt University, Nashville, Tennessee 37235, USA
[3] Centro de Radioastronomía y Astrofísica, UNAM, Apartado Postal 3-72, 58089 Morelia, Michoacán, México
[4] School of Physics and Astronomy, University of St Andrews, St Andrews, Fife KY16 9SS, UK
[5] Astrophysics Group, Keele University, Staffordshire, ST5 5BG, UK
[6] Observatoire astronomique de l'Université de Genève, 51 ch. des Maillettes, 1290 Sauverny, Switzerland
[7] Université de Liège, Allée du 6 août 17, Sart Tilman, Liège 1, 4000 Liège, Belgium
[8] Department of Physics, and Kavli Institute for Astrophysics and Space Research, Massachusetts Institute of Technology, Cambridge, MA 02139, USA
[9] Aix-Marseille Université, CNRS, LAM (Laboratoire d'Astrophysique de Marseille) UMR 7326, 13388 Marseille, France
[10] Department of Physics and Astronomy, Macquarie University, NSW 2109 Sydney, Australia
[11] Institut d'Astrophysique de Paris, UMR7095 CNRS, Université Pierre & Marie Curie, 75014 Paris, France
[12] Observatoire de Haute-Provence, CNRS/OAMP, 04870 St Michel l'Observatoire, France
[13] Department of Physical Sciences, The Open University, Milton Keynes, MK7 6AA, UK
[14] Max Planck Institut für Extraterrestrische Physik, Giessenbachstrasse 1, 85748 Garching, Germany
[15] Isaac Newton Group of Telescopes, Apartado de Correos 321, 38700 Santa Cruz de Palma, Spain
[16] Department of Physics, University of Cambridge, J J Thomson Av, Cambridge, CB3 0HE, UK
[17] Observatori Astronòmic de Mallorca, Camí de l'Observatori s/n, 07144 Costitx, Mallorca, Spain
[18] Department of Physics, Fisk University, Nashville, Tennessee 37208, USA
[19] Astrophysics Research Centre, Queen's University Belfast, University Road, Belfast BT7 1NN, UK

Received 18 July 2013 / Accepted 27 September 2013

ABSTRACT

We report the discovery of two transiting hot Jupiters, WASP-65b ($M_{\rm pl}$ = 1.55 ± 0.16 $M_{\rm J}$; $R_{\rm pl}$ = 1.11 ± 0.06 $R_{\rm J}$), and WASP-75b ($M_{\rm pl}$ = 1.07 ± 0.05 $M_{\rm J}$; $R_{\rm pl}$ = 1.27 ± 0.05 $R_{\rm J}$). They orbit their host star every ∼2.311, and ∼2.484 days, respectively. The planet host WASP-65 is a G6 star ($T_{\rm eff}$ = 5600 K, [Fe/H] = −0.07 ± 0.07, age ≳8 Gyr); WASP-75 is an F9 star ($T_{\rm eff}$ = 6100 K, [Fe/H] = 0.07 ± 0.09, age ∼ 3 Gyr). WASP-65b is one of the densest known exoplanets in the mass range 0.1 and 2.0 $M_{\rm J}$ ($\rho_{\rm pl}$ = 1.13 ± 0.08 $\rho_{\rm J}$), a mass range where a large fraction of planets are found to be inflated with respect to theoretical planet models. WASP-65b is one of only a handful of planets with masses of ∼1.5 $M_{\rm J}$, a mass regime surprisingly underrepresented among the currently known hot Jupiters. The radius of WASP-75b is slightly inflated (≲10%) as compared to theoretical planet models with no core, and has a density similar to that of Saturn ($\rho_{\rm pl}$ = 0.52 ± 0.06 $\rho_{\rm J}$).

Key words. planetary systems – stars: individual: WASP-65 – stars: individual: WASP-75

1. Introduction

Since the discovery of the first extrasolar planet around a main-sequence star, 51 Peg (Mayor & Queloz 1995), our understanding of planetary systems has dramatically evolved. Planetary science, which was previously based solely on our own Solar System, must be able to explain the observed diversity in physical properties and trends in the known exoplanet population (e.g., Baraffe et al. 2010; Cameron 2011). An exceptionally valuable subset of the known extrasolar planets are those that transit the disc of their host star. To date, there are over 300 confirmed transiting exoplanets in the literature[1]. Most of these discoveries have been the product of ground-based surveys, of which the Wide Angle Search for Planets (WASP; Pollacco et al. 2006) has

⋆ Light curves are only available at the CDS via anonymous ftp to cdsarc.u-strasbg.fr (130.79.128.5) or via http://cdsarc.u-strasbg.fr/viz-bin/qcat?J/A+A/559/A36

[1] See http://exoplanet.eu/

WASP-77 Ab: A transiting hot Jupiter planet in a wide binary system.⋆

P. F. L. Maxted[1], D. R. Anderson[1], A. Collier Cameron[2], A. P. Doyle[1], A. Fumel[3], M. Gillon[3], C. Hellier[1], E. Jehin[3], M. Lendl[4], F. Pepe[4], D. L. Pollacco[5,6], D. Queloz[4], D. Ségransan[4], B. Smalley[1], J. K. Southworth [1], A. M. S. Smith[1], A. H. M. J. Triaud[4], S. Udry[4], R. G. West[7],

ABSTRACT

We report the discovery of a transiting planet with an orbital period of 1.36 d orbiting the brighter component of the visual binary star BD −07° 436. The host star, WASP-77 A, is a moderately bright G8 V star (V=10.3) with a metallicity close to solar ([Fe/H]= 0.0 ± 0.1). The companion star, WASP-77 B, is a K-dwarf approximately 2 magnitudes fainter at a separation of approximately 3″. The spectrum of WASP-77 A shows emission in the cores of the Ca II H and K lines indicative of moderate chromospheric activity. The WASP lightcurves show photometric variability with a period of 15.3 days and an amplitude of about 0.3% that is probably due to the magnetic activity of the host star. We use an analysis of the combined photometric and spectroscopic data to derive the mass and radius of the planet ($1.76 \pm 0.06 M_{\rm Jup}$, $1.21 \pm 0.02 R_{\rm Jup}$). The age of WASP-77 A estimated from its rotation rate (~ 1 Gyr) agrees with the age estimated in a similar way for WASP-77 B (~ 0.6 Gyr) but is in poor agreement with the age inferred by comparing its effective temperature and density to stellar models (~ 8 Gyr). Follow-up observations of WASP-77 Ab will make a useful contribution to our understanding of the influence of binarity and host star activity on the properties of hot Jupiters.

Subject headings: Extrasolar planets

[1]Astrophysics Group, Keele University, Staffordshire, ST5 5BG, UK

[2]SUPA, School of Physics and Astronomy, University of St. Andrews, North Haugh, Fife, KY16 9SS, UK

[3]Institut d'Astrophysique et de Géophysique, Université de Liège, Allée du 6 Août, 17, Bat. B5C, Liège 1, Belgium

[4]Observatoire astronomique de l'Université de Genève 51 ch. des Maillettes, 1290 Sauverny, Switzerland

[5]Department of Physics, University of Warwick, Coventry, CV4 7AL

[6]Astrophysics Research Centre, School of Mathematics & Physics, Queen's University, University Road, Belfast, BT7 1NN, UK

[7]Department of Physics and Astronomy, University of Leicester, Leicester, LE1 7RH, UK

⋆Based on observations made with ESO Telescopes at the La Silla Paranal Observatory under programme ID 088.C-0011.

Astronomy & Astrophysics manuscript no. rbatch
October 22, 2013

Three irradiated and bloated hot Jupiters:

WASP-76b, WASP-82b & WASP-90b

R.G. West[1], J.-M. Almenara[2], D.R. Anderson[3], F. Bouchy[4], D. J. A. Brown[5], A. Collier Cameron[5], M. Deleuil[2], L. Delrez[6], A. P. Doyle[3], F. Faedi[1], A. Fumel[6], M. Gillon[6], G. Hébrard[4], C. Hellier[3], E. Jehin[6], M. Lendl[7], P.F.L. Maxted[3], F. Pepe[7], D. Pollacco[1], D. Queloz[7,8], D. Ségransan[7], B. Smalley[3], A.M.S. Smith[3,9], A.H.M.J. Triaud,[7,10]⋆, and S. Udry[7]

[1] Department of Physics, University of Warwick, Coventry CV4 7AL, UK
[2] Aix Marseille Université, CNRS, LAM (Laboratoire d'Astrophysique de Marseille) UMR 7326, 13388, Marseille, France
[3] Astrophysics Group, Keele University, Staffordshire, ST5 5BG, UK
[4] Institut d'Astrophysique de Paris, UMR 7095 CNRS, Université Pierre & Marie Curie, France; Observatoire de Haute-Provence, CNRS/OAMP, 04870, St Michel l'Observatoire, France
[5] SUPA, School of Physics and Astronomy, University of St. Andrews, North Haugh, Fife, KY16 9SS, UK
[6] Institut d'Astrophysique et de Géophysique, Université de Liège, Allée du 6 Août, 17, Bat. B5C, Liège 1, Belgium
[7] Observatoire astronomique de l'Université de Genève 51 ch. des Maillettes, 1290 Sauverny, Switzerland
[8] Cavendish Laboratory, J J Thomson Avenue, Cambridge, CB3 0HE, UK
[9] N. Copernicus Astronomical Centre, Polish Academy of Sciences, Bartycka 18, 00-716 Warsaw, Poland
[10] Department of Physics and Kavli Institute for Astrophysics & Space Research, Massachusetts Institute of Technology, Cambridge, MA 02139, USA

Preprint online version: October 22, 2013

ABSTRACT

We report three new transiting hot-Jupiter planets discovered from the WASP surveys combined with radial velocities from OHP/SOPHIE and Euler/CORALIE and photometry from Euler and TRAPPIST. All three planets are inflated, with radii 1.7–1.8 R_{Jup}. All orbit hot stars, F5–F7, and all three stars have evolved, post-MS radii (1.7–2.2 $R_{\odot}$). Thus the three planets, with orbits of 1.8–3.9 d, are among the most irradiated planets known. This reinforces the correlation between inflated planets and stellar irradiation.

Key words. stars: individual (WASP-76; BD+01 316) – stars: individual (WASP-82) – stars: individual (WASP-90) — planetary systems

1. Introduction

The naive expectation that a Jupiter-mass planet would have a one-Jupiter radius has been replaced by the realisation that many of the hot Jupiters found by transit surveys have inflated radii. Planets as large as ~ 2 R_{Jup} have been found (e.g. WASP-17b, Anderson et al. 2010; HAT-P-32b, Hartman et al. 2011).

It is also apparent that inflated planets are found preferentially around hot stars. For example Hartman et al. 2012 reported three new HAT-discovered planets, with radii of 1.6–1.7 R_{Jup}, all transiting F stars. Here we continue this theme by announcing three new hot Jupiters, again all inflated and all orbiting F stars.

For a discussion of the radii of transiting exoplanets we refer the reader to the recent paper by Weiss et al. (2013). It seems clear that stellar irradiation plays a large role in inflating hot Jupiters, since no inflated planets are known that receive less than 2×10^8 erg s^{-1} cm^{-2} (Miller & Fortney 2011; Demory & Seager 2011). There is also an extensive literature discussing other mechanisms for inflating hot Jupiters, such as tidal dissipation (e.g. Leconte et al. 2010, and references therein) and Ohmic dissipation (e.g. Batygin & Stevenson 2010).

⋆ Fellow of the Swiss National Science Foundation

2. Observations

The three transiting-planet systems reported here are near the equator, and so have been observed by both the SuperWASP-North camera array on La Palma and by WASP-South at Sutherland in South Africa. Our methods all follow closely to those in previous WASP discovery papers. The WASP camera arrays are described in Pollacco et al. (2006) while our planet-hunting methods are described in Collier-Cameron et al. (2007a) and Pollacco et al. (2007).

Equatorial WASP candidates are followed up by obtaining radial velocities using the SOPHIE spectrograph on the 1.93-m telescope at OHP (as described in, e.g., Hébrard et al. 2013) and the CORALIE spectrograph on the 1.2-m Euler telescope at La Silla (e.g., Triaud et al. 2013). Higher-quality lightcurves of transits are obtained using EulerCAM on the 1.2-m telescope (e.g., Lendl et al. 2013) and the robotic TRAPPIST photometer at La Silla (e.g., Gillon et al. 2013). The observations for our three new planets are listed in Table 1.

3. The host stars

The stellar parameters for WASP-76, WASP-82 and WASP-90 were derived from the co-added RV spectra using the methods given in Doyle et al. (2013). The excitation balance of the Fe I lines was used to determine the effective temperature ($T_{\rm eff}$). The

Mon. Not. R. Astron. Soc. **000**, range (0000) Printed 22 October 2013 (MN LATEX style file v2.2)

Transiting hot Jupiters from WASP-South, Euler and TRAPPIST: WASP-95b to WASP-101b

Coel Hellier[1], D.R. Anderson[1], A. Collier Cameron[2], L. Delrez[3], M. Gillon[3], E. Jehin[3], M. Lendl[4], P.F.L. Maxted[1], F. Pepe[4], D. Pollacco[5], D. Queloz[4,6], D. Ségransan[4], B. Smalley[1], A.M.S. Smith[1,7], J. Southworth[1], A.H.M.J. Triaud[4,8⋆], S. Udry[4] & R.G. West[5]

[1] *Astrophysics Group, Keele University, Staffordshire, ST5 5BG, UK*
[2] *SUPA, School of Physics and Astronomy, University of St. Andrews, North Haugh, Fife, KY16 9SS, UK*
[3] *Institut d'Astrophysique et de Géophysique, Université de Liège, Allée du 6 Août, 17, Bat. B5C, Liège 1, Belgium*
[4] *Observatoire astronomique de l'Université de Genève 51 ch. des Maillettes, 1290 Sauverny, Switzerland*
[5] *Department of Physics, University of Warwick, Gibbet Hill Road, Coventry CV4 7AL, UK*
[6] *Cavendish Laboratory, J J Thomson Avenue, Cambridge, CB3 0HE, UK*
[7] *N. Copernicus Astronomical Centre, Polish Academy of Sciences, Bartycka 18, 00-716 Warsaw, Poland*
[8] *Department of Physics and Kavli Institute for Astrophysics & Space Research, Massachusetts Institute of Technology, Cambridge, MA 02139, USA*

date

ABSTRACT

We report the discovery of the transiting exoplanets WASP-95b, WASP-96b, WASP-97b, WASP-98b, WASP-99b, WASP-100b and WASP-101b. All are hot Jupiters with orbital periods in the range 2.1 to 5.7 d, masses of 0.5 to 2.8 M_{Jup}, and radii of 1.1 to 1.4 R_{Jup}. The orbits of all the planets are compatible with zero eccentricity. WASP-99b shows the shallowest transit yet found by WASP-South, at 0.4%.

The host stars are of spectral type F2 to G8. Five have metallicities of [Fe/H] from –0.03 to +0.23, while WASP-98 has a metallicity of –0.60, exceptionally low for a star with a transiting exoplanet. Five of the host stars are brighter than $V = 10.8$, which significantly extends the number of bright transiting systems available for follow-up studies. WASP-95 shows a possible rotational modulation at a period of 20.7 d.

We discuss the completeness of WASP survey techniques by comparing to the HAT project.

Key words: planetary systems

1 INTRODUCTION

The WASP-South survey has dominated the discovery of transiting hot-Jupiter exoplanets in the Southern hemisphere. WASP-South is well matched to the capabilities of the Euler/CORALIE spectrograph and the robotic TRAPPIST telescope, with the combination of all three proving efficient for discovering transiting exoplanets in the range V = 9–13.

WASP-South has now been running nearly continuously for 7 years. Approximately 1000 candidates have been observed with Euler/CORALIE, while, since December 2010, TRAPPIST has observed 1000 lightcurves of WASP candidates and planets. Here we present new WASP-South planets which take WASP numbering above 100.

Since WASP host stars are generally brighter than host stars of *Kepler* exoplanets, ongoing WASP-South discoveries are important for detailed study of exoplanets and will be prime targets for future missions such as *CHEOPS* and *JWST,* and proposed missions such as *EChO* and *FINESSE.*

2 OBSERVATIONS

The observational and analysis techniques used here are the same as in recent WASP discovery papers (e.g. Hellier et al. 2012), and thus are described briefly. For detailed accounts see the early papers including Pollacco et al. (2006), Collier-Cameron et al. (2007a) and Pollacco et al. (2007).

In outline, WASP-South surveys the visible sky each

⋆ Fellow of the Swiss National Science Foundation

Mon. Not. R. Astron. Soc. **000**, 1–17 (2013) Printed 22 October 2013 (MN LATEX style file v2.2)

Three sub-Jupiter-mass planets: WASP-69b & WASP-84b transit active K dwarfs and WASP-70Ab transits the evolved primary of a G4+K3 binary⋆

D. R. Anderson,[1] A. Collier Cameron,[2] L. Delrez,[3] A. P. Doyle,[1] F. Faedi,[4] A. Fumel,[3] M. Gillon,[3] Y. Gómez Maqueo Chew,[4] C. Hellier,[1] E. Jehin,[3] M. Lendl,[5] P. F. L. Maxted,[1] F. Pepe,[5] D. Pollacco,[4] D. Queloz,[5,6] D. Ségransan,[5] I. Skillen,[7] B. Smalley,[1] A. M. S. Smith,[1,8] J. Southworth,[1] A. H. M. J. Triaud,[5,9] O. D. Turner,[1] S. Udry,[5] and R. G. West[4]

[1]*Astrophysics Group, Keele University, Staffordshire ST5 5BG, UK. E-mail:* **d.r.anderson@keele.ac.uk**
[2]*SUPA, School of Physics and Astronomy, University of St. Andrews, North Haugh, Fife KY16 9SS, UK*
[3]*Institut d'Astrophysique et de Géophysique, Université de Liège, Allée du 6 Août, 17, Bat. B5C, Liège 1, Belgium*
[4]*Department of Physics, University of Warwick, Coventry CV4 7AL, UK*
[5]*Observatoire de Genève, Université de Genève, 51 Chemin des Maillettes, 1290 Sauverny, Switzerland*
[6]*Cavendish Laboratory, J J Thomson Avenue, Cambridge, CB3 0HE, UK*
[7]*Isaac Newton Group of Telescopes, Apartado de Correos 321, E-38700 Santa Cruz de la Palma, Tenerife, Spain*
[8]*N. Copernicus Astronomical Centre, Polish Academy of Sciences, Bartycka 18, 00-716, Warsaw, Poland*
[9]*Department of Physics, and Kavli Institute for Astrophysics and Space Research, Massachusetts Institute of Technology, Cambridge, MA 02139, USA.*

Accepted Year Month Day. Received Year Month Day; in original form 2013 October 21

ABSTRACT

We report the discovery of the transiting exoplanets WASP-69b, WASP-70Ab and WASP-84b, each of which orbits a bright star ($V \sim 10$). WASP-69b is a bloated Saturn-mass planet ($0.26\,M_{\rm Jup}$, $1.06\,R_{\rm Jup}$) in a 3.868-d period around an active mid-K dwarf. We estimate a stellar age of 1 Gyr from both gyrochronological and age-activity relations, though an alternative gyrochronological relation suggests an age of 3 Gyr. ROSAT detected X-rays at a distance of 60±27″ from WASP-69. If the star is the source then the planet could be undergoing mass-loss at a rate of $\sim 10^{12}\,{\rm g\,s^{-1}}$. This is 1–2 orders of magnitude higher than the evaporation rate estimated for HD 209458b and HD 189733b, both of which have exhibited anomalously-large Lyman-α absorption during transit. WASP-70Ab is a sub-Jupiter-mass planet ($0.59\,M_{\rm Jup}$, $1.16\,R_{\rm Jup}$) in a 3.713-d orbit around the primary of a spatially-resolved G4+K3 binary, with a separation of 3.″3 ($\geqslant$800 AU). We exploit the binary nature of the system to construct a Hertzsprung-Russell diagram, from which we estimate its age to be 9–10 Gyr. WASP-84b is a sub-Jupiter-mass planet ($0.69\,M_{\rm Jup}$, $0.94\,R_{\rm Jup}$) in an 8.523-d orbit around an active early-K dwarf. Of the transiting planets discovered from the ground to date, WASP-84b has the third-longest period. From a combination of gyrochronological and age-activity relations we estimate the age of WASP-84 to be ∼1 Gyr.

For both the active stars WASP-69 and WASP-84 we find a modulation of the radial velocities with a period similar to the photometrically-determined stellar rotation period. We fit the residuals with a low-order harmonic series and subtract the best fit from the RVs prior to deriving the system parameters. In each case the solution is essentially unchanged, with much less than a 1-σ change to the planetary mass. We found this method of pre-whitening using a harmonic fit to result in a greater reduction in the residual RV scatter than the oft-used method of pre-whitening with a fit to the RV residuals and the bisector spans.

Key words: planets and satellites: detection – techniques: photometric – techniques: radial velocities – planets and satellites: individual: WASP-69b – planets and satellites: individual: WASP-70Ab – planets and satellites: individual: WASP-84b.

⋆ Based on observations made with the WASP-South (South Africa) and SuperWASP-North (La Palma) photometric survey instruments, the RISE camera on the 2-m Liverpool Telescope under program PL12B13, and, all located at La Silla, the 60-cm TRAPPIST photometer, EulerCam and the CORALIE spectrograph, both mounted on the 1.2-m Euler-Swiss telescope,

Astronomy & Astrophysics manuscript no. WASP˙68˙73˙88
December 9, 2013

Transiting planets from WASP-South, Euler and TRAPPIST:

WASP-68 b, WASP-73 b and WASP-88 b, three hot Jupiters transiting evolved solar-type stars⋆

L. Delrez[1], V. Van Grootel[1⋆⋆], D. R. Anderson[2], A. Collier-Cameron[3], A. P. Doyle[2], A. Fumel[1], M. Gillon[1], C. Hellier[2], E. Jehin[1], M. Lendl[4], M. Neveu-VanMalle[4,6], P. F. L. Maxted[2], F. Pepe[4], D. Pollacco[5], D. Queloz[6,4], D. Ségransan[4], B. Smalley[2], A. M. S. Smith[7,2], J. Southworth[2], A. H. M. J. Triaud[8,4⋆⋆⋆], S. Udry[4], R. G. West[5]

[1] Institut d'Astrophysique et Géophysique, Université de Liège, allée du 6 Août 17, B-4000 Liège, Belgium
[2] Astrophysics Group, Keele University, Staffordshire, ST5 5BG, UK
[3] SUPA, School of Physics and Astronomy, University of St. Andrews, North Haugh, Fife, KY16 9SS, UK
[4] Observatoire de Genève, Université de Genève, 51 Chemin des Maillettes, 1290 Sauverny, Switzerland
[5] Department of Physics, University of Warwick, Coventry CV4 7AL, UK
[6] Cavendish Laboratory, Department of Physics, University of Cambridge, JJ Thomson Avenue, Cambridge, CB3 0HE, UK
[7] N. Copernicus Astronomical Centre, Polish Academy of Sciences, Bartycka 18, 00-716 Warsaw, Poland
[8] Department of Physics and Kavli Institute for Astrophysics & Space Research, Massachusetts Institute of Technology, Cambridge, MA 02139, USA

Received date / accepted date

ABSTRACT

We report the discovery by the WASP transit survey of three new hot Jupiters, WASP-68 b, WASP-73 b and WASP-88 b. WASP-68 b has a mass of 0.95 ± 0.03 $M_{\rm Jup}$, a radius of $1.24^{+0.10}_{-0.06}$ $R_{\rm Jup}$, and orbits a V=10.7 G0-type star (1.24 ± 0.03 $M_\odot$, $1.69^{+0.11}_{-0.06}$ $R_\odot$, $T_{\rm eff}$ = 5911 ± 60 K) with a period of 5.084298 ± 0.000015 days. Its size is typical of hot Jupiters with similar masses. WASP-73 b is significantly more massive ($1.88^{+0.07}_{-0.06}$ $M_{\rm Jup}$) and slightly larger ($1.16^{+0.12}_{-0.08}$ $R_{\rm Jup}$) than Jupiter. It orbits a V=10.5 F9-type star ($1.34^{+0.05}_{-0.04}$ $M_\odot$, $2.07^{+0.19}_{-0.08}$ $R_\odot$, $T_{\rm eff}$ = 6036 ± 120 K) every 4.08722 ± 0.00022 days. Despite its high irradiation (∼2.3 10^9 erg $s^{-1}cm^{-2}$), WASP-73 b has a high mean density ($1.20^{+0.26}_{-0.30}$ $\rho_{\rm Jup}$) that suggests an enrichment of the planet in heavy elements. WASP-88 b is a 0.56 ± 0.08 $M_{\rm Jup}$ planet orbiting a V=11.4 F6-type star (1.45 ± 0.05 $M_\odot$, $2.08^{+0.12}_{-0.06}$ $R_\odot$, $T_{\rm eff}$ = 6431 ± 130 K) with a period of 4.954000 ± 0.000019 days. With a radius of $1.70^{+0.13}_{-0.07}$ $R_{\rm Jup}$, it joins the handful of planets with super-inflated radii. The ranges of ages we determine through stellar evolution modeling are 4.2-8.3 Gyr for WASP-68, 2.7-6.4 Gyr for WASP-73 and 1.8-5.3 Gyr for WASP-88. WASP-73 appears to be a significantly evolved star, close to or already in the subgiant phase. WASP-68 and WASP-88 are less evolved, although in an advanced stage of core H-burning.

Key words. planetary systems – stars: individual: WASP-68 – stars: individual: WASP-73 – stars: individual: WASP-88 – techniques: photometric – techniques: radial velocities – techniques: spectroscopic

1. Introduction

Since the discovery of the first extrasolar planet around a Solar-type star by Mayor & Queloz (1995), more than 1000 planets have been detected outside our Solar system[1]. Among this large harvest, the sub-sample of planets that transit the disc of their host star is extremely valuable. Indeed, transiting exoplanets allow parameters such as mass, radius and density to be accurately determined (e.g. Charbonneau et al. 2000), as well as their atmospheric properties to be studied during their transits and occultations (e.g. Seager & Deming 2010). At the time of writing, over 400 transiting planets have been discovered[1], a significant fraction of them being Jovian-type planets orbiting within 0.1 AU of their host star. Most of these so-called "hot Jupiters" were detected by ground-based transit surveys, among which the WASP survey (Wide Angle Search for Planets, Pollacco et al. 2006) has been the most successful, with now more than 100 planets discovered (Hellier et al. 2013). Ongoing WASP discoveries are important for the field of exoplanetology as these systems tend to be particularly prone to thorough characterizations, owing to their bright host stars ($9 < V < 13$), short orbits and favorable planet-to-star area ratios. Therefore, they will be prime targets for thorough characterizations with future facilities such as CHEOPS (CHaracterising ExOPlanets Satellite, Broeg et al. 2013) and JWST (James Webb Space Telescope, Gardner et al. 2006).

In this paper, we report the discovery of three additional transiting planets by the WASP survey. WASP-68 b is a 0.95 $M_{\rm Jup}$ planet in a 5 days orbit around a G0-type star, WASP-73 b is a dense 1.88 $M_{\rm Jup}$ planet orbiting an F9-type star every 4.1 days,

Send offprint requests to: ldelrez@ulg.ac.be

⋆ The photometric time-series used in this work are only available at the CDS via anonymous ftp to `cdsarc.u-strasbg.fr(130.79.128.5)` or via `http://cdsarc.u-strasbg.fr/viz-bin/qcat?J/A+A/`

⋆⋆ Chargée de recherches, Fonds de la Recherche Scientifique, FNRS, rue d'Egmont 5, B-1000 Bruxelles, Belgium

⋆⋆⋆ Fellow of the Swiss National Science Foundation.

[1] `http://exoplanet.eu/`

BIBLIOGRAPHY

Abe, L., Gonçalves, I., Agabi, A., et al. 2013, A&A, 553, A49

Agol, E., Steffen, J., Sari, R., & Clarkson, W. 2005, MNRAS, 359, 567

Alard, C. 2000, A&AS, 144, 363

Alard, C. & Lupton, R. H. 1998, ApJ, 503, 325

Albrecht, S., Winn, J. N., Johnson, J. A., et al. 2012, ApJ, 757, 18

Albrecht, S., Winn, J. N., Marcy, G. W., et al. 2013, ApJ, 771, 11

Alibert, Y., Mordasini, C., & Benz, W. 2004, A&A, 417, L25

Alibert, Y., Mordasini, C., Benz, W., & Winisdoerffer, C. 2005, A&A, 434, 343

Almenara, J. M., Deeg, H. J., Aigrain, S., et al. 2009, A&A, 506, 337

Alonso, R., Brown, T. M., Torres, G., et al. 2004, ApJ, 613, L153

Alonso, R., Guillot, T., Mazeh, T., et al. 2009, A&A, 501, L23

Anderson, D. R., Collier Cameron, A., Delrez, L., et al. 2013a, ArXiv e-prints

Anderson, D. R., Collier Cameron, A., Gillon, M., et al. 2011, A&A, 534, A16

Anderson, D. R., Gillon, M., Maxted, P. F. L., et al. 2010, A&A, 513, L3

Anderson, D. R., Smith, A. M. S., Madhusudhan, N., et al. 2013b, MNRAS, 430, 3422

Appenzeller, I., Fricke, K., Fürtig, W., et al. 1998, The Messenger, 94, 1

Astudillo-Defru, N. & Rojo, P. 2013, A&A, 557, A56

Baglin, A., Auvergne, M., Boisnard, L., et al. 2006, in COSPAR Meeting, Vol. 36, 36th COSPAR Scientific Assembly, 3749

Bakos, G., Noyes, R. W., Kovács, G., et al. 2004, PASP, 116, 266

Bakos, G. Á., Csubry, Z., Penev, K., et al. 2013, PASP, 125, 154

Bakos, G. Á., Howard, A. W., Noyes, R. W., et al. 2009, ApJ, 707, 446

Baranne, A., Queloz, D., Mayor, M., et al. 1996, A&AS, 119, 373

Barclay, T., Burke, C. J., Howell, S. B., et al. 2013a, ApJ, 768, 101

Barclay, T., Huber, D., Rowe, J. F., et al. 2012, ApJ, 761, 53

Barclay, T., Rowe, J. F., Lissauer, J. J., et al. 2013b, Nature, 494, 452

Barman, T. 2007, ApJ, 661, L191

Barros, S. C. C., Faedi, F., Collier Cameron, A., et al. 2011, A&A, 525, A54

Batalha, N. M., Rowe, J. F., Bryson, S. T., et al. 2013, ApJS, 204, 24

Bate, M. R., Lubow, S. H., Ogilvie, G. I., & Miller, K. A. 2003, MNRAS, 341, 213

Batygin, K. & Stevenson, D. J. 2010, ApJ, 714, L238

Bean, J. L., Désert, J.-M., Kabath, P., et al. 2011, ApJ, 743, 92

Bean, J. L., Désert, J.-M., Seifahrt, A., et al. 2013, ApJ, 771, 108

Bean, J. L., Miller-Ricci Kempton, E., & Homeier, D. 2010, Nature, 468, 669

Beaulieu, J. P., Kipping, D. M., Batista, V., et al. 2010, MNRAS, 409, 963

Belorizky, D. 1938, L'Astronomie, 52, 359

Bento, J., Wheatley, P. J., Copperwheat, C. M., et al. 2013, MNRAS

Bertin, E. & Arnouts, S. 1996, A&AS, 117, 393

Bessell, M. S. 1979, PASP, 91, 589

Binney, J. & Tremaine, S. 1987, Galactic dynamics

Bodenheimer, P., Lin, D. N. C., & Mardling, R. A. 2001, ApJ, 548, 466

Bonfils, X., Gillon, M., Udry, S., et al. 2012, A&A, 546, A27

Borucki, W. J., Agol, E., Fressin, F., et al. 2013, Science, 340, 587

Borucki, W. J., Koch, D., Basri, G., et al. 2010, Science, 327, 977

Borucki, W. J., Koch, D., Jenkins, J., et al. 2009, Science, 325, 709

Boss, A. P. 1997, Science, 276, 1836

Boss, A. P. 2011, ApJ, 731, 74

Bouchy, F., Mayor, M., Lovis, C., et al. 2009, A&A, 496, 527

Bouchy, F., Pont, F., Santos, N. C., et al. 2004, A&A, 421, L13

Bouchy, F., Udry, S., Mayor, M., et al. 2005, A&A, 444, L15

Brogi, M., Snellen, I. A. G., de Kok, R. J., et al. 2012, Nature, 486, 502

Brogi, M., Snellen, I. A. G., de Kok, R. J., et al. 2013, ApJ, 767, 27

Brown, D. J. A., Collier Cameron, A., Díaz, R. F., et al. 2012, ApJ, 760, 139

Brown, D. J. A., Collier Cameron, A., Hall, C., Hebb, L., & Smalley, B. 2011, MNRAS, 415, 605

Brown, T. M. 2001, ApJ, 553, 1006

Brown, T. M., Charbonneau, D., Gilliland, R. L., Noyes, R. W., & Burrows, A. 2001, ApJ, 552, 699

Buchhave, L. A., Latham, D. W., Johansen, A., et al. 2012, Nature, 486, 375

Burkert, A., Lin, D. N. C., Bodenheimer, P. H., Jones, C. A., & Yorke, H. W. 2005, ApJ, 618, 512

Burki, G., Rufener, F., Burnet, M., et al. 1995, A&AS, 112, 383

Burrows, A., Budaj, J., & Hubeny, I. 2008, ApJ, 678, 1436

Burrows, A., Hubeny, I., Budaj, J., & Hubbard, W. B. 2007a, ApJ, 661, 502

Burrows, A., Hubeny, I., Budaj, J., Knutson, H. A., & Charbonneau, D. 2007b, ApJ, 668, L171

Burrows, A., Hubeny, I., & Sudarsky, D. 2005, ApJ, 625, L135

Burrows, A., Sudarsky, D., & Hubeny, I. 2006, ApJ, 650, 1140

Burton, J. R., Watson, C. A., Littlefair, S. P., et al. 2012, ApJS, 201, 36

Butler, R. P., Vogt, S. S., Marcy, G. W., et al. 2004, ApJ, 617, 580

Cabrera, J., Csizmadia, S., Lehmann, H., et al. 2013, ArXiv e-prints

Carraro, G. 2013, Very Large Telescope - HAWK-I User Manual, 92nd edn., European Southern Observatory, Paranal Observatory

Carter, J. A., Winn, J. N., Gilliland, R., & Holman, M. J. 2009, ApJ, 696, 241

Castelli, F. & Kurucz, R. L. 2004, ArXiv Astrophysics e-prints

Chabrier, G. & Baraffe, I. 2007, ApJ, 661, L81

Charbonneau, D., Allen, L. E., Megeath, S. T., et al. 2005, ApJ, 626, 523

Charbonneau, D., Berta, Z. K., Irwin, J., et al. 2009, Nature, 462, 891

Charbonneau, D., Brown, T. M., Latham, D. W., & Mayor, M. 2000, ApJ, 529, L45

Charbonneau, D., Brown, T. M., Noyes, R. W., & Gilliland, R. L. 2002, ApJ, 568, 377

Charbonneau, D., Knutson, H. A., Barman, T., et al. 2008, ApJ, 686, 1341

Chatterjee, S., Ford, E. B., Matsumura, S., & Rasio, F. A. 2008, ApJ, 686, 580

Claret, A. 2000, A&A, 363, 1081

Claret, A. & Bloemen, S. 2011, A&A, 529, A75

Collier Cameron, A., Pollacco, D., Street, R. A., et al. 2006, MNRAS, 373, 799

Colón, K. D., Ford, E. B., Lee, B., Mahadevan, S., & Blake, C. H. 2010, MNRAS, 408, 1494

Cooper, C. S. & Showman, A. P. 2005, ApJ, 629, L45

Cooper, C. S. & Showman, A. P. 2006, ApJ, 649, 1048

Copperwheat, C. M., Wheatley, P. J., Southworth, J., et al. 2013, MNRAS, 434, 661

Cowan, N. B., Agol, E., & Charbonneau, D. 2007, MNRAS, 379, 641

Croll, B., Albert, L., Jayawardhana, R., et al. 2011, ApJ, 736, 78

Croll, B., Albert, L., Lafreniere, D., Jayawardhana, R., & Fortney, J. J. 2010a, ApJ, 717, 1084

Croll, B., Jayawardhana, R., Fortney, J. J., Lafrenière, D., & Albert, L. 2010b, ApJ, 718, 920

Crossfield, I. J. M., Barman, T., Hansen, B. M. S., & Howard, A. W. 2013, A&A, 559, A33

Crossfield, I. J. M., Hansen, B. M. S., Harrington, J., et al. 2010, ApJ, 723, 1436

Crouzet, N., McCullough, P. R., Burke, C., & Long, D. 2012, ApJ, 761, 7

Cumming, A., Butler, R. P., Marcy, G. W., et al. 2008, PASP, 120, 531

Cumming, A., Marcy, G. W., & Butler, R. P. 1999, ApJ, 526, 890

D'Angelo, G., Durisen, R. H., & Lissauer, J. J. 2011, Giant Planet Formation, ed. S. Seager, 319–346

de Kok, R. J., Brogi, M., Snellen, I. A. G., et al. 2013, A&A, 554, A82

de Mooij, E. J. W., Brogi, M., de Kok, R. J., et al. 2013, A&A, 550, A54

de Mooij, E. J. W., de Kok, R. J., Nefs, S. V., & Snellen, I. A. G. 2011, A&A, 528, A49

de Mooij, E. J. W. & Snellen, I. A. G. 2009, A&A, 493, L35

de Pater, I. & Lissauer, J. J. 2010, Planetary Sciences

de Wit, J., Gillon, M., Demory, B.-O., & Seager, S. 2012, A&A, 548, A128

Deeg, H. J., Moutou, C., Erikson, A., et al. 2010, Nature, 464, 384

Deleuil, M., Deeg, H. J., Alonso, R., et al. 2008, A&A, 491, 889

Deming, D., Harrington, J., Laughlin, G., et al. 2007a, ApJ, 667, L199

Deming, D., Harrington, J., Seager, S., & Richardson, L. J. 2006, ApJ, 644, 560

Deming, D., Richardson, L. J., & Harrington, J. 2007b, MNRAS, 378, 148

Deming, D., Seager, S., Richardson, L. J., & Harrington, J. 2005, Nature, 434, 740

Deming, D., Wilkins, A., McCullough, P., et al. 2013, ApJ, 774, 95

Demory, B.-O., Gillon, M., Barman, T., et al. 2007, A&A, 475, 1125

Demory, B.-O., Gillon, M., Deming, D., et al. 2011, A&A, 533, A114

Demory, B.-O., Gillon, M., Seager, S., et al. 2012, ApJ, 751, L28

Demory, B.-O. & Seager, S. 2011, ApJS, 197, 12

Désert, J.-M., Lecavelier des Etangs, A., Hébrard, G., et al. 2009, ApJ, 699, 478

Désert, J.-M., Vidal-Madjar, A., Lecavelier Des Etangs, A., et al. 2008, A&A, 492, 585

Dhillon, V. S., Marsh, T. R., Stevenson, M. J., et al. 2007, MNRAS, 378, 825

Díaz, R. F., Rojo, P., Melita, M., et al. 2008, ApJ, 682, L49

Doppler, C. 1842, Abhandlungen der K. Böhm. Gesellschaft der Wissenschaften, 5, 465

Doyle, L. R., Carter, J. A., Fabrycky, D. C., et al. 2011, Science, 333, 1602

Dragomir, D., Kane, S. R., Pilyavsky, G., et al. 2011, AJ, 142, 115

Dumusque, X., Pepe, F., Lovis, C., et al. 2012, Nature, 491, 207

Duquennoy, A. & Mayor, M. 1991, A&A, 248, 485

Durisen, R. H., Boss, A. P., Mayer, L., et al. 2007, Protostars and Planets V, 607

Eggleton, P. P. & Kiseleva-Eggleton, L. 2001, ApJ, 562, 1012

Ehrenreich, D., Hébrard, G., Lecavelier des Etangs, A., et al. 2007, ApJ, 668, L179

Ehrenreich, D., Lecavelier Des Etangs, A., Hébrard, G., et al. 2008, A&A, 483, 933

Einstein, A. 1905, Annalen der Physik, 322, 132

Enoch, B., Collier Cameron, A., Parley, N. R., & Hebb, L. 2010, A&A, 516, A33

Fabrycky, D. C., Ford, E. B., Steffen, J. H., et al. 2012, ApJ, 750, 114

Fabrycky, D. C. & Winn, J. N. 2009, ApJ, 696, 1230

Fath, E. A. 1935, PASP, 47, 232

Fazio, G. G., Hora, J. L., Allen, L. E., et al. 2004, ApJS, 154, 10

Fischer, D. A., Marcy, G. W., Butler, R. P., et al. 2008, ApJ, 675, 790

Fischer, D. A. & Valenti, J. 2005, ApJ, 622, 1102

Föhring, D., Dhillon, V. S., Madhusudhan, N., et al. 2013, MNRAS, 435, 2268

Ford, E. B. & Rasio, F. A. 2006, ApJ, 638, L45

Fortney, J. J., Baraffe, I., & Militzer, B. 2010, Giant Planet Interior Structure and Thermal Evolution, ed. Seager, S., 397–418

Fortney, J. J., Cooper, C. S., Showman, A. P., Marley, M. S., & Freedman, R. S. 2006a, ApJ, 652, 746

Fortney, J. J., Lodders, K., Marley, M. S., & Freedman, R. S. 2008, ApJ, 678, 1419

Fortney, J. J., Marley, M. S., & Barnes, J. W. 2007, ApJ, 659, 1661

Fortney, J. J., Marley, M. S., Lodders, K., Saumon, D., & Freedman, R. 2005, ApJ, 627, L69

Fortney, J. J., Saumon, D., Marley, M. S., Lodders, K., & Freedman, R. S. 2006b, ApJ, 642, 495

Fossati, L., Haswell, C. A., Froning, C. S., et al. 2010, ApJ, 714, L222

Fukui, A., Narita, N., Kurosaki, K., et al. 2013, ApJ, 770, 95

Gibson, N. P., Aigrain, S., Barstow, J. K., et al. 2013, MNRAS, 428, 3680

Gibson, N. P., Aigrain, S., Pollacco, D. L., et al. 2010, MNRAS, 404, L114

Gibson, N. P., Aigrain, S., Pont, F., et al. 2012, MNRAS, 422, 753

Gibson, N. P., Pollacco, D., Simpson, E. K., et al. 2008, A&A, 492, 603

Gibson, N. P., Pont, F., & Aigrain, S. 2011, MNRAS, 411, 2199

Gillon, M., Anderson, D. R., Collier-Cameron, A., et al. 2014, ArXiv e-prints

Gillon, M., Demory, B.-O., Madhusudhan, N., et al. 2013, ArXiv e-prints

Gillon, M., Demory, B.-O., Triaud, A. H. M. J., et al. 2009, A&A, 506, 359

Gillon, M., Doyle, A. P., Lendl, M., et al. 2011a, A&A, 533, A88

Gillon, M., Jehin, E., Magain, P., et al. 2011b, Detection and Dynamics of Transiting Exoplanets, St. Michel l'Observatoire, France, Edited by F. Bouchy; R. Díaz; C. Moutou; EPJ Web of Conferences, Volume 11, id.06002, 11, 6002

Gillon, M., Lanotte, A. A., Barman, T., et al. 2010, A&A, 511, A3

Gillon, M., Pont, F., Demory, B.-O., et al. 2007, A&A, 472, L13

Gillon, M., Pont, F., Moutou, C., et al. 2006, A&A, 459, 249

Gillon, M., Triaud, A. H. M. J., Fortney, J. J., et al. 2012, ArXiv e-prints

Goldreich, P. & Tremaine, S. 1980, ApJ, 241, 425

Gould, A., Dorsher, S., Gaudi, B. S., & Udalski, A. 2006, Acta Astron., 56, 1

Greiner, J., Bornemann, W., Clemens, C., et al. 2008, PASP, 120, 405

Griffin, R. F. 1967, ApJ, 148, 465

Grillmair, C. J., Burrows, A., Charbonneau, D., et al. 2008, Nature, 456, 767

Grillmair, C. J., Charbonneau, D., Burrows, A., et al. 2007, ApJ, 658, L115

Gu, P.-G., Lin, D. N. C., & Bodenheimer, P. H. 2003, ApJ, 588, 509

Guillot, T. 2008, Physica Scripta Volume T, 130, 014023

Harrington, J., Hansen, B. M., Luszcz, S. H., et al. 2006, Science, 314, 623

Hartman, J. D., Bakos, G. Á., Torres, G., et al. 2013, ArXiv e-prints

Hebb, L., Collier-Cameron, A., Loeillet, B., et al. 2009, ApJ, 693, 1920

Hebb, L., Collier-Cameron, A., Triaud, A. H. M. J., et al. 2010, ApJ, 708, 224

Hébrard, G., Bouchy, F., Pont, F., et al. 2008, A&A, 488, 763

Helled, R., Podolak, M., & Kovetz, A. 2006, Icarus, 185, 64

Hellier, C., Anderson, D. R., Collier Cameron, A., et al. 2013, ArXiv e-prints

Hellier, C., Anderson, D. R., Collier Cameron, A., et al. 2011a, A&A, 535, L7

Hellier, C., Anderson, D. R., Collier-Cameron, A., et al. 2011b, ApJ, 730, L31

Heng, K. 2012, ApJ, 748, L17

Heng, K. & Demory, B.-O. 2013, ApJ, 777, 100

Heng, K., Hayek, W., Pont, F., & Sing, D. K. 2012, MNRAS, 420, 20

Henry, G. W., Marcy, G. W., Butler, R. P., & Vogt, S. S. 2000, ApJ, 529, L41

Hilditch, R. W. 2001, An Introduction to Close Binary Stars

Holman, M. J., Fabrycky, D. C., Ragozzine, D., et al. 2010, Science, 330, 51

Holman, M. J. & Murray, N. W. 2005, Science, 307, 1288

Holman, M. J., Winn, J. N., Latham, D. W., et al. 2006, ApJ, 652, 1715

Houck, J. R., Roellig, T. L., Van Cleve, J., et al. 2004, in Society of Photo-Optical Instrumentation Engineers (SPIE) Conference Series, Vol. 5487, Optical, Infrared, and Millimeter Space Telescopes, ed. J. C. Mather, 62–76

Howard, A. W., Marcy, G. W., Bryson, S. T., et al. 2012, ApJS, 201, 15

Howard, A. W., Marcy, G. W., Johnson, J. A., et al. 2010, Science, 330, 653

Hubbard, W. B., Fortney, J. J., Lunine, J. I., et al. 2001, ApJ, 560, 413

Hubeny, I., Burrows, A., & Sudarsky, D. 2003, ApJ, 594, 1011

Huitson, C. M., Sing, D. K., Pont, F., et al. 2013, MNRAS, 434, 3252

Huitson, C. M., Sing, D. K., Vidal-Madjar, A., et al. 2012, MNRAS, 422, 2477

Ibgui, L. & Burrows, A. 2009, ApJ, 700, 1921

Ibgui, L., Spiegel, D. S., & Burrows, A. 2011, ApJ, 727, 75

Ida, S. & Lin, D. N. C. 2004, ApJ, 604, 388

Ida, S. & Lin, D. N. C. 2008, ApJ, 673, 487

Jehin, E., Gillon, M., Queloz, D., et al. 2011, The Messenger, 145, 2

Jensen, A. G., Redfield, S., Endl, M., et al. 2012, ApJ, 751, 86

Jensen, A. G., Redfield, S., Endl, M., et al. 2011, ApJ, 743, 203

Johnson, J. A., Butler, R. P., Marcy, G. W., et al. 2007, ApJ, 670, 833

Johnson, J. A., Gazak, J. Z., Apps, K., et al. 2012, AJ, 143, 111

Johnson, J. A., Winn, J. N., Albrecht, S., et al. 2009, PASP, 121, 1104

Johnson, J. B. 1928, Phys. Rev., 32, 97

Jordán, A., Espinoza, N., Rabus, M., et al. 2013, ApJ, 778, 184

Kane, S. R., Collier Cameron, A., Horne, K., et al. 2004, MNRAS, 353, 689

Kane, S. R., Horne, K., Street, R. A., et al. 2003, in Astronomical Society of the Pacific Conference Series, Vol. 294, Scientific Frontiers in Research on Extrasolar Planets, ed. D. Deming & S. Seager, 387–390

Karkoschka, E. 1994, Icarus, 111, 174

Kepler, J. 1609, Astronomia nova.

Knutson, H. A., Charbonneau, D., Allen, L. E., Burrows, A., & Megeath, S. T. 2008, ApJ, 673, 526

Knutson, H. A., Charbonneau, D., Allen, L. E., et al. 2007a, Nature, 447, 183

Knutson, H. A., Charbonneau, D., Cowan, N. B., et al. 2009a, ApJ, 703, 769

Knutson, H. A., Charbonneau, D., Cowan, N. B., et al. 2009b, ApJ, 690, 822

Knutson, H. A., Charbonneau, D., Deming, D., & Richardson, L. J. 2007b, PASP, 119, 616

Knutson, H. A., Charbonneau, D., Noyes, R. W., Brown, T. M., & Gilliland, R. L. 2007c, ApJ, 655, 564

Knutson, H. A., Howard, A. W., & Isaacson, H. 2010, ApJ, 720, 1569

Knutson, H. A., Lewis, N., Fortney, J. J., et al. 2012, ApJ, 754, 22

Konacki, M., Torres, G., Jha, S., & Sasselov, D. D. 2003, Nature, 421, 507

Konacki, M., Torres, G., Sasselov, D. D., et al. 2004, ApJ, 609, L37

Kopparapu, R. k., Kasting, J. F., & Zahnle, K. J. 2012, ApJ, 745, 77

Kornet, K., Bodenheimer, P., Różyczka, M., & Stepinski, T. F. 2005, A&A, 430, 1133

Kovács, G., Hodgkin, S., Sipőcz, B., et al. 2013, MNRAS, 433, 889

Kovács, G., Zucker, S., & Mazeh, T. 2002, A&A, 391, 369

Kozai, Y. 1962, AJ, 67, 591

Lang, D., Hogg, D. W., Mierle, K., Blanton, M., & Roweis, S. 2010, AJ, 139, 1782

Langland-Shula, L. E., Vogt, S. S., Charbonneau, D., Butler, P., & Marcy, G. 2009, ApJ, 696, 1355

Lardner, D. 1858, Hand-Books of Natural Philosophy and Astronomy

Laughlin, G., Crismani, M., & Adams, F. C. 2011, ApJ, 729, L7

Lecavelier Des Etangs, A., Ehrenreich, D., Vidal-Madjar, A., et al. 2010, A&A, 514, A72

Lecavelier Des Etangs, A., Pont, F., Vidal-Madjar, A., & Sing, D. 2008, A&A, 481, L83

Leconte, J., Chabrier, G., Baraffe, I., & Levrard, B. 2010, A&A, 516, A64

Lee, J.-M., Fletcher, L. N., & Irwin, P. G. J. 2012, MNRAS, 420, 170

Léger, A., Rouan, D., Schneider, J., et al. 2009, A&A, 506, 287

Lendl, M., Afonso, C., Koppenhoefer, J., et al. 2010, A&A, 522, A29

Lendl, M., Anderson, D. R., Collier-Cameron, A., et al. 2012, A&A, 544, A72

Lendl, M., Gillon, M., Queloz, D., et al. 2013, A&A, 552, A2

Levrard, B., Winisdoerffer, C., & Chabrier, G. 2009, ApJ, 692, L9

Lewis, N. K., Knutson, H. A., Showman, A. P., et al. 2013, ApJ, 766, 95

Lin, D. N. C. & Papaloizou, J. 1986, ApJ, 309, 846

Line, M. R., Knutson, H., Wolf, A., & Yung, Y. 2013a, ArXiv e-prints

Line, M. R., Knutson, H., Wolf, A., & Yung, Y. 2013b, ArXiv e-prints

Line, M. R. & Yung, Y. L. 2013, ApJ, 779, 3

Line, M. R., Zhang, X., Vasisht, G., et al. 2012, ApJ, 749, 93

Linsky, J. L., Yang, H., France, K., et al. 2010, ApJ, 717, 1291

Liu, X., Burrows, A., & Ibgui, L. 2008, ApJ, 687, 1191

López-Morales, M., Coughlin, J. L., Sing, D. K., et al. 2010, ApJ, 716, L36

Lucy, L. B. & Sweeney, M. A. 1971, AJ, 76, 544

Machalek, P., McCullough, P. R., Burke, C. J., et al. 2008, ApJ, 684, 1427

Machalek, P., McCullough, P. R., Burrows, A., et al. 2009, ApJ, 701, 514

Madhusudhan, N. 2012, ApJ, 758, 36

Madhusudhan, N., Harrington, J., Stevenson, K. B., et al. 2011, Nature, 469, 64

Madhusudhan, N. & Seager, S. 2009, ApJ, 707, 24

Madhusudhan, N. & Seager, S. 2010, ApJ, 725, 261

Madhusudhan, N. & Seager, S. 2011, ApJ, 729, 41

Majeau, C., Agol, E., & Cowan, N. B. 2012, ApJ, 747, L20

Mancini, L., Ciceri, S., Chen, G., et al. 2013, MNRAS

Mandel, K. & Agol, E. 2002, ApJ, 580, L171

Mandell, A., Haynes, K., Sinukoff, E., et al. 2013, ArXiv e-prints

Marcy, G., Butler, R. P., Fischer, D., et al. 2005, Progress of Theoretical Physics Supplement, 158, 24

Marcy, G. W. & Butler, R. P. 1996, ApJ, 464, L147

Marcy, G. W., Butler, R. P., Vogt, S. S., et al. 2008, Physica Scripta Volume T, 130, 014001

Markwardt, C. B. 2009, in Astronomical Society of the Pacific Conference Series, Vol. 411, Astronomical Data Analysis Software and Systems XVIII, ed. D. A. Bohlender, D. Durand, & P. Dowler, 251

Marley, M. S., Ackerman, A. S., Cuzzi, J. N., & Kitzmann, D. 2013, ArXiv e-prints

Marois, C., Macintosh, B., Barman, T., et al. 2008, Science, 322, 1348

Masset, F. S. & Papaloizou, J. C. B. 2003, ApJ, 588, 494

Matsumura, S., Peale, S. J., & Rasio, F. A. 2010, ApJ, 725, 1995

Maxted, P. F. L., Anderson, D. R., Collier Cameron, A., et al. 2013, PASP, 125, 48

Mayne, N. J., Baraffe, I., Acreman, D. M., et al. 2013, ArXiv e-prints

Mayor, M., Bonfils, X., Forveille, T., et al. 2009a, A&A, 507, 487

Mayor, M., Marmier, M., Lovis, C., et al. 2011, ArXiv e-prints

Mayor, M., Pepe, F., Queloz, D., et al. 2003, The Messenger, 114, 20

Mayor, M. & Queloz, D. 1995, Nature, 378, 355

Mayor, M., Udry, S., Lovis, C., et al. 2009b, A&A, 493, 639

Mayor, M., Udry, S., Lovis, C., et al. 2009c, A&A, 493, 639

Mazeh, T., Nachmani, G., Sokol, G., Faigler, S., & Zucker, S. 2012, A&A, 541, A56

Mazeh, T., Naef, D., Torres, G., et al. 2000, ApJ, 532, L55

McArthur, B. E., Endl, M., Cochran, W. D., et al. 2004, ApJ, 614, L81

McCullough, P. R., Stys, J. E., Valenti, J. A., et al. 2005, PASP, 117, 783

McLaughlin, D. B. 1924, ApJ, 60, 22

Menager, H., Barthélemy, M., Koskinen, T., et al. 2013, Icarus, 226, 1709

Menou, K. & Goodman, J. 2004, ApJ, 606, 520

Mihalas, D. 1978, Stellar atmospheres /2nd edition/

Miller, N., Fortney, J. J., & Jackson, B. 2009, ApJ, 702, 1413

Milne, E. A. 1921, MNRAS, 81, 361

Mislis, D., Schröter, S., Schmitt, J. H. M. M., Cordes, O., & Reif, K. 2010, A&A, 510, A107

Moehler, S., Freudling, W., Møller, P., et al. 2010, PASP, 122, 93

Moffat, A. F. J. 1969, A&A, 3, 455

Mordasini, C., Alibert, Y., & Benz, W. 2009a, A&A, 501, 1139

Mordasini, C., Alibert, Y., Benz, W., & Naef, D. 2009b, A&A, 501, 1161

Morton, T. D. & Johnson, J. A. 2011, ApJ, 729, 138

Moses, J. I., Line, M. R., Visscher, C., et al. 2013, ApJ, 777, 34

Moses, J. I., Visscher, C., Fortney, J. J., et al. 2011, ApJ, 737, 15

Moutou, C., Hébrard, G., Bouchy, F., et al. 2009, A&A, 498, L5

Muirhead, P. S., Johnson, J. A., Apps, K., et al. 2012, ApJ, 747, 144

Naef, D., Latham, D. W., Mayor, M., et al. 2001, A&A, 375, L27

Naoz, S., Farr, W. M., Lithwick, Y., Rasio, F. A., & Teyssandier, J. 2011, Nature, 473, 187

Narita, N., Enya, K., Sato, B., et al. 2007, PASJ, 59, 763

Narita, N., Fukui, A., Ikoma, M., et al. 2013, ApJ, 773, 144

Nelson, R. P., Papaloizou, J. C. B., Masset, F., & Kley, W. 2000, MNRAS, 318, 18

Nutzman, P. A., Fabrycky, D. C., & Fortney, J. J. 2011, ApJ, 740, L10

Orosz, J. A., Welsh, W. F., Carter, J. A., et al. 2012a, ApJ, 758, 87

Orosz, J. A., Welsh, W. F., Carter, J. A., et al. 2012b, Science, 337, 1511

Paardekooper, S.-J. & Mellema, G. 2006, A&A, 459, L17

Pepe, F., Mayor, M., Galland, F., et al. 2002, A&A, 388, 632

Perna, R., Menou, K., & Rauscher, E. 2010, ApJ, 724, 313

Petigura, E. A., Howard, A. W., & Marcy, G. W. 2013, Proceedings of the National Academy of Science, 110, 19273

Pollacco, D. L., Skillen, I., Collier Cameron, A., et al. 2006, PASP, 118, 1407

Pollack, J. B., Hubickyj, O., Bodenheimer, P., et al. 1996, Icarus, 124, 62

Pont, F., Bouchy, F., Queloz, D., et al. 2004, A&A, 426, L15

Pont, F., Gilliland, R. L., Knutson, H., Holman, M., & Charbonneau, D. 2009, MNRAS, 393, L6

Pont, F., Gilliland, R. L., Moutou, C., et al. 2007, A&A, 476, 1347

Pont, F., Tamuz, O., Udalski, A., et al. 2008, A&A, 487, 749

Pont, F., Zucker, S., & Queloz, D. 2006, MNRAS, 373, 231

Queloz, D., Bouchy, F., Moutou, C., et al. 2009, A&A, 506, 303

Queloz, D., Eggenberger, A., Mayor, M., et al. 2000, A&A, 359, L13

Queloz, D., Henry, G. W., Sivan, J. P., et al. 2001, A&A, 379, 279

Rasio, F. A. & Ford, E. B. 1996, Science, 274, 954

Rasio, F. A., Tout, C. A., Lubow, S. H., & Livio, M. 1996, ApJ, 470, 1187

Redfield, S., Endl, M., Cochran, W. D., & Koesterke, L. 2008, ApJ, 673, L87

Reif, K., Poschmann, H., Bagschik, K., et al. 2000, in Astrophysics and Space Science Library, Vol. 252, Astrophysics and Space Science Library, ed. P. Amico & J. W. Beletic, 143

Richardson, L. J., Deming, D., Horning, K., Seager, S., & Harrington, J. 2007, Nature, 445, 892

Richardson, L. J., Deming, D., & Seager, S. 2003, ApJ, 597, 581

Rieke, G. H. 2007, ARA&A, 45, 77

Rieke, G. H., Young, E. T., Engelbracht, C. W., et al. 2004, ApJS, 154, 25

Rodler, F., Kürster, M., & Barnes, J. R. 2013, MNRAS, 432, 1980

Rodler, F., Lopez-Morales, M., & Ribas, I. 2012, ApJ, 753, L25

Rogers, J. C., Apai, D., López-Morales, M., Sing, D. K., & Burrows, A. 2009, ApJ, 707, 1707

Rossiter, R. A. 1924, ApJ, 60, 15

Rufener, F. & Nicolet, B. 1988, A&A, 206, 357

Sackett, P. D. 1999, in NATO ASIC Proc. 532: Planets Outside the Solar System: Theory and Observations, ed. J.-M. Mariotti & D. Alloin, 189

Sanchis-Ojeda, R. & Winn, J. N. 2011, ApJ, 743, 61

Sanchis-Ojeda, R., Winn, J. N., Holman, M. J., et al. 2011, ApJ, 733, 127

Santos, N. C., Israelian, G., & Mayor, M. 2004, A&A, 415, 1153

Schmitt, J. R., Wang, J., Fischer, D. A., et al. 2013, ArXiv e-prints

Schneider, D. P., Gunn, J. E., & Hoessel, J. G. 1983, ApJ, 264, 337

Schwamb, M. E., Orosz, J. A., Carter, J. A., et al. 2013, ApJ, 768, 127

Schwarz. 1978, Annals of Statistics, 6, 461

Schwarzschild, K. 1906, Nachrichten von der Gesellschaft der Wissenschaften zu Göttingen, Mathematisch-Physikalische Klasse, 1906, 41

Seager, S. & Mallén-Ornelas, G. 2003, ApJ, 585, 1038

Seager, S., Richardson, L. J., Hansen, B. M. S., et al. 2005, ApJ, 632, 1122

Seager, S. & Sasselov, D. D. 1998, ApJ, 502, L157

Seager, S. & Sasselov, D. D. 2000, ApJ, 537, 916

Showman, A. P., Cooper, C. S., Fortney, J. J., & Marley, M. S. 2008, ApJ, 682, 559

Showman, A. P., Fortney, J. J., Lian, Y., et al. 2009, ApJ, 699, 564

Showman, A. P. & Guillot, T. 2002, A&A, 385, 166

Sing, D. K., Désert, J.-M., Fortney, J. J., et al. 2011a, A&A, 527, A73

Sing, D. K., Désert, J.-M., Lecavelier Des Etangs, A., et al. 2009, A&A, 505, 891

Sing, D. K., Huitson, C. M., Lopez-Morales, M., et al. 2012, MNRAS, 426, 1663

Sing, D. K. & López-Morales, M. 2009, A&A, 493, L31

Sing, D. K., Pont, F., Aigrain, S., et al. 2011b, MNRAS, 416, 1443

Sing, D. K., Vidal-Madjar, A., Désert, J.-M., Lecavelier des Etangs, A., & Ballester, G. 2008a, ApJ, 686, 658

Sing, D. K., Vidal-Madjar, A., Lecavelier des Etangs, A., et al. 2008b, ApJ, 686, 667

Smalley, B., Anderson, D. R., Collier-Cameron, A., et al. 2012, A&A, 547, A61

Smith, A. M. S., Anderson, D. R., Skillen, I., Collier Cameron, A., & Smalley, B. 2011, MNRAS, 416, 2096

Snellen, I. A. G. 2005, MNRAS, 363, 211

Snellen, I. A. G., Albrecht, S., de Mooij, E. J. W., & Le Poole, R. S. 2008, A&A, 487, 357

Snellen, I. A. G. & Covino, E. 2007, MNRAS, 375, 307

Snellen, I. A. G., de Kok, R. J., de Mooij, E. J. W., & Albrecht, S. 2010, Nature, 465, 1049

Snellen, I. A. G., de Mooij, E. J. W., & Albrecht, S. 2009, Nature, 459, 543

Socrates, A. 2013, ArXiv e-prints

Southworth, J., Hinse, T. C., Jørgensen, U. G., et al. 2009, MNRAS, 396, 1023

Southworth, J., Wheatley, P. J., & Sams, G. 2007, MNRAS, 379, L11

Spiegel, D. S. & Burrows, A. 2013, ApJ, 772, 76

Spiegel, D. S., Silverio, K., & Burrows, A. 2009, ApJ, 699, 1487

Stetson, P. B. 1987, PASP, 99, 191

Stevenson, K. B., Bean, J. L., Seifahrt, A., et al. 2013, ArXiv e-prints

Stevenson, K. B., Harrington, J., Nymeyer, S., et al. 2010, Nature, 464, 1161

Street, R. A., Pollaco, D. L., Fitzsimmons, A., et al. 2003, in Astronomical Society of the Pacific Conference Series, Vol. 294, Scientific Frontiers in Research on Extrasolar Planets, ed. D. Deming & S. Seager, 405–408

Struve, O. 1952, The Observatory, 72, 199

Sudarsky, D., Burrows, A., & Hubeny, I. 2003, ApJ, 588, 1121

Swain, M. R., Tinetti, G., Vasisht, G., et al. 2009a, ApJ, 704, 1616

Swain, M. R., Vasisht, G., & Tinetti, G. 2008, Nature, 452, 329

Swain, M. R., Vasisht, G., Tinetti, G., et al. 2009b, ApJ, 690, L114

Tamuz, O., Mazeh, T., & Zucker, S. 2005, MNRAS, 356, 1466

Tegmark, M., Strauss, M. A., Blanton, M. R., et al. 2004, Physical Review D, 69, 103501

Terquem, C. E. J. M. L. J. 2003, MNRAS, 341, 1157

Tinetti, G., Deroo, P., Swain, M. R., et al. 2010, ApJ, 712, L139

Todorov, K. O., Deming, D., Knutson, H. A., et al. 2012, ApJ, 746, 111

Toomre, A. 1964, ApJ, 139, 1217

Torres, G., Andersen, J., & Giménez, A. 2010, A&A Rev., 18, 67

Torres, G., Fressin, F., Batalha, N. M., et al. 2011, ApJ, 727, 24

Tregloan-Reed, J., Southworth, J., & Tappert, C. 2013, MNRAS, 428, 3671

Triaud, A. H. M. J. 2011, A&A, 534, L6

Triaud, A. H. M. J., Anderson, D. R., Collier Cameron, A., et al. 2013, A&A, 551, A80

Triaud, A. H. M. J., Collier Cameron, A., Queloz, D., et al. 2010, A&A, 524, A25

Trilling, D. E., Benz, W., Guillot, T., et al. 1998, ApJ, 500, 428

Udalski, A., Szymanski, M., Kaluzny, J., Kubiak, M., & Mateo, M. 1992, Acta Astron., 42, 253

Udry, S., Mayor, M., & Santos, N. C. 2003, A&A, 407, 369

Udry, S. & Santos, N. C. 2007, ARA&A, 45, 397

Vidal-Madjar, A., Désert, J.-M., Lecavelier des Etangs, A., et al. 2004, ApJ, 604, L69

Vidal-Madjar, A., Huitson, C. M., Bourrier, V., et al. 2013, ArXiv e-prints

Vidal-Madjar, A., Lecavelier des Etangs, A., Désert, J.-M., et al. 2003, Nature, 422, 143

Ward, W. R. 1997, Icarus, 126, 261

Weidenschilling, S. J. & Marzari, F. 1996, Nature, 384, 619

Welsh, W. F., Orosz, J. A., Carter, J. A., et al. 2012, Nature, 481, 475

Werner, M. W., Roellig, T. L., Low, F. J., et al. 2004, ApJS, 154, 1

Wheatley, P. J., Pollacco, D. L., Queloz, D., et al. 2013, in European Physical Journal Web of Conferences, Vol. 47, European Physical Journal Web of Conferences, 13002

Wilson, D. M., Gillon, M., Hellier, C., et al. 2008, ApJ, 675, L113

Winn, J. N. 2011, Exoplanet Transits and Occultations, ed. S. Seager, 55–77

Winn, J. N., Fabrycky, D., Albrecht, S., & Johnson, J. A. 2010, ApJ, 718, L145

Winn, J. N. & Holman, M. J. 2005, ApJ, 628, L159

Winn, J. N., Holman, M. J., Torres, G., et al. 2008, ApJ, 683, 1076

Winn, J. N., Johnson, J. A., Albrecht, S., et al. 2009, ApJ, 703, L99

Winn, J. N., Johnson, J. A., Marcy, G. W., et al. 2006, ApJ, 653, L69

Winn, J. N., Matthews, J. M., Dawson, R. I., et al. 2011, ApJ, 737, L18

Wood, P. L., Maxted, P. F. L., Smalley, B., & Iro, N. 2011, MNRAS, 412, 2376

Wright, J. T., Marcy, G. W., Howard, A. W., et al. 2012, ApJ, 753, 160

Wu, Y. & Murray, N. 2003, ApJ, 589, 605

Wu, Y., Murray, N. W., & Ramsahai, J. M. 2007, ApJ, 670, 820

Young, A. T. 1967, AJ, 72, 747

Young, A. T. 1993, The Observatory, 113, 41

Zahnle, K., Marley, M. S., Freedman, R. S., Lodders, K., & Fortney, J. J. 2009, ApJ, 701, L20

Zhou, G. & Bayliss, D. D. R. 2012, MNRAS, 426, 2483

Zhou, G., Kedziora-Chudczer, L., Bayliss, D. D. R., & Bailey, J. 2013, ApJ, 774, 118